Title

Kinetics of Low Abundant Intracellular Molecules, Including Receptors, Signaling Molecules, and Hormones in Human Health and Disease Using Heavy Water (2H2O) Labeling and Mass Spectrometry

Author

Dandan, Mohamad Talal

Publication Date

2022

Kinetics of Low Abundant Intracellular Molecules, Including Receptors, Signaling Molecules, and Hormones in Human Health and Disease Using Heavy Water (^2H_2O) Labeling and Mass Spectrometry

By

Mohamad T Dandan

A dissertation submitted in partial satisfaction of the

requirements for the degree of

Doctor of Philosophy

in

Metabolic Biology

in the

Graduate Division

of the

University of California, Berkeley

Committee in charge:

Professor Marc Hellerstein, Chair
Professor Andreas Stahl
Professor George Brooks

Spring 2022

Abstract

Kinetics of Low Abundant Intracellular Molecules, Including Receptors, Signaling Molecules, and Hormones in Human Health and Disease Using Heavy Water (^2H_2O) Labeling and Mass Spectrometry

by

Mohamad T Dandan

Doctor of Philosophy in Metabolic Biology

University of California, Berkeley

Professor Marc Hellerstein, Chair

My broad goals are to use new stable isotopic metabolic labeling techniques with tandem mass spectrometric analysis to measure in both preclinical models and human subjects, the synthesis and breakdown rates of low abundance proteins that play key roles in common metabolic disorders such as heart disease, diabetes, non-alcoholic fatty liver disease and counterregulatory hormones on muscle protein metabolism. First, I developed a mass spectrometry method to measure the turnover rates of the low-density lipoprotein receptor (LDLR) and proprotein convertase subtilisin/kexin type 9 (PCSK9). We revealed that lower hepatic synthesis and secretion of PCSK9, an SREBP2 (sterol response element binding protein) target gene, results in longer hepatic LDLR t½ in response to cholesterol feeding in mice in the face of high intracellular cholesterol content. PCSK9 modulation opposes the canonical lowering of LDLR mRNA and synthesis by cholesterol surplus and preserves LDLR levels. Secondly, I developed a non-invasive technique using ^2H_2O labeling and mass spectrometry for measuring the synthesis of pancreatic beta cell insulin in circulation as a tool to monitor the progression of diabetes in human beings. The significance of this work is that a) we have revealed how long pancreatic beta cell insulin lives for, and b) the effect of prediabetes on insulin biogenesis. Our third objective was to develop a method to determine the kinetics of PNPLA3, Patatin-like phospholipase domain-containing protein 3. This gene single nucleotide polymorphisms confers susceptibility for non-alcoholic fatty liver disease (NAFLD) by accumulating PNPLA3 proteins on lipid droplets. To understand the kinetic basis of this genetic polymorphisms associated with NAFLD, we would like to determine how PNPLA3 turnover rates are altered in the liver in NAFLD patients with different PNPLA3 genetic backgrounds. Our fourth objective investigated how the treatment with acetyl-CoA carboxylase inhibitors (ACCi) increases plasma triglyceride (TG) concentrations in patients with non-alcoholic steatohepatitis (NASH), with variable results reported for concentrations of plasma apolipoprotein B (ApoB). We determined the effects of treatment with the ACCi, firsocostat in NASH on production and clearance rates of plasma LDL ApoB-containing particles. For the last part of this dissertation, I used stable isotopic labeling with ^2H_2O combined with mass spectrometry to measure the turnover rates of proteins across the proteome in response to glucocorticoid treatment and/or in a Pik3r1 (a glucocorticoid response gene) knockout mouse model. We revealed a suppressive effect on lowering protein turnover rates in muscle of Pik3r1 knockout mice when

given dexamethasone. This dynamic proteomic study revealed how Pik3r1 regulates skeletal muscle protein metabolism. Collectively, these studies are anticipated to shed insight into the metabolic physiology of common metabolic diseases such as atherosclerotic cardiovascular disease (ASCVD), type 2 diabetes mellitus (T2D), non-alcoholic fatty liver disease, and muscle protein metabolism.

Dedication Page

To my father, Talal "Baba" Rashad Dandan, RIP: Approximately, one year ago on January 28. 2021, my father passed away at the age of 78 from cardiac arrest. He suffered from heart disease, type II diabetes, hypertension, diabetic kidney disease and associated diabetic complications. He survived a triple by-pass surgery and a stroke. As a child, I remember spending a lot of time at the pharmacy, doctor offices and medical facilities. Unconsciously, I had an innate interest to understand his conditions and apply this knowledge for my graduate study. Today, I luckily had the privilege to carry out my studies in metabolic biology that have made instrumental discoveries in metabolic diseases such as of arteriosclerosis, diabetes, and fatty liver disease. He was a great man of wisdom and practicality who taught to me to keep calm, cool, collective, and proactive. He highly valued education as it is your "life insurance" that no one can take away from you and to always "keep digging" for what you value in this world. I remember his last words to me was to "Save your energy, because you will need it when you get older." As for graduate studies, it certainly takes persistence, perseverance, and proactivity to push the boundaries of knowledge. Even though he will not be here for my PhD graduation, he will always be in my heart.

Table of Contents

Preface

We measured the turnover rates of the low-density lipoprotein receptor (LDLR) and proprotein convertase subtilisin/kexin type 9 (PCSK9) in mice by metabolic labeling with heavy water (^2H_2O) and mass spectrometry. In liver of mice fed high-cholesterol diets, LDLR mRNA levels and synthesis rates were markedly lower with complete suppression of cholesterol synthesis and higher cholesterol content, consistent with the Brown-Goldstein model of tissue cholesterol homeostasis. We observed markedly lower PCSK9 mRNA levels and synthesis rates in liver and lower concentrations and synthesis rates in plasma. Hepatic LDLR half-life (t ½) was prolonged, consistent with an effect of reduced PCSK9, and resulted in no reduction in hepatic LDLR content despite reduced mRNA levels and LDLR synthesis rates. These changes in PCSK9 synthesis complement and expand the well-established model of tissue cholesterol homeostasis in mouse liver, in that reduced synthesis and levels of PCSK9 counterbalance lower LDLR synthesis by promoting less LDLR catabolism, thereby maintaining uptake of LDL cholesterol into liver despite high intracellular cholesterol concentrations. Lower hepatic synthesis and secretion of PCSK9, an SREBP-2 target gene, results in longer hepatic LDLR t ½ in response to cholesterol feeding in mice in the face of high intracellular cholesterol content. PCSK9 modulation opposes the canonical lowering of LDLR mRNA and synthesis by cholesterol surplus and preserves LDLR levels. The physiologic and therapeutic implications of these opposing control mechanisms over liver LDLR are of interest and may reflect subservience of hepatic cholesterol homeostasis to whole body cholesterol needs. Next, we will apply our technology to not only measure the turnover rates of receptors, but we would like to measure the turnover rates of secreted hormones such as insulin.

Insulin is a peptide hormone that regulates the metabolism of carbohydrates, proteins, and fats. Pancreatic beta cells specifically synthesize and secretes insulin into blood circulation. Type II diabetes is characterized as the inability to respond to and produce insulin. As a progressive disease from a normal to a diabetic state, patients exhibit severe hyperglycemia, beta cell exhaustion and inability to synthesize insulin. There is currently minimal knowledge to measure insulin kinetics and methods to monitor the transition over the course of diabetic disease, however. Our objective is to measure the kinetics of insulin synthesis and secretion from pancreatic beta cells into blood in humans by use of stable isotopic metabolic labeling with heavy water (^2H_2O) and mass spectrometry. We hypothesize that pancreatic reserve or treatment thereof can be monitored or diagnosed by measuring plasma insulin kinetics as a non-invasive metric of pancreatic insulin. To test our hypothesis, insulin was isolated by immunoprecipitation from plasma in humans and its synthesis rate measured by ^2H_2O labeling and mass spectrometry. We recently determined by metabolic labeling that insulin in the human body has a half-life on the order of days, reflecting the turnover (replacement) of insulin in beta cell secretory granules by newly synthesized molecules. Whereas in metabolically abnormal obese patients, insulin turnover was significantly increased, reflecting increased insulin synthesis and secretion, and reduced insulin reserve capacity. These are the first insulin turnover direct experimental data in humans and the results are very promising, suggesting that pancreatic beta cell reserve, the key factor in progression from insulin resistance to type II diabetes, can be monitored by measuring plasma insulin kinetics in human subjects. Moreover, we did not only investigate hormonal kinetics in human beings, but we also further applied our technology to investigate the turnover rates of low abundant signaling proteins in humans with fatty liver disease.

My next objective was to determine the kinetics of Patatin-like phospholipase domain-containing protein 3 (PNPLA3). Single nucleotide polymorphisms in PNPLA3 confers susceptibility for the development non-alcoholic fatty liver disease (NAFLD). This leads to the accumulation of PNPLA3 proteins on lipid droplets which impairs accessibility for lipases. To understand the kinetic basis of this genetic polymorphisms (I148M) of PNPLA3 that is associated with NAFLD, we would like to determine how PNPLA3 turnover rates are altered in the liver in NAFLD patients with different PNPLA3 genetic backgrounds. PNPLA3 fractional synthesis rates displayed a trend of slower turnover from wildtype to heterozygote to homozygote genotypes, and slower PNPLA3 turnover correlated with intrahepatic triglyceride content (IHTG). These results suggests that impaired PNPLA3 clearance in I148M mutations lead to higher IHTG. This research provides a flux-based approach to measure the synthesis of rare intracellular molecules such as PNPLA3 to examine its for molecular kinetics to provide insight into their functions NAFLD. Additionally, we sought to investigate another issue of the pharmacological effects of acetyl-Coa carboxylase inhibitors on lipoprotein metabolism in NAFLD patients.

Treatment with acetyl-CoA carboxylase inhibitors (ACCi) increases plasma triglyceride (TG) concentrations in patients with non-alcoholic steatohepatitis (NASH), with variable results reported for concentrations of plasma apolipoprotein B (ApoB). Our objective here was to determine effects of treatment with the ACCi, firsocostat in NASH on production and clearance rates of plasma LDL ApoB-containing particles. We also evaluated the effects of combination therapy with fenofibrate. Metabolic labeling with heavy water and tandem mass spectrometric analysis of LDL-ApoB was carried out in 16 NASH patients at baseline and after 12 weeks of ACCi; in 29 subjects before and after concurrent ACCi and fenofibrate therapy for 12 weeks; and in 9 normolipidemic controls at baseline and after 4 weeks of ACCi treatment. In NASH, plasma TG increased significantly by 17% at week 12 (p=0.0056). LDL-ApoB fractional synthesis rate (FSR) significantly increased from baseline to week 12 (31 ± 5 to 46 ± 6 %/day, p=0.03) with a 47% increase in absolute synthesis rate (ASR) of LDL-ApoB (30.8 to 45.2 mg/dl/day, p=0.016). The effect on ASR was restricted to cirrhotic subjects: non-cirrhotic ASR 39.8 ± 20.8 and 46.3 ± 14.8 mg/dl/day at baseline and week 12 (p=0.51); cirrhotic 21.0 ± 9.6 and 44.2 ± 17 mg/dl/day at baseline and week 12 (p=0.002). No effects of ACCi treatment were seen in healthy controls on FSR, ASR or concentrations of ApoB or TG. Treatment with fenofibrate in combination with ACCi prevented increases in plasma TG and LDL-apoB FSR or ASR in cirrhotic NASH patients. In summary, our results show that ACCi treatment increases LDL-ApoB100 production rate in NASH with cirrhosis and that this can be prevented by concurrent fenofibrate therapy. Given the common theme of measuring individual protein turnover rates in metabolic disease, we concluded this dissertation work on the evaluating protein turnover on the proteomic wide level.

Lastly, we investigated chronic glucocorticoid exposure on muscle protein synthesis rates in skeletal muscle. Phosphoinositide-3-kinase regulatory subunit 1 (Pik3r1) was identified as a primary target of glucocorticoid receptors in skeletal muscle. However, how Pik3r1functions in vivo remains unclear. We created striated muscle specific Pik3r1 knockout (MKO) mice that were treated with dexamethasone (DEX). Wildtype (WT) mice with DEX suppressed insulin activity on Akt in liver, epididymal white adipose tissue, and gastrocnemius (GA) muscle. The DEX effect was reduced in GA muscle of the KO mice that lead to improved tolerance of glucose and insulin. Metabolic turnover studies with stable isotope labeling with heavy water lead that DEX treatment in wild type mice decreased protein fractional synthesis rates in GA muscle. Myotube diameters were reduced in MKO mice, along with increased fast twitch oxidative fibers. DEX was shown to not further reduce myotube diameters in MKO mice. Decreased basal protein synthesis rate (likely caused by lower 4E-BP1 phosphorylation at Thr37/Thr46) were observed in in Pik3r1 knockout mice. Lastly, in DEX suppressed eIF2α phosphorylation, and insulin-induced 4E-BP1 phosphorylation was reduced in MKO mice. Our results highlight the function of Pik3r1 in glucocorticoid-mediated effects on glucose and protein metabolism in skeletal muscle.

Acknowledgements

To my wife Braelyn Dandan. My love, spirit, best friend, and soulmate who has always unconditionally been there by my side. We met in the high school drama room when she was 14 and I was 16. I recall seeing her throughout the hallways and I finally had the chance to introduce myself. She was wearing a white tee-shirt with a spray-painted peace sign, denim shorts and rainbow-colored socks. I first said to her, “I like your style.” We made small talk and didn’t see each other for a few weeks, until I met her again after I broke my arm in a football accident. She signed my cast, and I got her number to get to know each other better. Time past and we made chats here and there until one day on my 18th birthday, she made me brownies out of cake mix. I knew something was special about her and we began to spend more time together, eventually forming a long-distance relationship while in college. I would commute back and forth on the weekends from UC Irvine to my hometown, or to her college at the University of La Verne. I always looked forward to seeing and spending time with her. She was instrumental in my success as we spent numerous hour study with each other at her college or at mine. I remember when I applied to graduate school. I did not know which program to apply for when I applied to Cal. So, I asked her what she thought, and her response was “do what makes you happy.” So, I applied to the Metabolic Biology, Ph.D. program. I truly thank her for being the best person, wife, and soulmate. This dissertation would not be possible with her overwhelming support (i.e., revising, editing, listening, late night lab dates, staying up at night), and her unconditional love.

To my mentor, Marc Hellerstein, M.D., Ph.D and his lab. When I arrived at Berkeley for the Metabolic Biology, Ph.D. program. I was not aware of Marc Hellerstein’s research until I met him during the required faculty research presentation class. I immediately was drawn to his research due to the technological perspective of using stable isotopes as metabolic labels combined with mass spectrometry to investigate the flux of metabolic pathways in human health and disease. I remember the first graphs he showed to the class was on DNA proliferation data in T.cells. I continued to read about his research and knew that this was the right lab for me. In the first part of my graduate career, I honestly learned more about Marc Hellerstein’s philosophies though his publications and brief discussion in the lab or meetings. However, as time went on and through the pandemic, his mentorship became closer as we frequently had discussions over text, calls, and zoom where we analyzed data and wrote manuscripts together. He has been a great mentor that looks out for students no matter their walks of life. He has taught me to take ahold of your research to really push your work. When you put the work in, he has been reciprocal in return. In a sense, he has been a great coach that has guided me to become a critical thinker, problem solver, and independent scientist. I am honored to have him as my mentor, Ph.D. dissertation committee chair, and colleague.

A special thanks to others that had a significant impact on my scientific development: Mark Fitch, Edna Nyangua, Kelvin Lee, Shubha, Hussein Mohammed, Wally Wang, Andreas Stahl, and George Brooks.

1. Chapter 1

1.1. History and Discovery: From Cholesterol to Low-density Lipoproteins to Low Density Lipoprotein Receptors.

Cardiovascular diseases (CVD) remain the number one cause of death in the United States and across the globe[1]. According to the Centers for Disease Control and Prevention (CDC), 659,000 Americans perished from heart disease, and the World Health Center predicts that 17.9 million pass away globally each year[2]. Treatment and prevention of heart disease-related cost about $363 billion each year[2]. These statistics arise alarming concerns. How can we prevent cardiovascular diseases by understanding their biology?

High blood pressure, smoking, diets rich in saturated fat, and high cholesterol represents key risk factors for the development of heart disease[3]. Atherosclerotic plaques represent the hallmark of cardiovascular diseases that can contribute to the occlusion of coronary arteries resulting in heart attacks[4]. Almost 3,500 years ago, hardening of arteries have been detected in Egyptian mummies[5]. As early as the 19th century, German pathologists described plaques on the surface of aortas. The term atherosclerosis was derived from the Greeks in which athero- meant gruel and -sclerosis meant hardness[6]. By 1910, Adolf Windaus found aortas enriched in plaque-like substance attributed later as cholesterol, a waxy-like substance made entirely of hydrocarbons and aliphatic rings[7]. Early evidence suggested that diets rich in cholesterol can induce atherosclerosis was shown by the work of Nikolai Antishkow who fed cholesterol to rabbits leading to heart disease[8].

One of the first studies to show nutritional regulation of cholesterol biosynthesis was when Rudolph Schoenheimer fed mice a cholesterol-free diet and observed increased cholesterol content[9]. Whereas mice that were fed a high cholesterol diet, there was no cholesterol present. This study showed that animals can synthesize cholesterol de-novo, and inhibition of cholesterol synthesis when present in the diet[9]. In 1950, Konrad Bloch uncovered the synthesis of the 27-carbon, 4-ring cholesterol molecule by polymerization of Acetyl-CoA that are all derived from the intermediate 3-hydroxy-3-methylglutaryl-CoA (HMG-CoA)[10]. International epidemiological studies have proposed the relationship between heart attacks and plasma cholesterol levels. Comparative studies showed diets less enriched in cholesterol had fewer incidences of cardiovascular disease[11]. Keys et al. showed an association between low blood cholesterol and low heart attacks before the methodology of plasma lipoprotein separation[12]. Hallmark investigations to determine the molecules responsible for transporting dietary cholesterol and that could potentially be atherogenic occurred here on the UC Berkeley campus.

In 1955, John Gofman applied analytical ultracentrifugation to isolate cholesterol yielding lipoproteins based on their hydrated densities[13]. This was the first time that researchers characterized two major lipoprotein particle classes known as low-density lipoproteins (LDL) and high-density lipoproteins (HDL). It was observed in plasma samples from heart attack patients that cholesterol levels were higher in the LDL fraction and lower in the HDL fraction[13]. These findings were not highly appreciated during their initial discoveries until researchers questioned and rekindled this relationship in the Framingham study[14]. This study established a strong inverse relationship between the incidences of coronary heart diseases and HDL cholesterol. An association was observed between LDL cholesterol against CVD. The relationship between low

HDL cholesterol and atherosclerosis development remains debated, whereas high plasma LDL is strongly associated with atherosclerosis in each of the mammalian species studied[15].

Could there be a genetic predisposition to the development of heart disease? The relationship between the dietary influence of high plasma cholesterol and atherosclerosis was clear but could there be a genetic explanation. Carl Muller described patients with familial hypercholesterolemia (FH). FH is an inherited autosomal dominant trait that is associated with high plasma cholesterol levels, early incidence of heart disease, and premature death[16]. The population frequencies are approximately 1 in 500 and 1 in 1,000,000 for heterozygotes or homozygotes individuals, respectively[17]. In 1964, a three-year-old patient John Despota was evaluated by his primary care physician for displaying a phenotype of eruptive xanthomas. The doctors checked his cholesterol which was reported six times as the normal concentration. As a preteen, John would experience chest pains, shortness of breath, and fatigue. John was diagnosed with FH and his physicians predicted his death in years. Thankfully to understand the pathology of FH and treatment through diet and pharmacology, he continues to live in his middle 50s. Most of his family also suffered from cardiovascular diseases, suggesting a familial inherited disease.

The physician that treated John questioned if his cells might have a genetic defect. In early 1970, John and his family cells were shipped to the University of Texas Southwestern where the pioneering work of Michal Brown and Joseph Goldstein was conducted[18]. They published a series of works that determined genetic defects in LDL uptake that pointed towards the cell surface[19]. By incubating FH cells with LDL, no suppression of cholesterol biosynthesis occurred in FH patients' skin cells, leading to dysregulated cholesterol metabolic feedback and thus increased levels. These experiments suggested LDL may bind a receptor for cellular uptake and the concept of cell surface transport receptors was only a preliminary idea. In ten years, Brown, and Goldstein isolated low-density lipoprotein receptors (LDLR) from bovine adrenal glands, determined the genetic defects in LDLR leading to FH and performed molecular cloning on the LDLR gene[20]. Cell microscopy and biochemical studies showed that FH patients either had defects in LDL uptake by altering synthesis, trafficking, binding, internalization, and recycling[21]. The predicted lifespan of LDLR is about 20 hours and it recycles back to the cell surface several hundred times that last about 10 minutes each[18].

John Despota was the first FH patient documented to have both a null synthesis and defective uptake[18]. Ultimately, these studies established evidence of the idea of receptor-mediated endocytosis. Transferrin receptor for iron uptake and even the insulin receptor for insulin metabolism joined this concept of internalizing specific molecules. They further showed the connection between the regulation of metabolism and receptor internalization. For example, when LDL is internalized by receptor-mediated endocytosis, the endosome fuses with the lysosome to form the endolysosome resulting in the deposition of cholesterol for its storage, use, or breakdown. The apolipoproteins are broken by acid hydrolyses to contribute to the amino acid pool. As a result, cholesterol levels increase leading to suppression of cholesterol biosynthesis and suppression of LDLR by its own receptor[21].

Around the world, epidemiological studies showed a relationship between LDL cholesterol and the development of heart disease. This led to investigations to determine compounds to decrease LDL levels. In 1970, Akira Endo identified extracts in a fungus that can decrease LDL levels later shown as statins which lowered cholesterol synthesis, increased LDLR levels, and decreased LDL cholesterol[22]. Today more than 30 million people take statins[18]. Additional studies were conducted to find other genetic predispositions to decreased incidence of heart disease. Helen Hobbs and Jay Horton identified in a genome-wide association sequencing study, genetic variants in a protein designated as Proprotein Convertase Subtilisin/Kexin Type 9 (PSCK9) that correlated with low cholesterol levels and incidence of heart disease[23]. Interestingly, biochemical studies eventually showed that PCSK9 binds to LDLR for lysosomal degradation[24]. Thus, genetic variants with less activity or levels of PCSK9 would have more LDLR levels and the ability to uptake LDL lowering cholesterol levels[25]. As a result, anti-PCSK9 antibodies have been developed to treat patients with severe LDL cholesterol concentrations[26].

1.2. Stable isotope tracer studies to study cell receptor turnover: LDLR to PCSK9 and beyond.

Schneider et al 1982 showed LDLR can be purified by a two-step method from crude bovine adrenal membranes by DEAR-cellulose chromatography and sepharose affinity chromatography conjugated to LDL or antibodies specific to LDLR[27]. These techniques allowed investigators like Brown and Goldstein to measure the synthesis, degradation, and turnover of LDLR using radioactive tracers in cell culture[20,28]. This helped to show that LDLR is initially synthesized as a 120 kDa precursor and matures to a 160 kDa form. More interesting are the applications which helped to identify FH patients with defective LDLR posttranslational processing[29]. Knight et al. showed in other FH patients that their LDLR precursor proteins exhibited a longer half-life than healthy cells. LDLR proteins eventually matured but had a significantly less binding affinity in FH patients. In lipoprotein deficient serum, LDLR synthesis increased in normal cells and healthy cells illustrating the relationship between receptor and cell metabolism[30].

Investigators like James Hare studied the compartmentation and turnover of LDLR in skin fibroblast. He questioned whether there is a difference in LDLR turnover in different cellular compartments such as the plasma membrane vs endocytic compartments. Approximately half of LDLR proteins partition between the cell surface and intracellular compartments but LDLR was shown to turnover faster on the cell surface, suggesting preferential localization to the cell surface then partitions to other membranes[31,32]. The accumulation of cholesterol in atrial monocyte-derived macrophages leading to inflammation presents a crucial process in atherosclerosis[33]. In other cells than skin fibroblast, human monocytic THP-1 LDLR turnover was studied due to these cells present a useful model for foam cell formation and their differentiation can be controlled by phorbol ester[34]. After phorbol treatment, LDLR displayed less binding activity which may be attributed to its rapid degradation than untreated cells[35].

The last example presented here of metabolic labeling with ^{35}S-methionine to measure LDLR turnover concludes with regulatory studies from Casciola et al[36]. They were interested in how short-lived mediators' proteins and sterol supply in the presence or absence of protein synthesis inhibitors (ie. cycloheximide) could influence the turnover of LDLR. The half-life was determined as 12 hours in human skin fibroblast and like previously mentioned studies, LDLR degradation rate was not affected in presence of LDL. In the presence of cycloheximide, the rate of LDLR degradation was inhibited which provided a clue of potential short-lived mediator proteins (ie. PSCK9) that regulate LDLR turnover since these putative proteins synthesis was inhibited in this experimental conditions[36]. The early tracers' studies were paramount for understanding the basic kinetic parameters of LDLR such as its half-life, cellular dynamics like receptor-mediated endocytosis, response to cell metabolism, nutrition, therapeutic interventions, and novel regulators such as PCSK9[22,23].

1.3. Where are we today?

LDLR turnover stands at the forefront of its biological function of LDL uptake/cholesterol delivery into the cell and the development of atherosclerosis[22]. Transcriptionally, the sterol response element-binding proteins (SREBP) regulate the expression of the LDLR based on sterol availably[37]. As cholesterol increases in content in the cell, cholesterol biosynthesis and LDLR synthesis are decreased[22]. Genetic studies determined a key regulator known as proprotein convertase subtilisin kexin (PSCK9) of LDLR turnover. This protein was discovered in patients with missense mutation associated with autosomal dominant hypercholesterolemia and loss of function associated with reduced coronary heart disease[23]. Biochemical studies showed that PSCK9 binds LDLR to traffic it to the lysosome for degradation resulting in less LDLR to uptake cholesterol and increased LDL cholesterol levels[23]. Common techniques to measure protein turnover were ^{35}S-methionine or radioactive labeling that determined the half-life of LDLR in cultured skin fibroblast as 12 hours whereas exogenous radioiodine PSCK9 clearance from the plasma half-life was determined as 5 mins[36,38]. Current approaches to measure low abundant molecules were shown in Lassman et al study that combined modern tracer techniques with deuterated leucine and high precision mass spectrometry and determined the fractional catabolic rate of PSCK9 in human plasma as 1.92 pools/day[39]. There was no effect of statins on PCSK9 turnover, but levels were increased which were consistent with other investigations[40]. From radioactive to stable isotopic metabolic labeling coupled with highly sensitive mass spectrometry, molecular flux analysis of these proteins and other low abundant/unique proteins can provide crucial information and methods to study and explain the role of LDLR and PCSK9 turnover in the canonical Brown and Goldstein model of cholesterol homeostasis[36,41,42].

1.4. Modern technology to measure the kinetics of LDLR and PCSK9 using heavy water labeling and mass spectrometry with Mass Isotopomer Distribution analysis.

The advent of state-of-the-art tandem mass spectrometry combined with stable isotopic metabolic labeling using heavy water (^2H_2O) offers a unique approach to studying LDLR and PSCK9 kinetics to explain pathophysiological processes in cardiovascular disease[41]. We will fill the gap in establishing this method and apply it in the following study as described below to determine the novel involvement of these proteins in metabolic diseases. Dynamic proteomics technology has been useful to understand how the global proteome turnover and associated biochemical pathways change with disease and treatment[41]. However, if we are interested in a particular low abundant target that does not appear in a common proteomic run (i.e., in-solution tryptic digest). Alternative approaches are to enrich, isolate and purify your target of interest by fractionation, chromatography, gel electrophoresis, or affinity purification[39]. This will open an avenue of research centered on molecular kinetics pathways that complement traditional static and shotgun proteomics approaches, meaning focused on a more targeted molecular approach than the global change.

The use of ^2H_2O labeling for metabolic labeling protein synthesis studies offers many advantages to traditional stable isotopic labeled amino acid tracer techniques[43]. ^2H_2O can be administered safely with minimal supervision in outpatient studies. It freely and rapidly equilibrates after administration followed by incorporation into amino acids via metabolic incorporation in the TCA cycle or transamination reactions. The labeled ^2H amino acids are incorporated into proteins during translation that can be monitored over time. The change in isotopic enrichment in tryptic peptides of LDLR and PCSK9 are analyzed by mass isotopomer distribution analysis (MIDA) to ultimately determine the fractional synthesis of these single proteins or on the global scale[44,45] (**Figure 2**).

To our knowledge, there are no studies that have measured LDLR and PSCK9 turnover using our tracer technology within in vivo systems. Therefore, we propose to method measure the synthesis of LDLR and associated regulatory proteins PSCK9 using ^2H_2O labeling and mass spectrometry in whole intact in-vivo systems. Quadrupole time of flight instruments is routinely used in protein kinetic studies by evaluating the ratio of isotopomers (isomers of organic compounds that differ by position in isotope) after label incorporation on the MS level. This has been beneficial for accurate measurements of isotopomer ratio analysis using MIDA[45]. Recently, the development of orbitrap mass analyzers that evaluate the change in isotopologue (groups of compounds that differ by isotopic compositions) distributions will enable improved sensitivity to measure low abundant, and less enriched molecules over a short period on the MS/MS level[46]. Therefore, we will apply these methods to determine the half-life of LDLR and regulatory protein PSCK9 using LC/MS and ^2H_2O labeling in vivo in mice[41,46].

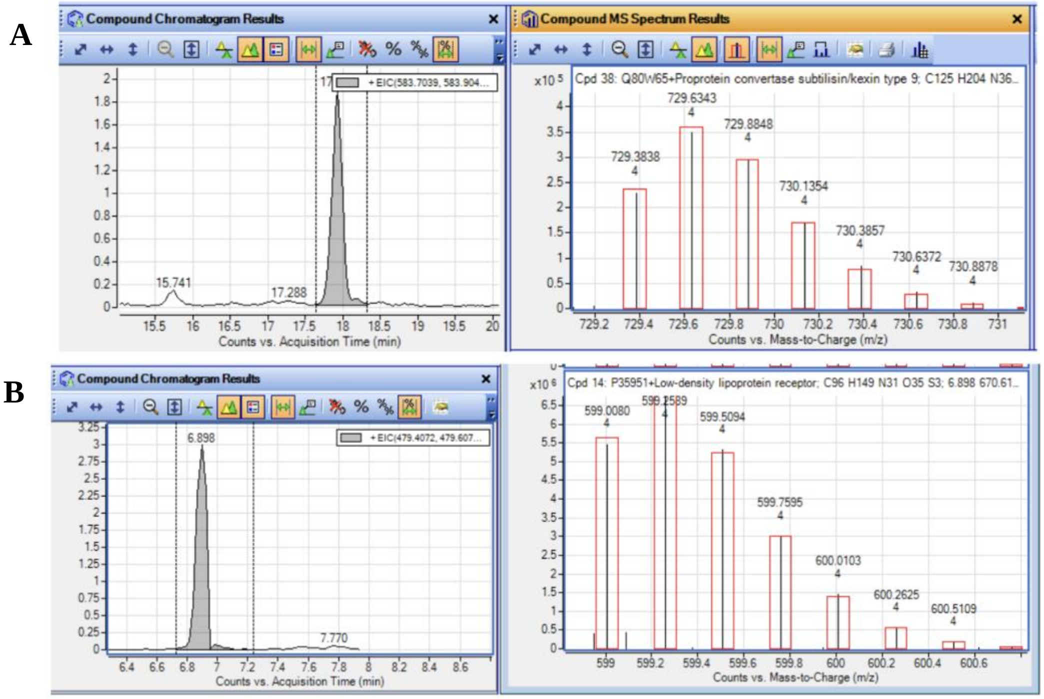

Figure 2. LDLR and PCSK9 chromatogram and mass isotopomer distribution. **A)** PCSK9 was separated from a complex immunoprecipitated mixture by high-performance liquid chromatography (HPLC) and identified by mass spectrometry. The resulting isotopomer distribution envelope displays how the enrichment of mass isotopomer changes over time with respect to the labeling period allowing us to calculate the fractional synthesis of PCSK9 over time.

B) LDLR was separated from a complex immunoprecipitated mixture by HPLC and identified by mass spectrometry. The resulting isotopomer distribution displays how the enrichment of mass isotopomer changes over time with respect to the labeling period allowing us to calculate the fractional synthesis of LDLR over time.

1.5. How are LDLR/PCSK9 turnover rates regulated (synthesis, degradation) under high cholesterol diet and what is their role in the canonical Brown and Goldstein model?

The current model of cholesterol regulation describes how increased cholesterol content in the cell downregulates the number of LDLR however minimal knowledge is known about how LDLR/PCSK9 kinetics are affected by this process and how diet enriched in cholesterol effect LDLR/PCSK9 kinetics in vivo. As crucial molecules in cholesterol homeostasis and the development of heart disease, LDLR uptakes low-density lipoprotein cholesterol whereas the secreted protein, PCSK9, targets LDLR for lysosomal degradation. A high-fat diet or high cholesterol diet fed mice resulted in fewer LDLR levels perhaps by modulating LDLR synthesis[47]. As cellular cholesterol levels increase, this leads to the inactivation of SREBP2, a transcription factor that promotes cholesterol synthesis and cholesterol uptake by increasing LDLR expression. Genetic mouse models have been informative for studying LDLR in lipid metabolism and atherosclerotic disease[48]. PSCK9 was identified as an SREBP regulated gene from microarrays in SREBP knockout and overexpression studies[49,50]. Overexpression of PCSK9 led to increasing degradation of LDLR but did not affect LDLR synthesis[49,50]. Rashid et al demonstrated that PCSK9 KO mice had increased hepatic protein LDLR levels[48]. Evolocumab, an approved FDA biological therapy, has been prescribed to patients with hypercholesterolemia. These antibodies bind and inhibit PSCK9 resulting in less LDLR degradation and more LDLR to uptake LDL particles to reduce LDL cholesterol[48,51]. Gain of function mutations in PSCK9 increased CVD development in humans[52].

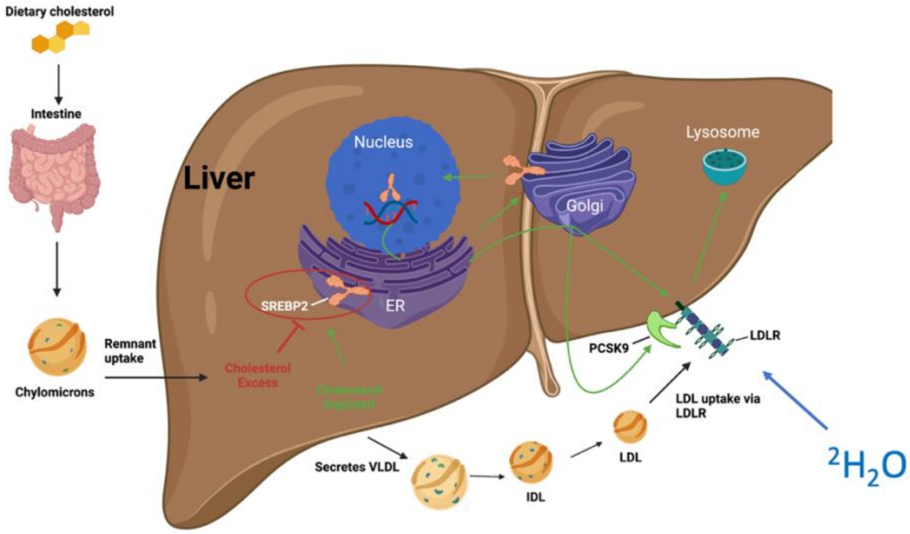

Figure 3. The rationale for the study. As dietary cholesterol increases in the liver, cholesterol biosynthesis, LDLR expression, and synthesis are decreased, resulting in less LDLR to uptake cholesterol. However, as cholesterol is depleted in the liver, the cholesterol-regulated SREBP2 transcription factor is released from the endoplasmic reticulum, transports to the Golgi apparatus, and enters the nucleus to activate the transcription of both LDLR and PCSK9. LDLR expression

and levels are then increased to uptake cholesterol from circulation. Simultaneously, the catabolic regulator of LDLR, PCSK9, is increased to perhaps decrease the levels and activity of LDLR. Interestingly, feeding-induced increases in PCSK9 are reduced when supplemented with cholesterol and statins increase circulating PCSK9 levels. Therefore, there is a potential futile cycle that occurs between LDLR and PCSK9. For example, as LDLR increases, PCSK9 increases as well to downregulate the receptor, but when LDLR decreases, PCSK9 decreases to upregulate the receptor. We tested the interactions between PCSK9 and LDLR under high cholesterol conditions and test how PCSK9 fits in the current Brown and Goldstein model of cholesterol homeostasis.

Past studies have evaluated LDLR and PCSK9 kinetics using different tracer methods, but none have evaluated their kinetics with ^2H_2O labeling and mass spectrometry in vivo to test a novel hypothesis in the cholesterol homeostatic pathway (**Figure 3**). We plan to test the hypothesis that LDLR and PCSK9 synthesis will decrease in response to high cholesterol diet. Therefore, our objective(s) were to establish a method 1) to measure the kinetics of LDLR/PCSK9 via stable isotopic metabolic labeling with heavy water (^2H_2O) in vivo and 2) to further test established models of cholesterol metabolic regulation on LDLR and PCSK9 turnover rate after feeding mice a cholesterol-enriched diet. To answer these objectives, mice were fed a cholesterol enriched (n=15) or control diet (n=15) for one week and metabolically labeled with heavy water (^2H_2O) for 0, 4, 8, and 12 hours. LDLR and PCSK9 were then immunoprecipitated from the liver and deuterium incorporation into LDLR and PCSK9 were measured via mass spectrometry

We revealed for the first time that LDLR and PCSK9 turnover can be measured in mouse tissues or plasma by ^2H_2O labeling and mass spectrometry. The half-lives of both hepatic PCSK9 and LDLR and PCSK9 in circulation in an in-vivo system. Surprisingly, one week of high cholesterol diet did not alter LDLR levels which can be explained by reduced LDLR absolute synthesis rates via the SREPB2 pathway and increased half-life or reduced breakdown by PCSK9. We observed reduced expression, levels, and absolute synthesis rates of hepatic and plasma PCSK9. Reduced levels and secretion rates of PCSK9 in circulation slow the catabolism of LDLR, thus preserving LDLR levels to maintain the uptake of LDL. Therefore, PCSK9 acts as a sensor for LDL plasma cholesterol levels to increase LDL uptake at the expense of increased hepatic cholesterol levels. We have discovered an added dimension to the negative feedback system of the cholesterol homeostatic pathway, but by a positive regulatory arm to preserve LDLR levels acting through PCSK9 at the expense of high intracellular concentrations.

2. Chapter 2

Turnover Rates of the Low-Density Lipoprotein Receptor and Proprotein Convertase Subtilisin/Kexin Type 9 (PCSK9) by Stable Isotope Labeling: An Added Dimension to the Cholesterol Homeostasis Model

2.1. Abstract

We measured the turnover rates of the low-density lipoprotein receptor (LDLR) and proprotein convertase subtilisin/kexin type 9 (PCSK9) in mice by metabolic labeling with heavy water (^2H_2O) and mass spectrometry. In liver of mice fed high-cholesterol diets, LDLR mRNA levels and synthesis rates were markedly lower with complete suppression of cholesterol synthesis and higher cholesterol content, consistent with the Brown-Goldstein model of tissue cholesterol homeostasis. We observed markedly lower PCSK9 mRNA levels and synthesis rates in liver and lower concentrations and synthesis rates in plasma. Hepatic LDLR half-life (t ½) was prolonged, consistent with an effect of reduced PCSK9, and resulted in no reduction in hepatic LDLR content despite reduced mRNA levels and LDLR synthesis rates. These changes in PCSK9 synthesis complement and expand the well-established model of tissue cholesterol homeostasis in mouse liver, in that reduced synthesis and levels of PCSK9 counterbalance lower LDLR synthesis by promoting less LDLR catabolism, thereby maintaining uptake of LDL cholesterol into liver despite high intracellular cholesterol concentrations. Lower hepatic synthesis and secretion of PCSK9, an SREBP-2 target gene, results in longer hepatic LDLR t ½ in response to cholesterol feeding in mice in the face of high intracellular cholesterol content. PCSK9 modulation opposes the canonical lowering of LDLR mRNA and synthesis by cholesterol surplus and preserves LDLR levels. The physiologic and therapeutic implications of these opposing control mechanisms over liver LDLR are of interest and may reflect subservience of hepatic cholesterol homeostasis to whole body cholesterol needs.

2.2. Introduction

The Brown-Goldstein model of cellular cholesterol homeostasis has proven to be remarkably predictive at the molecular level[21,22]. The central concept is that a cholesterol-related metabolite in cells induces multiple adaptations that tend to restore basal intracellular concentrations of cholesterol[15]. This framework has predicted the subsequent discovery of transcription factors (e.g., sterol response element binding proteins [SREBP])[37], proteolytic enzymes (site 1 and 2 proteases), and some surprising physiologic interactions (such as hepatic de novo lipogenesis also being induced by SREBP-1C). Indeed, the Brown-Goldstein model is probably the most well-known integrative metabolic hypothesis of the past half-century[15].

Proprotein convertase subtilisin/kexin type 9 (PCSK9) interacts with the low-density lipoprotein receptor (LDLR) and loss-of-function mutations result in lower plasma LDL cholesterol concentrations in humans and reduced risk of atherosclerotic cardiovascular disease[23,25,53,54]. The molecular basis of low blood LDL cholesterol concentrations in subjects with PCSK9 mutations proved to be through the role of PCSK9 in directing the LDLR to lysosomes for catabolic removal[24,51], established by investigators in Dallas led by Helen Hobbs and Jay Horton [23,25,54]. The physiologic role of PCSK9 in living animals remains uncertain, although some functions have been proposed [24,25,51].

Transcriptionally, both LDLR and PCSK9 are target genes of SREBP2 which suggests coordinate regulation of LDLR and PCSK9 expression based on sterol availability[15,25,37,49,50,55]. As cholesterol content increases in the cell, cholesterol synthesis, LDLR mRNA levels and LDLR synthesis rates are decreased[15,21]. Increases in PCSK9 expression by refeeding can be prevented by dietary cholesterol supplementation[55].

Plasma PCSK9 levels and hepatic LDLR levels are also increased in humans taking statins[15,40]. The increased PCSK9 levels could lower hepatic LDLR levels and limit the statin cholesterol lowering effect on blood cholesterol. A more comprehensive understanding of the coordinated regulation of PCSK9 and LDLR metabolism would be helpful and might have nutritional or therapeutic implications.

The synthesis, degradation, and turnover of LDLR have been measured using radioactive tracers in cell culture[20,29]. These approaches showed that LDLR is initially synthesized as a 120 kD precursor and matures to a 160 kD form. The application of this methodology helped to identify familial hypercholesterolemic (FH) patients with defective LDLR posttranslational processing [19,29]. Knight et al. also showed in FH patients that their LDLR precursor proteins exhibited a longer half-life than in healthy cells[30]. Early tracer studies were key for understanding the basic kinetic parameters of LDLR such as its half-life and its response to nutritional and therapeutic interventions[22]. Studies of LDLR turnover carried out with radiolabeled amino acids or sugars reported the half-life of LDLR in cultured human skin fibroblasts as ~9-12 hours[31,32,36,56,57].

Stable isotope metabolic labeling combined with tandem mass spectrometric analysis allows measurement of turnover of targeted proteins as well as fluxes of proteins across the global proteome[41,44,45,58]. This approach has not been used to explore the turnover of low abundance intracellular receptors or signaling molecules and their homeostatic interactions, however. Here, we applied heavy water labeling with tandem mass spectrometric analysis to study fluxes of LDLR in liver and PCSK9 in liver and plasma.

Our objectives here were to, 1) measure the synthesis and breakdown kinetics of LDLR and PCSK9 by metabolic labeling with ^2H_2O in vivo in living animals, and 2) to test how the PCSK9 response fits into the current model of intracellular cholesterol homeostasis[15,21,22,23,24,25,51]. The results suggest a potential additional dimension to the cholesterol homeostasis model in the liver and the whole body in mice.

2.3. Materials and Methods

The data that support the findings of this study are available from the corresponding author upon reasonable request.

Animals and Research diet

Male 8-week-old C57B6/J mice (n=30) (The Jackson Laboratory, Stock No:000664) were randomized and fed a low-fat, high-cholesterol diet (n=15) (Research Diets, Inc., Catalogue #D12104C containing 10% kcal from fat with 11.25 gm cholesterol per 4057 kcal or 1.0% by weight) or control diet (n=15) (Research Diets, Inc., Cat #D12102C containing 10% kcal from fat without added cholesterol) for 7 days. Male mice were chosen to minimize sex as a biological variable through estrous cycle effects in female mice. Mice were injected by the intraperitoneal route with 99.9% ^2H_2O to rapidly label the intracellular amino acid pool[41] then were maintained on 8.0% ^2H_2O in drinking water until the time of sacrifice. All animal experiments were approved and followed standard protocol by the Animal Care and Use Committee at the University of California, Berkeley.

Lipid and plasma biochemistry

Blood was collected by cardiac puncture, transferred to EDTA-coated tube, and centrifuged at 2000 RCF for 15 min to separate plasma from the other blood components. Plasma was stored at -80 °C and thawed on ice until analysis. Total cholesterol concentrations (cholesterol ester and free cholesterol) were measured directly from extracted liver lipids using a calorimetric assay, as directed by the manufacturer's instructions (Wako L-Type Triglyceride M FUJIFILM Medical Systems U.S.A., Inc). Total cholesterol concentrations (free cholesterol and cholesterol-ester) in different lipoprotein fractions such as total, very low-density lipoproteins / low density lipoproteins, and high-density lipoproteins were measured as directed by the manufacturer's instructions (Abcam, Cholesterol Assay kit – HDL and LDL/VLDL, ab-65390).

Hepatic de novo cholesterol synthesis and total cholesterol measurements

30mg of liver tissue was homogenized in 500ul methanol. 1,000ul chloroform was then added, agitated followed by addition of 500ul H_2O to separate the aqueous and organic layer, and centrifuged at 1,500 RPM. The entire chloroform layer was transferred to a glass vial, dried with nitrogen gas, and reconstituted in 200ul of methanol. Total cholesterol content (cholesterol ester and free cholesterol) was measured from this fraction using a calorimetric assay kit as directed by the manufacturer's instructions (Wako L-Type Triglyceride M FUJIFILM Medical Systems U.S.A., Inc). Total cholesterol was hydrolyzed with 1.0ml Methanolic HCL and 1.0ml chloroform for 1 hour at 60 °C. 1.0ml of water and 2 ml of hexane was added to separate the organic and aqueous layers. The organic layer was transferred to a new glass tube and dried completely with nitrogen gas followed by acylation with 10.0ul of acetic anhydride, 20.0ul pyridine and 200ul of toluene for 15 min at room temperature (RT). Cholesterol derivate was extracted with petroleum ether and submitted in toluene for deuterium incorporation analysis using gas chromatography mass spectrometry (GC/MS)[58]. The percent of newly labeled cholesterol (EM1, %) was calculated as described elsewhere by the difference between the natural abundance M1 fraction and the labeled M1 fraction[58].

Heavy body water enrichments

Precursor pool enrichment (p) was determined from distillation of water from plasma samples. Briefly, 100ul of plasma underwent distillation overnight (O/N) at 80 °C, followed by addition of 1.0ul of 10M NAOH, and 5ul of acetone. By hydrogen exchange reactions between ^2H_2O and acetone methyl hydrogens, heavy body water percent enrichment (%) was then measured in acetone via GC/MS. A standard curve of body water percent enrichments was used to interpolate the body water enrichments for each sample. Ultimately, heavy body enrichments were used as a surrogate of labeled ^{2}H-amino acid precursors that is implemented by mass isotopomer distribution analysis (MIDA) to determine the theoretical asymptotic enrichment of the protein product of interest[41,44,45].

LDL receptor and PCSK9 isolation by immunoprecipitation

We isolated hepatic LDLR and PCSK9 in one preparation (Schematic shown in Figure I in Data Supplement). Pierce™ MS-compatible magnetic kit with protein A/G magnetic beads (Thermo Fisher Scientific) was used for immunoprecipitation of LDLR and PCSK9. 50 mg of mouse liver was homogenized with a Qiagen™ tissue lyzer in 1,000ul of IP-MS (immunoprecipitation-mass spectrometry) cell lysis buffer with one 3.2mm steel beads for 1.0min at 30 hz. Homogenates were centrifuged at 10,000 RCF at 4 °C for 10 minutes. Supernatants were transferred to a fresh tube and assayed for protein concentration based on Pierce™ BCA protein assay kit[59].1000ug of protein and 1.5ug of antibodies (PCSK9, Invitrogen Cat# MA5-24114, and LDLR LS-bio, Cat# LS-C291055) were added into fresh tubes followed by addition of IP-MS cell lysis buffer for a total volume of 500ul. Samples were incubated at 4 °C O/N. On the following day, 0.25mg or 25ul of 10mg/ml protein A/G magnetic beads were added and incubated for 1 hr. at RT. The beads were collected with a magnetic stand for 2 min. The flow through was stored for future analysis at -80 °C. The samples were washed 3x with 500ul of buffer A and 2x with 500ul of buffer B followed by elution with 100ul of elution buffer. The elute was transferred to a new low-bind tube and speed vacuumed until completely dry. Mass spectrometry preparation included reduction of the immunoprecipitate with 2.3ul of 50 mM dithiothreitol, 8.0ul of 100mM ammonium bicarbonate, 8.0ul of 2,2,2-trifluoroethanol and incubated at 60 °C for 1 hr. Samples were allowed to cool in which 6.0ul of 50mM iodoacetamide was then added and incubated for 20 min at RT. 50ul of 100mM ammonium bicarbonate and 150ul of H_2O were added to dilute the samples and to adjust the pH to ~8 prior to addition of 50ng of trypsin. Tryptic digest occurred O/N at 37 °C. Lastly, samples were centrifuged at 10,000 RCF for 10 min at RT to pellet undigested debris. Supernatants were speed vacuumed dried and resuspended in 25ul of 3.0% acetonitrile and 0.1% formic acid buffer for mass spectrometry analysis.

Search parameters and acceptance criteria (MS/MS and/or peptide fingerprint data)

The software used for peak list generation was Mass Hunter release version B.07.00. Spectrum Mill released version B.04.01 was the search engine for proteomic analysis based on MS/MS identifications. The sequence database searched for mouse protein identifications was Uniprot (2019)[60]. 17,019 was the number of entries searched in the data base. Trypsin was used for specifically cleaving the C-terminal side of lysine and arginine amino acid residues. 2 was the number of missed cleavages permitted. Carbamidomethylation (C) was for fixed modifications. Acetylated lysine (K), oxidized methionine (M), N-terminal pyroglutamic acid (N-termQ), deamidated asparagine (N), and hydroxylated prolines (P) were for variable modifications. 20 ppm and 30 ppm were the mass tolerance for precursor ions and fragment ions, respectively. The threshold score/expected value was 30% that was based on the minimum match peak intensity for accepting individual spectra. 1.0% global false discovery rate (FDR) was determined by algorithms of the Spectrum Mill software and confirmed at the peptide and protein levels.

Protein flux measurements using liquid chromatography tandem mass spectrometry (LC/MS-MS) and MIDA

Comprehensive reviews of protein kinetic measurements using stable isotopic metabolic labeling with ^2H_2O coupled with high precision LC/MS-MS and MIDA have been presented elsewhere[41,44,45]. Briefly, high performance liquid chromatography separated the complex immunoprecipitated samples. The mass isotopomer distribution of ^2H-labeled tryptic peptides were analyzed with 6550 Agilent technology quadrupole time of flight (Q-TOF) mass spectrometer that was equipped with a chip cube ion source (Agilent technologies, Santa Clara, CA). 3.0% acetonitrile/0.1% formic acid (v/v) to 95% acetonitrile/0.1% formic acid (v/v) composed of the mobile phase. Sample enrichment occurred for 18 minutes followed by elution from the analytical column for 12 minutes until a 95.0% acetonitrile to 5.0% water ratio. Specific peptides for LDLR or PCSK9 were identified in the daughter MS/MS spectrum, whereas the peptide ratios and abundances were analyzed in parent MS mode. Agilent Spectrum Mill software analyzed the MS/MS data for protein identification with Uniport database of the mouse proteome[60]. Agilent Mass hunter qualitative analysis software determined the mass isotopomer distribution in the MS spectrum[45]. Baseline abundance of 30,000, a false discovery rate of 1.0%, and ± 5.0% of the predicted abundance for each mass isotopomer were included in the filtering criteria. Peptide sequence was informative of elemental composition. For any given peptide, the molecular formula, mass, and retention time were determined in the MS mode. We achieved good peptide counts and coverage. For PCSK9, the mean peptide count was 19.6 and for LDLR, the mean peptide counts as 11.3. Based on precursor body water enrichments (p), number of exchangeable C-H positions (n) in the summed amino acids, measured ^2H-peptide enrichments, and mass isotopomer distribution patterns for tryptic peptides, this can calculate the parent protein fractional replacement (f) by MIDA[41,44,45]. Fractional replacement (f, %) is calculated from the change in enrichment of the M_0 isotopomer at time (t) / asymptote enrichment of the M_0 isotopomer predicted by MIDA for 100% new synthesis at the measured precursor pool enrichment. Values of f (%, Figure 1) were converted to fractional replacement rate constants (FRR, %/hr.) by the equation FRR = -ln(1-f)/time, based on first order kinetic calculations[45]. Half-life ($t_{1/2}$) was calculated as, $t_{1/2}$= ln(2)/FRR. Calculation of absolute synthesis rate (ASR, ng/mg tissue weight/hr.) was defined as FRR (hr^{-1}) * pool size (ng/mg tissue)[41,44,45,58]. The remaining data analysis was performed with Microsoft excel (Version 16.28) and Prism V9.2.0.

LDLR and PCSK9 ELISA

50mg of liver tissue was homogenized in 500ul IP-MS cell lysis buffer and centrifuged at 10,000 RCF at 4 °C for 10 minutes. Supernatants were transferred to a fresh tube and assayed for protein concentration based on Pierce™ BCA protein assay kit. The rest of protocol was based on the ELISA procedure for mouse LDLR (R & D biotechnology, cat # MLDLR0) and PCSK9 (R & D biotechnology, cat #MPC900). LDLR and PCSK9 protein content was normalized by total tissue or protein amount, respectively.

RNA extraction and quantitative Polymerase Chain Reaction (qPCR) gene expression analysis

Total RNA was extracted from 30mg of liver tissue by TRIzol method. Livers were homogenized with 1.0ml TRIzol in 1.5 ml tubes using the Qiagen tissue lyzer (2X for 1 min at 30 Hz). 200ul of chloroform was added, vortexed and spun at 9,500 rpm for 10 min at 4 °C to initiate phase distribution of the organic and aqueous material. The top aqueous layer was transferred to a new tube then RNA was precipitated with 500ul of 100% isopropanol and stored O/N at -80°C. Samples were pelleted at 14,000 rpm for 15 min at 4 °C. Supernatants were discarded, pellets were washed twice in 500ul of 70% ethanol, air dried for 5 to 10 min at RT and resuspended in 20 to 100ul of nuclease free water depending on the pellet size. Thermo Fisher Scientific^{TM} nanodrop 2000 was used to measure RNA concentration. Thermo Fisher Scientific^{TM} revert aid kit was employed for cDNA synthesis with 2.5ug staring RNA input in a 20ul reaction that was diluted 1:10 in nuclease free water. 4.0ul of diluted cDNA, 10ul of SsoFast SYBR green super mix, 1ul each of reverse/forward primers (500nm concentration) and 4.0ul of water were used for qPCR. QPCR plate reader, hard-shell skirted 96 well plate and optical seal tape were obtained from Bio-Rad^{TM} technologies. The SsoFast advanced SYBR Green thermocycler protocol was used for expression analysis. The $\Delta\Delta C_q$ method computed the relative gene expression data using actin as an internalization control. Data is shown as the mean biological replicates fold change in expression that were triplicated in each sample and averaged according to control dietary treatment or high cholesterol diet treatment.

Statistics

Student's or Welch's t-test were used to calculate statistical significance for comparisons between two groups of $n \geq 6$ for hepatic cholesterol levels, mRNA expressions, protein content, fractional replacement rates, half-lives, and absolute synthesis rates. Statistical significance for lipoprotein cholesterol content or hepatic cholesterol enrichments were analyzed by a Mann-Whitney test given a sample size of $n \leq 5$. Biological replicates were used in each experiment. A one-phase association, non-linear regression line was used to fit LDLR, and PCSK9 fractional synthesis over time in (Figure 1). The equation included $Y=Y0 + (\text{Plateau}-Y0) *(1-\exp(-K*x))$ where $Y0=0$, plateau=100%, x=time, and K= fractional replacement rate (FRR) constant. The rate constants (K) were considered statistically different based on an exact sum of squares F test. Data are expressed as mean values ± SEM or SD, or data are expressed as median with 95% confidence interval as stated in each figure. Data sets were not tested for normality and equal variance to determine whether a parametric or non-parametric test were applicable. Statistics and graph generations were performed with GraphPad Prism version 9.2.0 for macOS, GraphPad Software, San Diego, California USA, www.graphpad.com.$^{*}p \leq 0.05$, $^{**}p \leq 0.01$, $^{***}p \leq 0.001$, $^{****}p \leq 0.0001$.

2.4. Results

Time-course of LDLR and PCSK9 turnover using metabolic labeling with ^2H_2O and mass spectrometry.

C57B6/J mice (8-week-old) were randomized into high cholesterol diet-fed or control diet-fed groups for 1 week and underwent metabolic labeling with ^2H_2O for 12 hours. We isolated LDLR and PCSK9 by immunoprecipitation. A time-course labeling experiment was first carried out. Based on previous investigations with ^{35}S-methionine showing a 9-12 hour half-life of LDLR in skin fibroblast cell cultures[31,32], a 12-hour sampling period was chosen.

LDLR and PCSK9 fractional synthesis (f, %) time-courses are shown (Figure 1). Fractional replacement values for each protein were fit to a one-phase association non-linear regression line, Y=Y0+(plateau-Y0) *(1-exp(-K*x) where Y0=0, plateau=100%, x=time, and K= fractional replacement rate constant (FRR). The control and high cholesterol diet fed mice FRR for LDLR were 0.10 ± 0.04 $hrs.^{-1}$ and 0.06 ± 0.012 $hrs.^{-1}$ (mean ± SD, $p<0.0001$), respectively, representing a significant prolongation of hepatic LDLR half-life (t ½) from 7 ± 2 hrs. in control mice to 11 ± 1 hrs. with cholesterol feeding. The control diet and high cholesterol diet-treated turnover rate constants for PCSK9 were not different, with FRR values of 0.013 ± 0.005 $hrs.^{-1}$ and 0.012 ± 0.005 $hrs.^{-1}$ ($p=0.37$), representing t ½ for liver PCSK9 of 54 ± 13 hrs. and 59 ± 15 hrs., respectively.

The 95% confidence intervals for FRR were as follows: control and high cholesterol diet LDLR FRR confidence intervals were 0.0895 $Hrs.^{-1}$ to 0.1103 $Hrs.^{-1}$ and 0.0601 $Hrs.^{-1}$ to 0.0661 $Hrs.^{-1}$, respectively. The control and high cholesterol diet PCSK9 FRR confidence intervals were 0.0111 $Hrs.^{-1}$ to 0.0143 $Hrs.^{-1}$ and 0.0099 $Hrs.^{-1}$ to 0.0135 $Hrs.^{-1}$, respectively.

Effects of high cholesterol diet on liver cholesterol content and cholesterol synthesis.

High cholesterol diet increased hepatic total cholesterol content (free cholesterol and cholesterol-ester) from 0.28 ± 0.04 to 0.34 ± 0.02 (ug total cholesterol / mg of liver weight) ($p<0.0001$) (Figure IIA in Data Supplement). High cholesterol diet significantly suppressed de novo hepatic cholesterol synthesis to near zero values as compared to control mice at each time point over the 12-hour labeling period ($p=0.008$) (Figure IIB in Data Supplement).

High cholesterol diet decreases hepatic LDLR mRNA expression and absolute synthesis rate (ASR) but prolongs tissue LDLR half-life.

Mice (8-week-old) were randomized into high cholesterol diet-fed or control diet-fed groups for 1 week and underwent metabolic labeling with ^2H_2O for 12 hours. LDLR mRNA relative levels (Figure 2A) were significantly reduced by 70% in high cholesterol diet-fed animals as compared to controls ($p<0.0001$). High cholesterol diet for 1 week did not significantly alter LDLR levels (4.3 vs. 4.9 ng of LDLR / mg tissue weight, ($p=0.204$) (Figure 2B).

The ASR of LDLR was determined by multiplying LDLR pool size by its FRR[41,44,45,58]. High cholesterol diet lowered LDLR ASR by 31%, from 0.45 to 0.31 ng LDLR /mg liver weight/ hr. ($p=0.025$) (Figure 2D). Interestingly, despite the 31% reduction in ASR in the setting of 70% lower mRNA levels, there was no reduction in LDLR content, due to the prolongation of LDLR t½ ($p<0.0001$) (Figure 2C). LDLR mRNA levels changed to a greater extent than LDLR ASR ($p=0.0007$), suggesting that post-transcriptional factors also influence LDLR synthesis rates[24,25,51,53] (Figure 2E).

High cholesterol diet decreases hepatic PCSK9 mRNA expression, protein levels and ASR but does not change tissue half-life.

Since both LDLR and PCSK9 are transcriptionally coregulated by SREBP2 based on sterol availability, and PCSK9 acts in concert to degrade LDLR[24,25,51], we evaluated the impact of high cholesterol diet on PCSK9 content and turnover rate in liver. Hepatic PCSK9 mRNA levels (Figure 3A) were 90% lower in high cholesterol-diet fed animals as compared to controls (p=0.0002). PCSK9 content in liver tissue homogenates was 70% reduced in high cholesterol diet-fed animals, from 0.9 to 0.3 ng/mg of total protein (p=0.0019) (Figure 3B). The t½ of PCSK9 was not significantly different on the control diet compared to the high cholesterol diet (p=0.7094) (Figure 3C). The high cholesterol diet decreased PCSK9 ASR by ~70%, from 0.3 to 0.09 ng PCSK9/mg total protein/day (p=0.005) (Figure 3D). Hepatic PCSK9 mRNA levels were reduced more than hepatic ASR after high cholesterol diet (p=0.006) (Figure 3E), consistent with post-transcriptional factors influencing PCSK9 synthesis rates[24,25,51,53].

PCSK9 turns over faster in the plasma than the liver and high cholesterol diet lowers ASR of plasma PCSK9.

PCSK9 is secreted from the liver and binds surface LDLR on tissues to promote LDLR degradation in the lysosome[24,25,51]. Previous work has suggested that PCSK9 secreted from the liver preferentially binds to hepatic LDLR relative to adrenal gland LDLR[38], thereby altering LDL cholesterol delivery to peripheral tissues. We compared PCSK9 synthesis between the plasma and liver compartments and established the plasma flux in response to high cholesterol diet. PCSK9 FRR in the plasma was higher than in the liver (4.98 ± 1.50 %/hr. vs 1.38 ± 0.32 %/hr., p=0.0015), (Figure 4A and Figure III in Data Supplement). Plasma PCSK9 concentrations were lower by 78%, from 10.7 ng/ml in the control diet to 2.4 ng/ml on the high cholesterol diet (p=0.004) (Figure 4B). One week of high cholesterol diet had no effect on PCSK9 t½ in the plasma (15.6 hr. vs 16.1 hr., p=0.877) (Figure 4C). ASR of PCSK9 in the plasma was 79% lower on high cholesterol diet compared to the control diet, from 0.53 to 0.11 ng PCSK9/ ml /hr., (p=0.0004) (Figure 4D).

Plasma total, VLDL/LDL, and HDL cholesterol concentrations.

Plasma total, VLDL/LDL and HDL cholesterol concentrations were quantified (Figure 5). Total cholesterol content (free cholesterol plus cholesterol ester) was measured in each fraction. We applied a heparin sulfate method to precipitate apolipoprotein B-containing (VLDL/LDL) particles. LDL particles contain the majority of cholesterol in circulation in humans, whereas mice are HDL-dominated animals[17,61,62,63]. Total cholesterol in plasma HDL was not altered (1.1 to 1.0 ug/ul, p=0.5476). Total cholesterol in the VLDL/LDL fractions was higher in the high cholesterol diet treated mice (0.4 vs 0.8 ug/ul, p=0.0079) and approached HDL cholesterol concentrations. Total cholesterol levels trended higher but were not significantly different from controls on high cholesterol diet (1.3 ± 0.7 to 2.2 ± 0.87 ug/ul, p=0.3095).

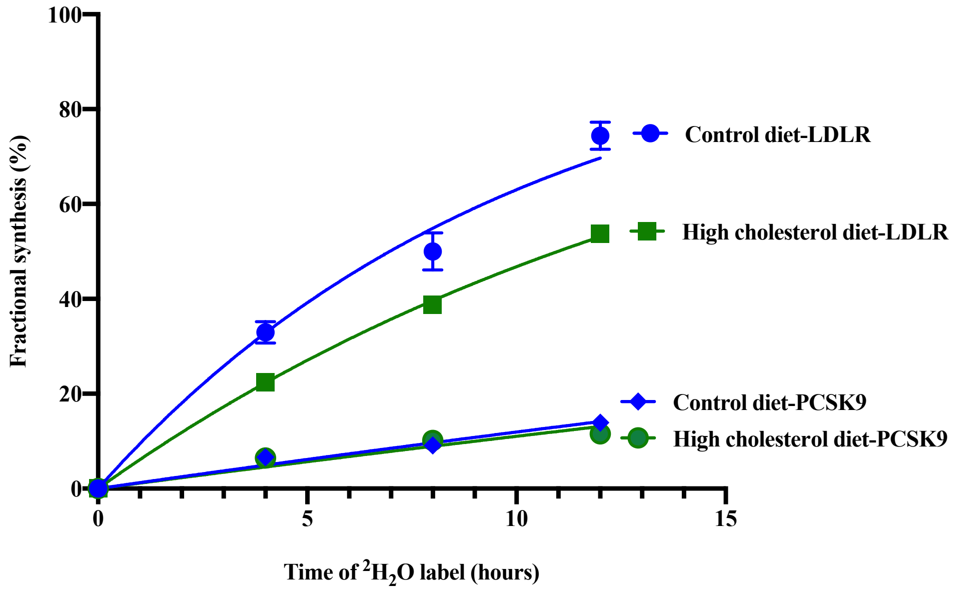

Figure 1. Fractional synthesis of LDLR and PCSK9 over 12 hours of ${}^{2}H_{2}O$ labeling. C57B6/J mice were fed a low fat-high cholesterol diet (1.0% by weight) or control diet for 1 week. Metabolic labeling was by intraperitoneal bolus injection of 99.9% ${}^{2}H_{2}O$ (35.0ul/gram BW) followed by 8.0% ${}^{2}H_{2}O$ in drinking water to maintain stable body water ${}^{2}H$-enrichments. Animals were euthanized at 4, 8 and 12 hours of ${}^{2}H_{2}O$ labeling ($n \geq 3$ animals per time point). A one-phase association non-linear regression line, Y=Y0 + (Plateau-Y0) *(1-exp(-K*x)), where Y0=0, plateau=100%, x=time, and K= fractional replacement rate (FRR) constant, was used to fit LDLR and PCSK9 fractional synthesis over time. The control and high cholesterol diet fed mice FRR (hrs^{-1}) for LDLR were 0.10 ± 0.04 hrs.$^{-1}$ and 0.06 ± 0.012 hrs.$^{-1}$ (mean ± SD, $p<0.0001$), respectively. The turnover rate constants for PCSK9 were not different in mice on high-cholesterol and control diets, with FRR values of 0.013 ± 0.005 hrs.$^{-1}$ and 0.012 ± 0.005 hrs.$^{-1}$ ($p=0.37$), respectively. Data are expressed as mean fractional synthesis (%) ± SD. Exact sum of squares F-test was used for calculation of statistical significance between FRR values. LDLR, low density lipoprotein receptor. PCSK9, proprotein convertase subtilisin/kexin type 9.

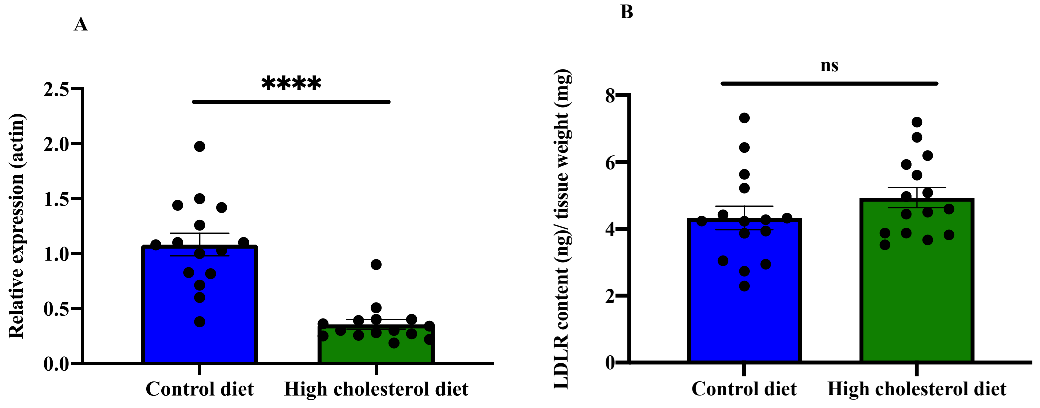

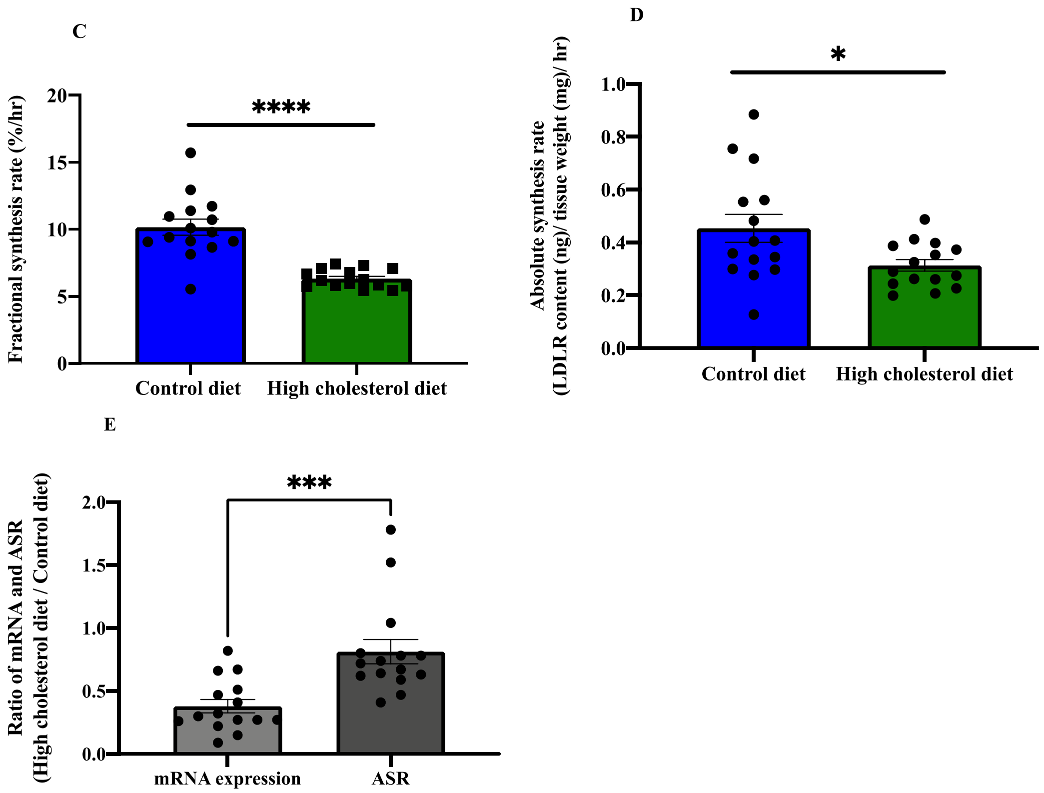

Figure 2. The effect of one week of high cholesterol diet on LDLR mRNA expression, content, half-life, and ASR. A, Hepatic LDLR mRNA expression was significantly lower by 70% in high cholesterol diet-fed animals as compared to controls ($p<0.0001$). **B**, Hepatic LDLR content (ng/mg tissue weight) was not significantly altered in high cholesterol diet compared to the control animals (4.3 vs. 4.9 ng of LDLR /mg tissue weight, respectively, $p=0.2042$). **C**, Hepatic LDLR t ½ (hours) was increased from 7 hrs. in control mice to 11 hrs. in high cholesterol diet treated mice ($p<0.0001$). **D**, Hepatic LDLR ASR (ng/ total protein/hr.) was lower by 31%, from 0.45 to 0.31 ng LDLR /mg liver weight/ hr. ($p=0.025$). **E**, Relative reductions in LDLR mRNA and ASR after high cholesterol diet. LDLR mRNA levels changed to a greater extent than LDLR ASR ($p=0.0007$). Data are expressed as mean ± SEM, n=15 per group. Unpaired Student's or Welch's t-test was used to calculate statistical significance. LDLR, low density lipoprotein receptor, ASR, absolute synthesis rate.

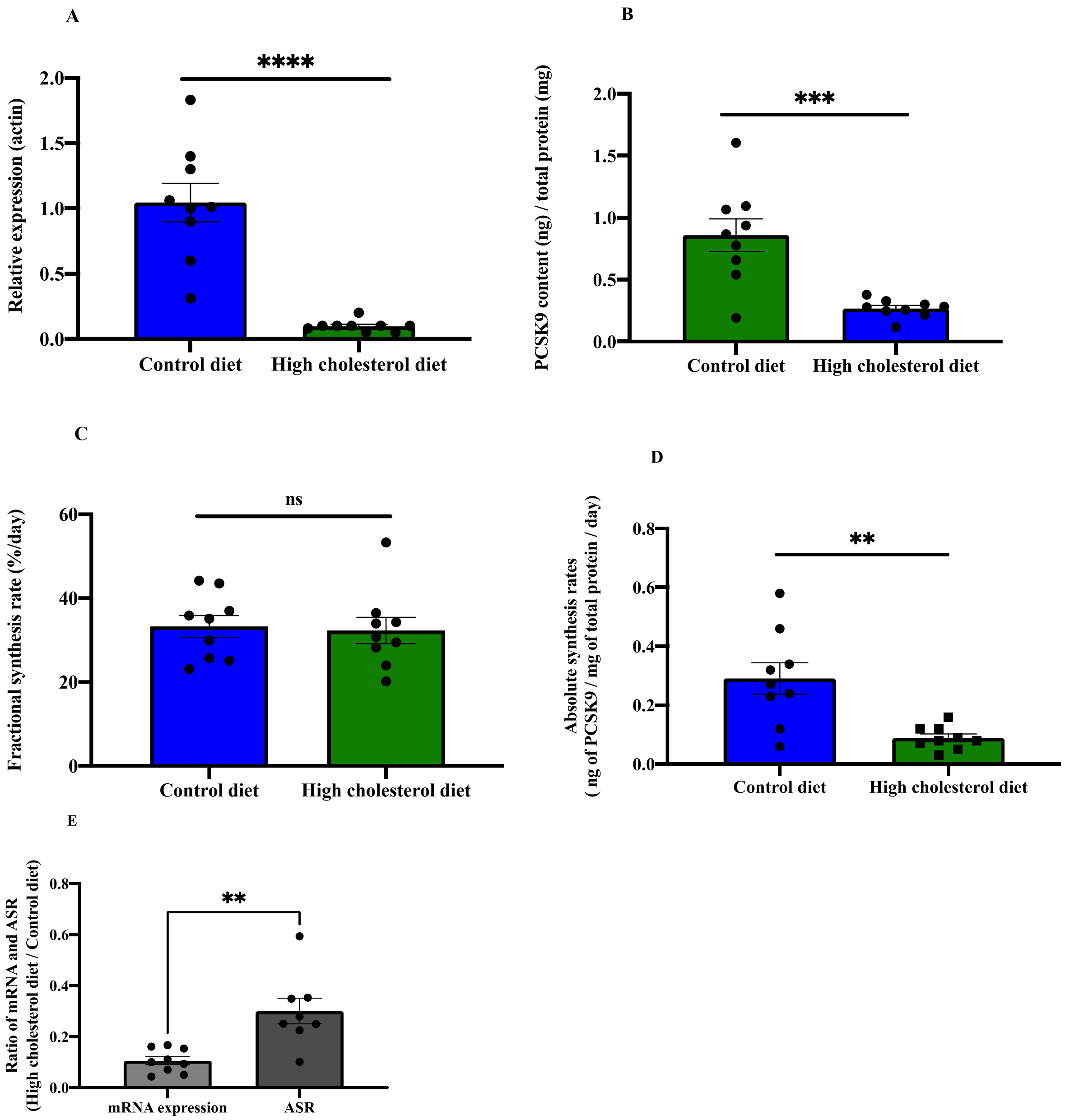

Figure 3. **The effect of one week of high cholesterol diet on hepatic PCSK9 mRNA expression, content, half-life, and ASR. A**, Hepatic PCSK9 mRNA expression was 90% lower (0.09/1.04) in high cholesterol-diet fed animals as compared to controls (p=0.0002). **B**, Hepatic PCSK9 content (ng/mg total protein) was 70% lower in high cholesterol diet-fed animals, from 0.9 to 0.3 ng/mg of total protein (p=0.0019). **C**, PCSK9 t ½ (hours) was not different between dietary treatments (p=0.7094). **D**, PCSK9 absolute synthesis rate (ASR) (ng PCSK9/mg total protein/day) was decreased by ~70%, from 0.3 to 0.09 ng PCSK9/mg total protein/day (p=0.0051). **E**, Relative reduction in PCSK9 mRNA and ASR after high cholesterol diet. Hepatic PCSK9 mRNA levels were reduced more than hepatic ASR after high cholesterol diet (p=0.0057). Data are expressed at the mean values ± SEM, n=8-9 per group. Unpaired Student's or Welch's t-test was used to calculate statistical significance. PCSK9, proprotein convertase subtilisin/kexin type 9, ASR, absolute synthesis rate.

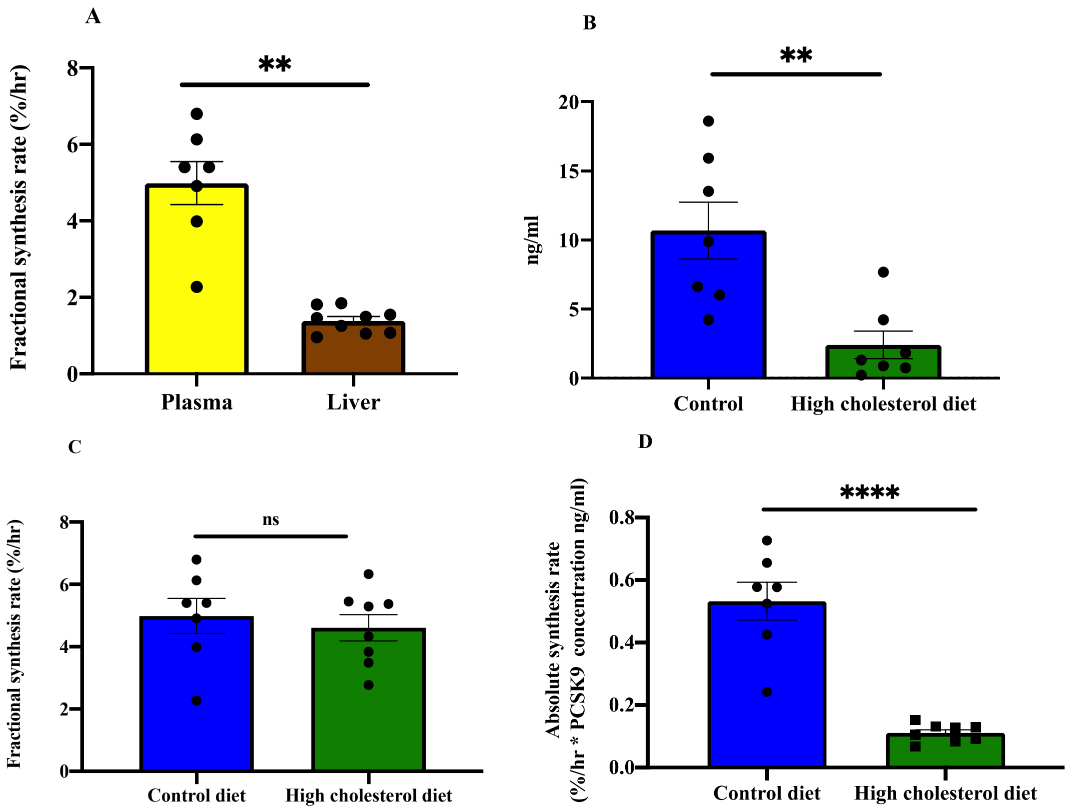

Figure 4. Plasma vs liver t ½ of PCSK9 and the effects of high cholesterol diet on plasma PCSK9 concentration, half-life, and ASR. **A**, Plasma vs liver PCSK9 fractional replacement rate (%/hr.). PCSK9 fractional replacement rate in the plasma was higher than in the liver (4.98 ± 1.50 %/hr. vs 1.38 ± 0.32 %/hr., p=0.0015), **B**, Plasma PCSK9 concentration (ng/ml) was lower by 78% on the high cholesterol diet (p=0.0036). **C**, PCSK9 t ½ (hours) in the plasma was not affected by one week of high cholesterol diet (15.6 hr. vs 16.1 hr., p=0.8769). **D**, Plasma PCSK9 ASR (ng/ml/hr.) was 79% lower on high cholesterol diet compared to the control diet, from 0.53 to 0.11 ng PCSK9/ ml /hr., (p=0.0004). Data are expressed as mean values ± SEM, n=7-9 per group. A paired t-test was used to evaluate statistical significance between PCSK9 half-life in the plasma vs the liver. Unpaired Student's or Welch's t-test was used to evaluate the effects of high cholesterol diet. PCSK9, proprotein convertase subtilisin/kexin type 9, ASR, absolute synthesis rate.

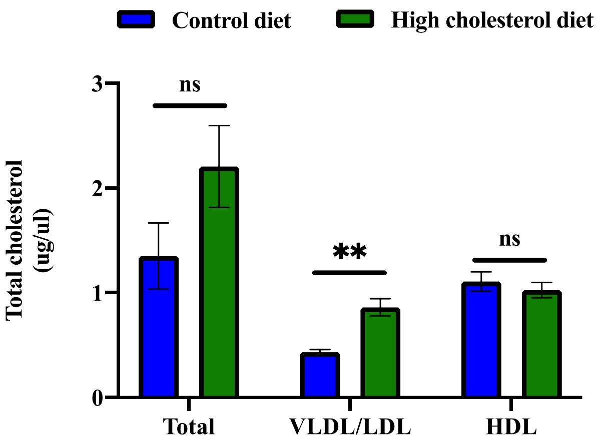

Figure 5. Total plasma, HDL, and VLDL/LDL cholesterol levels after 1 week of high cholesterol diet. Total cholesterol (cholesterol ester plus free cholesterol) was measured in plasma and in lipoprotein fractions. Total cholesterol in HDL fraction was not affected (1.1 to 1.0 ug/ul, p=0.5476). Total cholesterol in the VLDL/LDL fraction was higher in the high cholesterol diet-treated mice (0.8 vs. 0.4 ug/ul, p=0.0079). Total plasma cholesterol levels were non-significantly increased on high cholesterol diet (2.2 ± 0.87 vs 1.3 ± 0.7 ug/ul, p=0.3095). Data are expressed as the median values shown with the upper and lower limits of the 95% confidence interval, n=5 per group. A Mann-Whitney test was used to compute statistical significance. VLDL, very low-density lipoproteins, LDL, low density lipoproteins, HDL, high density lipoproteins.

2.5. Discussion

Our objectives here were, first, to develop a method to measure the in vivo flux rates of tissue LDLR and tissue and plasma PCSK9 by stable isotope metabolic labeling; and second, to compare the adaptive flux response to cholesterol feeding of LDLR and PCSK9. The physiologic roles of PCSK9 in living animals remain uncertain[24,25,38,51]. PCSK9 is known to alter LDLR turnover in the liver[24,25,51,54] while high cholesterol diet alters the metabolism of LDLR and its associated regulatory factors[15,21,22]. High cholesterol diet provided a well-characterized intervention to compare the physiologic responses and potential interactions between in vivo fluxes of LDLR and PCSK9.

We established that the t½ values for hepatic LDLR and PCSK9 were 7 hrs. and 54 hrs., respectively, in control mice (Figure 1). A high cholesterol diet prolonged hepatic LDLR t½ from 7 hrs. to 11 hrs. and significantly lowered LDLR ASR by 31%, with no change in liver LDLR content. High cholesterol feeding increased hepatic cholesterol content and markedly suppressed de novo cholesterol synthesis, as expected by the canonical cholesterol homeostasis model. Hepatic PCSK9 mRNA levels and ASR were also markedly reduced, as were plasma PCSK9 concentrations and synthesis rates.

The coordinated response to cholesterol feeding for PCSK9 compared to the well-established response of LDLR is extremely interesting and adds an extra dimension in context of cellular cholesterol homeostasis. Both LDLR and PCSK9 are transcriptionally coregulated by SREBP2 in response to sterol availability[15,37,25,50,55]. According to the Brown-Goldstein model[15,21,22], an increase in hepatocyte cholesterol content should reduce synthesis of cholesterol and of the LDLR, and our stable isotope labeling data are consistent with these metabolic flux responses. The results for PCSK9 gene expression, concentrations in liver and synthesis rates in liver and plasma, however, counterbalanced and opposed these effects on LDLR levels. Cholesterol feeding reduced hepatic mRNA expression, protein levels and ASR of PCSK9 in liver and markedly reduced plasma PCSK9 synthesis rates and concentrations. Reduced PCSK9 synthesis and concentrations in plasma would be predicted to reduce catabolism of hepatic LDLR, resulting in preserved capacity of liver cells to take up cholesterol.

Indeed, we observed ~50% prolongation of LDLR t½ in liver with no significant change in LDLR content, despite the ~70% lower LDLR mRNA and ~31% lower ASR in liver. The net effect of reduced PCSK9 synthesis in liver and secretion into plasma thereby further <u>increases</u> already high intrahepatic concentrations of cholesterol – i.e., this represents a positive feedback loop (Illustrated in Graphical Abstract). Why there are two opposing control mechanisms at work in the liver in response to high cholesterol intake raises several interesting questions.

One possibility is that the additional modulation of LDLR by PCSK9 in the liver allows liver cells to play a subservient role to whole body cholesterol needs in mice. Grefhorst et al.[38] proposed that PCSK9 may serve to reduce hepatic re-uptake of newly secreted LDL particles and direct LDL to peripheral tissues, like the adrenal. This could apply in settings like statin therapy, where there are elevated PCSK9 concentrations in blood, but we observed here the opposite response to hepatic cholesterol surplus. Our results suggest that the liver may reduce delivery of LDL cholesterol to peripheral tissues in time of cholesterol excess, at the expense of elevated intra-hepatocellular cholesterol content. By this model, PCSK9 allows subservience to and coordination of liver cholesterol homeostasis with extrahepatic cholesterol needs.

Another consideration is that the mouse is a plasma HDL-dominated animal[61,62,63]. In addition to the well-known effects of cholesterol-ester transfer protein absence in mice[61,62,63], the PCSK9 response observed here may help explain the relatively modest increases in plasma LDL cholesterol reported in mice after cholesterol feeding[50,61,62,63]. Getz et al. showed that dietary cholesterol loading leads to a non-significant increase in total plasma cholesterol, as we observed, and Maxwell et al. reported increased liver cholesterol but not plasma total cholesterol concentrations and a reduction in PCSK9 mRNA[50,63]. On the other hand, 30 – 40% increased PCSK9 levels have been observed in humans given statins[40], which suggests that a similar biology applies in humans. Measurements of flux rates are typically more sensitive than static changes[41,58,64] so it will be of interest to explore PCSK9 flux responses to statins or other interventions in human subjects.

This model also has potential therapeutic implications. If increased PCSK9 synthesis and secretion occur in response to statin therapy and result in higher LDLR degradation rates, efficacy of treatment might be improved by combining with agents that oppose PCSK9 effects. PCSK9 responses may also be relevant to other observations with statins such as "escape", non-linear dose-response curves, and species differences[40]. Moreover, if the signals in liver by which dietary cholesterol suppresses PCSK9 synthesis and secretion can be dissociated from suppression of LDLR synthesis, hepatic LDLR levels might be amplified. We observed greater reductions of hepatic mRNA levels than ASR for both LDLR and PCSK9. These results suggest that post-transcriptional factors are likely to be present that alter the synthesis rates of both LDLR and

PCSK9 in mouse liver[24,25,51,53]. This observation of post-transcriptional effects of cholesterol feeding on both PCSK9 and LDLR synthesis rates may provide a therapeutic approach.

Some other physiologic implications of this more layered regulatory model might also be considered. Important circulating small molecules, most notably glucose but also calcium, phosphate, amino acids, and other metabolites, stimulate feedback loops wherein blood concentrations are regulated through secretion of hormones by sensing tissues that restores homeostasis in the bloodstream. Insulin is secreted from a specialized cell into the bloodstream in response to changes in blood glucose concentrations and interacts with cellular receptors that mediate glucose uptake, for example, just as parathyroid hormone is secreted from a specialized cell into the bloodstream to restore blood calcium homeostasis.

By analogy, we observe here that the response to cholesterol feeding and increases in liver cholesterol and plasma LDL cholesterol concentrations includes markedly reduced concentrations and synthesis rates of PCSK9 in plasma (each by ~70%), which consequently keeps LDLR levels in liver unchanged, thereby tending to reduce blood LDL cholesterol levels (Illustrated in Graphical Abstract). If we allow the possibility that plasma cholesterol concentrations might be a regulated parameter, an intriguing metabolic model is suggested. By this conception, the liver may be seen as an endocrine organ that responds to increased cholesterol availability by reducing PCSK9 release and allowing LDL cholesterol re-uptake by liver or, conversely, increases PCSK9 synthesis and release under conditions of low cholesterol availability such as statin therapy to allow more delivery of cholesterol to extra-hepatic tissues. The analogy is imperfect here, as we did not establish whether plasma LDL cholesterol is involved in the signaling pathway that reduces PCSK9 synthesis. This will be an interesting question to explore in subsequent studies.

Another interesting finding about PCSK9 synthesis rates was that the FRR measured in the circulation was considerably faster than in the liver (5.0 %/hr. vs. 1.4 %/hr., representing $t_{1/2}$ of 15.6 hr. vs 54 hr., respectively), even though most PCSK9 in plasma presumably was synthesized in the liver[24]. This kinetic result is anomalous for classic linear biosynthetic pathways. Although it is common in linear metabolic pathways to see dilution of label between a precursor and its product pool - for example, due to the presence of previously synthesized, unlabeled molecules in the product pool - the only explanation for a higher fraction of newly made molecules in a product like blood PCSK9 compared to its precursor pool, in this case liver PCSK9, is a preferentially secreted pool of newly synthesized molecules released from the precursor compartment. Stated differently, it is generally not possible for a higher fraction of molecules to be labeled in plasma than in liver if the molecules were synthesized in and released from the liver, unless there is also an unlabeled pool in the precursor compartment. This occurs in endocrine cells, for example: some newly synthesized insulin is sorted into storage granules and some into the readily accessible secretory pool in the pancreatic beta cell[65,66,67]. Whether there is partitioning of newly synthesized hepatic PCSK9 into secreted vs stored pools will be an interesting question to explore.

Another question is whether this PCSK9 feedback loop is different or absent in animals with a more LDL-centered plasma lipid profile, such as humans with contemporary diet and activity. The stable isotope labeling approach with mass spectrometric analysis is readily applicable in humans. Lassman et al[39] gave deuterated leucine and used mass spectrometry to measure the t ½ of PCSK9 in human plasma. Heavy water labeling combined with tandem mass spectrometric analysis in our laboratory has been used to measure the turnover kinetics of several low abundance proteins in the bloodstream that were derived from liver or other tissues[68,69,70,71]. The flux response of PCSK9 to altered cholesterol homeostasis and the interaction with hepatic LDLR turnover have not been explored in humans, however.

Our study has some limitations. The effects of PCSK9 binding to lipoproteins was not assessed and plasma PCSK9 concentrations may not accurately reflect binding to the liver LDLR. We did document effects on LDLR turnover and content in liver, however, that are consistent with reduced actions of PCSK9.

In conclusion, we measured the turnover of PCSK9 in liver and plasma and of LDLR in liver using heavy water labeling and tandem mass spectrometric analysis. The data suggest that PCSK9 synthesis may be part of a feedback regulatory mechanism in the liver that opposes the canonical homeostatic defense of intracellular cholesterol content. The response of PCSK9 mRNA levels, synthesis rates and blood levels counterbalanced the well-established effects of cholesterol feeding on liver cholesterol content and LDLR levels[15,21,22]. Through this added regulatory loop, the liver may be conceived as an endocrine organ that tends to modulate cholesterol homeostasis through secretion of PCSK9 in a manner that coordinates LDL cholesterol release with peripheral tissue needs. This model will need to be tested directly in humans, but there could be physiologic and therapeutic implications, if for example the suppressive effect of cholesterol intake on PCSK9 synthesis and secretion could be amplified as a strategy for lowering plasma LDL cholesterol in hypercholesterolemia.

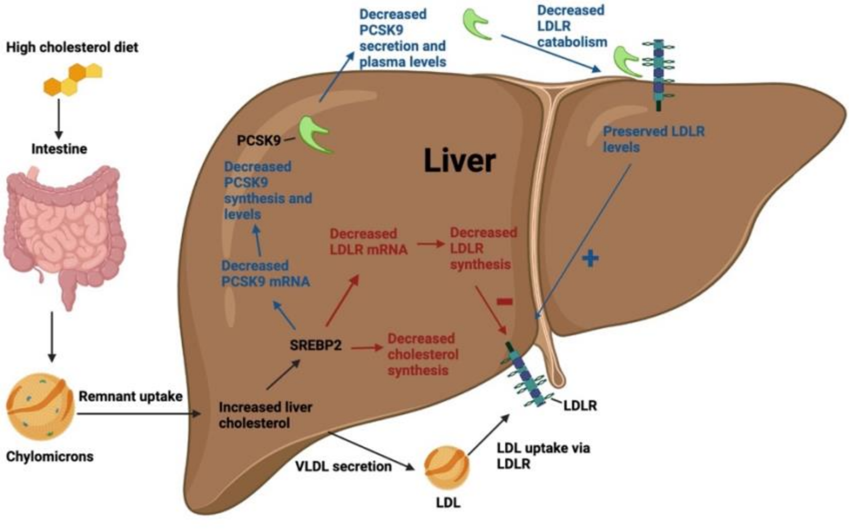

Proposed homeostatic mechanism of regulating blood cholesterol levels via LDLR and PCSK9 interactions after 1 week of high cholesterol diet in rodent liver. High cholesterol in the diet is absorbed by the intestine that is secreted in chylomicron particles, which undergo lipolysis to form chylomicron remnants that are up taken by the liver, resulting in increased dietary liver cholesterol. The liver secretes VLDL particles that are converted to IDL then to cholesterol rich LDL cholesterol, followed by clearance of LDL leading to increased liver LDL cholesterol levels that suppresses the sterol response element binding protein transcriptional pathway, resulting in less PCSK9 mRNA levels and a decrease absolute synthesis rate and protein levels. Less hepatic PCSK9 levels correlate with decreased PCSK9 secretion and plasma levels followed by a decrease in LDLR catabolism via PCSK9 resulting in preserved LDLR levels to uptake LDL and reduce LDL cholesterol. ApoB, apolipoprotein B. LPL, lipoprotein lipase. VLDL, very low-density lipoprotein particles. IDL, intermediate density lipoprotein particles. LDL, low-density lipoprotein particles. PCSK9, Proprotein Convertase Subtilisin/Kexin Type 9. LDLR, low-density lipoprotein receptor.

Acknowledgments. MD designed, executed experiments, and contributed to writing the manuscript. JH, SM and RK helped to perform experiments. HM and EN conducted the mass spectrometric analysis. MH contributed to the hypotheses, helped to design experiments, interpreted data, and contributed to writing the manuscript. Graphical abstract was created with by BioRender.com and publication license is available upon request.

Source of funding. This work was partly funded by the UC Berkeley Chancellor's Fellowship and Department of Nutritional Sciences and Toxicology Li-Chang Chu Fellowship.

Disclosures. We declare no competing interest.

2.6. Supplemental Material

A Mice underwent stable isotopic metabolic labeling with ^2H_2O to monitor protein synthesis rates by intraperitoneal (IP) injection with 99.9% ^2H_2O and maintained on 8.0% ^2H_2O drinking water.

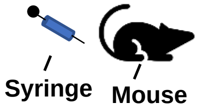

B Liver was homogenized with IP-MS (Immunoprecipitation-Mass Spectrometry) cell lysis buffer.

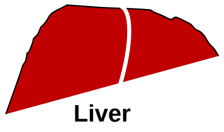

C Immunoprecipitation of LDLR and PCSK9 with antibodies and capture with protein A/G magnetic beads.

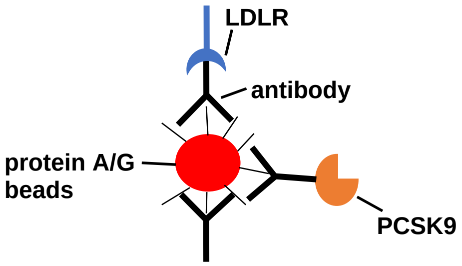

D Liquid chromatography (LC) tandem mass spectrometry (MS/MS) determined the replacement rates of PCSK9 and LDLR by the shift in their labeled ^2H-peptides after ^2H_2O incorporation.

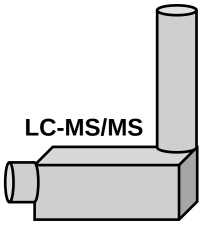

Figure I. Schematic of flux measurements of signaling molecules and cell surface receptors by immunoprecipitation and LC-MS/MS. A, Mice underwent heavy water labeling by a bolus IP injection of 99.0% $^{2}H_2O$ (35.0ul/gram body weight) and maintenance on 8.0% $^{2}H_2O$ drinking water. **B,** Blood, and organs were collected for LDLR and PCSK9 kinetic measurements. **C,** Tissue was homogenized followed by multiplex immunoprecipitation of PCSK9 and LDLR and ligand capture with protein A/G magnetic beads. **D,** Immunoprecipitants underwent in-solution digest with trypsin then measurement by LC-MS/MS of deuterium labeling pattern and content in peptides. Fractional replacement values (f, %) were calculated as described in the materials and methods and section. LDLR, Low-density lipoprotein receptor, PCSK9, Proprotein convertase subtilisin/kexin type-9.

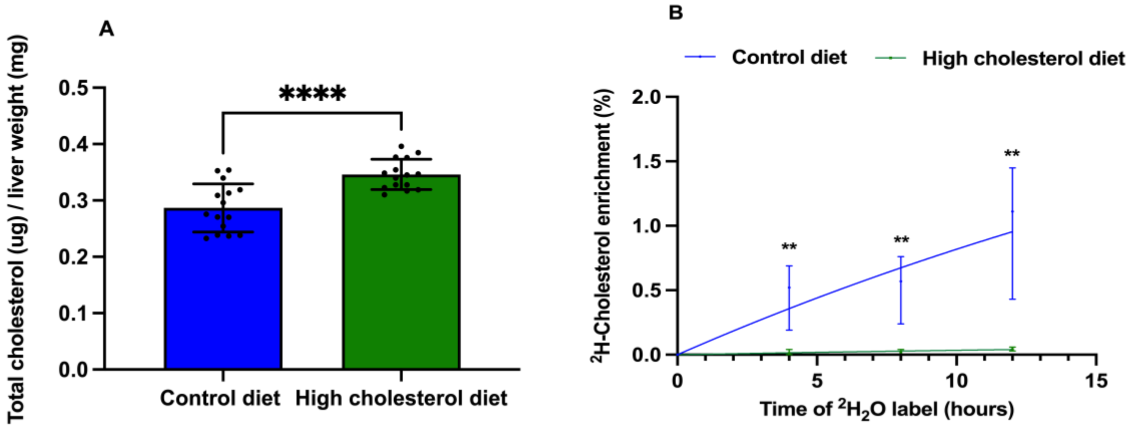

Figure II. Total hepatic cholesterol amount (ug / tissue weight (mg)) and percent deuterium enrichment (EM1) of newly synthesized cholesterol in liver. 8-week-old C57B6/J mice were fed a low fat-high cholesterol diet (n=15) (1.0% by weight) or control diet (n=15) for 1 week. Lipids were extracted from liver tissue using methanol chloroform extraction. Total cholesterol (cholesterol-ester and free cholesterol) was measured calorimetrically (Wako Inc.). **A,** High cholesterol diet increased total cholesterol amount from 0.28 ± 0.04 to 0.34 ± 0.02 ug total cholesterol / mg of liver weight, ($p<0.0001$). **B,** Hepatic de novo cholesterol synthesis (%, EM1) over 4, 8 and 12 hours of the $^{2}H_2O$ labeling period was measured by GC/MS (n=5 at each time point). High cholesterol diet significantly and almost completely suppressed total cholesterol synthesis over time to near zero values ($p=0.008$ at each time point). Data are expressed as the mean ± SD for the total cholesterol content, or median with upper and lower limits of the 95% confidence interval for the total cholesterol enrichments. Student's t-test or Mann-Whitney test calculated statistical significance for hepatic cholesterol content or cholesterol enrichment, respectively.

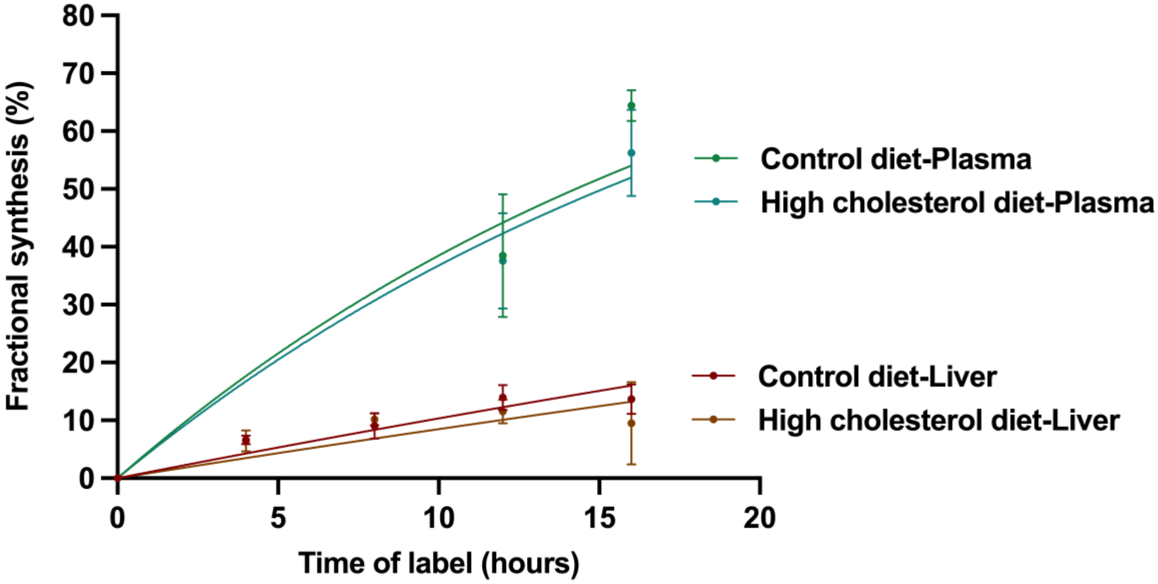

Figure III. Fractional synthesis of PCSK9 in the liver vs plasma after ^2H_2O labeling. C57B6/J mice were fed a low fat-high cholesterol diet (1.0% by weight) or control diet for 1 week. Metabolic labeling was by bolus IP injection of 99.9% ^2H_2O (35.0ul/gram BW) followed by 8.0% ^2H_2O in drinking water to maintain stable body water ^{2}H-enrichments. Animals were euthanized at 4, 8,12 and 16 hours of ^2H_2O labeling. PCSK9 was immunoprecipitated from plasma (at the 12hr and 16hr timepoints only) and liver samples from the same mice. Fractional synthesis values (%) is shown over time. A one-phase association, non-linear regression line, Y=Y0 + (Plateau-Y0) *(1-exp(-K*x)), where Y0=0, plateau=100%, x=time, and K= fractional replacement rate (FRR) constant, was used to fit PCSK9 fractional synthesis over time. PCSK9 FRRs were faster in the plasma vs the liver regardless of dietary treatments ($p<0.0001$). No statistical difference was observed in FRRs between dietary treatments in the liver or plasma. Exact sum of squares F test calculated statistical significance between FRR's, n=6-12 per group. Data are expressed as mean fractional synthesis (%) ± SD.

3. Chapter 3

Literature Review of Insulin Dynamics and Kinetics in Human Health and Disease.

In the United States alone, there are over 34.2 million people that have been diagnosed with diabetes, and 88 million individuals have prediabetes based on a previously published report from the Center for Disease Control and Prevention (CDC)[72]. Accordingly, diabetes was ranked as the 7th leading cause of death in the US. Diabetes is highly associated with metabolic conditions such as obesity[73]. Now, what is diabetes, how is it caused, and why should we investigate the causes of this disease by modern metabolic approaches via stable isotopes as metabolic labels combined with high-performance mass spectrometry?

3.1. Pathophysiology of Type II Diabetes: leading to beta-cell failure and methods are lacking to evaluate this relationship in vivo.

Since the discovery and production of insulin, parallel research studies were conducted to ask fundamental questions about diabetes: what is the disease of diabetes, what are the types of diabetes, what causes diabetes, what are the pathophysiological consequences, how can we diagnose patients with diabetes, how can we treat diabetes, and what are the past, present and modern approaches to measure the concentrations of insulin and new approaches to measure the biogenesis of insulin? Diabetes is a complex disease that can be subdivided into classes such as diabetes insipidus, diabetes mellitus (i.e., type 1 diabetes and type 2 diabetes), gestational diabetes, and maturity-onset diabetes in the young (MODY)[74,75].

For this dissertation, we will focus on diabetes mellitus, which can be viewed as a progressive disorder, and characterized by three main different types, prediabetes, type I, and type II diabetes. The disease can be diagnosed by evaluating fasting glucose levels, glycated hemoglobin A1c levels, and performing a series of tests such as glucose tolerance test, or insulin tolerance test[76]. In prediabetes, individuals exhibit high glucose levels or hyperglycemia based on the above test, but their insulin levels remain normal. As this condition worsens, prediabetes leads to type II diabetes (TIID) characterized by insulin resistance, reduced pancreatic beta-cell reserve of insulin, low insulin levels, and high glucose levels. The development of TIID can be influenced by our genetics, environment, dietary insults, and lack of physical exercise[73,77,78]. Essentially, these forms of diabetes boil down to the destruction of beta cells and reduced reserve capacity to produce and store insulin.

Rather than study the physiological consequences of insulin resistance and diabetes (specifically type II), we lack methods and approaches to measure the cause of the disease, which is insulin pancreatic reserve governed by beta-cell insulin biogenesis. Due to the high demand for beta cells to increase the synthesis of insulin to maintain euglycemia in hyperglycemic states, beta cells begin to increase in size and number. The principal etiological roots of this metabolic condition are insulin resistance (IR), beta-cell secretory failure, and loss of beta-cell mass[79,80]. Insulin resistance or decreased action from insulin impairs glucose utilization in muscle, increases hepatic glucose output in the liver, and promotes lipolysis and free fatty acid release in the adipose tissue. This all contributes to metabolic syndrome in human beings and accelerated cardiovascular disease. The transition to TIID from compensated insulin resistance is characterized by pancreatic beta cells' inability to respond to increased insulin demand from prolonged hyperglycemia[79].

These adaptations have been characterized in both rodent models as well as human[81], yet despite this body of knowledge, approaches lack to measure the pancreatic insulin reserve capacity in vivo. Therapeutic interventions that stimulate or preserve the capacity for beta-cell proliferation and mass, and biomarkers such as insulin biogenesis that reflect the health and death of beta cells are therefore of great interest[82,83,84]. Therefore, methods are lacking to measure pancreatic beta-cell reserve in response to diabetic treatment or for the diagnosis and predisposition from prediabetes to diabetes as shown in **Figure 1**.

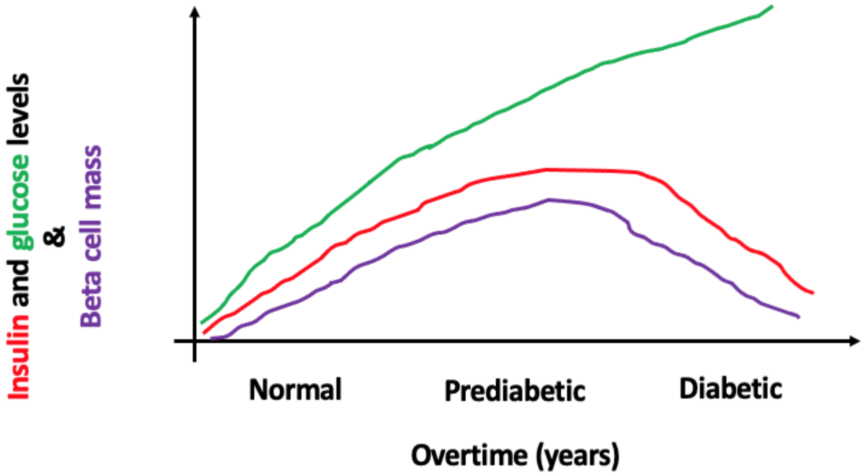

Figure 1. Our first objective is to develop a non-invasive measurement of in vivo dynamics of the passage of newly synthesized insulin through pancreatic beta cells for monitoring the progression of diabetes. As a progressive disorder, patients exhibit hyperglycemia when insulin resistance leads to secretory exhaustion or death of insulin-producing beta cells, resulting in relative or absolute insulin deficiency. A question we investigated was does the turnover rate of secretory granules ("reserve pool") or total release of newly synthesized insulin plasma differ between obese insulin resistant, prediabetic and lean humans?

3.2. Insulin Biogenesis and Secretory Dynamics.

The impairment to respond to insulin or inability to produce insulin illustrates the pathology of type 2 diabetes and type 1 diabetes, respectively. Therefore, we need to investigate the biogenesis of insulin secretory dynamics in the blood and pancreatic beta-cell biology to understand this disease. The biogenesis of insulin occurs in the rough endoplasmic reticulum. Membrane docking sites for ribosomal translation machinery translate insulin mRNA into a polypeptide of 110 amnio acids that starts with N-terminal signal peptide, B chain, C peptide, and C-terminal A chain in which this pre-pro-insulin is then that cleaved to release the signal peptide to generate proinsulin, following subsequent disulfide bond formation. Research suggests that a combination of post-transcriptional mechanisms accounts for an abrupt increase in insulin biosynthesis by glucose[85]. Preproinsulin mRNAs account for the majority of transcript in beta cells in which repressed copies are converted to the active form during hyperglycemia allowing beta-cells to bypass transcription for insulin biogenesis. RNA binding proteins, therefore, regulate proinsulin mRNA stability, rates of translation, and ER transfer[86]. Beta-cells maintain insulin storage by storage of preproinsulin polysomes that are regulated by glucose stimulation[87].

The proinsulin enters the trans-Golgi network to form a secretory granule where pro-insulin matures into insulin by proteolytic cleavage by Proprotein convertase 1/3 (PCSK3) and PCSK2 actively, and exopeptidase carboxypeptidases remove basic residues, resulting in C-peptide release. Each time an insulin molecule is synthesized and secreted into circulation, C-peptide is secreted at equal molar ratios and exhibits a longer half-life and is readily secreted into the urine. C-peptide also doesn't have a significant first pass by the liver as compared to insulin. This provides C-peptide as a clinically useful metric of insulin secretory dynamics[86,88]. Other researchers have relied on proinsulin levels in the blood as a marker of beta-cell dysfunction [89,90]. This infers that the beta-cells have an alteration in the processing and storage of proinsulin given the excessive insulin demand, promoting beta-cell degranulation without sufficient time for insulin maturation[89]. Methods of stable isotopic metabolic labeling of insulin with ^2H_2O combined with static measurements can help to determine the pool sizes of insulin in the beta cell and the types of pools/secretory dynamics.

The exact explanations for defining insulin secretion in type 2 diabetes and type 1 diabetes, along with insulin production and release remains a mystery without directed methods to measure insulin biosynthesis. An overwhelming amount of research has shown two phases of insulin secretion[65,66,91]. The route of administration of glucose such as intravenously, or orally can have profound impacts on insulin secretory dynamics[92]. During the initial glucose load in the first phase of insulin secretion, plasma insulin levels in humans and insulin secretion rates in pancreatic beta-cell culture rise significantly from basal levels[65,66,91]. In the second phase, insulin levels drop and plateau. Insulin is secreted by the b cell into the portal vein in which ~50% undergoes extraction by the liver, whereas C-peptide is not. Under physiological conditions of gradual glucose increase, the biphasic stages are less prominent.

From biphasic to pulsative models, other models have argued for an oscillatory nature during a meal as compared to intravenous glucose administration[93,94]. The investigators illustrated that oscillatory pattern of insulin secretion in which the amplitude and frequency are influenced by glucose, exemplifying an on/off pattern[94]. Additionally, the Incretin effect seems to be facilitated by this pulsative nature. This data suggest insulin action on the liver is improved when secreted in an oscillatory manner[93]. TIIDs and impaired glucose tolerance patients have shown defects in pulsatile insulin release, perhaps as a marker of beta-cell dysfunction. C-peptide secretion measurements from its concentrations can obtain peptide kinetics modeling and deconvolution, known as the Eaton-Polonsky approach, or methods by Van Cauter, or the combined model as an alternative to deconvolution, along with the minimal model[96,97,98,99,100]. TIID patients show fewer pulses and lower amplitudes. Insulin secretory dynamics and biogenesis remains under-investigated and the use of ^2H_2O water labeling and mass spectrometry could help to understand us to further understand this process in vivo.

3.3. Isotope labeling strategies enabled fundamental discoveries of insulin biogenesis and secretory dynamics.

Seminal studies that have attempted to understand the biogenesis, processing, and secretion of insulin revolve around tracer methodology in the 1960s. First approaches utilized tritium labeled amino acids (i.e., [^{3}H]-Leucine) into slices or cell cultures of primary ox, rabbit, and rat pancreas in vitro[101,102,103,104,105,106]. Interestingly, Taylor et al showed a small effect of labeled leucine incorporation into insulin after increasing glucose concentration that was observed in toadfish pancreas as well, suggesting insulin levels may be regulated by secretion[101,103]. Others have used ^{35}S-methionine injected intraperitoneally into rats in vivo [107,108]. Researchers observed an increase in the incorporation of radioactive methionine into insulin over a 120 min period, displaying that ^{35}S- methionine is incorporated into insulin and is an amino acid for this protein. Recent studies have used ^{35}S- methionine to evaluate the effect of MODY mutations, and late-onset diabetes contributes to preproinsulin translocation defects[109,110].

The biogenesis and formation of insulin to proinsulin were studied in isolated rat islets labeled with ^{3}H-L-leucine[111]. Initially, over 3 hours, radioactive counts for proinsulin increase faster than incorporation into insulin, but an inflection point occurs in which the radioactive count for proinsulin reaches a plateau, and insulin radioactive counts increase steeply from 3 to 12 hours in the in vitro experiment. This result has been observed before by Howell and colleagues[106]. They also observed minimally labeled proinsulin/insulin in the medium and highly labeled proinsulin in the islets at basal conditions, but the amount of radioactivity of proinsulin and mainly insulin increased significantly in both compartments after glucose administration. These studies established the following: precursor product relationship of preproinsulin to insulin, insulin conversion from one polypeptide chain, the site of biosynthesis and transformation of proinsulin in the islets, glucose regulatory role on insulin secretion, the role of proteases, and oxidation processes for the biogenesis of insulin[112].

Techniques that measured concentrations of insulin, if any hormonal measurements, were lacking in clinical biochemistry in the past. The invention of the "Radioimmunoassays" of peptide hormones, specifically insulin, revolutionized the field of diabetes and other hormonal diseases for monitoring insulin levels in different states of diabetes[113]. This technique involved the use of radioactive isotopes such as radioactive iodine attached to antibodies to detect the levels of insulin in response to nutrient and hormonal status in the blood as a function of radioactivity. Radioimmunoassay was very sensitive and fast but requires hazardous radioactive materials. Kats et. al. used the radioimmunoassay to determine the relative extraction kinetics of proinsulin, insulin, and C-peptide in the rat. They determined that the clearance rate of insulin was significantly higher than that of proinsulin and C-peptide[114]. Compartmental modeling with simulation modeling analysis software was implemented to evaluate the kinetics of insulin in men[115]. Other studies with ^{125}I-insulin infusion evaluated observed minimally less clearance, but elevated reentry rates in late-stage diabetic patients[116].

Work by Rhodes et al 1987. established that proinsulin/insulin recently synthesized and insulin storage is released from pancreatic beta cells via predominantly regulated, rather than a constitutive pathway[117]. They used isolated pancreatic rats' islets pulsed with [^{3}H]-Leucine at basal and stimulatory glucose concentrations over 180 min. They found no effect of glucose on proinsulin to insulin conversion, and release of newly made proinsulin. Insulin was also regulated by glucose with an overwhelming amount originating from newly synthesized insulin, but a minimal amount of proinsulin released in a glucose-independent fashion[117]. Based on

^{125}monoiodoinsuilin decay curves after exogenous injections, insulin half-life was shown to be ~10 min and ~35 min for C-peptide from circulation[98,118].

Studies that have measured the balance between insulin synthesis and releases also incorporated isotopic tracers. Schuit et al labeled isolated pancreatic rat beta cells and tracked protein synthesis rates with L-[3,5-^{3}H] tyrosine or L-[2,5-^{3}H] histidine. An increase in glucose levels did not increase insulin synthesis rates, but elevated insulin release. Insulin synthesis rates were not affected by glucagon or epinephrin treatment, but insulin release was significantly elevated with phorbol ester or glucagon treatment, then decreased with simultaneously glucagon/epinephrine treatment. They estimated that >3 x 10^{3} of new insulin molecules per sec per beta cell[119]. However, issues arise with radioactive isotope labeling studies such as safety, chemical modifications of native proteins, distribution kinetics, cross-reactivity, and incompatible with outpatient studies. Therefore, stable isotopes offer a much safer approach to measuring insulin kinetics in humans.

3.4. Contemporary approaches to measuring insulin levels using mass spectrometry to insulin kinetics with $^{2}H_2O$ water labeling and mass spectrometry.

Modern approaches to measuring insulin levels include ultra-precise liquid-chromatography tandem mass spectrometry technology (LC/MS-MS), however, this has yet to be coupled with flux-based measurements with $^{2}H_2O$ labeling[120,121,122]. For example, isotope dilution assay (IDA) mass spectrometry allowed researchers to calculate insulin levels without radioactivity[123,124,125]. This involved a known amount of isotopically labeled insulin as an internal standard spiked into a sample and comparison of relative intensities for precise identification between endogenous and exogenous sources and quantification[124,126]. Kippen et al demonstrated via IDA higher levels of insulin, C-peptide, and proinsulin in TIID vs normal individuals[125].

Typical approaches for sample clean-up involve solid-phase extraction, ion-exchange chromatography, immunoaffinity, derivatization, or a combination of each followed by mass spectrometry analysis[127,128,129,130]. Variations in normal or nanoscale flow and mass analyzers (i.e., Q-TRAP, Q-TOF, orbitrap, MALDI, and ion-mobility) can influence the ability to detect insulin levels[130]. These approaches have been instrumental in the determination of synthetic analogs and animal insulin in human plasma, urine, or dried blood spots for doping control purposes, forensic investigations, and in response to diet, drugs, and disease[131,132,133]. A golden approach typically involves a sample clean-up before and/or after immunoaffinity to eliminate matrix interference[134]. Recent studies have shown that insulin, its synthetic analogs, and C-peptide can be measured in human plasma by LC/MS without immunoaffinity by mixed-mode cation-exchange and orbitrap mass spectrometry[135]. This approach can be applied to multiple small peptide molecules such as luteinizing hormone-releasing hormone, growth releasing hormones, insulin-like growth factors, and glucagon [134,136,137,138,139,140]. An in-depth review of immunoaffinity techniques coupled with mass spectrometry for the analysis of human peptide hormones can be found elsewhere[121]. In all, these studies have been pivotal for the method development of precise measurement of insulin concentrations, but studies that have measured the biosynthesis of intact insulin in vivo remain under-investigated. We wish to evaluate the relationship between both insulin concentration and flux for a holistic view of insulin metabolism in human health and disease.

Currently, no method exists to measure insulin biosynthesis using ^2H_2O labeling and mass spectrometry but has been proposed[141]. Moreover, indirect measurement of insulin biosynthesis from the pancreatic beta-cell in circulation in vivo applies to ^{13}C labeling and measuring of C-peptide enrichments. Healthy human volunteers received isotopically labeled ^{13}C-leucine followed by an oral glucose tolerance test[142]. The incorporation of isotopically labeled leucine in the urine was measured as an indirect readout of insulin biogenesis from the pancreas. They revealed that ~80% of labeled C peptide originates from 'old' and ~ 20 % was contributed by newly synthesized insulin. In support, correlation analysis showed tracer/Tracee ratio (t/T) of C peptide was negatively correlated with early C-peptide release and high glucose concentrations during the early phase of insulin secretion from 0-60 minutes after glucose, suggesting in the first phase of insulin secretion is accompanied by high dependence of de novo synthesis. Early studies with radioactively labeled insulin support this data in which an increase in insulin release occurred after more than 1 hr. after glucose load[106].

In times of large storage capacity in healthy humans under a high glucose load, C-peptide enrichments support preferential secretion of newly synthesized insulin. But in the late phase in normal humans, the release of insulin was not completely explained by de novo, suggesting a mixed pool of newly synthesized insulin and old[142]. Studies of isolated islets labeled with radioactive leucine display evidence that glucose marks beta cells to preferentially release newly synthesized insulin[143]. Urinary C-peptide fractional synthesis rate was 9.9%/hr., and de novo c peptide value of ~1600 pmol/l over the 210 min sampling period[142]. The issue that surrounds this study is that C-peptide measurements in the urine are only a proxy of insulin biogenesis from the pancreas and do not truly represent insulin. ^{13}C-leucine tracers may be confounded by surrogate measurements of precursor ^{13}C-leucine ketoisocaproic acid compartmentalization effects that could underestimate ^{13}C-leucine C-peptide enrichments given high insulin demand. This study only evaluated short-term acute C-peptide kinetics rather than daily C-peptide kinetics. In all, these observations collectively make this approach an approximation of insulin biogenesis from the pancreas.

Methods are lacking to measure de novo insulin biogenesis using ^2H_2O labeling and mass spectrometry that can reveal these questions. Some questions we wish to address in this dissertation include: What are the dynamics of the different pools (i.e., constitutive, rapidly releasable, storage) in the beta cell? How long does insulin live in the beta cell and how is this different in the above pools? What are the effects of physiological stimuli such as meal intake as compared to clinically controlled conditions such as glucose tolerance tests or under CLAMP conditions? How does the route of administration of nutrients (intravenous vs oral) alter insulin secretory dynamics? Is there a preferentially secreted pool of old and/or new insulin molecules depending on external stimuli or at basal conditions? How does insulin kinetics differ between normal, prediabetes, and TIIDs? What's the relationship between obesity and the development of diabetes? How can we accurately diagnose who is going to be diabetic? Does the pattern of insulin labeling in the urine, pancreas, and blood reflect each other? All these questions can be pursued with new methodologies for measuring insulin biosynthesis via ^2H_2O labeling and mass spectrometry as presented in this dissertation.

The overall static concentrations of insulin in the plasma are governed by insulin secretion and the rate of insulin removal by the tissues. High plasma insulin content under fasted and fed states have been documented in obesity[144]. What studies have evaluated the secretory dynamics, metabolism, and kinetics of insulin in circulation in humans[145]? Studies by Smith et al examined the influence of adiposity, insulin resistance, and intrahepatic triglyceride content on insulin kinetics[146,147]. In response to a glucose load, modeling methods combined with C-peptide deconvolution revealed insulin secretion rates, tissue extraction rates, hepatic, extrahepatic, and plasma insulin clearance rates. Under high rates of insulin delivery, the total amount of insulin extraction reached saturation. Insulin appearance and extrahepatic extraction increased in lean-to obese subjects. Therefore, hyperinsulinemia in obese individuals with insulin resistance and NAFLD is due to beta-cell hypersecretion combined with saturable extraction in the liver.

This study and others observed that elevated plasma insulin concentration in obesity is caused by both increased insulin secretion and decreased extraction and clearance of portal and peripheral insulin[148]. In NAFLD, extrahepatic insulin clearance and hepatic insulin extraction did not between healthy subjects, did not correlate with insulin resistance in adipose and muscle tissue or liver fat, but did correlate with insulin sensitivity[149]. Under conditions of obesity in the absence of insulin resistance, basal and postprandial beta insulin secretion were significantly elevated as compared to lean subjects[150]. Weight loss did decrease insulin secretion which suggests adiposity had a profound impact on insulin secretion. To accurately determine whether hypersecretion in the beta-cell in obese insulin-resistant NAFLD patients, in vivo stable isotopic labeling methods are lacking to peer into the dynamics of beta cell secretory processes. We present here an approach using stable isotopic metabolic labeling with ^2H_2O and mass spectrometry to evaluate endogenous insulin kinetics derived from the beta-cell as shown in **Figure 2**.

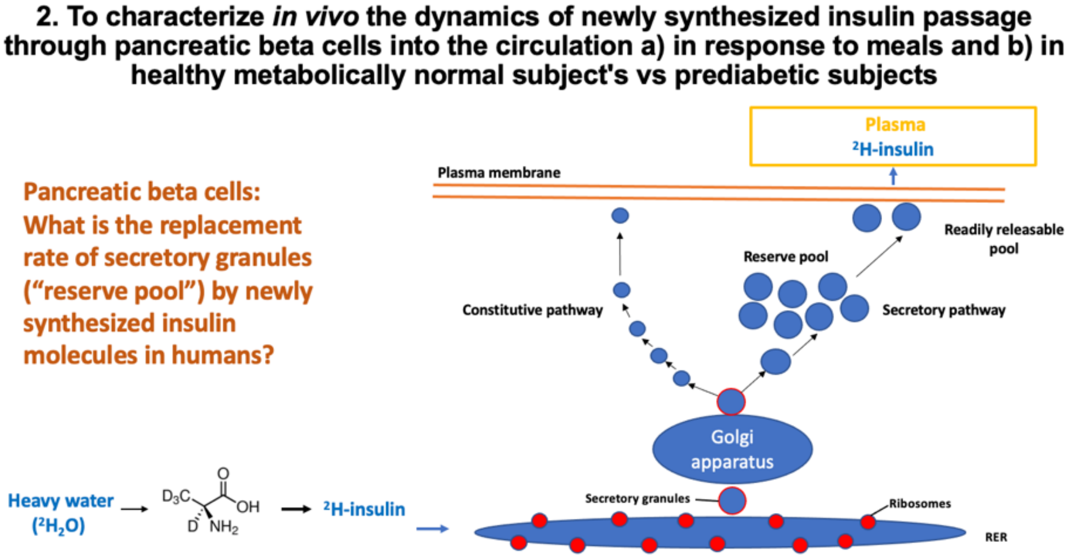

Figure 2. Our second objective is to characterize the in vivo dynamics of newly synthesized insulin passage through pancreatic beta cells into circulation in 1) response to meals and b) in healthy metabolically normal subject's vs prediabetic subjects. The diagram illustrates how stable isotopic metabolically labeling with heavy water of the pancreatic beta-cell amino acid pool. The 2H-labeled amino acids are incorporated into ^2H-insulin during protein synthesis on the rough endoplasmic reticulum. Secretory granules are then trafficked through the trans-Golgi network to be sorted in either the constitutive pathway or secretory pathway. A reserve pool maintains

pancreatic beta-cell insulin storage capacity and a readily releasable pool quickly responds to insulin secretory stimulations[151]. The figure was Adapted from Hou et al[152].

Metabolic labeling with stable isotopic ^2H_2O water combined with tandem mass spectrometry analysis provides a solution to meet this unmet need in clinical medicine. ^2H_2O provides a simple and safe metabolic label for evaluating protein synthesis rates across the proteome[41,43,44,45]. ^2H_2O is safe to ingest, freely equilibrates in the body within minutes, and labels the non-liable position of amino acids in metabolic reactions to allow measurements of protein synthesis rates in real-world outpatient conditions. The measurement of protein synthesis rates by mass isotopomer distribution analysis (MIDA) has been in development by our lab for the past 30 years[44,58,153]. MIDA is a mass spectrometry stable isotope labeling approach based on combinatorial analysis of the precursor and product relationship[153]. This has allowed researchers to determine the true precursor pool from the product pool enrichments and vice versa, the predicted theoretical distribution of mass isotopomer distribution patterns to allow calculations for fractional synthesis values, fractional synthesis rates, half-lives, and absolute synthesis rates[153]. An in-depth review can be found elsewhere[41,153].

Recent developments to measure the kinetics of low abundant proteins are lacking using stable isotopes have been proposed, but are in development[39,68,69,70,71]. This approach has allowed researchers to evaluate the molecular kinetics of clinically relevant metabolic pathways for biomarkers of muscle metabolism, and NAFLD, and recently revealed an added dimension to the cholesterol homeostatic model[69,70,71,154]. For this dissertation, we developed a method to evaluate the kinetics of insulin by our technology a) in healthy individuals over time to characterize the half-life and pool dynamics of insulin, b) in response to meal intake in healthy, prediabetic, postprandial hypoglycemia, and TIID patients, c) in metabolically normal lean, metabolically normal obese, and metabolically abnormal obese patients.

4. Chapter 4

The Kinetics of Newly Synthesized Insulin Appearance in Circulation during Metabolic Labeling is a Marker of Beta Cell Insulin Storage Pool Turnover. A Preliminary, Proof-of-Concept Study.

4.1. Abstract

Methods are lacking to evaluate the biogenesis and kinetics of insulin in vivo. Type 2 diabetes is characterized by progressive loss of insulin secretory reserve in pancreatic beta cells. My objective is to measure the replacement rate of serum insulin in humans using our tracer techniques. In this pilot study, we measured the replacement rate of serum insulin in humans as a marker of insulin half-life in the pancreatic beta cell, using metabolic labeling with heavy water and mass spectrometric analysis. We show here for the first time the rate of newly synthesized insulin appearance in human plasma and of C-peptide in urine and blood. This measurement reveals the lifespan or transit time of insulin stored in secretory granules in the beta cell. Insulin replacement rates were in the range of 24.1%/day in fasted state in normal subjects and was 2.4%/day in an obese subject. C-peptide turnover rates were also measured in urine and blood.

4.2. Introduction

Type 2 diabetes (T2D) stands as one of the most important metabolic diseases in the 21st century[72]. T2D has two dimensions: tissue insulin resistance (IR) and beta-cell failure to secrete sufficient insulin to compensate[77,78,144,155]. During insulin biogenesis, proteolytic cleavage events of preproinsulin to proinsulin occurs followed by disulfide bond formation between insulin alpha and beta chains, ultimately creating a mature insulin molecule. This is accompanied by C-peptide release along with insulin and C-peptide storage in secretory granules[86]. In addition, C-peptide is cleared into the urine, so that 24-hour C-peptide content of urine provides a useful and clinical marker of cumulative insulin synthesis and secretion, but this still represents an indirect measurement of insulin biogenesis[156].

The half-life of insulin clearance kinetics from the plasma has been reported as ~5-10 minutes due to rapid clearance though the liver and kidney[157]. Plasma insulin concentrations are governed by pancreatic beta-cell synthesis, secretion, and plasma clearance rates[158]. Obesity is associated with IR and hyperinsulinemia which may advance to developing T2D[144]. As a progressive disorder, beta-cells respond to IR by increasing their cellular mass and insulin production that both successively decrease in T2D[78,155,158]. In obese prediabetic conditions, increased insulin secretion and reduced plasma clearance both contribute to hyperinsulinemia, but hepatic extraction of plasma insulin saturates at high insulin stimulatory conditions[146]. Basal insulin secretion rates (ISR) were reported to be higher in obese T2D than in normal lean healthy humans, but clearance rates were similar[158]. Lower ISR and plasma insulin concentrations correlated with higher plasma glucose levels in obese T2D patients. These observations pinpoint that hyperinsulinemia in prediabetic obese conditions is due to increased pancreatic beta-cell insulin secretion, whereas in diabetes, diminished insulin secretion rates as well as reduced pancreatic beta-cell reserve contribute to inadequate insulin levels. The relative contributions to the higher plasma insulin concentrations in obese prediabetic conditions from newly synthesized insulin or from an older reserve pool remains uncertain in humans. Diagnostic approaches are lacking to measure and predict the progression of diminished insulin pancreatic reserve[77,78,144,155], and the ability to measure the biosynthesis and turnover of insulin in the pancreatic beta cell in humans could provide insight.

The biogenesis and formation of insulin from proinsulin have been studied with isotopic approaches in isolated rat islets labeled with ^{3}H-L-leucine[111]. Over 3 hours, proinsulin radioactive incorporation increased faster than insulin, but an inflection point occurred in which proinsulin radioactivity reached a plateau, and insulin radioactivity sharply increased from 3 to 12 hours after glucose administration. Modern but indirect approaches to measuring insulin biosynthesis from the pancreatic beta-cell in vivo apply to ^{13}C labeling for C-peptide kinetics[98,142]. Here, healthy human volunteers received isotopically labeled ^{13}C-leucine followed by an oral glucose tolerance test (OGT)[142]. The incorporation of isotopically labeled leucine in the urine was measured as an indirect readout of insulin biogenesis from the pancreas. Over a 210 min period of OGT, ~80% of C-peptide originated from an 'old' or an unlabeled pool, and ~ 20 % was contributed by newly synthesized insulin in the late phase of insulin secretion.

Within the beta-cell, data suggest that insulin fate can be directed into two pathways, a constitutive and a secretory pathway[65,66]. The latter pathway contributes to the reserve or storage pool, and a rapidly releasable pool[151]. From a biphasic to a pulsative model, others have also argued for an oscillatory nature during a meal as compared to only oral glucose administration[91,92,93,94]. The oscillatory pattern of insulin secretion in which the amplitude and frequency are influenced by glucose exemplifies an on/off pattern[94].

^2H_2O labeling and mass spectrometry have been used extensively in our lab[41,43,44,45] to measure the kinetics of low abundant proteins such as receptors, signaling molecules, and enzymes. These approaches have revealed crucial insights into several conditions[69,70,71,154]. Here, we applied this heavy water labeling/tandem mass spectrometry approach to measure the kinetics of insulin synthesis and secretion from pancreatic beta cells into the blood in humans.

We measured for the first time in humans the replacement rate of serum insulin by newly synthesized insulin made in the beta cell, using in vivo metabolic labeling. It is important to recognize that this reflects the turnover (replacement) of old, unlabeled insulin molecules in the beta-cell, including secretory granules, by newly synthesized, labeled molecules. These are the first direct experimental data for insulin synthesis and secretion in humans. The results suggest that pancreatic beta-cell reserve, the key factor in the progression from insulin resistance to T2D, can be monitored in vivo in humans.

4.3. Materials and Methods

Reagents and chemicals

Hyclone molecular grade water (GE health care™), phosphate buffer saline (PBS) (Gibco™), anti-human insulin antibodies (M677, M678, Calbio™), and ^2H_2O (Sigma-Aldrich). All products here were obtained from ThermoFisher™: EZ-Link™ NHS-PEG4-Biotin, No-Weigh™ Format, Thermo Scientific™ Zeba Spin Desalting Columns (7K MWCO), Pierce™ Streptavidin Magnetic

Beads, Tween 20, acetonitrile, methanol, formic acid, and acetic acid. 1.5 and 2mL Low bind tubes from Eppendorf were used as necessary. Liquid chromatography and mass spectrometry (LC/MS) related materials were obtained from Agilent™.

Biotinylating insulin antibodies

Insulin antibodies were biotinylated using the EZ-Link™ NHS-PEG4-Biotin, No-Weigh™ Format reagents. The protocol was adapted to the Thermo Scientific™ Pierce™ Antibody Biotinylation Kit for immunoprecipitation (IP). Briefly, 680ul of water was added to 2mg of single-use biotin (5mM). Typically, 100ug of antibody and 6.6ul of 5mM biotin reagent (50-fold excess) were added to 100ul total reaction buffered with PBS, followed by incubation in the dark for 1 hour. Excess biotin was removed by the Thermo Scientific™ Zeba Spin Desalting Columns (7K MWCO). Biotinylated antibodies were used fresh for each experiment and the remainder was stored at 4 ° C.

Sample preparation

For beta chain insulin kinetics, plasma samples were centrifuged for 10 min at 2,000g at 4 °C to remove debris. The clean plasma was transferred to a new 1.5mL tube containing a 1x protease inhibitor cocktail, and 3ug of M677 and M678 anti-insulin antibodies followed by overnight incubation at 4 °C while rotating. 20uL of 10mg/mL of Pierce™ Streptavidin Magnetic Beads were added to each sample followed by incubation for 1 hour at room temperature. Samples were collected on a magnetic stand and supernatants were stored at -80 °C. Beads were washed 3X with PBST (0.1% Tween 20 and 1x phosphate buffer saline) and 3X with ultrapure water. Antigen-antibody interactions were disrupted 2x with 100uL elution buffer of 40% acetonitrile and 1% formic acid. The top 90% of eluent was transferred to a new 1.5mL low bind tube and speed vacuumed dry. 10uL of 100mM ammonium bicarbonate, 10uL of trifluoroethanol, and 2.8uL of 50mM dithiothreitol were added, mixed, and incubated for 1 hour at 60 °C. Samples were allowed to cool for 5 min at room temperature before addition with 8ul of 50mM iodoacetamide and incubated for 30min at room temperature in the dark. Samples were diluted with 150ul of water, 50ul of 100mM ammonium bicarbonate, and 250ng of Promega mass spectrometry grade trypsin followed by overnight incubation at 37 °C. The next day, tubes were centrifuged for 10min at 10,000g and supernatants were speed vacuumed. Peptides were resuspended in 25uL of mass spectrometry submission buffer of 3.0% acetonitrile and 0.1% formic acid.

For intact insulin analysis, to deplete high abundant and large molecular weight proteins from plasma such as albumin and immunoglobulins, these proteins, and others from 1ml of plasma were precipitated with 2,400ul of ice-cold 1:1 (acetonitrile: methanol) mixture with 1% acetic acid[135]. 500ul were divided between two 2ml tubes. The samples were vortexed and centrifuged for 17,000g for 10 min at 4 °C. Supernatants were speed vacuumed dry with gentle heating, resuspended in 500ul of PBS by vigorous vertexing, and placed in a bath sonicator for 15 min. 3ug of anti-insulin antibodies M677 and M678 were added followed by overnight incubation at 4 °C while rotating. The next day, the samples were allowed to equilibrate to room temperature for 10 min while rotating. 20ul of 10mg/ml of Pierce™ Streptavidin Magnetic Beads were added to each sample followed by incubation for 1 hour at room temperature. Samples were collected on a magnetic stand and supernatants were stored at -80 °C. Beads were washed 3X with PBST (0.1%

Tween 20 and 1x phosphate buffer saline) and 3X with ultrapure water. Antigen-antibody interactions were disrupted 2x with 100uL elution buffer of 40% acetonitrile and 1% formic acid. The top 90% of eluent was transferred to a new 1.5mL low bind tube. This tube was centrifuged again for 17,000g for 10 minutes, and the supernatant was transferred to another 1.5mL low bind tube. The samples were speed vacuumed dry, resuspended in 30uL of 1% formic acid, vortexed for 10sec, centrifuged for 17,000g for 10 minutes, and transferred supernatants to plastic LC/MS vials.

Finally, for C-peptide urinary isolation, oasis prime hydrophilic-lipophilic balanced columns (3cc volume, 60mg sorbent weight) were implemented from Waters™. 10mL of urine was fortified with 10% acetonitrile by volume, vortexed, and centrifuged at 5,525 x g for 10 minutes[134]. The supernatant was applied to HLB columns preconditioned with 2mL acetonitrile and 2 mL of water, followed by a wash with 2 mL of water and elution with 1.2mL 80:20 (acetonitrile: water) into a 2 mL low bind tube. The eluent was speed vacuumed completely dry and reconstituted with 1mL of PBS. Anti-proinsulin-C-peptide antibodies (3ug) that were biotinylated according to the protocol above were added and incubated overnight at 4 °C. The next day, the samples were allowed to equilibrate to room temperature for 10 min while rotating. 20uL of 10mg/mL of Pierce™ Streptavidin Magnetic Beads were added to each sample followed by incubation for 1 hour at room temperature. Samples were collected on a magnetic stand and supernatants were stored at -80 °C. Beads were washed 3X with PBST (0.1% Tween 20 and 1x phosphate buffer saline) and 3X with ultrapure water. Antigen-antibody interactions were disrupted 2x with 100uL elution buffer of 40% acetonitrile and 1% formic acid. The top 90% of eluent was transferred to a new 1.5mL low bind tube. This tube was centrifuged again for 17,000g for 10 minutes, and the supernatant was transferred to another 1.5mL low bind tube. The samples were speed vacuumed dry, resuspended in 30uL of 1% formic acid, vortexed for 10sec, centrifuged for 17,000g for 10 minutes, and transferred supernatants to plastic LC/MS vials.

Measuring Insulin or C-peptide Turnover Rates with ^2H_2O Labeling and Mass Isotopomer Distribution Analysis

Comprehensive reviews of protein kinetic measurements using stable isotopic metabolic labeling with ^2H_2O coupled with high precision LC/MS-MS and MIDA have been presented elsewhere [41,43,44,45]. Briefly, gas-chromatography mass-spectrometry (GC/MS) measured ^2H_2O body water precursor pool enrichment, p (%) [41,58,153]. P was used as a surrogate of amino acid enrichment and provided the precursor labeling value to calculate theoretical protein product enrichments using MIDA. HPLC separated the complex immunoprecipitated samples. The mass isotopomer distribution of ^2H-labeled intact insulins or beta chain insulins were analyzed with a 6550 Agilent technology quadrupole time of flight (Q-TOF) mass spectrometer that was equipped with a chip cube ion source (Agilent Technologies, Santa Clara, CA). 3.0% acetonitrile/0.1% formic acid (v/v) to 95% acetonitrile/0.1% formic acid (v/v) composed of the mobile phase. Sample enrichment occurred for 18 minutes followed by elution from the analytical column for 12 minutes until a 95.0% acetonitrile to 5.0% water ratio. Peptide ratios and abundances were analyzed in parent MS mode. Agilent Spectrum Mill software analyzed the MS/MS data for protein identification with the Uniprot database of the human proteome[45]. Agilent Mass hunter qualitative analysis software determined the mass isotopomer distribution in the MS spectrum[45]. A baseline abundance of 10,000, a false discovery rate of 1.0%, and ± 5.0% of the predicted abundance for each mass isotopomer were included in the filtering criteria. For any given insulin charge state, the molecular formula, mass, and retention time were determined in the MS mode. Based on precursor body water enrichments (p), the number of exchangeable C-H positions (n) in the summed amino acids, measured ^{2}H-insulin enrichments, and mass isotopomer distribution patterns for insulin, this can calculate the fractional replacement (f) by MIDA[41,43,44,45]. Fractional replacement (f, %) is calculated from the change in the enrichment of the M_0 isotopomer at a time (t) / asymptote enrichment of the M_0 isotopomer predicted by MIDA for 100% new synthesis at the measured precursor pool enrichment. Values of f (%) were converted to fractional replacement rate constants (FRR, %/hr.) by the equation FRR = -ln(1-f)/time, based on first-order kinetic calculations. Half-life ($t_{1/2}$) was calculated as, $t_{1/2}$= ln (2)/FRR. Calculation of absolute synthesis rate (ASR, uU /ml /day, or pmol/L/day.) was defined as FRR (hr^{-1}) * concentration (pmol/L or uU/mL) as explicitly stated in each figure[45,153]. The remaining data analysis was performed with Microsoft Excel (Version 16.28) and Prism V9.2.0.

Subject characteristics, study design, and ^2H_2O labeling protocol

The study was performed at Washington University, St Louis. Plasma samples were obtained from an approved clinical study (ClinicalTrials.gov NCT02706262) titled, “Complex Effects of Dietary Manipulation on Metabolic Functions, Inflammation and Health.” The patients were split into three groups. The first group was denoted as metabolically normal lean (MNL) defined as lean patients with normal glucose control, normal plasma triglyceride (TG) levels, and low liver fat. The second group was denoted as metabolically normal obese (MNO) defined as obese patients with normal glucose control, normal plasma TG levels, and low liver fat. The third group was denoted as metabolically abnormal obese (MAO) with high glucose levels, and moderate to high liver fat content. Detailed subject information such as BMI (kg/m^2), body fat (%), hemoglobin A1c (%), fasting (mg/dL), fasting insulin (uU/mL), and other relevant metabolic characteristics can be found in the clinical trials website https://clinicaltrials.gov/ct2/show/NCT02706262. The use of ^2H_2O to monitor the rate of incorporation into proteins was approved for use in this study for insulin biogenesis. We used preexisting aliquots of ^2H_2O labeled plasma samples containing ^{2}H-insulin and other ^{2}H-labeled proteins, and metabolites. Patients were given 50 mL doses of 70% ^2H_2O every day for 3 weeks. For the first 5 days, patients consumed 70% ^2H_2O 3 to 4 times per day proceeded by 2 times per day for the final study duration. Body ^2H_2O and insulin enrichments were measured at weeks 1, 2, and 3 from plasma.

Statistics

Fractional synthesis values were fit to a one-phase mono exponential association curve using PRISM where, Y= Y0 + (1-Y0) * Plateau(1-e^(-kt), Y0=0, Plateau = 100%, k = fractional replacement rate, t = time (days). Half-life (t1/2) = ln (2)/FRR. Differences between fractional replacement rate constants were evaluated by an exact sum of squares F test. Unpaired T.test compared the average fractional synthesis rates, insulin concentrations, and newly synthesized insulin values between normal and prediabetic individuals. Data are shown as mean fractional synthesis values ± SEM between peptides or subjects for the individual or average measurements, respectively.

4.4. Results

The half-life of beta-chain insulin appearance in serum in both MNL and MAO subjects are on the order of days, not minutes.

To directly measure insulin biosynthesis from pancreatic beta cells as revealed in circulation using ^2H_2O labeling and mass spectrometry, we performed immunoprecipitation of insulin using anti-insulin antibodies on healthy human plasma. Insulin beta chain kinetics were used for this analysis. ^{2}H-labeled insulin beta chain half-lives in plasma in MNL (n=14) subjects showed a range of 2.5 to 7 days and an average half-life of 4.4 days with a fractional replacement rate of 15.4%/day (**Figures 1A and 1B**). Insulin beta chain half-lives in plasma in MAO ranged from 3 to 10 days and the average insulin beta chain half-life was 5.5 days with a fractional replacement rate of 12.5 % / day (**Figures 2A and 2B**).

Insulin beta chain fractional synthesis rates were similar between MAO and MNL, but absolute newly synthesized insulin rates were higher in MAO.

To determine how obese prediabetes alters insulin beta chain fractional replacement rates, we compared the FRR between MAO and MNL. Based on an exact sum of squares F test, obese prediabetic people had a similar insulin beta chain FSR of 12.5 % / day vs healthy people's FRR of 15.4 % / day (p=0.056) (**Figure 3**). We also converted the insulin beta chain fractional synthesis values to average fractional synthesis rates in **Figure 4A**. We observed no differences in FRRs between MAO and MNL subjects (p=0.1). Average fasting insulin concentrations were significantly higher in MAO vs MNL subjects (23.1 vs 5.7 uU/mL, p<0.0001), respectively (**Figure 4B**). We calculated the absolute newly synthesized insulin rates (uU/mL/day) by using the insulin beta chain FSR (%/day) * plasma insulin concentration (uU/mL). We observed a dramatically significant increase in newly synthesized insulin rates in MAO than MNL subjects, 2.8 vs 0.93 uU/mL/day, p<0.0001, respectively (**Figure 4C**).

Difference between insulin beta chain kinetics and intact insulin kinetics.

Proinsulin contains the beta chain but is released from the pancreatic beta cell with different kinetics than insulin[106,111,114,117,118,152]. Because of the possibility that variable contamination by proinsulin in the insulin pull-down preparations could alter measured beta chain kinetics, we compared intact insulin (not subjected to trypsinization) to beta chain kinetics. MNL subjects displayed slower insulin fractional as compared to one MAO subject who had a higher insulin fractional replacement rates of 24.1%/day and a half-life of 2.9 days (**Figures 5A and 5B**).

C-peptide fractional synthesis (%) in both urine and blood positively correlated with each other.

We sought to determine whether C-peptide fractional synthesis correlates between the blood and urine compartments[142]. After 5 days of heavy water labeling, C-peptide fractional synthesis rapidly approached 100% (**Figure S1A**). In the urine, C-peptide half-lifes were 1.7, 1.8, 1.2, and 1.8 days in patients 02, 04, 06 and 08, respectively. When we correlated C-peptide fractional synthesis in the urine vs the plasma, we observed a significant and positive correlation between the two compartments (**Figure S1B**). These results suggest that when a newly synthesized C-peptide in the urine can be used to represent newly synthesized C-peptide secreted into the bloodstream.

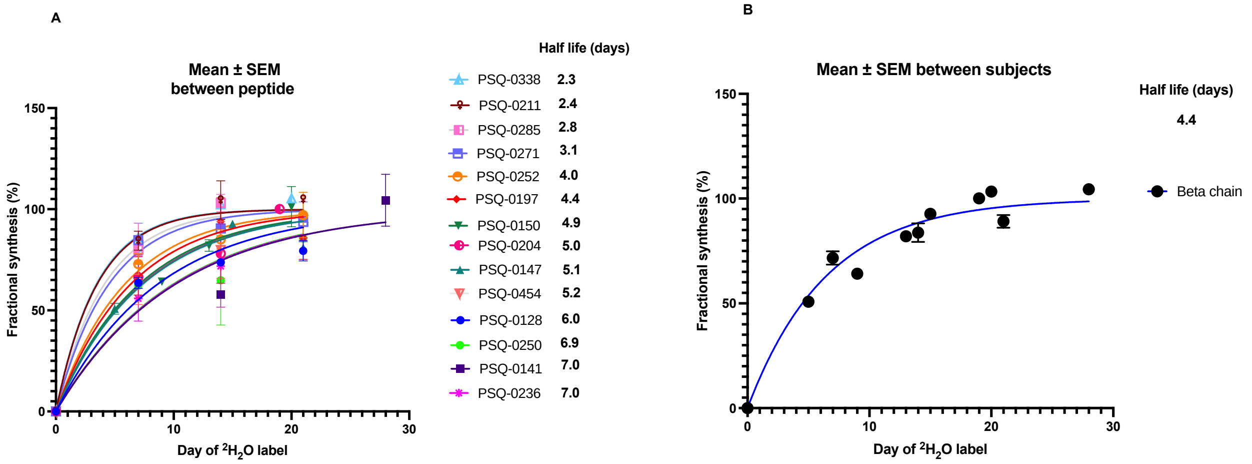

Figure 1. Individual and average insulin beta chain kinetics in healthy people (metabolically normal lean [MNL]). A) Individual insulin beta chain kinetics in metabolically normal individuals. Insulin beta chain half-lives ranged from 2.5 to 7 days (n=14). **B)** Average insulin beta chain kinetics between 14 healthy people. The average insulin beta chain half-life was 4.4 days with a fractional replacement rate of 15.4 % / day. Fractional synthesis values were fit to a one-phase monoexponentially association curve where, Y= Y0 + (1-Y0) * Plateau(1-e^(-kt), Y0=0, Plateau = 100%, k = fractional replacement rate, t = time (days). Half-life (t½) = ln (2)/FRR. Data are shown as mean fractional synthesis values ± SEM between peptides or subjects for the individual or average measurements, respectively.

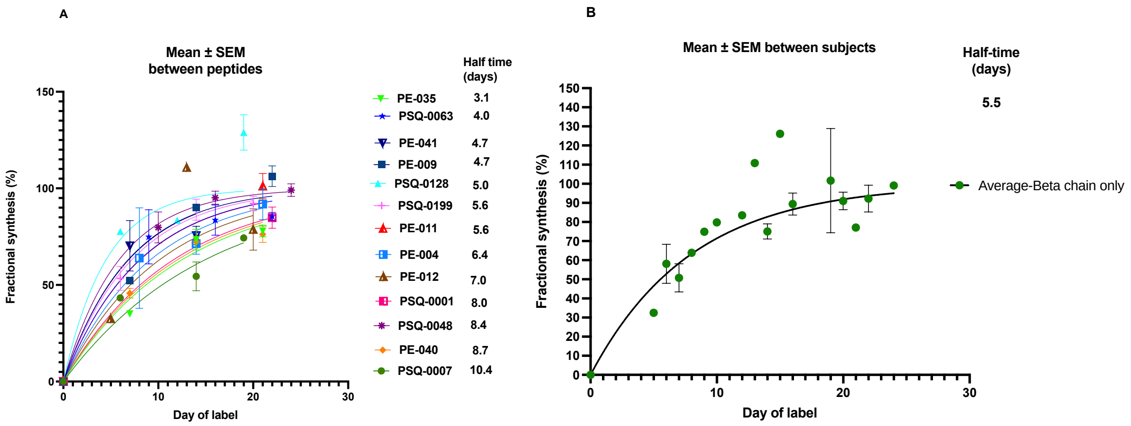

Figure 2. Individual and average insulin beta chain kinetics in prediabetic, insulin-resistant metabolically abnormal obese (MAO) people. A) Individual insulin beta chain kinetics in metabolically abnormal obese individuals. Insulin beta chain half-lives ranged from 3 to 10 days (n=13). **B)** Average insulin beta chain kinetics between 13 obese and prediabetic people. The average insulin beta chain half-life was 5.5 days with a fractional replacement rate of 12.5 % / day. Fractional synthesis values were fit to a one-phase monoexponentially association curve where, Y= Y0 + (1-Y0) * Plateau(1-e^(-kt), Y0=0, Plateau = 100%, k = fractional replacement rate, t = time (days). Half-life (t½) = ln (2)/FRR. Data are shown as mean fractional synthesis values ± SEM between peptides or subjects for the individual or average measurements, respectively.

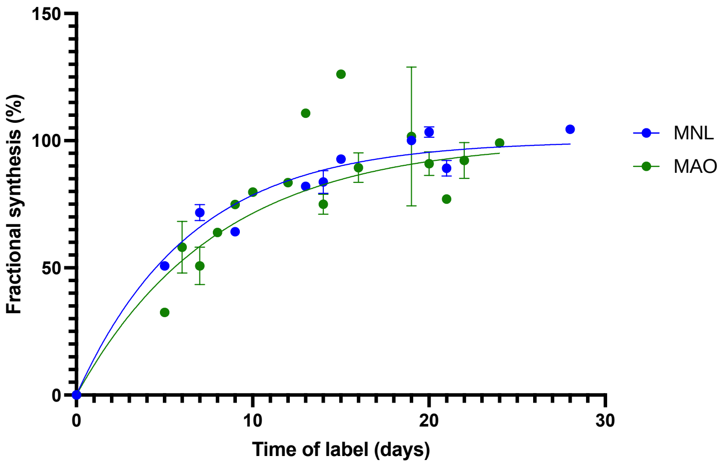

Figure 3. Average insulin beta chain kinetics in healthy people (n=14) vs prediabetic, insulin resistant, metabolically abnormal obese people (n=13). The average insulin beta chain half-life was 4.4 days for healthy vs 5.5 days for prediabetic obese people, respectively. Based on an exact sum of squares F test, obese prediabetic people had borderline significantly slower insulin beta chain FRR of 12.5 % / day vs healthy people's FRR of 15.4 % / day (p=0.056). Fractional synthesis values were fit to a one-phase monoexponentially association curve where, Y= Y0 + (1-Y0) * Plateau(1-e^(-kt), Y0=0, Plateau = 100%, k = fractional replacement rate, t = time (days). Half-life (t½) = ln (2)/FRR. Data are shown as mean fractional synthesis values ± SEM between peptides or subjects for the individual or average measurements, respectively.

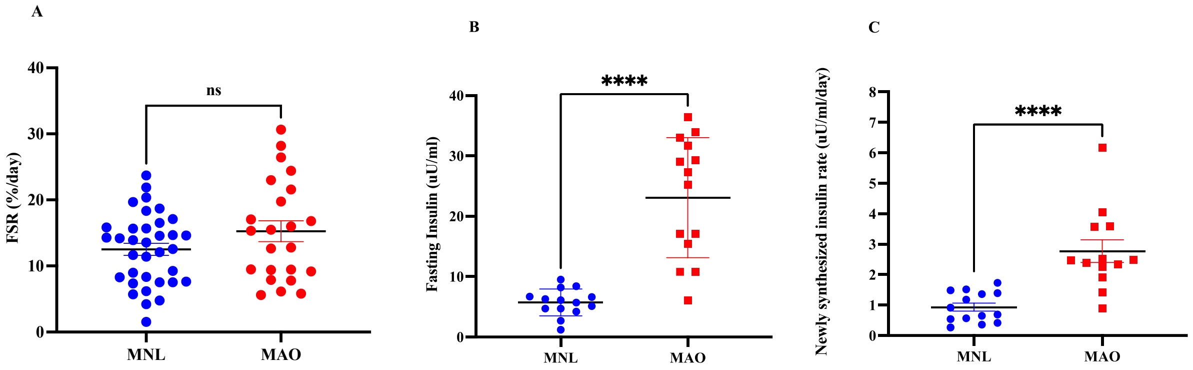

Figure 4. Insulin beta chain fractional replacement rates (%/day), fasting insulin concentrations (uU/mL), and absolute synthesis rates (uU/mL/day) of insulin beta chains between lean healthy vs prediabetic obese subjects. A) The average fractional replacement rates of insulin beta chain kinetics were not different in in MNL vs MAO subjects, 12.5 vs. 15.4 % /day, p = 0.10, respectively. **B)** Average fasting insulin concentrations were significantly higher in MAO vs MNL subjects, 23.1 vs 5.7 uU/mL, p<0.0001, respectively. **C)** Absolute synthesis rates of insulin beta chain kinetics were significantly higher in MAO than MNL subjects, 2.8 vs 0.93 uU/mL/day, p<0.0001, respectively. Data are shown as mean values ± SEM. Absolute newly synthesized rates of insulin beta chain kinetics were calculated by FRR (%/day) * insulin concentration (uU/mL). Statistical significance was calculated by unpaired student T.test.

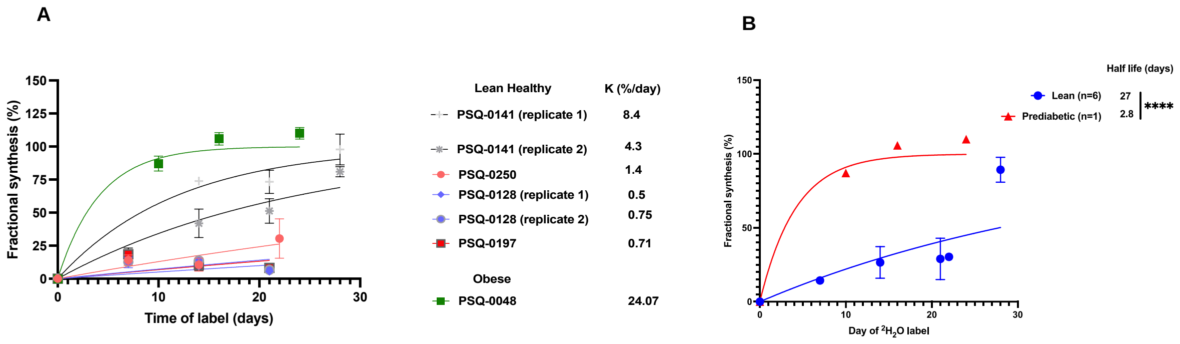

Figure 5. Individual and average intact insulin biosynthesis (%) in MNL and MAO subjects. A) Both MNL and MAO subjects were labeled with ^2H_2O for 1, 2, and 3 weeks. Intact ^2H-insulin fractional synthesis (%) was measured in plasma samples by mass spectrometry. One MAO subject displayed a higher fractional replacement rate of 24.1%/day and a half-life of 2.8 days. **B)** One MAO subject displayed significantly faster insulin production rate (24.1 vs 2.4 %/day, $p<0.0001$) as compared to MNL subjects. Fractional synthesis values were fit to a one-phase monoexponentially association curve where, Y= Y0 + (1-Y0) * Plateau(1-e^(-kt), Y0=0, Plateau = 100%, k = fractional replacement rate, t = time (days). Data are shown as the mean fractional synthesis values ± SEM values between subjects. Statistical significance between the production rates constants was compared by an exact sum of squares F test.

4.5. Discussion

We measured for the first time in humans the replacement rate of unlabeled serum insulin by newly synthesized insulin made in the beta cell, using in vivo metabolic labeling. It is important to recognize that this reflects the turnover (replacement) of old, unlabeled insulin in beta cell secretory granules by newly synthesized, labeled molecules, which are then released into the circulation. These are the first direct experimental data for insulin synthesis dynamics in humans. The data shown here should be seen as a pilot study, primarily as proof-of-concept for the methodology and approach. We have not yet determined the optimal analyte for these kinetics measurements- e.g., intact insulin, beta-chain insulin from immunoprecipitated insulin, beta chain insulin from gel purifications or C-peptide.

We measured the appearance of biosynthetically incorporated ^2H-beta chain insulin from the beta-cell appearing in circulation. ^2H-labeled insulin beta chain half-lives in plasma revealed in MNL subjects a range from 2.5 to 7 days, and an average half-life of 4.4 days with a fractional replacement rate of 15.4%/day (**Figures 1A and 1B**). Our data suggest in fasting conditions that insulin exhibits one phase mono-exponential rise to a plateau that is consistent with a homogenously mixed pool[152]. Newly formed insulin molecules can populate either a reserve pool, or a readily releasable pool in the secretory pathway[152]. Based on radioactive tracer studies of insulin and proinsulin in cell culture, Rhodes et al showed that newly synthesized proinsulin/insulin and stored insulin are preferentially released via a regulated pathway[117]. After meals and in response to insulin secretory agents, how insulin synthetic dynamics may alter the relative contributions of secreted insulin from newly synthesized insulin, old or less labeled insulin or a mixture of both remains an interesting question. Additionally, our data show heavy water labeling incorporation and appearance of labeled insulin in the plasma takes days. Whereas other data based on ^{125}monoiodoinsuilin or ^{25}monoiodoc-peptide decay curves after exogenous injections, insulin half-life was shown to be ~10 min and ~35 min for C-peptide from circulation [98,118]. Our metric of insulin biogenesis reflects a different biologic pathway – synthesis of new molecules in a specialized cell then releases into the bloodstream, not removal of molecules injected into the bloodstream – and may help to guide future pharmaceutical developments aimed at altering the half-life of insulin in diabetes and response to therapies.

To evaluate how insulin beta chain biosynthetic rates contribute to hyperinsulinemia in prediabetic patients, we measured ^{2}H-insulin plasma appearance after metabolic incorporation with ^2H_2O in MAO. Insulin beta chain half-lives ranged from 3 to 10 days and had an average half-life of 5.5 days with a fractional replacement rate of 12.5 % / day (**Figures 2A and 2C**). Interestingly, obese prediabetic people had a borderline significantly slower insulin FRR than healthy people, but no differences were observed (**Figures 3 and 4A**).

To determine how the pool size of plasma insulin changes in MNL vs MAO, we compared the average fasting insulin concentrations that were significantly higher in MAO vs MNL subjects (**Figure 4B**). We calculated the newly synthesized insulin beta chain production rates (uU/mL/day) by factoring insulin beta chain FSRs (%/day) * plasma insulin concentrations (uU/mL). We observed a dramatically significant increase in newly synthesized insulin beta chain rates in MAO than MNL subjects. These results are consistent with previously published results [146,158].

To remove the possibility of contamination of our beta chin measurements by proinsulin, which has a faster appearance rate in the beta cell and appearance in the bloodstream[106, 111, 114,117,118], we attempted to isolate and measure intact insulin kinetics from subjects who were labeled with ^2H_2O for 1, 2, and 3 weeks (**Figures 5A and 5B**). As noted above, slow turnover of intact insulin may be a marker of a healthy pancreas with intact secretory granule pool size[77,78,159,160]. As a newly synthesized insulin molecule is created in the pancreas, a normal healthy beta cell has time to complete insulin biosynthesis, processing, trafficking, storage, and secretion. The one MAO subject displayed significantly faster insulin production rates as compared to MNL subjects. In an unhealthy obese prediabetic pancreas suffering from glucotoxicity, inflammation, and insulin resistance, the increased demand to biosynthesize and secrete insulin results in beta-cell stress, exhaustion, apoptosis, and overall decreased beta-cell mass. Increased proinsulin levels represent a marker of susceptibility to T2D given a stressed beta-cell demands to create and secrete insulin, along with concurrent hyperinsulinemia[109,161,162]. Faster insulin turnover may be a marker of predisposition to diabetes and correlates with higher fasting insulin concentrations. Future studies will increase the overall sample size, and differentiate the differences between intact insulin and proinsulin kinetics. These results are of course very preliminary (n = 1-4 per group) and await more analyses.

Finally, we evaluated C-peptide kinetics in both the urine and the plasma in four patients. Over the 5-day labeling period with heavy water, C-peptide fractional synthesis was near plateau enrichments (**Figure S1A**). Patients 02, 04, 06 and 08 displayed C-peptide half-lifes of 1.7, 1.8, 1.2, and 1.8 days in the urine, respectively. Both C-peptide kinetics in the urine and blood displayed a positive and significant correlation, suggesting that these two compartments display similar labeling patterns, indicating origination from the same pool, the pancreatic beta-cell (**Figure S1B**). Therefore, our data support that C-peptide is synthesized in the pancreas and displays the same labeling pattern as the cleared C-peptide from the plasma. C-peptide kinetics from the urine may be an alternative to evaluate insulin secretory dynamics in a non-invasive and accessible fluid.

Others have applied indirect measurements of insulin biosynthesis in vivo with ^{13}C labeling and measuring of C-peptide enrichments in urine[142]. Healthy human volunteers received isotopically labeled ^{13}C-leucine followed by an oral glucose tolerance test. They revealed that ~80% of C-peptide originated from an 'old' or unlabeled pool and ~ 20 % was contributed by newly synthesized insulin. Correlation analysis showed tracer/Tracee ratio (t/T) of C peptide was negatively correlated with early C-peptide release, and high glucose concentrations during the early phase of insulin secretion from 0-60 minutes after glucose ingestion, suggesting the first phase of insulin secretion is accompanied by high dependence of de novo synthesis. Earlier studies with radioactively labeled insulin support this data in which an increase in insulin release occurred after more than 1 hour after glucose load[106]. The issue surrounding this study is that C-peptide measurements in the urine are only a proxy of insulin biogenesis from the pancreas and such a brief labeling protocol cannot reveal the dynamics of insulin that enters storage pools in the pancreas. These observations collectively make this approach an approximation of insulin biogenesis from the pancreas.

In conclusion, in this proof of-concept pilot study, we developed a method to measure the biosynthesis rates of insulin (beta chain insulin and intact insulin) in human beings based upon stable isotopic metabolic labeling with heavy water and mass spectrometry. We report insulin turnover rates in blood during metabolic labeling and observed half-life values in the plasma on the order of days to weeks. These results are very different from insulin clearance kinetics from the plasma which is on the order of minutes. Prediabetic obese individuals may exhibit increased newly synthesized beta chain insulin rates as compared to normal individuals, but further analytic validation is required to confirm this preliminary observation. Rapid appearance kinetics of insulin in the blood could represent a marker of increased beta-cell demand. Finally, we report that C-peptide labeling kinetics correlated in the blood vs the urine. Future studies will evaluate how insulin kinetics are altered in T2D and response to meals in the same subject. We believe that our stable isotope labeling strategy may help to guide the diagnosis, prognosis, and treatment of altered diseases surrounding dysregulated glucose metabolism such as T2D and post-prandial hypoglycemia[163].

Acknowledgments

Mohamad Dandan wrote the manuscript, performed experiments, analyzed, and interpreted the data. Marc Hellerstein conceived the original study idea, revised, and edited the manuscript. Samuel Klein designed and provided the available sample for the analysis of MNL and MAO patients. Hussein Muhammad performed LC/MS experiments and data analysis. Kelvin Li provided technical and conceptual assistance.

4.6. Supplemental Material

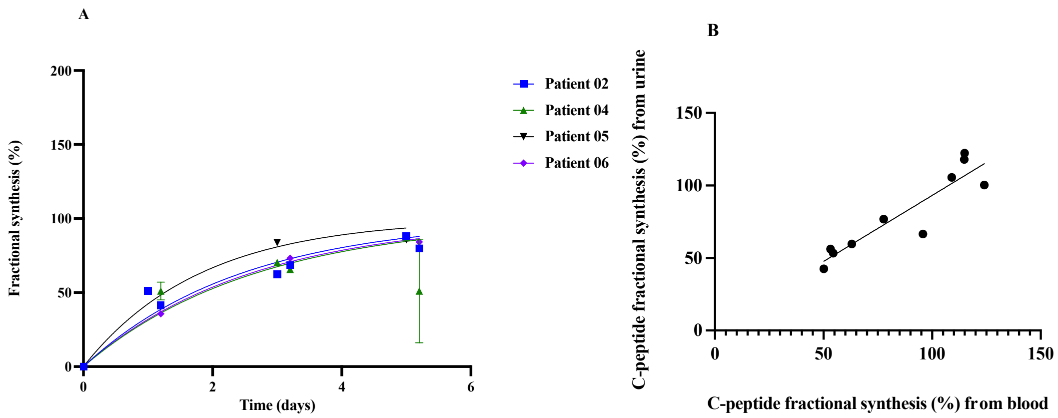

Supplemental Figure 1. Urinary C-peptide fractional synthesis (%) in human subjects (n=4), and correlations between urinary and blood C-peptide kinetics. **A)** Four patients were labeled with heavy water for 5 days and C-peptide fractional synthesis in the urine reached plateau enrichment near 100%. Patients 02, 04, 06 and 08 displayed C-peptide half-lifes of 1.7, 1.8, 1.2, and 1.8 days in the urine, respectively. **B)** C-peptide fractional synthesis (%) was correlated in the blood and urine in the same patients. This correlation was significantly correlated and positively associated (y=0.91x+2.15, R^2=0.84, p=0.0002) between each compartment.

5. Chapter 5

The Kinetics of Patatin-like Phospholipase Domain-containing Protein 3 in Non-Alcoholic Fatty Liver Disease.

5.1. Abstract

Our objective was to determine the kinetics of Patatin-like phospholipase domain-containing protein 3 (PNPLA3). Single nucleotide polymorphisms in PNPLA3 (I148M) are associated with susceptibility to the development of non-alcoholic fatty liver disease (NAFLD). The prevailing hypothesis is that accumulation of mutant PNPLA3 proteins on lipid droplets impairs accessibility by active lipases. To understand the kinetic basis of increased risk of NAFLD associated with this genetic polymorphism (I148M) of PNPLA3, we measured PNPLA3 turnover rates in the liver by heavy water labeling and tandem mass spectrometric analysis. Subjects with NAFLD and different PNPLA3 genetic polymorphisms were studied. PNPLA3 fractional synthesis rates were slower ($t_{1/2}$ of 7-49 days) than predicted from ex-vivo studies in isolated hepatocytes (2-5 hours) and displayed a trend of slower turnover from wildtype to heterozygote to homozygote genotypes, and slower PNPLA3 turnover correlated significantly with intrahepatic triglyceride content (IHTG). Hepatic absolute synthesis rates of palmitate in triglycerides were higher in heterozygotes vs wild-type patients, and faster PNPLA3 turnover correlated with fractional synthesis rates of palmitate in liver triglycerides. These results suggest that impaired PNPLA3 clearance in I148M mutations leads to higher IHTG. This research provides a flux-based approach to measure the synthesis of low abundance intracellular molecules such as PNPLA3 to examine its molecular kinetics in NAFLD, and response to diet and therapies targeted at PNPLA3 kinetics.

5.2. Introduction

Over 25% of the global population suffers from non-alcoholic fatty liver disease that is characterized by the accumulation of hepatic liver fat[164,165]. NAFLD is highly associated with obesity, diabetes, and cardiovascular disease[166,167]. A subset of NAFLD patients progresses into a more severe form accompanied by inflammation, known as non-alcoholic steatohepatitis (NASH) [164,165]. NAFLD is typically associated with a combination of environmental, dietary, and behavioral factors such as excess energy intake and physical inactivity[164,165]. However, genetic studies have revealed a genetic component for increased risk for the development of NAFLD[168,169,170,171,172].

A sequence variant of Patatin-like phospholipase domain-containing protein 3 (PNPLA3, I148M mutation) is a major genetic risk factor for nonalcoholic fatty liver disease[168,173]. This variant is common (17 – 49%) in U.S. populations[168,174]. PNPLA3 (I48M) mutants were strongly associated with increased hepatic liver fat, inflammation, and NAFLD disease severity[168,175]. Human PNPLA3 transgenic or knock-in mice develop NAFLD on chow or high sucrose diet, respectively[176,177,178]. Reports have suggested that PNPLA3 is a triglyceride lipase, or transacetylase, but it does not have high lipolytic activity so that its functions remain unclear[173,179]. PNPLA3 localizes on lipid droplets in the liver and, PNPLA3 I148M mutants may block activation of adipose tissue triglyceride lipase by competing with cofactors for lipolysis (i.e., CGI-58), thus resulting in reduced lipolysis[174,180,181,182].

Accordingly, the I148M mutation is hypothesized to be resistant to degradation by ubiquitination, accumulates on lipid droplets, inhibit the activity of a more active lipase, and thereby result in accumulation of triglycerides[178,179,184]. If PNPLA3 inhibits triglyceride lipase activity and the I148M mutation is hypothesized to have a slower breakdown rate, stimulating the breakdown of PNPLA3 in the human liver may be a therapeutic target in fatty liver disease[174]. The theory that impaired breakdown of PNPLA3 rather than increased synthesis in the liver causes triglyceride accumulation is based on preclinical and indirect studies, however.

Our central objective here was to measure the turnover (breakdown) rate of wild-type and I148M PNPLA3 in the human liver. We were able to isolate PNPLA3 and measure its' in vivo kinetics using tracer techniques (heavy water labeling and tandem mass spectrometric analysis) in NAFLD subjects undergoing bariatric surgery. Previous studies of cultured human-derived HepG2 cells given ^{35}S-methionine pulse-chase reported $t_{1/2}$ to be on the order of hours and to be prolonged by the addition of oleate, suggesting that slower turnover is induced by lipid accumulation[179]. This has yet to be tested in human studies with NAFLD. We sought to determine the differences in PNPLA3 turnover in human NAFLD liver with wild-type, heterozygote, and homozygote genotypes. We also sought to correlate PNPLA3 turnover with intrahepatic triglyceride content and kinetics between each genotype.

5.3. Materials and Methods

Reagents and chemicals

RIPA lysis and extraction buffer, HyClone™ water, Halt™ Protease Inhibitor Cocktail (100X), Phosphate Buffered Saline (PBS, pH=7.4), PNPLA3 antibody (PA5-47709), EZ-Link™ NHS-PEG4-Biotin No-Weigh™ Format, M-280 streptavidin magnetic beads, Tween-20, Formic acid, Proteomics grade trypsin, Trifluoracetic acid, and Acetonitrile were obtained from Thermo Fisher Scientific. Dithiothreitol, Iodoacetamide, Ammonium bicarbonate and Trifluoroethanol were obtained from Sigma Aldrich.

Subject characteristics, clinical measurements, and heavy water labeling protocol

Patients were diagnosed with non-alcoholic fatty liver disease (NAFLD) via established criteria by the Clinical Research Network[166,167]. Each patient was genotyped to determine whether they contain wild type (CC), heterozygote (CG), or homozygote (GG) genotypes of PNPLA3. Patients' body mass index (weight (kg) / height (M^2), NAFLD activity score, liver fibrosis score, whole-body fat mass by dual-energy x-ray absorptiometry (DXA), % body fat by magnetic resonance imaging (MRI), intrahepatic triglyceride content IHTG (%) by MRI, fasting glucose (mg/dl), hepatic de-novo lipogenesis DNL (%) were measured in each group[185]. NAFLD patients were labeled variably with heavy water for 7-43 days followed by bariatric surgery and collection of liver biopsies for PNPLA3 isolation (5-20mg).

Biotinylating PNPLA3 antibodies

PNPLA3 antibodies were biotinylated using the EZ-Link™ NHS-PEG4-Biotin No-Weigh™ Format with slight modifications from the manufacturer. Ensure to warm the 2mg vial to room temperature before use and use immediately. 800uL of water was added to the 2mg biotin vial to make 4.25mM (20x) solution. 7.065uL of biotin reagent was added for every 100ug of antibody for a 50x solution in a 100uL total reaction and incubated for 1 hr. at room temperature in the dark. Excess biotin was removed with a Zeba™ Spin Desalting Columns, 7K MWCO, 0.5 mL. One small 7K Zeba column (0.5mL) was inserted into a 1.5mL collection tube. The tube top was slightly opened while centrifuging for 1,500 x g for 1 min. The bottom filtrate was removed and 300uL of PBS was added followed by 2x more rounds of washing. After the last wash, the column was transferred to a new 1.5mL tube and the biotin antibody was added to the column's resin and spun for 1,500 x g for 2 min. The biotin antibody was stored at 4 °C for up to two weeks.

Isolation of PNPLA3 from human liver biopsies via immunoprecipitation and mass spectrometry preparation

Human liver biopsies were homogenized in RIPA buffer (10:1, volume (uL): weight (mg)) supplemented with 1x halt protease inhibitor cocktail using fast prep 2ml tubes with silica beads in a Qiagen Tissue Lyzer set to 30 HZ for 1min. Samples were prepared on ice with freshly made and ice-cold solutions. After homogenization, samples were spun for 3,500 RPM at 4 °C, and supernatants were transferred to a fresh low bind tube containing 500uL of ice-cold PBST (0.02% Tween-2). 2.5 ug of biotinylated PNPLA3 antibodies were added to each sample for overnight incubation at 4 °C. Samples were allowed to warm up to room temperature by rotating for 15 min on the bench top. 50ul of 10mg/mL streptavidin beads (M-280) was added and allowed to incubate for 1 hr. at room temperature while rotating. Magnetic beads were collected using a magnetic stand and flow-through was pipetted off and stored at -80 °C. Beads were washed 3x with 300ul of PBST and 3X with H_2O. Antibody antigen interactions were disrupted with 100uL of 33.0% acetonitrile and 0.4% trifluoroacetic acid elution buffer 2x for 200uL total reaction. Elution occurred by mixing and incubating the samples for 3min followed by the collection of beads with the magnetic stand. The elution was transferred to a new low bind tube with 15.0uL of 1M tris-base and speed vacuumed dry. Samples were resuspended in 10.0uL of trifluoroethanol, 10uL of 100mM ammonium bicarbonate (AB), and reduced with 2.8uL of 50mM dithiothreitol for 1 hr. at 60 °C. Samples were alkylated with 8uL of 50mM iodoacetamide and incubated for 30 min at room temperature in the dark. 150uL of H_2O, 50uL of 100mM ammonium bicarbonate, and 250ng of pierce proteomics grade trypsin were added and allowed to incubate overnight at 37 °C. 1.7uL of 20% trifluoracetic acid was added and samples were centrifuged for 14,000 x g for 10min. The supernatants were transferred to LC/MS vials, and speed vacuumed dry. Finally, peptides were resuspended in 25ul of LC/MS submission buffer (0.1 % formic acid, and 3% acetonitrile).

Measurement of PNPLA3 fractional synthesis rates using heavy water labeling and tandem mass spectrometry

Metabolic labeling for the measurement of protein kinetics using mass isotopomer distribution analysis has been well established and thoroughly reviewed[41,43,44,45]. Briefly, high-performance liquid chromatography (HPLC) separated the complex mixture of ^{2}H-labeled peptides that was equipped with a Chip cube interface (Agilent, Santa Clara, CA). Electrospray ionization charged the PNPLA3 peptides that were subsequently injected into the mass spectrometer. The isotopomer distributions were resolved with a quadrupole time of flight mass analyzer (Q-TOF) on the first mass spectrometry detection level. Tandem mass spectrometry (MS/MS) fragmented the PNPLA3 peptides for identification using the human proteome database from uniprot[186] via Spectrum Mill software from Agilent. MassHunter software was used for data acquisition and quantitative analysis. Algorithms developed by Price et al were able to incorporate the molecular formula, mass, mass isotopomers, and label type to determine the fractional synthesis (EM0/EM*), or percentage of molecules that were newly synthesized over some time (t), or the measured enrichment divided by the asymptote enrichment predicted by MIDA[41,43,44,45]. Precursor body water values were obtained from heavy body water enrichments[58,153]. This was used as a surrogate value of labeled precursor amino acids to determine the theoretical asymptotic product enrichment. Fractional synthesis values can be converted to fractional synthesis rates by the following equation, f =1-e^-kt, where k = fractional synthesis rate (%/time), t = time, f=fractional synthesis. Half-lives were determined by T1/2= ln2/k. All equations follow first-order protein kinetic principles [41,43,44,45].

Statistics

When comparing three or more group average measurements, statistical significance was evaluated by an ANOVA. For the correlation analysis, statistical significance was evaluated by a non-parametric Spearman or Pearson correlation, $*p \leq 0.05$.

5.4. Results

Characteristics of the patient population.

Table 1 displays the typical clinical characteristics of NAFLD patients enrolled in this study. All subjects were obese or morbidly obese (BMI ≥ 40). No significant differences in BMI, liver fibrosis score, body mass, whole-body fat mass, and % body fat observed in the plasma or liver, and fasting blood glucose measurements were observed between each group. These results resemble clinical characteristics of morbidly obese individuals with different PNPLA3 genotypes in which only markers of liver damage (i.e., AST, and ALT) were elevated in I148M mutant subjects[187]. NAFLD activity score was higher in heterozygote individuals as compared to wild type (4 vs 1.3, p=0.02). IHTG content (%) were also elevated in homozygote (22.25%, p=0.02) and heterozygote (17.6%, p=0.01) individuals as compared to wild types (5.95%). Lastly, hepatic triglyceride de-novo lipogenesis absolute synthesis rates were significantly elevated in heterozygotes (7.4 vs 19.2 %TG content/ day, p=0.01) vs wild-type subjects.

Human liver PNPLA3 half-life range on the order of days or weeks, and not hours.

Initial investigations of PNPLA3 kinetics in HepG2 cells revealed t½ values on the order of hours, based on ^{35}S-Methionine pulse-chase studies[179]. We sought to determine the kinetics of PNPLA3 in human liver biopsies of NAFLD patients labeled with ^2H_2O for 1 to 7 weeks. Surprisingly, PNPLA3 fractional synthesis rates (%/day) ranged from 1.4% to 9.5% (**Figure 1A**), representing PNPLA3 half-lives ranging from 7 to 49 days (**Table 2, Figure 1B**).

Human liver PNPLA3 FSR trend slower from wild type to heterozygote to homozygote genotypes.

To evaluate whether the I148M mutation may lead to increased PNPLA3 levels on lipid droplets by higher synthesis or lower degradation rates, we examined PNPLA3 FSR (%/day) among genotypes (**Figure 1A**). As a function of genotype, PNPLA3 FSR trended towards slower synthesis from wild type to heterozygote to homozygote genotypes (5.4 ± 1 to 3.9 ± 0.9 to 2.5 ± 1 %/day), although no statistically significant differences were observed ($p > 0.05$ all).

PNPLA3 fractional synthesis rates and half-lives correlated to IHTG and hepatic DNL FSR.

We compared intrahepatic triglyceride content (IHTG) and PNPLA3 kinetics. A striking statistically significant inverse correlation was observable between PNPLA3 FSR and IHTG (r= -0.63, *p=0.011, **Table 3**). Slower PNPLA3 fractional synthesis rates correlated with higher IHTG content. PNPLA3 half-life correlated with IHTG content (r= 0.65, *p=0.008, **Table 3**). PNPLA3 FSR's (p= *0.014, r= 0.61), and half-lives (p=*0.014, r=-0.61) were significantly correlated to hepatic palmitate triglyceride FSR (**Table 3**). Hepatic and plasma DNL were measured in each subject and correlated to each other. A significant ($p<0.005$) and positive association (r=0.6073) was observed between plasma DNL and hepatic DNL (**Figure 2A**). Moreover, both hepatic DNL and liver PNPLA3 fractional synthesis were significantly ($p<0.05$) and positively (r=0.5875) associated (**Figure 2B**).

Table 1: NAFLD patient subject characteristics undergoing bariatric surgery (n=16, with at least 3 peptides per measurement for PNPLA3).

				P-value		
Genotype	**Wild type (n=6)**	**Heterozygous (n=8)**	**Homozygous (n=2)**	**WT vs HT**	**WT vs HM**	**HT vs HM**
Age	49.1	42.3	43.1	0.33	0.63	0.99
Sex (Male or Female)	2 or 2	1 or 7	0 or 2	N/A	N/A	N/A
Baseline BMI (kg/m2)	52.0	50.2	39.36	0.87	0.08	0.10
NAFLD activity Score	1.3	4	2.50	*0.02	0.48	0.45
Liver Fibrosis Score	1.3	2	2.00	0.85	0.63	0.83
Body mass (kg)	158.4	134.8	118.60	0.52	0.24	0.58
Whole-body fat mass (g)	81.7	69.5	57.04	0.91	0.29	0.36
% Body Fat	0.5	0.53	0.50	0.81	0.92	0.65
IHTG (%)	5.95	17.6	22.28	*0.01	*0.02	0.63

Fasting glucose (mg/dL)	107	118	112.50	0.55	0.93	0.90
Hepatic palmitate TG DNL FSR (%/day)	1.3	1.4	1.08	0.99	0.99	0.33
Hepatic TG DNL ASR (% TG content/day)	7.4	19.2	19.6	*0.01	0.07	0.99

All values are shown as group averages. BMI, body mass index, NAFLD, non-alcoholic fatty liver disease, IHTG, intrahepatic triglyceride content, DNL, de-novo lipogenesis, WT, wild-type, HT, heterozygote, HM, homozygote. Statistical significance was evaluated by ANOVA, *p≤0.05.

Table 2: Human liver PNPLA3 kinetics in bariatric surgery subjects (n=16, with at least 3 peptides per measurement for PNPLA3).

Subject	**Fractional synthesis (%)**	**Peptide count**	**SEM**	**FSR (%/day)**	**Half-life (days)**	**Genotype**	**Tissue amount (mg)**	**Day of sample**	**SD**
LF9	53.40%	6	20.6%	2.73%	25	WT	11	28	50.50%
LF13	48.30%	8	10.0%	2.87%	24	WT	8	23	28.40%
PF143	38.60%	3	8.2%	6.97%	10	WT	20	7	14.20%
LF-135	72.50%	6.0	12.7%	5.61%	12	WT	20	23	31.10%
LF-032	70.00%	6.0	11.8%	4.63%	15	WT	20	26	29.00%
PF148	48.50%	3	4.1%	9.48%	7	WT	20	7	7.10%
LF-028	68.70%	6.0	11.3%	5.28%	13	HT	20	22	27.60%
LF-129	58.30%	7.0	11.7%	2.03%	34	HT	20	43	31.00%
LF-026	84.20%	5.0	11.2%	8.39%	8	HT	20	22	25.10%
LF-147	72.10%	3.0	16.2%	5.80%	12	HT	20	22	28.10%
LF-154	50.30%	4.0	18.1%	2.80%	25	HT	20	25	36.10%
LF17	43.20%	10	16.1%	2.02%	34	HT	15	28	51.00%
LF20	48.60%	4	24.7%	3.17%	22	HT	5	21	49.40%
LF10	29.00%	5	13.4%	1.43%	49	HT	6	24	29.90%
LF4	31.40%	4	18.8%	1.51%	46	HM	8	25	37.60%
LF8	48.90%	3	21.9%	3.53%	20	HM	5	19	37.90%

FSR, fractional synthesis rate, WT, wild-type, HT, heterozygote, HM, homozygote, SD, Standard deviation, SEM, standard error mean, IHTG, intrahepatic triglyceride content.

Table 3: Spearman correlations between PNPLA3 kinetics, IHTG (%), hepatic, and plasma triglyceride kinetics.

Correlation	**P-value and Spearman r values**

PNPLA3 FSR (%/day) vs IHTG (%)	*0.011, -0.63
PNPLA3 FSR (%/day) vs hepatic DNL FSR (%/day)	*0.014, 0.61
PNPLA3 FSR (%/day) vs hepatic TG ASR (% TG content/day)	0.72, -0.09
PNPLA3 half-life (days) vs IHTG (%)	*0.008, 0.65
PNPLA3 half-life (days) vs hepatic DNL FSR (%/day)	*0.014, -0.61
PNPLA3 half-life (days) vs hepatic TG ASR (% TG content/day)	0.62, 0.13
IHTG (%) vs hepatic DNL FSR (%/day)	0.27, -0.29

FSR, fractional synthesis rate, ASR, absolute synthesis rate, DNL, de-novo lipogenesis, and IHTG, intrahepatic triglyceride content. Statistical significance for each correlation was evaluated by a non-parametric spearman analysis, *, p≤0.05.

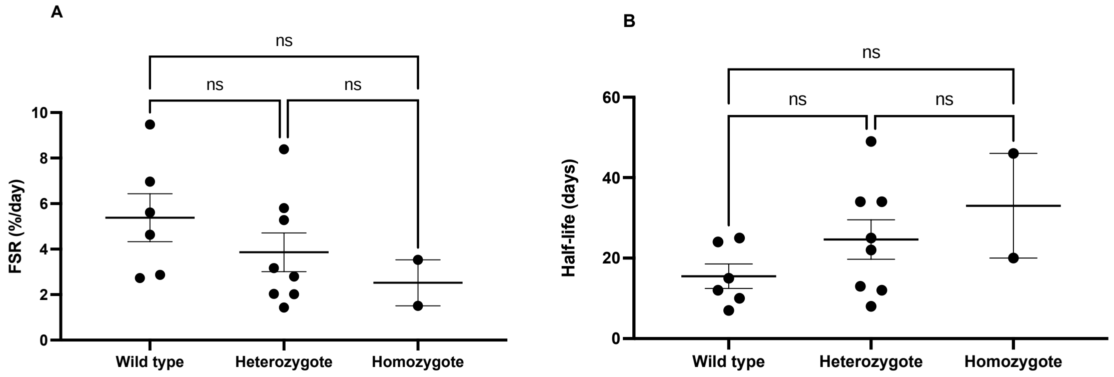

Figure 1: PNPLA3 fractional synthesis rates (%/day), half-life's (days), and intrahepatic triglyceride content (IHTG) in subjects with different NAFLD genotypes. A) A trend of slower PNPLA3 FSR (%/day) ± SEM was observed from wild type (5.4 ± 1 %/day, n=6), heterozygote (3.9 ± 0.9 %/day, n=8), and homozygote genotypes (2.5 ± 1 %/day, n=2), but no statistically significant differences were observable (p > 0.05 for all). **B)** PNPLA3 half-life (days) ± SEM trended longer from wildtype (16 ± 3 days, n=6) to heterozygote (25 ± 5 days, n=8) to homozygote groups (33 ±13 days, n=2), but no differences were observed (p > 0.05 for all). Data are presented as mean values ± SEM. Statistical significance was evaluated via an ANOVA, $^*p \leq 0.05$.

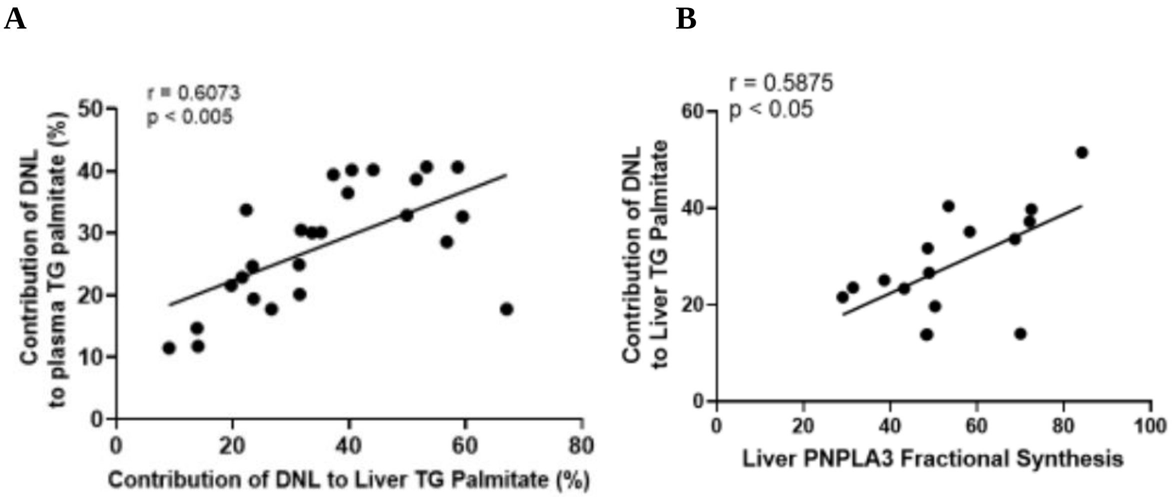

Figure 2: Correlations between de-novo lipogenesis (DNL, %) observed in the plasma vs liver DNL (%), and liver DNL (%) correlations to PNPLA3 fractional synthesis (%). A) Hepatic and plasma DNL was measured in each subject and correlated to each other. A significant ($p<0.005$) and positive association ($r=0.6073$) was observed between plasma DNL and hepatic DNL. **B)** Both hepatic DNL and liver PNPLA3 fractional synthesis were significantly ($p<0.05$) and positively ($r=0.5875$) associated.

5.5. Discussion

Polymorphisms in PNPLA3 are a common genetic risk factors for the development of NAFLD. The current hypothesis is that PNPLA3 impairs triglyceride hydrolysis[164,165,168,180,188], and its accumulation on lipid droplets therefore predisposes to higher hepatic fat stores. PNPLA3 was found to be a lipid droplet-associated protein, putatively with lipase and transacylase activity[173,179]. The PNPLA3 variant associated with fatty liver disease (I148M) has since been reported to accumulate on lipid droplets by evading ubiquitylation[178,184].

Our central question here was, how are PNPLA3 turnover kinetics in human liver in vivo different between different genotypes. Our central objective was to measure the turnover (breakdown) rate of wild type and I148M mutants in NAFLD human liver biopsies after bariatric surgery[178,184]. Accordingly, we asked whether PNPLA3 in subjects with I148M mutations exhibited higher synthesis or reduced degradation rates.

We were able to immunoprecipitate PNPLA3 from human liver, and measure newly synthesized PNPLA3 peptides after heavy water administration for 1 to 6 weeks (**Table 2**). Our in-solution digest method using an indirect immunoprecipitation provided the best recovery (5-14 peptides, depending on tissue amount). The average fractional synthesis rate values in morbidly obese human subjects (n = 16) with wildtype, I148M heterozygous and I148M homozygous genotypes were 5.4, 3.9, and 2.5 %/day, respectively (**Figure 1A**). PNPLA3 kinetics trended towards slower turnover with increasing homozygosity, but no significant differences were observed between each group. This preliminary study may be underpowered, particularly with the low sample size of homozygote individuals (n=2).

Our data show for the first time the in-vivo turnover of human PNPLA3, in this case in subjects with fatty liver disease. PNPLA3 turnover rates in living humans with NAFLD are very different from kinetics in HepG2 cells[189]. In principle, HepG2 and Huh7 cells are not ideal models for assessing PNPLA3 as both cells express the mutant allele[190,191]. Clearly, PNPLA3 turnover kinetics are different in human livers than in this immortalized cell line.

Additionally, intrahepatic triglyceride content was significantly higher in homozygotes and heterozygotes vs wildtype subjects (**Table 1 and Figure 1C**). Possible explanations can be attributed to defects in VLDL secretion. For example, Pirazzi et al showed that carries of PNPLA3 I148M displayed lower secretion of TG-rich very-low-density lipoproteins in humans and lower ApoB secretion in cell lines overexpressing the mutant protein[192]. It seems mutant PNPLA3 promotes lipid accumulation in the liver by reduced VLDL lipidation. Interestingly, we observed a significant correlation between PNPLA3 kinetics and intrahepatic triglyceride content (**Table 3**). Slower PNPLA3 turnover was significantly inversely associated with higher IHTG. This relationship is consistent with the observation of increased hepatic triglyceride content with increasing homozygosity[180,188]. In support of our observation in preclinical models, Li et al overexpressed I148M PNPLA3 mutant protein in mice that caused steatosis, and PNPLA3 knock-in mice resulted in PNPLA3 accumulation on lipid droplets and NAFLD as well[176,180]. The biochemical model proposed is that mutant PNPLA3 evades ubiquitinoylation resulting in the accumulation on lipid droplets that impairs access to lipases, thus reducing lipolysis and resulting in the accumulation of lipid droplet[184].

PNPLA3 is mostly a lipid droplet-associated protein, but its functions remain unclear[174]. PNPLA3 turnover is regulated in response to feeding and fasting[189], but the mutant I148M PNPLA3 is resistant to degradation by ubiquitination or autophagy[178,184]. PNPLA3 may compete for ATGL activators such as comparative gene identification-58 (CGI-58) and abhydrolase domain containing 5 (ABHD5)[181,182,183]. Our data suggest that slower PNPLA3 clearance from the lipid droplet may explain why PNPLA3 accumulates on lipid droplets and be a risk factor for steatosis. These results have pathophysiological implications for the regulation of PNPLA3, and therapeutic implications for the development of drugs that can enhance PNPLA3 clearance from lipid droplets.

Our next objective was to measure hepatic triglyceride turnover to determine the intrahepatic triglyceride absolute synthesis rates and correlate these metrics with PNPLA3 kinetics. PNPLA3 FSRs were significantly and positively correlated to hepatic palmitate triglyceride FSR (**Table 3**), suggesting an interplay of newly synthesized palmitate in TG on PNPLA3 synthesis and lifespan. A significant and positive association was observed between plasma DNL and hepatic DNL (**Figure 2A**). Moreover, both hepatic DNL and liver PNPLA3 fractional synthesis were significantly and positively associated (**Figure 2B**). Therefore, faster PNPLA3 fractional synthesis may drive higher hepatic DNL, or vice versa. Given how insulin resistance drives hepatic DNL, this relationship warrants further investigation to determine the metabolic drivers (i.e., insulin sensitivity, HOMA-IR) of PNPLA3 fractional synthesis and its association with hepatic DNL[185].

Indeed, overexpression of I148M PNPLA3 results in increased TG synthesis based on ^{14}C-oleic acid tracers' studies in cell culture[192,193]. However, this has not been tested in humans diagnosed with NAFLD and that contain different PNPLA3 genotypes. Fractional synthesis rates of palmitic acid in liver TG were not different between each group (**Table 1**), but measurements were consistent with DNL values obtained in NAFLD patients[185,194]. We calculated the absolute synthesis rates of hepatic TG by factoring in both the FSR of palmitate in liver TG and hepatic triglyceride content. Hepatic TG ASRs were significantly higher in heterozygotes as compared to wild-type, and no differences were observed between the wild type and homozygote genotypes that were borderline significant. Our small sample size in homozygote individuals (n=2) underpowered our calculations, but the increase was still borderline significant (p=0.07). Intrahepatic triglyceride content was not associated with the FSR of hepatic palmitate in TG. Possible explanations include different sources of triglycerides from the diet, uptake, recycling, and synthesis[194]. These correlations suggest PNPLA3 kinetic interactions with hepatic TG content and fractional turnover rate.

In conclusion, we measured the turnover of hepatic PNPLA3 in-vivo in human subjects with NAFLD. Slower PNPLA3 turnover (longer half-life) correlated significantly with higher intrahepatic triglyceride content, suggesting that impaired clearance of PNPLA3 promotes accumulated levels, and increases triglyceride content in the NAFLD liver. PNPLA3 fractional synthesis rates correlated with hepatic palmitate TG FSR, and hepatic absolute synthesis rates of palmitate TG were evaluated in mutant individuals. Alternatively, there could be a gene-environment interaction whereby IHTG accumulation may prolong mutant PNPLA3 half-life, which then initiates a positive feedback loop that further increases hepatic triglyceride levels. Our technology of stable isotopic metabolic labeling with heavy water to measure low abundant protein turnover rates can be applied to other systems as well[69,70,71,154]. We believe this research will provide a molecular kinetic understanding of both the static and kinetic dynamics of signaling pathways. Either way, these findings provide potential insights into the dynamics of PNPLA3 in NAFLD that are relevant for the design of therapeutics targeted at PNPLA3 kinetics[195].

6. Chapter 6

LDL-ApoB Production Rate Increases in NASH Patients with Cirrhosis Treated with the Acetyl-CoA Carboxylase Inhibitor Firsocostat But is Prevented by Fenofibrate Therapy.

6.1. Abstract

Increased plasma triglycerides (TG) may occur in nonalcoholic steatohepatitis (NASH) patients treated with acetyl-CoA carboxylase inhibitors (ACCi), while variable changes in apolipoprotein B (ApoB) have been reported. Our objectives were to determine the effects of treatment with the ACCi, firsocostat, on production and clearance rates of plasma low-density lipoprotein (LDL) ApoB-containing particles, and to evaluate the effects of combination therapy with fenofibrate in patients with NASH. Metabolic labeling with heavy water and tandem mass spectrometric analysis of LDL-ApoB was carried out in 16 NASH patients treated with firsocostat for 12 weeks; in 29 NASH subjects treated with firsocostat and fenofibrate combination therapy for 12 weeks; and in 9 normolipidemic healthy volunteers treated with firsocostat for 4 weeks. In NASH patients on firsocostat, plasma TG increased 17% from baseline to week 12 (p=0.0056). Significant increases were also observed in LDL-ApoB fractional synthesis rate (FSR) (baseline to week 12: 31 ± 5 to 46 ± 6 %/day, p=0.03) and absolute synthesis rate (ASR) (30.4 to 45.2 mg/dl/day, p=0.016), but not plasma ApoB concentration. The effect of firsocostat on LDL-ApoB ASR was restricted to patients with cirrhosis (21.0 ± 9.6 at baseline and 44.2 ± 17 mg/dL/day at week 12, p=0.002, n=8); ASR in non-cirrhotic patients did not change (39.8 ± 20.8 at baseline and 46.3 ± 14.8 mg/dL/day at week 12, p=0.51, n=8). No effects of ACCi treatment on FSR, ASR, or concentrations of ApoB or TG were observed in healthy controls. Combination treatment with fenofibrate and firsocostat prevented the increases in plasma TG and LDL-ApoB FSR and ASR in NASH patients. In summary, in NASH patients with cirrhosis, ACCi treatment increases LDL-ApoB100 production rate, but this effect can be prevented by concurrent fenofibrate therapy.

6.2. Introduction

Over 90 million Americans have nonalcoholic fatty liver disease (NAFLD), a condition characterized by excessive liver fat and chronic inflammation[196,197]. The cause is unclear, but it is associated with obesity, diabetes, and metabolic syndrome[198]. In a subset of individuals with NAFLD, progression to nonalcoholic steatohepatitis (NASH), cirrhosis, and hepatocellular carcinoma may occur[198,199]. Dyslipidemias are common in NAFLD patients and are associated with an increased risk of cardiovascular disease (CVD) and progression to NASH[200,201,202,203]. Hypertriglyceridemia is particularly common in NAFLD and can be influenced by pharmacological treatment[200,204].

An attractive therapeutic target for NAFLD is the inhibition of acetyl-CoA carboxylase (ACC), which catalyzes the rate-limiting step of hepatic de novo lipogenesis (DNL) and regulates fatty acid oxidation[204,205]. Interestingly, observations in NASH patients in phase 2 clinical trials, ACC knockout mouse models, and preclinical models exhibited not only reductions in liver fat content but also hypertriglyceridemia[204,206,207,208,209,210,211,212]. The latter was unexpected, as reduced hepatic malonyl-CoA production by ACC inhibition (ACCi) was anticipated both to reduce the synthesis and increase oxidation of fatty acids in the liver[213]. In addition, ACCi in NASH patients has been reported to increase apolipoprotein B (ApoB)-containing lipoproteins as well as very-low-density lipoprotein (VLDL) particle number, TG content, and secretion[204,206,207,208,209,210,211,212].

A key question is whether this effect of ACCi acts on the liver through increased production of ApoB-100 containing particles or on tissue clearance of plasma lipids or ApoB-containing lipoproteins, as these may confer differences in atherogenicity. Data from animal models have suggested that ACCi can cause both changes in hepatic lipid metabolism[204] and peripheral lipoprotein lipase activity[207] but definitive data in humans are not available. During the process of metabolic conversion of VLDL to LDL, the main structural protein of VLDL and LDL particles, apolipoprotein B100 (ApoB100) remains intact, whereas receptor-mediated uptake removes the intact particle including ApoB[17,214]. Accordingly, LDL-ApoB production and clearance kinetics may be useful as a window into the behavior and dynamics of ApoB-containing particles and may indicate the tissue site of action of ACCi that alters plasma TG levels.

The half-life of VLDL-ApoB is rapid (hours) while LDL ApoB exhibits a half-life of 2-5 days[42,43,215,216,217,218]. Stable isotopic metabolic tracers such as heavy water (^2H_2O) can be used to measure synthesis and removal rates of blood proteins, including apolipoproteins, such as ApoB100 in VLDL and LDL[41,42,43]. In humans, ^{2}H-label in body water equilibrates rapidly throughout all tissues and ^{2}H-label rapidly enters free nonessential amino acids during intermediary metabolic processes, but not into peptide-bound amino acids, thereby allowing newly synthesized proteins to be labeled[41].

Here, as part of studies to measure the effects of ACCi treatment on hepatic DNL, NASH patients were given heavy water before and after experimental treatment with the ACCi, firsocostat[210]. We measured the kinetics of LDL-ApoB to explore the underlying metabolic mechanisms associated with reported hypertriglyceridemia and changes in ApoB particle number in ACCi-treated patients[204,206,207,208,209,210,211,212]. The primary question was whether ACCi treatment alters synthesis rates or clearance rates of ApoB-containing particles and whether the stage of liver disease influences ApoB kinetic response to ACCi treatment. In addition, we evaluated the preventive effects of concurrent therapy with fenofibrate and firsocostat on plasma ApoB kinetics.

6.3. Materials and Methods

Reagents

All reagents were acquired and prepared of the highest quality. Hyclone molecular grade water was obtained from GE health care. Sodium chloride, formic acid, acetonitrile, and methanol were obtained from Thermo Fisher Scientific. Tris base buffer, Ethylenediaminetetraacetic acid, acetic acid, ammonium bicarbonate, tris(2-carboxyethyl) phosphine, iodoacetamide, and proteomics grade trypsin were obtained from Sigma-Aldrich.

Patient treatment, characteristics, and clinical measurements

Adults 18 to 75 years of age with suspected NASH were studied in a phase 2a clinical trial of the ACCi, firsocostat, and fenofibrate (ClinicalTrials.gov Identifier: NCT02781584). All NASH subjects (n=20) were administered firsocostat 20 mg orally once daily for 12 weeks[208,210]. Of the 20 NASH subjects, 10 had F2-F3 fibrosis and 10 had cirrhosis (F4). The non-cirrhotic NASH subjects treated with firsocostat subjects were enrolled with non-invasive tests using the following parameters. Screening FibroTest® < 0.75, unless a historical liver biopsy within 12 months of screening does not reveal cirrhosis, magnetic resonance imaging-estimated proton density fat fraction (MRI-PDFF) with ≥ 10% steatosis, magnetic resonance elastography (MRE) with liver stiffness ≥ 2.88 kPa, or historical liver biopsy within 12 months of screening consistent with NASH (defined as the presence of steatosis, inflammation, and ballooning) with stage 2-3 fibrosis according to the NASH Clinical Research Network (CRN) classification (or equivalent). For cirrhotic NASH subjects treated with firsocostat, patients must have a clinical diagnosis of NAFLD and have at least one of the following criteria (a-d): a) Screening MRE with liver stiffness ≥ 4.67 kPa, b) A historical FibroScan® ≥ 14 kPa within 6 months of Screening, c) Screening FibroTest® ≥ 0.75, d) A historical liver biopsy consistent with stage 4 fibrosis according to the NASH CRN classification (or equivalent). Additional details of patient clinical characteristics have been described elsewhere[208,210].

For the cohort of NASH subjects treated with fenofibrate and firsocostat combination therapy, all subjects had hypertriglyceridemia (TG >150 and <500 mg/dL) and advanced fibrosis (F3-F4) due to NASH, as determined by historic liver biopsy or liver stiffness by MRE ≥ 3.64 kPa or transient elastography (FibroScan; Echosens, Paris, France) ≥ 9.9 kPa[210]. A historical liver biopsy was conducted within 6 months of screening consistent with NASH and bridging fibrosis (F3) or within 12 months of screening consistent with NASH and compensated cirrhosis (F4) in the opinion of the investigator. All patients were either pretreated with a low (48 mg) or high dose (145 mg) of fenofibrate once daily for two weeks, then a combination of firsocostat 20 mg daily plus fenofibrate at 48 mg/day (n=14) or 145 mg/day (n=15) for 24 weeks (**Figure S4A**). Healthy controls (n=10) included males and non-pregnant, non-lactating females aged 18 to 45 years with a body mass index (BMI) > 19 and <28 kg/m^2, normal serum alanine aminotransferase (ALT), and no significant medical conditions (Study GS-US-426-3987)[210].

Heavy water labeling protocol and measurements

Heavy water labeling was performed as part of labeling studies to investigate hepatic DNL and fibrogenesis[210]. Plasma samples were taken on day 3 (baseline) and again during week 11 of treatment for LDL-ApoB kinetics. ^2H_2O was administered for seven days in each of the labeling periods, with subjects drinking 50 mL of 70% ^2H_2O three times daily. During each labeling period, average body ^2H_2O enrichments rose to ~0.01 fractional enrichment (1%) (see **Figure S1**), as previously described[210]. Blood samples were drawn after 12 hours of overnight fasting. Heavy water enrichments in each subject were analyzed by distillation followed by acetone exchange and measured via gas-chromatography mass-spectrometry[41].

Sample preparation

Lipoproteins were isolated via preparative ultracentrifugation[219]. NativePAGE™ Novex® Bis-Tris Gels using XCell™ SureLock™ Mini-Cell from Life Technologies were employed to further purify LDL-ApoB100 from other ApoB100-containing lipoproteins. The LDL-ApoB100 band was excised, subjected to an in-gel tryptic digest, and desalted using a C-18 SPEC tip before submission for mass spectrometry kinetic analysis (Thermo Scientific, In-gel Tryptic Digestion Kit).

Serum TG and ApoB measurements

Serum metabolic markers including triglycerides, total cholesterol, low-density lipoprotein cholesterol (LDL-C), high-density lipoprotein cholesterol (HDL-C), and total ApoB were measured through a central laboratory (Covance, Indianapolis, IN). Plasma TG and total ApoB levels for healthy volunteers before and after ACCi treatment were measured using a kit from WAKO (Fujifilm Healthcare), and an ELISA kit from Assaypro.

Mass spectrometry and mass isotopomer distribution analysis

^{2}H-labeled LDL-ApoB100 tryptic peptides were analyzed after 3 days of ^2H_2O labeling at baseline and week 12 of ACCi treatment, or fenofibrate + ACCi. Liquid chromatography tandem mass spectrometry (LC-MS/MS) was used to obtain fractional synthesis rates of ApoB100[41,43,44,45]. Agilent 6550 ion funnel Q-TOF mass analyzer coupled with HPLC-Chip/MS interface was used to separate, analyze, and quantify the distribution of ApoB100 labeled tryptic peptides. Mass Isotopomer Distribution Analysis (MIDA) was employed to determine the predicted isotopomer distribution pattern of the ApoB100 tryptic peptides to reveal the fractional synthesis of LDL-ApoB100[41,43,44,45]. Fractional synthesis rates (FSR, %/day) were calculated as f=1-e^-kt and k=-ln(1-f)/t where f=fractional synthesis (%) and k=fractional synthesis rate. Half-lives (days) were calculated by $T_{1/2}$ = ln (2)/k. Kinetic equations have been described previously[41,43,44,45]. Absolute synthesis rates (ASR, mg/dL/day) were calculated by multiplying the FSR by plasma ApoB100 concentration (mg/dL). We used the measured total plasma-ApoB100 concentrations in this calculation because it is a more reliable metric of ApoB100 pool size than LDL-ApoB content by avoiding potential variability of recovery through LDL isolation, and because over 90% of plasma ApoB is in LDL[17,214,215,216,218,220]. The data analysis was handled with Microsoft excel version 16.28 and Graphpad Prism version 9.2.0.

Search parameters and acceptance criteria (MS/MS and/or peptide fingerprint data)

The software used for peak list generation was Agilent MassHunter Qualitative Analysis release version B.07.00. Spectrum Mill released version B.04.01 as the search engine for proteomic analysis based on MS/MS identifications. The sequence database searched for human protein identifications was Uniprot Release 2019_04[16]. 20,421 was the number of entries searched in the database. Trypsin proteolysis was used. Two missed cleavages were permitted. Carbamidomethylation © was for fixed modifications. Acetylated lysine (K), oxidized methionine (M), N-terminal pyroglutamic acid (N-termQ), deamidated asparagine (N), and hydroxylated prolines (P) were for variable modifications. 20 ppm and 30 ppm were the mass tolerance for precursor ions and fragment ions, respectively. The threshold score was 30% based on the minimum match peak intensity for accepting individual spectra. 1.0% global false discovery rate was determined by algorithms of the Spectrum Mill software and validated at the peptide and protein levels.

Experimental design and statistical rationale

Data are presented as means ± SEM or SD as indicated in each figure. Statistical significance was calculated by a mixed model analysis of variance (ANOVA) with Tukey's multiple comparisons test. To establish differences in clinical measurements between healthy, non-cirrhotic, and cirrhotic NASH patients in table 1, statistical significance was evaluated by the Kruskal-Wallis rank sum test or Fisher’s exact test. To address differences between non-cirrhotic and cirrhotic NASH patients, statistical significance was computed by the Wilcoxon rank-sum test, Pearson’s Chi-squared test, or Wilcoxon rank-sum exact test. Changes in synthesis rates (FSR or ASR) between groups were compared using a paired T-test in the same subjects. Unpaired student T-test with or without a Welch’s correction was used for specific comparisons as explicitly stated in the Figures. Linear regression and Spearman non-parametric correlation analyses were implemented using GraphPad Prism version 9.2.0 for Mac (GraphPad Software, La Jolla, CA).

Study oversight

This study was approved by the institutional review board or independent ethics committees at all participating sites and was conducted in compliance with the Declaration of Helsinki, Good Clinical Practice guidelines, and local regulatory requirements.

6.4. Results

Clinical and biochemical characteristics of healthy, non-cirrhotic, and cirrhotic NASH patients

To establish patient population demographics of defined NASH subjects with clinical correlates of fibrosis and cirrhosis, common clinical and metabolic characteristics were evaluated between healthy, non-cirrhotic, or cirrhotic NASH patients (**Table 1**). NASH patients displayed common hallmarks of metabolic syndrome such as elevated plasma triglycerides, free fatty acids, ketone bodies, hyperglycemia, hyperinsulinemia, insulin resistance, and diabetes as compared to healthy controls ($p<0.001$). Markers of liver damage such as alanine aminotransferase, aspartate amino transferase, gamma-glutamyl transpeptidase, ($p<0.001$), and alkaline phosphatase (0.027) were all elevated in NASH as compared to healthy controls. MRE-PDFF showed that hepatic liver fat was lower in NASH cirrhotic subjects as compared to non-cirrhotic NASH subjects ($p<0.001$). However, non-invasive markers of liver cirrhosis such as MRE ($p<0.001$), Fib-4 ($p=0.17$), Fibrosure ($p=0.003$), ELF ($p<0.001$), hyaluronic acid ($p=0.001$), PIII-NP ($p=0.17$), and TIMP-1 ($p=0.031$) were all elevated in NASH patients with cirrhosis vs non-cirrhotic NASH subjects.

ACCi treatment increases fasting plasma triglycerides in patients with NASH

At baseline, plasma TG concentrations were significantly higher in non-cirrhotic and cirrhotic NASH patients as compared to healthy subjects ($p<0.001$), whereas ApoB content did not differ ($p=0.5$) between each group (**Table 1**). Among 20 patients with NASH, mean (± SD) plasma TG increased 17%, from 180 ± 79 mg/dL at baseline to 211 ± 83 mg/dL at week 12 of firsocostat treatment ($p=0.0056$, **Figure 1C**). While changes in TG were not statistically significant among 10 non-cirrhotic NASH patients (197.4 ± 84.4 at baseline vs 229.4 ± 78.9 mg/dL at week 12, $p=0.1276$; **Figure 1A**), significant increases were observed among the 10 cirrhotic patients (163.3

± 73.3 at baseline vs 192.5 ± 86.1 mg/dL at week 12, p=0.0014; **Figure 1B**). Healthy volunteers showed no changes in plasma TG after 4 weeks of ACCi treatment (**Figure S2A**).

LDL-ApoB synthesis rates in NASH and healthy control subjects

To determine whether ACCi treatment alters the synthesis of ApoB-containing particles or has different effects in NASH subjects versus healthy controls, we measured ApoB FSR in VLDL and LDL particles by ^2H_2O labeling combined with LC-MS/MS analysis. The earliest time point available for analysis was on day 3 of heavy water administration. ApoB FSRs were monitored in each lipoprotein fraction after preparative ultracentrifugation. On day 3, fractional synthesis measured in VLDL-ApoB in NASH subjects had reached or exceeded 100% values, which precluded inference of kinetic behavior. LDL-ApoB had an average fractional synthesis of 68% ± 19%, representing an average FSR of 37%/day or a half-life (t½) of just under 2 days. LDL-ApoB FSR was not different between healthy subjects and NASH patients, or between cirrhotic and non-cirrhotic subjects (**Figure S3A**), however, LDL-ApoB ASR was significantly lower in cirrhotic vs non-cirrhotic NASH subjects (p=0.03, **Figure S3B**).

ACCi treatment did not affect plasma ApoB concentrations in NASH patients

Among patients with NASH (n=20), mean (± SD) plasma ApoB concentrations did not differ between baseline and week 12 of ACCi therapy (106 ± 8 vs 106 ± 9 mg/dL, p=0.9; **Figure 2C)**. Similar findings were observed in subgroup analyses of non-cirrhotic (115.5 ± 38.4 vs 117.5 ± 34.7 mg/dL, p=0.6461; **Figure 2A**) and cirrhotic patients (96.3 ± 35.3 and 94.9 ± 41.1 mg/dL, p=0.6550; **Figure 2B)**. Similarly, no effect of 4 weeks of ACCi treatment was observed on total plasma ApoB levels among healthy volunteers (**Figure S2B**).

ACCi treatment increased synthesis rates of plasma ApoB in NASH patients with cirrhosis

ApoB ASR was calculated from plasma ApoB100 concentrations multiplied by the FSR of LDL-ApoB in each subject[41,220]. Among the overall NASH population, mean (± SD) LDL-ApoB FSR increased significantly from baseline to week 12 of ACCi therapy (31 ± 20.2 vs 46 ± 22.6 %/day, p=0.03, n=16, **Figure 2F**). Subgroup analysis revealed that significant effects were restricted to NASH patients with cirrhosis. Specifically, mean (± SD) LDL-ApoB FSR at baseline and week 12 of ACCi therapy were 38.5 ± 22.6 %/day and 40.5 ± 14.6 %/day among non-cirrhotic subjects (p=0.8197, n=8, **Figure 2D**), compared with 23.5 ± 15.4 and 51.38 ± 28.6 %/day, respectively, among cirrhotic subjects (p=0.006, n=8, **Figure 2E**).

Similar observations were made concerning to plasma-ApoB ASR. Specifically, mean (± SD) plasma-ApoB ASR at baseline and week 12 of ACCi therapy were 39.8 ± 20.8 and 46.3 ± 14.8 mg/dL/day among non-cirrhotic subjects (p=0.5060, n=8, **Figure 2G**), compared with 21.0 ± 9.6 and 44.2 ± 17 mg/dL/day, respectively, among cirrhotic subjects (p=0.0021, n=8, **Figure 2H**). Combined, cirrhotic and non-cirrhotic NASH patients exhibited a significant 47% increase in plasma-ApoB ASR from baseline to week 12 of ACCi therapy (30.4 ± 18.4 vs 45.2 ± 15.4 mg/dl/day, p=0.016, n=16, **Figure 2I**). No changes in LDL-ApoB FSR or plasma-ApoB ASR were observed among normolipidemic healthy volunteers treated with ACCi for 4 weeks (**Figures S2C and S2D**).

Effects of concurrent fenofibrate plus firsocostat therapy on LDL-ApoB kinetics in NASH

We evaluated the effects of the PPAR-α agonist, fenofibrate, in combination with firsocostat on ApoB kinetics in NASH[209,211] (**Figure S4A**). Patients were pre-treated with fenofibrate 48 mg/day or 145 mg/day for 2 weeks before adding firsocostat, and LDL-ApoB kinetics were sampled by heavy water labeling during the first three days of fenofibrate monotherapy. Mean (± SD) LDL-ApoB FSR were 31 ± 20, 38 ± 32, and 38 ± 27 %/day for the untreated, 3 days of fenofibrate 48 mg/day, and 3 days of fenofibrate 145 mg/day groups, respectively (all p>0.05, **Figure S4B**). The absence of significant differences between groups suggests that three days of fenofibrate treatment did not influence acute LDL-ApoB kinetics. There were no significant differences in LDL-ApoB FSRs and ASRs between baseline values (after 3 days of fenofibrate treatment) and 12 weeks of combination therapy with fenofibrate plus the ACCi (**Figure S5A and S5B**). ACCi in combination with both doses of fenofibrate treatment, vs ACCi alone in both non-cirrhotic and cirrhotic NASH patients, significantly lowered LDL-ApoB FSR (± SEM) (33 ± 4 vs 46 ± 6 %/day, p=0.032, **Figure 3A**) and LDL-ApoB ASR (± SEM) (34 ± 4 vs 45 ± 4 mg/dL/day, p=0.026, **Figure 3B**). The change in LDL-ApoB FSR ± SEM from baseline to ACCi treatment, and from baseline to fenofibrate plus ACCi in the two fenofibrate groups combined (48 mg/day and 145 mg/day) were +15 ± 6 and -2 ± 5 %/day, respectively (p=0.028, **Figure 3C**). Additionally, the change in LDL-ApoB ASR ± SEM from baseline to ACCi treatment, and from baseline to fenofibrate plus ACCi in the two fenofibrate combined groups (48 mg/day and 145 mg/day) were 15 ± 5 and 3 ± 4 mg/dL/day, respectively (p=0.04, **Figure 3D**). Individual subgroup analysis of the change in LDL-ApoB ASR revealed non-significant effects between each group (**Figure S6A**), except for the change in LDL-ApoB FSRs from baseline to ACCi in cirrhotic groups, as compared to baseline vs ACCi + low dose fibrate subjects with no cirrhosis (p=0.05) (**Figure S6B**).

Correlation between changes in plasma TG and plasma ApoB content or kinetics

Changes in plasma-ApoB100 and TG levels were compared to changes in plasma ApoB100 kinetics from baseline to 12 weeks of ACCi treatment. While changes in TG and plasma-ApoB100 content between baseline and week 12 were significantly correlated (r=0.47, p=0.018, **Table 2**), no significant correlations were observed between changes in TGs and plasma-ApoB kinetics but trended in the negative direction. Interestingly, the change in LDL-ApoB FSR and plasma ApoB concentration from baseline to week 12 of ACCi treatment displayed a borderline significant association (p=0.053) and negative correlation (r = -0.42).

Table 1: Clinical and metabolic characteristics of healthy, non-cirrhotic, and cirrhotic NASH patients.

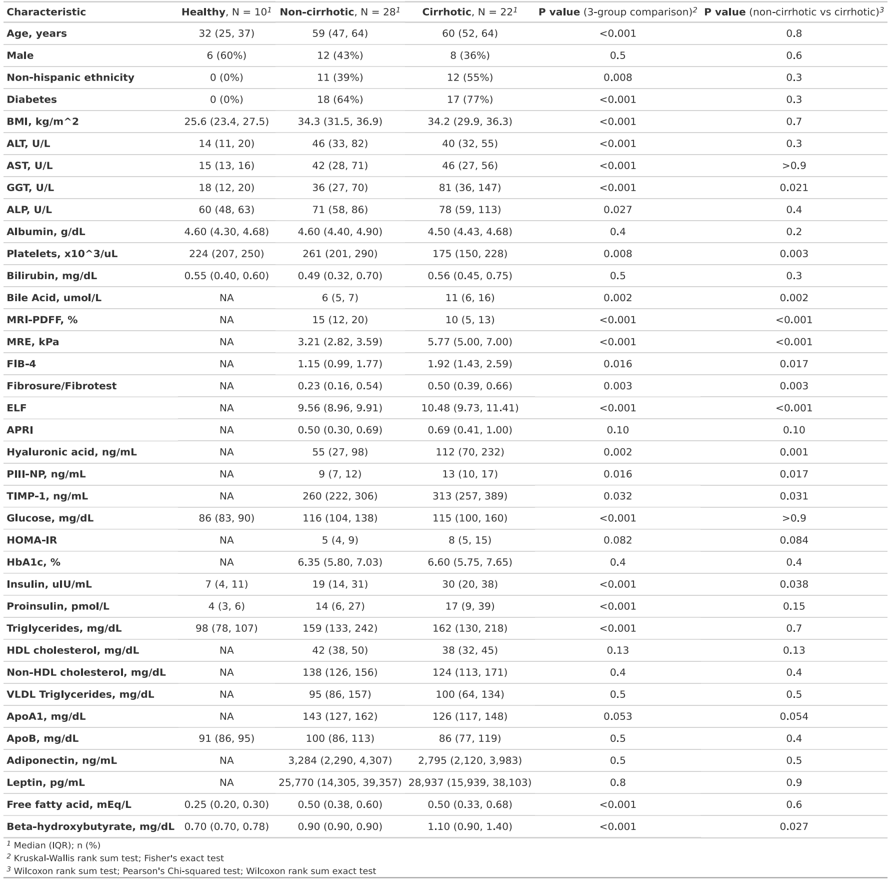

Characteristic	**Healthy**, N = 10[1]	**Non-cirrhotic**, N = 28[1]	**Cirrhotic**, N = 22[1]	**P value** (3-group comparison)[2]	**P value** (non-cirrhotic vs cirrhotic)[3]
Age, years	32 (25, 37)	59 (47, 64)	60 (52, 64)	<0.001	0.8
Male	6 (60%)	12 (43%)	8 (36%)	0.5	0.6
Non-hispanic ethnicity	0 (0%)	11 (39%)	12 (55%)	0.008	0.3
Diabetes	0 (0%)	18 (64%)	17 (77%)	<0.001	0.3
BMI, kg/m^2	25.6 (23.4, 27.5)	34.3 (31.5, 36.9)	34.2 (29.9, 36.3)	<0.001	0.7
ALT, U/L	14 (11, 20)	46 (33, 82)	40 (32, 55)	<0.001	0.3
AST, U/L	15 (13, 16)	42 (28, 71)	46 (27, 56)	<0.001	>0.9
GGT, U/L	18 (12, 20)	36 (27, 70)	81 (36, 147)	<0.001	0.021
ALP, U/L	60 (48, 63)	71 (58, 86)	78 (59, 113)	0.027	0.4
Albumin, g/dL	4.60 (4.30, 4.68)	4.60 (4.40, 4.90)	4.50 (4.43, 4.68)	0.4	0.2
Platelets, x10^3/uL	224 (207, 250)	261 (201, 290)	175 (150, 228)	0.008	0.003
Bilirubin, mg/dL	0.55 (0.40, 0.60)	0.49 (0.32, 0.70)	0.56 (0.45, 0.75)	0.5	0.3
Bile Acid, umol/L	NA	6 (5, 7)	11 (6, 16)	0.002	0.002
MRI-PDFF, %	NA	15 (12, 20)	10 (5, 13)	<0.001	<0.001
MRE, kPa	NA	3.21 (2.82, 3.59)	5.77 (5.00, 7.00)	<0.001	<0.001
FIB-4	NA	1.15 (0.99, 1.77)	1.92 (1.43, 2.59)	0.016	0.017
Fibrosure/Fibrotest	NA	0.23 (0.16, 0.54)	0.50 (0.39, 0.66)	0.003	0.003
ELF	NA	9.56 (8.96, 9.91)	10.48 (9.73, 11.41)	<0.001	<0.001
APRI	NA	0.50 (0.30, 0.69)	0.69 (0.41, 1.00)	0.10	0.10
Hyaluronic acid, ng/mL	NA	55 (27, 98)	112 (70, 232)	0.002	0.001
PIII-NP, ng/mL	NA	9 (7, 12)	13 (10, 17)	0.016	0.017
TIMP-1, ng/mL	NA	260 (222, 306)	313 (257, 389)	0.032	0.031
Glucose, mg/dL	86 (83, 90)	116 (104, 138)	115 (100, 160)	<0.001	>0.9
HOMA-IR	NA	5 (4, 9)	8 (5, 15)	0.082	0.084
HbA1c, %	NA	6.35 (5.80, 7.03)	6.60 (5.75, 7.65)	0.4	0.4
Insulin, uIU/mL	7 (4, 11)	19 (14, 31)	30 (20, 38)	<0.001	0.038
Proinsulin, pmol/L	4 (3, 6)	14 (6, 27)	17 (9, 39)	<0.001	0.15
Triglycerides, mg/dL	98 (78, 107)	159 (133, 242)	162 (130, 218)	<0.001	0.7
HDL cholesterol, mg/dL	NA	42 (38, 50)	38 (32, 45)	0.13	0.13
Non-HDL cholesterol, mg/dL	NA	138 (126, 156)	124 (113, 171)	0.4	0.4
VLDL Triglycerides, mg/dL	NA	95 (86, 157)	100 (64, 134)	0.5	0.5
ApoA1, mg/dL	NA	143 (127, 162)	126 (117, 148)	0.053	0.054
ApoB, mg/dL	91 (86, 95)	100 (86, 113)	86 (77, 119)	0.5	0.4
Adiponectin, ng/mL	NA	3,284 (2,290, 4,307)	2,795 (2,120, 3,983)	0.5	0.5
Leptin, pg/mL	NA	25,770 (14,305, 39,357)	28,937 (15,939, 38,103)	0.8	0.9
Free fatty acid, mEq/L	0.25 (0.20, 0.30)	0.50 (0.38, 0.60)	0.50 (0.33, 0.68)	<0.001	0.6
Beta-hydroxybutyrate, mg/dL	0.70 (0.70, 0.78)	0.90 (0.90, 0.90)	1.10 (0.90, 1.40)	<0.001	0.027

[1] Median (IQR); n (%)
[2] Kruskal-Wallis rank sum test; Fisher's exact test
[3] Wilcoxon rank sum test; Pearson's Chi-squared test; Wilcoxon rank sum exact test

Data are expressed as median values (interquartile range) or as a percentage, n (%). To determine whether these groups differ from each other, statistical significance was evaluated by the Kruskal-Wallis rank-sum test, or Fisher's exact test. To address differences between non-cirrhotic and cirrhotic NASH patients, statistical significance was calculated by the Wilcoxon rank-sum test, Pearson's Chi-squared test, or Wilcoxon rank-sum exact test. BMI, body mass index, ALT, alanine aminotransferase, AST, aspartate aminotransferase, GGT, gamma-glutamyl transpeptidase, ALP, alkaline phosphatase, MRI-PDFF, magnetic resonance imaging-estimated proton density fat fraction, MRE, magnetic resonance elastography, FIB-4, fibrosis-4, ELF, enhanced liver fibrosis test, APRI, AST to platelet ratio index, PIII-NP, Type III procollagen peptide, TIMP-1, Tissue inhibitor of metalloproteinase-1, HOMA-IR, homeostatic model assessment for insulin resistance, HbA1c, hemoglobin A1c, HDL, high-density lipoprotein particles, VLDL, very-low-density lipoprotein particles, ApoA1, apolipoprotein A1, ApoB, apolipoprotein B.

Table 2: Correlations between the change in plasma triglycerides, plasma-ApoB, and ApoB kinetics at week 12 compared to baseline after ACCi treatment.

Correlation	**Spearman r**	**p value**
Triglyceride concentration vs plasma-ApoB concentration	0.47	*0.018
Triglyceride concentration vs	-0.18	0.25

LDL-ApoB FSR		
Triglyceride concentration vs ApoB ASR	-0.14	0.31
Plasma-ApoB concentration vs LDL-ApoB FSR	-0.42	0.053

Data are expressed as a spearman r correlation value with a corresponding p-value. Changes in mean plasma ApoB concentrations, triglyceride concentrations, and LDL-ApoB FSR or LDL-ApoB ASR kinetic values from baseline to week 12 were calculated by the following formula week 12 values - baseline value. *p ≤ 0.05 based on Spearman correlation analysis. FSR, fractional synthesis rate, ASR, absolute synthesis rate.

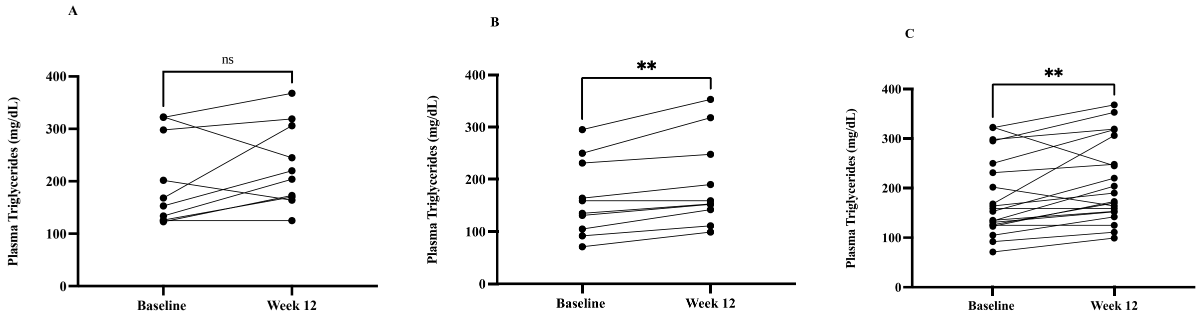

Figure 1: Plasma TG concentrations in NASH patients given ACCi. **A)** Plasma triglyceride (TG, mg/dl ± SD) concentrations in non-cirrhotic NASH patients were 197.4 ± 84.4 at baseline and 229.4 ± 78.9 at week 12 of ACCi treatment (p=0.1276, n=10). **B)** Plasma triglyceride (TG, mg/dl ± SD) concentrations in cirrhotic NASH patients were 163.3 ± 73.3 at baseline and 192.5 ± 86.2 at week 12 of ACCi treatment (p=0.0014, n=10). **C)** Plasma triglyceride (TG, mg/dl ± SD) concentrations in both non-cirrhotic and cirrhotic NASH patients were 180 ± 79 at baseline and 211 ± 83 at week 12 of ACCi treatment. At week 12 plasma TG displayed a significant increase of 17 % (p=0.0056) as compared to baseline. Data are expressed as mean ± SD. Statistical significance was calculated by paired T-test. *p≤0.05.

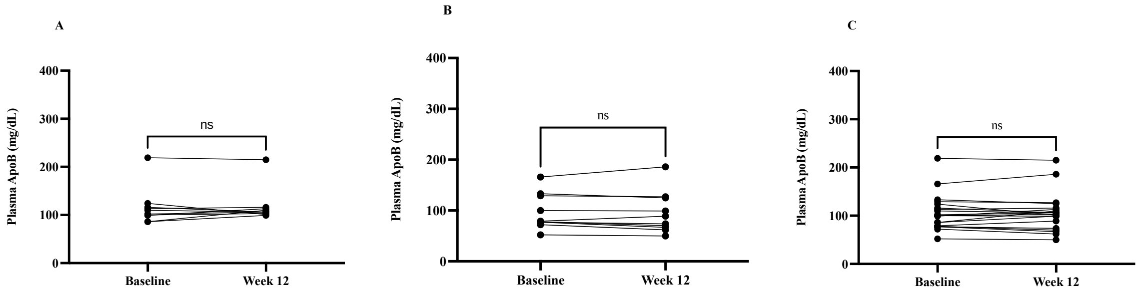

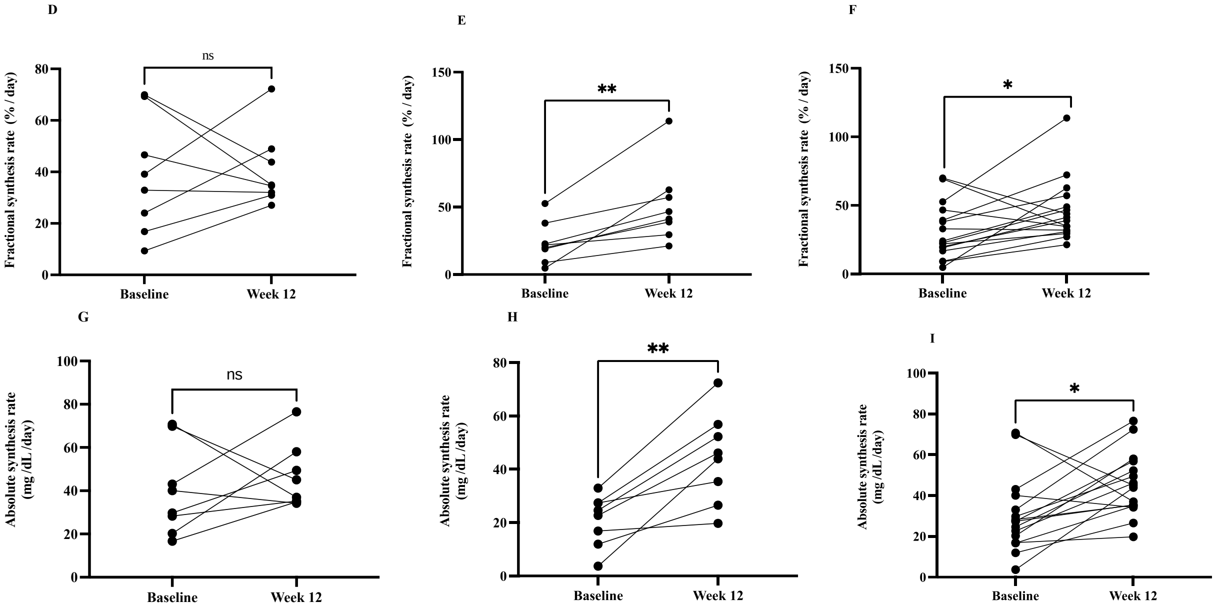

Figure 2: Plasma-ApoB concentrations, LDL-ApoB fractional synthesis rates (FSR), and ApoB absolute synthesis rates (ASR) in non-cirrhotic and cirrhotic NASH patients at baseline and after 12 weeks of ACCi. A) Non-cirrhotic plasma ApoB concentrations were 115.5 ± 38.4 and 117.5 ± 34.7 mg/dl (mean ± SD, p=0.6461, n=10) at baseline and week 12, respectively. **B)** Cirrhotic plasma ApoB concentrations were 96.3 ± 35.3 and 94.9 ± 41.1 mg/dl (mean ± SD, p=0.6550, n=10) at baseline and week 12, respectively. **C)** Plasma ApoB concentrations in combined cirrhotic and non-cirrhotic subjects were 106 ± 8 and 106 ± 9 mg/dl (mean ± SD, p=0.9, n=20) at baseline and week 12, respectively. **D)** Non-cirrhotic LDL-ApoB FSR values ± SD were 38.5 ± 22.6 and 40.5 ± 14.6 %/day at baseline and week 12, respectively, (p=0.8197, n=8). **E)** Cirrhotic LDL-ApoB FSR values ± SD were 23.5 ± 15.4 and 51.38 ± 28.6 %/day (p=0.006, n=8) at baseline and week 12, respectively. **F)** LDL-ApoB FSR values ± SD in combined cirrhotic and non-cirrhotic subjects were 31 ± 20.2 and 46 ± 22.6 %/day (p=0.03, n=16) at baseline and week 12, respectively. **G)** Non-cirrhotic plasma-ApoB ASR values ± SD were 39.8 ± 20.8 and 46.3 ± 14.8 mg/dl/day at baseline and week 12 (p=0.5060, n=8), respectively. **H)** Cirrhotic plasma-ApoB ASR values were 21.0 ± 9.6 and 44.2 ± 17 mg/dl/day at baseline and week 12 (p=0.0021, n=8), respectively. **I)** Plasma-ApoB ASR values in combined cirrhotic and non-cirrhotic subjects were 30.4 ± 18.4 and 45.2 ± 15.4 mg/dl/day (p=0.016, n=16) at baseline and week 12, respectively. Plasma-ApoB ASR was calculated as LDL-ApoB100 FSR (fraction/day) x plasma-ApoB concentration (mg/dl). Data are expressed as mean values ± SD. Statistical significance was calculated by a paired T-test.

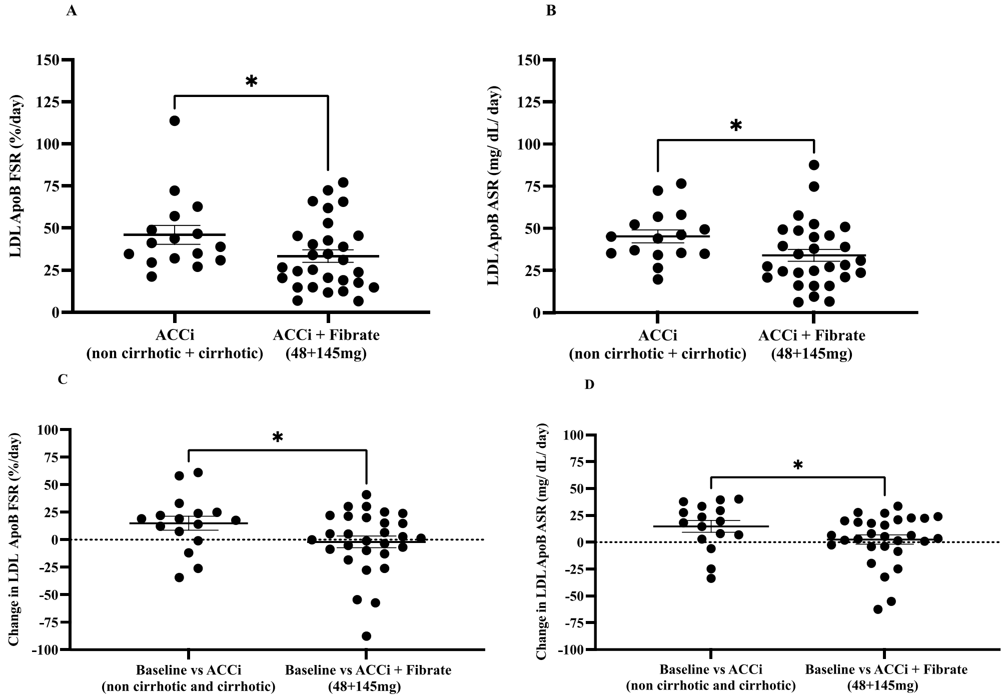

Figure 3: The effect of either low or high dose of fenofibrate in combination with ACCi on LDL-ApoB FSR and ASR in NASH patients with or without cirrhosis. A) LDL-ApoB FSR (mean values ± SEM) for ACCi alone in both non-cirrhotic and cirrhotic subjects vs, ACCi + two combined fenofibrate (48 mg/day and 145 mg/day) doses were 46 ± 6 and 33 ± 4 %/day, respectively. ACCi+fenofibrate lowered LDL-ApoB FSR as compared to the ACCi treated group alone, p=0.032. **B)** LDL-ApoB ASR (mean values ± SEM) for ACCi alone in both non-cirrhotic and cirrhotic subjects vs, ACCi + two combined fenofibrate (48 mg/day and 145 mg/day) doses were 45 ± 4 and 34 ± 4 mg/dL/day, respectively. ACCi+fenofibrate lowered LDL-ApoB ASR to near baseline levels as compared to the ACCi treated group alone, p=0.026. **C)** Change in LDL-ApoB FSR ± SEM from baseline to ACCi treatment in NASH subjects with both non-cirrhosis and cirrhosis, and from baseline to ACCi + two combined fibrate doses (48mg+145mg) were 15 ± 6 and -2 ± 5 %/day (p=0.028), respectively. **D)** Change in LDL-ApoB ASR ± SEM from baseline to ACCi treatment in NASH subjects with both non-cirrhosis and cirrhosis, and from baseline to ACCi + two combined fibrate doses (48mg+145mg) were 15 ± 5 and 3 ± 4 mg/dL/day (p=0.04), respectively. Data are expressed as mean ± SEM. Statistical significance was evaluated by a one-tailed unpaired T-test. *p≤0.05.

6.5. Discussion

Treatment with ACC inhibitors leads to hypertriglyceridemia in a minority of patients with NASH[204,206,207,208,209,210,211,212]. In this study, our goals were to determine whether high plasma TG concentrations in this setting are associated with altered LDL-ApoB particle production or clearance, whether the stage of liver disease alters the ApoB kinetic response to ACCi therapy, and whether concurrent treatment with a fibrate can prevent changes in ApoB kinetics.

Endogenously derived TG are trafficked in the blood primarily in VLDL. During the process of metabolic conversion of VLDL to LDL, the main structural protein of these particles, ApoB100, remains intact, whereas receptor-mediated uptake removes the intact particle, which includes resident ApoB100[214]. The majority (~90%) of circulating ApoB100 resides in LDL. The half-life of VLDL is hours, whereas LDL, for which VLDL is the precursor, has a half-life of days[17,42,43,215,216,218]. In this study, blood was not sampled during the first day of heavy water labeling to measure VLDL-ApoB kinetics, however, a sample at 3 days of labeling enabled analysis of LDL-ApoB kinetics and provided a window into upstream production of ApoB-containing particles by the liver[43,220]. The half-life of ~2 days measured here for ApoB in the LDL fraction is consistent with prior reports[42,43,215,216,217,218].

In NASH patients in this study, plasma concentrations of TG, but not ApoB, increased after 12 weeks of firsocostat treatment (**Figures 1C and 2C)**. No changes in these parameters were observed in healthy controls treated with firsocostat for 4 weeks (**Figures S2A and S2B**). Our primary finding is a significant increase in the synthesis of LDL-ApoB at week 12 of firsocostat treatment. This finding was restricted to the subgroup of NASH patients with cirrhosis (**Figures 2E and 2H**). The half-life of LDL-ApoB was not prolonged; in fact, a non-significant reduction in half-life (increased FSR) was observed (data not shown). These findings argue against an LDL-ApoB clearance defect induced by ACCi as the cause of these findings. If we had seen no changes in ApoB100 turnover, it would have suggested altered lipid turnover without a change in particle metabolism (e.g., a lipoprotein lipase or ApoCIII effect)[207]. The correlation between relative changes in plasma-ApoB and TG concentrations at week 12 of firsocostat treatment suggests a relationship between increased particle production and plasma TG concentrations (**Table 2**). However, since our study did not directly assess VLDL particle production, we cannot confirm this hypothesis.

These observations should be considered in the context of previous reports describing higher VLDL secretion in a genetic model of ACC ablation (ACC double knock-out mice) and hypertriglyceridemia in humans treated with different ACCi compounds[204,206,207,208,209,210,211,212]. These observations in mice have been attributed to reduced malonyl-CoA levels in the liver that results in reduced polyunsaturated fatty acids, activation of SREBP-1c, and upregulation of downstream genes such as GPAT, followed by increased VLDL secretion[204]. Indeed, Goedeke and colleagues reported an increase in VLDL secretion rates in fasted overnight rodents treated with an ACCi after Poloxamer 405 administration to inhibition lipolysis of triglyceride-rich lipoproteins[207,221]. Our data are consistent with an effect of ACCi on hepatic ApoB particle production.

Loomba et. al. conducted nuclear magnetic resonance lipoprotein analysis in a similar cohort of NASH patients treated with firsocostat in a 12-week phase 2a study[208]. While increased particle number and TG concentration of VLDL were observed over 1 week of ACCi treatment, the number of small LDL particles; total cholesterol, HDL cholesterol, and LDL cholesterol concentrations and particle number, and glycemic parameters did not change during the study as compared to placebo[208]. In a multivariate analysis adjusting for demographics and lipids at baseline, grade 3 or 4 hypertriglyceridemias (>500 mg/dl) were associated with baseline plasma TG over 250 mg/dl. Importantly, despite ongoing treatment with firsocostat in all patients, treatment with fibrates or fish oil led to the resolution of grade 3 or 4 hypertriglyceridemia in all patients[208].

The utility of fibrates to mitigate ACCi-induced hypertriglyceridemia has been evaluated in several additional clinical studies[210,211]. For example, in a proof-of-concept study of NASH patients with hypertriglyceridemia (>150 mg/dL) and advanced (F3-F4) fibrosis, Lawitz et al. showed that a 2-week course of pre-emptive therapy with fenofibrate (48 or 145 mg) prevented any increase in TG after 24 weeks of fenofibrate and firsocostat combination therapy[210,211]. Similarly, a recent report confirmed that fenofibrate 145 mg prevents TG elevations in the setting of combination therapy with firsocostat and the farnesoid X receptor agonist, cilofexor, in hypertriglyceridemia patients with NASH[211]. These data suggest that concurrent ACCi and fenofibrate treatment prevents the increase in plasma TG that may be observed with ACCi treatment alone.

To explore these clinical observations, we evaluated whether combination therapy with fenofibrate and firsocostat altered LDL-ApoB production rates. In the cross-sectional and subgroup comparisons, the change in LDL-ApoB kinetics in the low or high fibrate doses + ACCi treatments, were not significantly different from ACCi treatment alone, regardless of cirrhotic state (**Figures 6SA and 6SB**). When we combined the data for both doses of fenofibrate and stages of NASH, ApoB FSR and ASR were significantly lower than ACCi treatment alone (**Figures 3A and 3B**). Although the longitudinal analyses were potentially confounded by concurrent 3 days of fibrate therapy at baseline, longitudinal comparisons supported the cross-sectional analyses. There were no apparent effects of the initial 3 days of fibrate treatment on ApoB FSR (**Figure S4B**) and the addition of ACCi treatment did not increase ApoB FSR (**Figure S5A & S5B**). Moreover, we observed a significant reduction in the change in LDL-ApoB FSR and ASR with the ACCi + two combined fibrate doses (**Figure 3C and 3D**).

Previous lipoprotein kinetic studies have been reported in men with metabolic syndrome treated with fibrates[222]. In one study, treatment with fenofibrate 200 mg/day for 5 weeks led to increased fractional catabolic rate and decreased pool size of ApoB-containing particles[223]. Caslake et. al. reported decreased VLDL particle size after fenofibrate treatment, as well as increased LDL-ApoB degradation by the receptor route, but not for receptor-independent routes[224]. Another study, which only labeled for 12 hours, showed no effect of fibrate treatment on LDL-ApoB concentration, pool size, or fractional catabolic or production rates[225]. Nevertheless, fenofibrate treatment did lower VLDL ApoB concentrations, and secretion rates in NAFLD patients, consistent with our data of suppression of LDL ApoB ASR with concurrent fenofibrate and ACCi treatment acting upon the liver[226].

Importantly, we observed differential effects of the ACCi on lipid and lipoprotein metabolism between non-cirrhotic and cirrhotic NASH patients. After ACCi treatment, cirrhotic NASH patients displayed elevated plasma TG levels, LDL-ApoB FSR and ASR as compared to non-cirrhotic subjects[210]. The explanation for this differential effect is uncertain but may be explained by the pathophysiological progression of NASH on lipoprotein metabolism[198,227]. NASH patients with cirrhosis typically exhibit decreased hepatocellular mass, lower hepatic blood flow, lower ApoB biogenesis, and secretion from the liver[198,202,227]. We showed NASH patients with cirrhosis exhibit lower ApoB synthesis as compared to their non-cirrhotic counterparts but displayed increased ApoB synthesis after ACCi treatment (**Figure S3B, Figure 2G-H**). This data may suggest restoration of hepatocellular function with firsocostat treatment in cirrhosis. Data to support this hypothesis include improvements in liver function such as decreased liver fat, stiffness, neuroinflammatory activity, and fibrosis[207,208,209,210,211,221]. In rodents treated with

ACCi's, decreased expression of markers of macrophage activation, and fibrosis such as CCL2, and COL1A1 were observed, respectively. Decreased staining of alpha-SMA, and CD3, markers of hepatic stellate cell activation, fibrogenesis, and T cell activation were observed as well[212,221].

In conclusion, we report that treatment with the ACCi firsocostat significantly increases the synthesis rate of ApoB-containing LDL particles in NASH subjects with cirrhosis, without a significant increase in plasma ApoB concentrations (**Graphical abstract**). These results suggest that the site of action of previously reported effects of ACCi treatment on plasma TG is the liver. Fenofibrate combination therapy prevented the increased LDL-ApoB particle production induced by firsocostat therapy.

Data availability

All data can be viewed in the manuscript. Any or additional data is available upon the reviewer's request from the corresponding author.

Author contributions

Jen-Chieh Chuang, Kaiyi Zhu, Andrew N. Billin, Ryan S. Huss, Chuhan Chung, Robert P. Myers, Marc Hellerstein: Conceptualization, Methodology, and Software. Mohamad Dandan, Kaiyi Zhu: Data curation, Writing- Original draft preparation, Visualization, and Investigation. Marc Hellerstein and Jen-Chieh Chuang: Supervision, Software, and Validation. Robert P. Myers, Marc Hellerstein, and Jen-Chieh Chuang: Writing- Reviewing and Editing.

Acknowledgments

This work was supported by Gilead Sciences, Inc. The graphical abstract was created with BioRender.com.

6.6. Supplemental Material

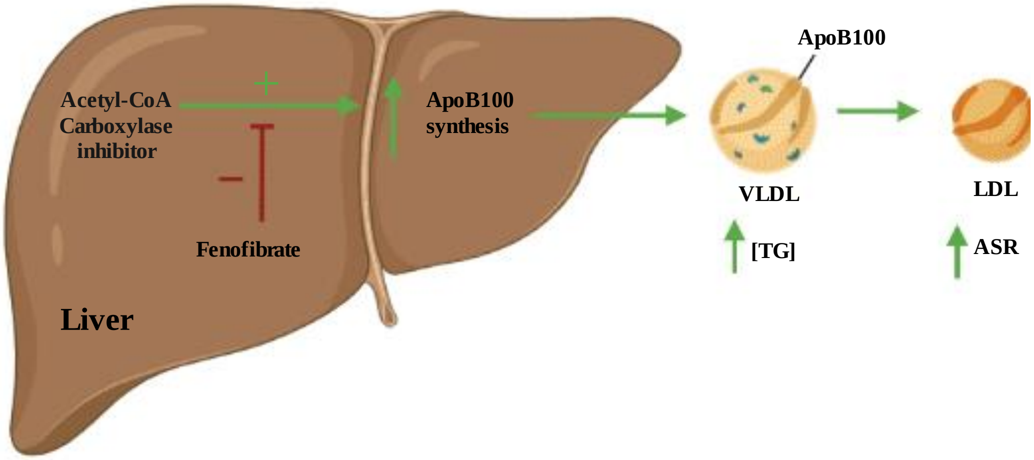

Graphical abstract: ACCi treatment alone (green arrow) leads to increased ApoB particle production in the liver as shown by increased production of LDL ApoB. Fenofibrate combined with ACCi treatment (red inhibitory symbol) prevented the increased LDL-ApoB particle production.

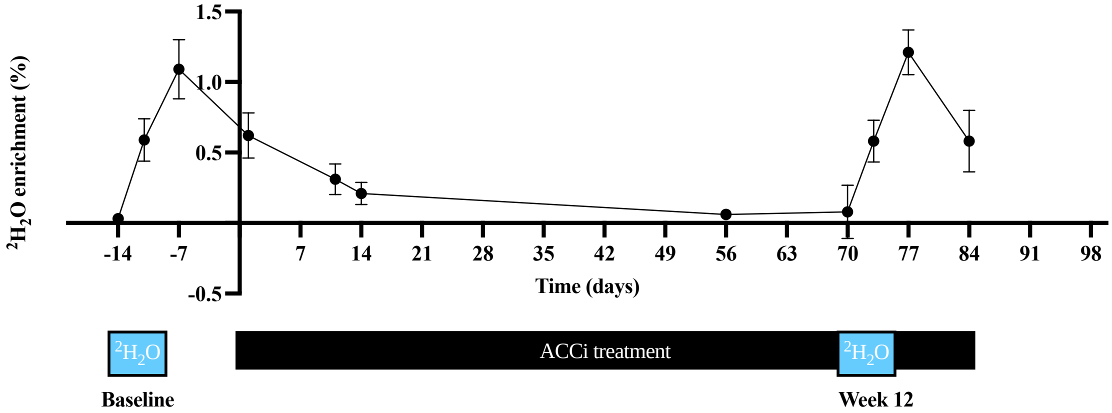

Supplemental figure S1: Heavy water labeling and study design. Labeling design and time course of ^2H_2O enrichment over the study period with average body water enrichments of both non-cirrhotic and cirrhotic NASH subjects (n=10-20 per time point). Subjects were labeled with heavy water at baseline and week 12 of ACCi treatment. On day 0, subjects were administered firsocostat 20 mg per day orally once a day, for 12 weeks.

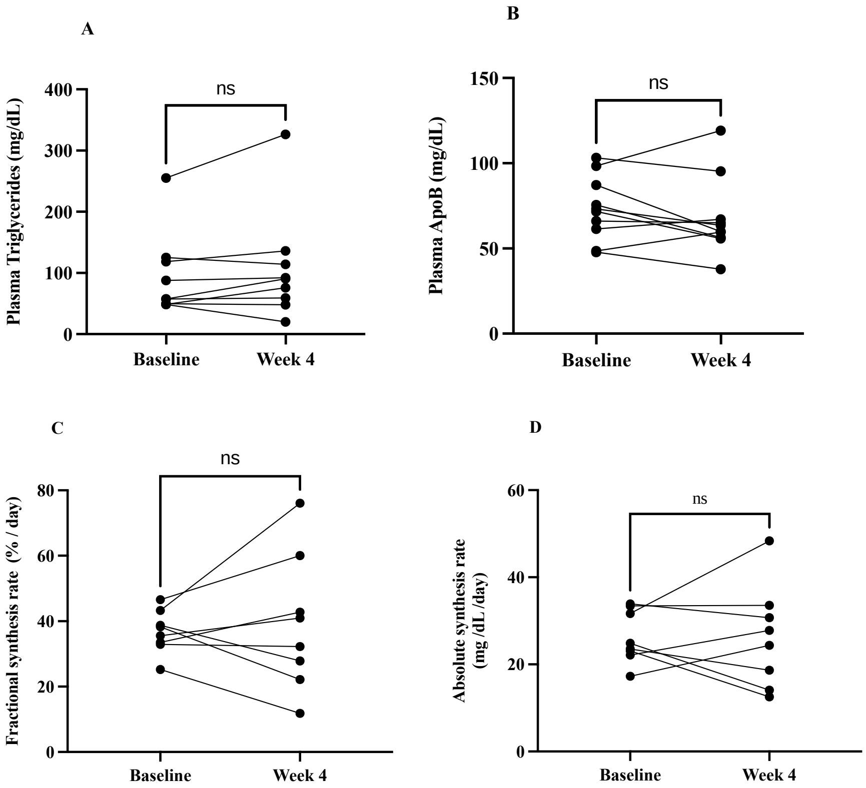

Supplemental figure S2. Data for healthy volunteers' plasma triglycerides concentrations, plasma-ApoB concentrations, LDL-ApoB fractional synthesis rate, and plasma-ApoB absolute synthesis rate after ACCi for 4 weeks. **A)** Plasma triglycerides (mg/dl, mean value ±

SEM) at baseline and week 4 were 94 ± 23 and 107 ± 30 (p=0.2, n=9), respectively. **B)** Plasma-ApoB concentrations (mg/dl, mean value ± SEM) at baseline and week 4 were 73 ±6 and 68 ± 7 (p=0.3, n=10), respectively. **C**) LDL-ApoB fractional synthesis rates (%/day ± SEM) at baseline and week 4 were 37 ± 2 and 39 ± 7 (p=0.7, n=8), respectively. **D)** ApoB absolute synthesis rate (mg/dl/day, mean value ± SEM) at baseline and week 4 were 26 ± 2 and 26 ± 4 (p=0.9, n=8), respectively. We observed no statistically significant effect on plasma triglycerides, ApoB concentrations, and LDL-ApoB kinetics after 4 weeks of ACCi in healthy volunteers. Statistical significance was evaluated by paired T-test, *p≤0.05.

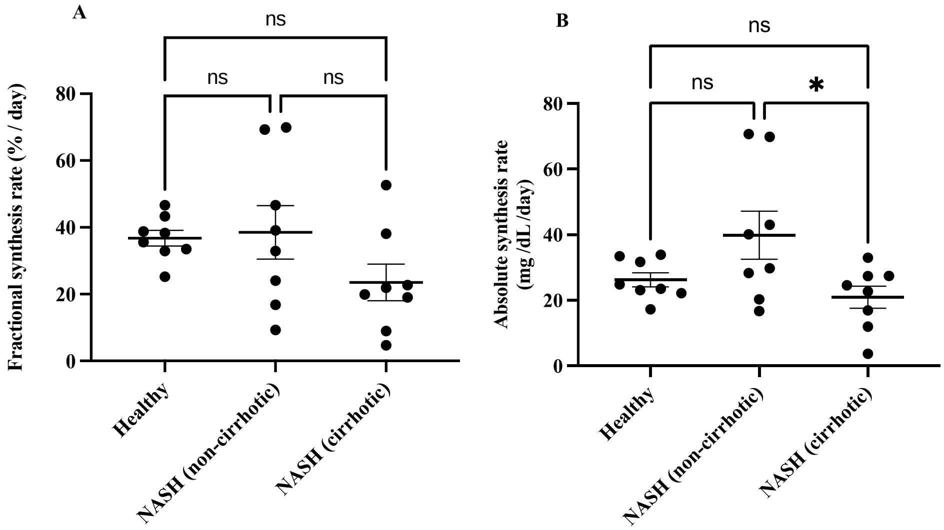

Supplemental figure S3. Baseline characteristics of LDL-ApoB fractional synthesis rates (FSR), and ApoB absolute synthesis rates (ASR) in healthy volunteers vs baseline values from non-cirrhotic or cirrhotic NASH patients treated with ACCi. A) LDL-ApoB fractional synthesis rates (%/day) in non-cirrhotic (n=8, p=0.98) and cirrhotic NASH patients (n=8, p=0.25) were not significantly different when compared to healthy volunteers (n=8). **B)** LDL-ApoB absolute synthesis rates (mg/dl/day) in non-cirrhotic (n=8, p=0.14) and cirrhotic NASH patients (n=8, p=0.72) were not significantly different when compared to healthy volunteers (n=8), but LDL-ApoB ASRs were significantly lower in cirrhotic (p=0.03) than non-cirrhotic NASH patients. Data are expressed as mean ± SEM. Statistical significance was evaluated by an ANOVA, *p≤0.05.

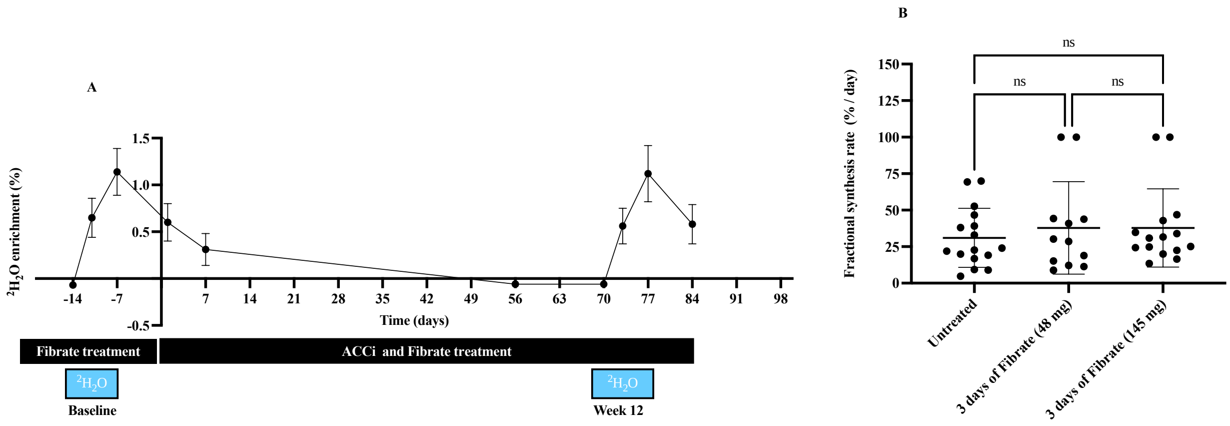

Supplemental figure S4. Lack of effect of 3 days of fenofibrate administration at baseline on ApoB FSR. A) Study design; B) LDL-ApoB FSR (%/day). No difference was observed between treatments. Data are expressed as mean ± SD. Statistical significance was calculated by an ANOVA, *p≤0.05.

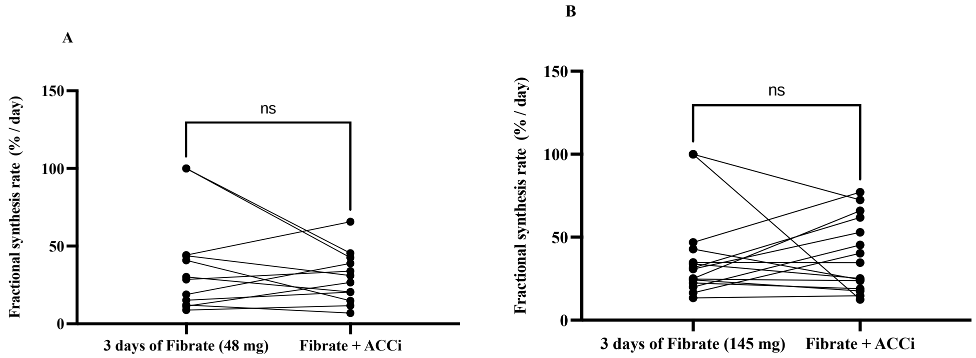

Supplemental figure S5. Effects of 12 weeks of ACCi + fenofibrate therapy on ApoB FSR (%/day). A) ACCi + Fenofibrate 48 mg/day. **B)** ACCi + Fenofibrate 145 mg/day. No difference was observed between treatments. Statistical significance was evaluated by a paired T. test, *p≤0.05.

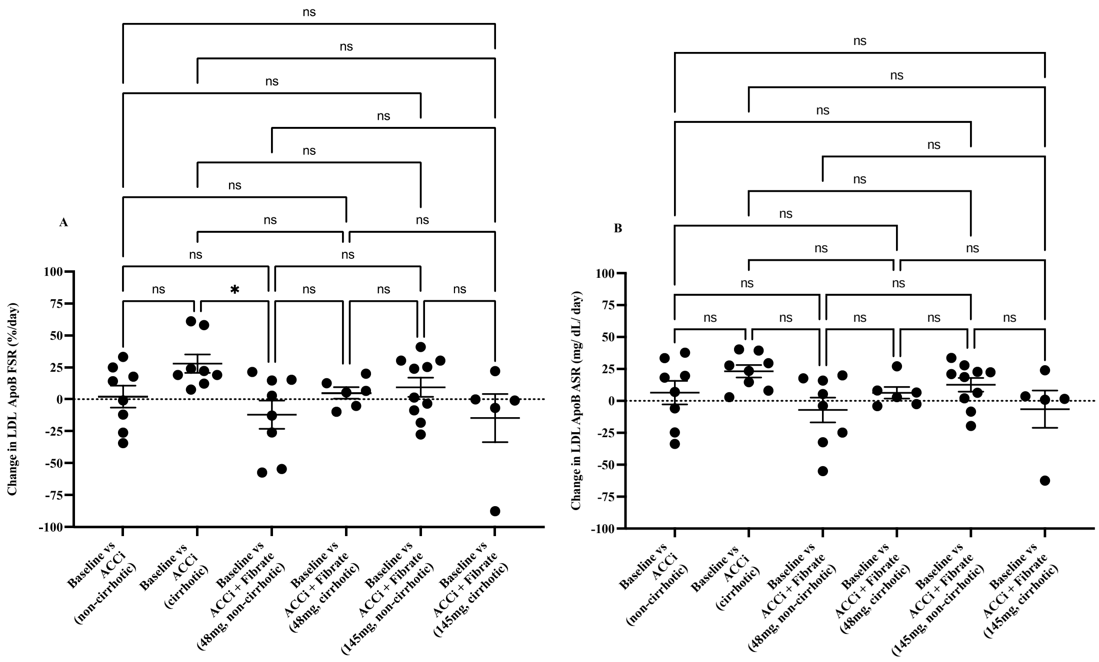

Supplemental Figure S6: The effect of either low or high dose of fenofibrate in combination with ACCi on LDL-ApoB FSR in NASH patients with or without cirrhosis. A) Change in LDL-ApoB FSR (mean ± SEM) from baseline to ACCi treatment in NASH subjects with non-cirrhosis or cirrhosis, and from baseline to ACCi + two individual low or high fibrate doses (48mg or 145mg) with or without cirrhosis were 2 ± 9, 28 ± 7, -12 ± 11, 5 ± 5, 9 ± 7, -15 ± 19, respectively. No statistical significance was observed between each group, except for baseline vs ACCi cirrhotic groups, as compared to baseline vs ACCi + low dose fibrate subjects with no cirrhosis (p=0.05). **B)** Change in LDL-ApoB ASR (mean ± SEM) from baseline to ACCi treatment in NASH subjects with non-cirrhosis or cirrhosis, and from baseline to ACCi + two individual low or high fibrate doses (48mg or 145mg) with or without cirrhosis were 6 ± 9, 23 ± 5, -7 ± 10, 6 ± 5, 13 ± 5, -7 ± 15, respectively. Data are expressed as mean ± SEM. Statistical significance between each group was calculated by ANOVA, *$p \leq 0.05$.

7. Chapter 7

The role of striated muscle Pik3r1 in glucose and protein metabolism following chronic glucocorticoid exposure

7.1. Abstract

Chronic glucocorticoid exposure causes insulin resistance and muscle atrophy in skeletal muscle. We previously identified phosphoinositide-3-Kinase regulatory subunit 1 (Pik3r1) as a glucocorticoid receptor primary target gene in skeletal muscle involved in glucocorticoid suppressed insulin action. We generated striated muscle specific Pik3r1 knockout mice (MKO) to investigate its role in glucocorticoid actions in vivo. Treating wild type (WT) mice with dexamethasone (DEX), a synthetic glucocorticoid, attenuated insulin activated Akt activity in liver, epididymal white adipose tissue, and gastrocnemius muscle. This DEX effect was attenuated in gastrocnemius muscle of MKO mice, resulting in better glucose and insulin tolerance in DEX treated MKO mice. Stable isotope labeling techniques revealed that in WT mice, DEX treatment decreased protein fractional synthesis rates in gastrocnemius muscle. Histology showed that in WT mice, DEX treatment reduced gastrocnemius muscle myotube diameters. In MKO mice, myotube diameters were smaller than WT mice and there were more fast oxidative fibers. Importantly, DEX failed to further reduce myotube diameters. In MKO mice, the basal protein synthesis rate was decreased (likely caused by lower 4E-BP1 phosphorylation at Thr37/Thr46) and the ability of DEX to attenuate protein synthesis rate was attenuated. DEX-reduced protein synthesis was likely caused by its ability to increase eIF2α phosphorylation at Ser51 and inhibit insulin-induced p70S6 kinase phosphorylation at Thr389, and 4E-BP1 at Thr37/Thr46. In MKO mice, the ability of DEX to inhibit eIF2α phosphorylation and insulin-induced 4E-BP1 phosphorylation was reduced. Overall, our results demonstrate Pik3r1's role in glucocorticoid actions on glucose and protein metabolism in skeletal muscle.

7.2. Introduction

Glucocorticoids are steroid hormones that play important roles in regulating whole body metabolism under stress conditions, mainly by mobilizing energy sources to face severe challenges. In skeletal muscle, glucocorticoids inhibit protein synthesis, facilitate protein degradation, and suppress glucose utilization. Amino acids generated from glucocorticoid-induced protein mobilization are the precursors for hepatic gluconeogenesis and inhibiting glucose utilization raises plasma glucose concentrations[228,229]. While these glucocorticoid effects are critical for metabolic adaptations during stress, chronic/excess glucocorticoid exposure causes hyperglycemia, insulin resistance, and muscle atrophy[228,230,231,232].

Glucocorticoids convey their functions through the glucocorticoid receptor (GR), which is a transcription factor that binds to genomic glucocorticoid response elements to modulate the transcriptional rate of its target genes. Thus, GR primary target genes initiate the physiological actions of glucocorticoids. To understand the mechanisms underlying glucocorticoid actions in skeletal muscle, we previously used a combination of global gene expression analysis and chromatin immunoprecipitation sequencing to identify a list of potential GR primary target genes in murine C2C12 myotubes[233]. Phosphoinositide-3-kinase regulatory subunit 1 (Pik3r1, a.k.a.

p85α) is one of these potential GR primary target genes[233] and encodes a regulatory subunit of phosphoinositide 3-kinase (PI3K), which is composed of a regulatory subunit (Pik3r1, Pik3r2 or Pik3r3) and a catalytic subunit (Pik3ca1 or Pik3ca2)[234,235]. When insulin signaling is activated, PI3K is recruited to the activated insulin receptor substrate 1 (IRS1) to convert phosphatidylinositol-4, 5 bisphosphate (PIP_2) to phosphatidylinositol-3, 4, 5 triphosphate (PIP_3). Binding to PIP_3 at the plasma membrane is required to activate protein kinase Akt[236], a key signaling molecule in mediating the metabolic functions of insulin. Though Pik3r1 is a key component of the insulin pathway, overexpression of monomeric Pik3r1 was found to suppress insulin signaling in myotubes and hepatocytes[237,238]. Conversely, Pik3r1 deficiency has been shown to improve insulin sensitivity[239,240]. Several mechanisms have been proposed for the inhibitory effect of excess Pik3r1 on insulin signaling. First, monomeric Pik3r1 competes with heterodimeric PI3K for binding to insulin receptor substrate-1 (IRS-1) to suppress insulin signaling[241]. Alternatively, Pik3r1 could enhance the activity of phosphatase and tensin homolog (PTEN) to inhibit PI3K[242]. Another report shows that homodimeric but not monomeric Pik3r1 suppresses PI3K by protecting PTEN from ubiquitin-mediated proteasomal degradation. Further, the p85alpha homodimer enhances lipid phosphatase activity and membrane association of PTEN[243].

We previously found that the overexpression of Pik3r1 in C2C12 myotubes reduced cell diameter while reduction in Pik3r1 expression compromised glucocorticoid suppression of insulin signaling[233]. To further investigate the role of Pik3r1 in glucocorticoid actions in skeletal muscle, we created striated muscle specific Pik3r1 knockout mice (MKO)[244]. We treated MKO and $Pik3r1^{flox/flox}$ mice (will be referred as wild type, WT, mice in this report) with or without a synthetic glucocorticoid, dexamethasone (DEX), and studied the effects on insulin signaling in metabolic tissues, including liver, gastrocnemius muscle, and epididymal white adipose tissue. We also examined the effect of striated muscle Pik3r1 deletion on systemic glucose and insulin tolerance. In addition, using stable isotope labeling techniques and tandem mass spectrometry, we analyzed the DEX effects on protein synthesis rates in gastrocnemius muscle of WT and MKO mice. Finally, we investigated the signaling pathways involved in the regulation of protein synthesis and conducted histological analysis of the gastrocnemius muscle in WT and MKO mice.

7.3. Results

GR increased Pik3r1 gene transcription and protein expression in mouse gastrocnemius muscle

We previously showed that Pik3r1 gene expression was elevated in mouse gastrocnemius muscle upon DEX treatment[233]. We examined whether Pik3r1 protein expression was indeed increased by DEX treatment. Male WT mice were injected intraperitoneally with DEX or PBS daily for 1, 4 or 7 days. Gastrocnemius muscles were collected to detect the expression of Pik3r1 using immunoblotting. We found that Pik3r1 expression was significantly increased upon DEX treatment for 4 and 7 days (Fig. 1a).

To confirm the activation of Pik3r1 gene transcription by GR in vivo, chromatin immunoprecipitation (ChIP) was performed to test the recruitment of GR to the GRE of Pik3r1 gene in mouse gastrocnemius muscle. Eight-week old male WT mice were injected intraperitoneally with PBS or DEX for 4 days before tissue collection for ChIP given that Pik3r1 had the highest protein expression with 4 days of DEX treatment. The glucocorticoid response element of Pik3r1 has been located between -43938 and -43924 upstream of the mouse Pik3r1 gene[233]. We found that GR was significantly recruited to the Pik3r1 GRE by DEX treatment (approximately 15 fold comparing to IgG ChIP control) (Fig. 1b). Interestingly, GR was also recruited to the Pik3r1 GRE in PBS treated animals to a lesser degree (approximately 5 fold, Fig. 1b). This suggests that plasma corticosterone levels are enough to activate Pik3r1 gene transcription through GR.

Transcriptional activation is associated with elevated histone acetylation in the enhancer regions[245,246]. We performed ChIP to monitor the acetylated histone H3 (AcH3) and H4 (AcH4) and total H3 and H4 at the Pik3r1 GRE in the gastrocnemius muscle of PBS and DEX treated WT mice. The ratios of AcH3/H3 and AcH4/H4 represent the degrees of the histone acetylation in H3 and H4, respectively. As shown in figure 1c, the level of total histone H3 and H4 was not significantly affected by DEX treatment. However, comparing to IgG control, the ratios of AcH3/H3 and AcH4/H4 were significantly increased by 8 and 10 folds with DEX treatment, respectively (Fig. 1c). In PBS treated animals, the ratios of AcH3/H3 and AcH4/H4 were also significantly higher than the IgG ChIP control (approximately 3 and 7 folds, respectively, Fig. 1c). This observation was consistent with the finding that GR was also recruited to the Pik3r1 GRE under PBS treatment. Nonetheless, the ratios of AcH3/H3 and AcH4/H4 were higher in DEX treated mice than those of PBS treated mice. This was in agreement with a stronger GR recruitment to the Pik3r1 GRE under DEX treatment (Fig. 1c). We next examined which histone acetyltransferase is recruited to the Pik3r1 GRE using ChIP. We found that p300, but not Tip60 and GCN5 was significantly recruited to the GRE upon DEX treatment (Fig. 1d). These results suggested that p300 accounted for the higher histone acetylation status at the GRE upon DEX treatment. Notably, neither p300, Tip60, nor GCN5 were recruited to the GRE upon PBS treatment (Fig. 1d). These results suggest that histone acetyltransferase(s) other than these 3 are involved in the acetylation of the Pik3r1 GRE in PBS treated mice.

To test whether p300 is involved in GR activated Pik3r1 gene transcription, C2C12 myoblasts were infected with lentivirus expressing scramble small hairpin RNA (sh-scrRNA, control) or shRNA against p300 (sh-p300). After puromycin selection, cells were differentiated into myotubes, then treated with DEX or equal amounts of EtOH for 6 hr. RNA was isolated from these cells and qPCR was performed to monitor the expression of Pik3r1. In sh-scrRNA expressing C2C12 myotubes, DEX treatment increased the expression of Pik3r1 approximately 3 fold (Fig. 1e). However, in sh-p300 expressing C2C12 myotubes, such DEX effect was abolished (Fig. 1e). Western blot showed that p300 was efficiently reduced by RNAi (Fig. 1e).

The ability of DEX to suppress insulin signaling was attenuated in gastrocnemius muscle of MKO mice

We generated striated muscle specific Pik3r1 knockout mice (MKO) by crossing Pik3r1$^{flox/flox}$ mice with transgenic mice carrying muscle creatine kinase promoter driving the expression of Cre recombinase[247]. In MKO mice, Pik3r1 expression was indeed depleted in skeletal muscles, including gastrocnemius muscle, tibialis anterior muscle, and soleus muscle (Fig. 2a). Notably, Pik3r1 expression was similar in the liver of WT and MKO mice (Fig. 2a). These results validated the specific deletion of Pik3r1 in the striated muscle. We also tested the ability of DEX to induce the expression of GR primary target gene in gastrocnemius muscle of WT and MKO mice. WT and MKO mice were treated with or without DEX for 7 days. Gastrocnemius muscle RNA was isolated and qPCR was performed to examine the DEX induction of Fkbp5[248] and Sesn1[233]. DEX treatment increased approximately 3 fold of expression of Sesn1 in WT mice. In MKO mice, similar DEX response was observed (Fig. 2b). DEX treatment elevated the expression of Fkbp5 approximately 5 fold in WT mice (Fig. 2b). The basal Fkbp5 expression was lower in MKO mice, though not statistically significant (p=0.11). DEX treatment also efficiently increased Fkbp5 expression in MKO mice (Fig. 2b). These results indicated that depleting Pik3r1 expression did not affect general GR activity in gastrocnemius muscle.

WT and MKO mice treated with or without DEX for 7 days were injected with insulin for 10 min. Gastrocnemius muscle, liver, and epididymal white adipose tissue were isolated and the activity of a key molecule in insulin signaling, Akt, was monitored. For Akt activity, we monitored the levels of phosphorylated Akt (pAkt) at serine 473 residue[249] and total Akt. The activity of Akt was represented by the ratio of pAkt and Akt. Insulin treatment elevated pAkt/Akt ratio in gastrocnemius muscle, liver, and epididymal white adipose tissue of WT mice (Fig. 2b). In MKO mice, insulin treatment significantly increased pAkt/Akt ratio in gastrocnemius muscle, liver and epididymal white adipose tissue (Fig. 3a). We found that DEX treatment reduced Akt activity in all three tissues of WT mice (Fig. 3a). In epididymal white adipose tissue and liver of MKO mice, DEX treatment was still able to inhibit Akt activity (Fig. 3a). However, in gastrocnemius muscle, the ability of DEX to reduce insulin stimulated Akt activity was significantly attenuated (Fig. 3a). These results demonstrate that Pik3r1 deficiency in striated muscle reduced the DEX effect on insulin action in gastrocnemius muscle but not in other insulin responsive metabolic tissues, such as epididymal white adipose tissue and liver.

DEX-induced glucose and insulin intolerance were improved in MKO mice

To examine whether Pik3r1 deletion in striated muscle affects the ability of DEX to modulate insulin sensitivity, WT and MKO mice were treated with or without DEX for 1 week. After 16 hours fasting, intraperitoneal glucose tolerance test (IPGTT) was performed in these mice. In WT mice, DEX treatment caused glucose intolerance and hyperinsulinemia. (Fig. 3b and c). In contrast, in MKO mice, although DEX treatment still caused hyperinsulinemia (Fig. 2d), DEX induced glucose tolerance was significantly improved (Fig. 2d). We also performed insulin tolerance test (ITT) in WT and MKO mice treated with or without DEX for 1 week. We found that DEX treatment resulted in insulin intolerance in WT mice (Fig. 3d). In MKO mice, DEX treatment still caused insulin intolerance, but to with a lesser degree (Fig. 3d). Thus, DEX effect on insulin tolerance was somewhat reduced in MKO mice (Fig. 3d). Without DEX treatment, MKO and WT mice had similar glucose and insulin tolerance and plasma insulin levels were similar (Fig. 3b-d). These results agree with the previous report[244]. Overall, our results demonstrate that Pik3r1 depletion in striated muscle attenuates the DEX treatment-induced glucose and insulin intolerance.

Proteome dynamics of WT and MKO mice gastrocnemius muscle treated with DEX

To determine how Dex treatment in WT and MKO mice leads to muscle atrophy, muscle proteome wide fractional synthesis rates were measured by LC-MS/MS after ^2H_2O labeling[41,43,44,45]. Mice were administered DEX or PBS for 10 days followed by ^2H_2O labeling in drinking water for the last 7 days. GA protein fractional synthesis criteria for each group ($n \leq 3$) filtered the data set to 57 proteins common among each group. Detailed filtering criteria was further explained in the method section[41]. DAVID ontology analysis was employed to characterize the biochemical function and cellular localization for the proteomics data set. The proteins were grouped as either glucose metabolism (n=16), mitochondrial (n=16), cytoplasmic (n=20) and myofibril proteins, (n=5) of which, 19 individual proteins were significantly decreased by DEX after Bonferroni correction for multiple comparisons. (Supporting Information 1). Global average gastrocnemius muscle protein fraction synthesis rates are shown in WT and MKO mice gastrocnemius muscle treated with or without or DEX (represented as WT, WT+DEX, MKO and MKO+DEX, respectively, Fig. 4a). The mean gastrocnemius protein fraction synthesis values were 18.0%, 13.5%, 15.2%, and 12.9% for WT, WT+DEX, MKO and MKO+DEX mice, respectively. The overall protein synthesis rate in MKO mouse gastrocnemius muscle was significantly lower than that of WT mouse gastrocnemius muscle (15.5% reduction (15.2%/18.0%), $p \leq 0.0001$). DEX significantly reduced protein synthesis in both WT and MKO mice. However, in WT mouse gastrocnemius muscle, the overall protein synthesis rate was decreased by an average of 25.1% (13.5%/18.0%), whereas in MKO mouse gastrocnemius muscle, the overall protein synthesis rate was reduced by only 15.1% (12.9%/15.2%) with DEX treatment. The relative reduction in the change in gastrocnemius muscle individual protein fractional synthesis rates were also compared among groups. Experimental fractional synthesis (f) values for the proteins common among each model were plotted in dot plot and sorted from low to high, and then by protein (Fig. 4b). Graphically, in WT+DEX (red line), MKO (green line) and MKO+DEX mice (purple line), most proteins exhibited a decrease in fractional synthesis as compared to WT (blue line). We then compared the percent change in each protein's fractional synthesis for WT animals treated with or without DEX (Fig. 4c). Statistical significance was assessed by a binomial distribution of the proportion of proteins showing a negative or positive percent change in fractional synthesis with DEX treatment (Fig. 4c). In WT+DEX, 96.5% or 55/57 proteins showed lower fractional synthesis rates as compared to WT mice (Fig. 4c). Only two proteins, electron transfer flavoprotein subunit beta and peroxiredoxin-1, did not have lower fractional synthesis by DEX treatment (Supporting Information 1). Surprisingly, in MKO animals, 48/57 or 84.2% of gastrocnemius muscle proteins showed lower fractional synthesis compared to WT mice (Fig. 4c). In addition, 48/57 or 84.2% of proteins in MKO mice were reduced by DEX treatment. Thus, 7 proteins whose protein synthesis rates were reduced in WT mice by DEX were not affected by DEX in MKO mouse gastrocnemius muscle, whereas two proteins, alpha-enolase and phosphoglycerate kinase-1, had a higher protein synthesis rate (17% and 9.4%, respectively) in MKO mice treated with DEX (Supporting Information 2). Finally, 37/57 or 64.9% of GA proteins had lower fractional synthesis in WT+DEX mice compared to MKO+DEX mice, while 35.1% had higher fractional synthesis (p=0.016). Overall, these results indicated that DEX effect on lowering protein synthesis was compromised without Pik3r1 in gastrocnemius muscle.

DEX-induced gastrocnemius muscle atrophy was attenuated in MKO mice

We also performed histological analysis (Fig. 5a) to monitor the cross-section area and fiber count of gastrocnemius muscle of WT, MKO, WT+DEX and MKO+DEX mice, asking whether DEX induced muscle atrophy is compromised in MKO mice. Cross sectional area of gastrocnemius muscle fibers significantly decreased from a mean of 2277 um^2 in WT animals to 1382 um^2 in

WT+DEX mice (Fig. 5b). In MKO mice, cross sectional area of gastrocnemius muscle fibers was 1709 um^2 (Fig. 5b). This is in agreement with the lower protein synthesis rates in MKO gastrocnemius muscle shown above. Importantly, there was no reduction in cross sectional area of gastrocnemius muscle fibers in MKO+DEX mice (1979 um^2) compared to MKO mice. Gastrocnemius muscle fiber count showed similar results. DEX treatment increased fiber count in WT gastrocnemius muscle and MKO had higher fiber count than WT mice, but DEX did not alter fiber count in MKO mice (Fig. 5c).

Immunohistochemical staining was used to analyze the fiber types of gastrocnemius muscle of WT and MKO mice. The antibodies against MHC I, MHC IIa, MHC IIb and MHC IIx were used. MHC I is encoded by Myh7 and represents slow oxidative fibers whereas MHC IIa is encoded by Myh2 and represents fast oxidative fibers[250]. MHC IIb is encoded by Myh4 and MHC IIx is encoded by Myh1 and represent fast glycolytic fibers IIb and IIx, respectively[250]. The fiber type composition of gastrocnemius muscle of WT mice was similar to previous reports (Fig. 5d)[251]. It appears that gastrocnemius muscle of MKO mice had more fast oxidative fibers, as MHC IIa levels were higher than those of WT mice (Fig. 5d).

DEX effect on signaling pathways regulating protein synthesis

We further analyzed the DEX effect on signaling processes that regulate protein synthesis. As described above, WT and MKO mice were treated with or without DEX and were injected with insulin for 10 min before gastrocnemius muscle was isolated. We first monitored the phosphorylation at threonine 389 of p70S6 kinase (S6K)[252], which is critical for S6K activity, using ELISA. S6K phosphorylates the S6 protein of the 40S ribosomal subunit and is involved in translational control of 5' oligopyrimidine tract mRNAs[252]. We found that insulin treatment increased the levels of Thr389 of S6K in WT mice (Fig. 6a). DEX treatment abolished this insulin induction (Fig. 6a). Interestingly, in MKO mice, neither insulin nor DEX affected S6K Thr389 phosphorylation (Fig. 6a).

Next, we monitored the phosphorylation of threonine 37 and 46 of 4E-BP1[253]. 4E-BP1 is a translational repressor that inhibits cap-dependent translation by binding to the translation initiation factor eIF4E[254]. Phosphorylation at Thr37 and Thr46 is required for subsequent phosphorylation at serine 65 and threonine 70, which are critical for 4E-BP1 function[253,255]. We found that insulin induced 4EBP1 phosphorylation in WT mice whereas DEX treatment abolished such effect (Fig. 6b). Interestingly, the basal levels of 4E-BP1 phosphorylation were lower in MKO mice (Fig. 6b). DEX treatment reduced such insulin effect (Fig. 6b). However, unlike in WT mice, DEX treatment did not abolish insulin effect. Thus, without Pik3r1, some degree of the insulin effect on 4E-BP1is restored (Fig. 6b).

Finally, we monitored the phosphorylation at serine 52 of translational initiator eIF2α. eIF2 consists of three subunits, eIF2α, eIF2β, and eIF2γ, that promotes a new round of translation initiation by exchanging GDP for GTP, which is catalyzed by eIF2B[256,257]. The phosphorylation of eIF2α stabilizes the eIF2-GDP-eIF2B complex that inhibits the turnover of eIF2B to attenuate the translation[256,257]. This phosphorylation is not regulated by insulin. Thus, we just compared the phosphorylation status of eIF2α in WT and MKO mice treated with or without DEX. Interestingly, DEX treatment elevated eIF2α phosphorylation in WT but not MKO mice (Fig. 6c). The basal eIF2α phosphorylation was similar between MKO and WT mice (Fig. 6c). However, in contrast to the DEX effect in WT mice, DEX treatment did not affect eIF2α phosphorylation in MKO mice (Fig. 6c).

In summary, there are three major observations from these results. First, in gastrocnemius muscle, DEX inhibited insulin induced p70S6K and 4E-BP1 activity. Moreover, DEX treatment increases eIF2α phosphorylation. All these responses could contribute to the suppression of protein synthesis. Second, without Pik3r1, the basal 4E-BP1 phosphorylation was decreased. This phenomenon could contribute to the lower protein synthesis rate in gastrocnemius muscle of MKO mice. Third, without Pik3r1, the ability of DEX to suppress insulin's effect on 4E-BP1 was impaired and DEX was unable to potentiate eIF2α phosphorylation. These results could explain the partial maintenance of protein synthesis rates in gastrocnemius muscle of MKO mice.

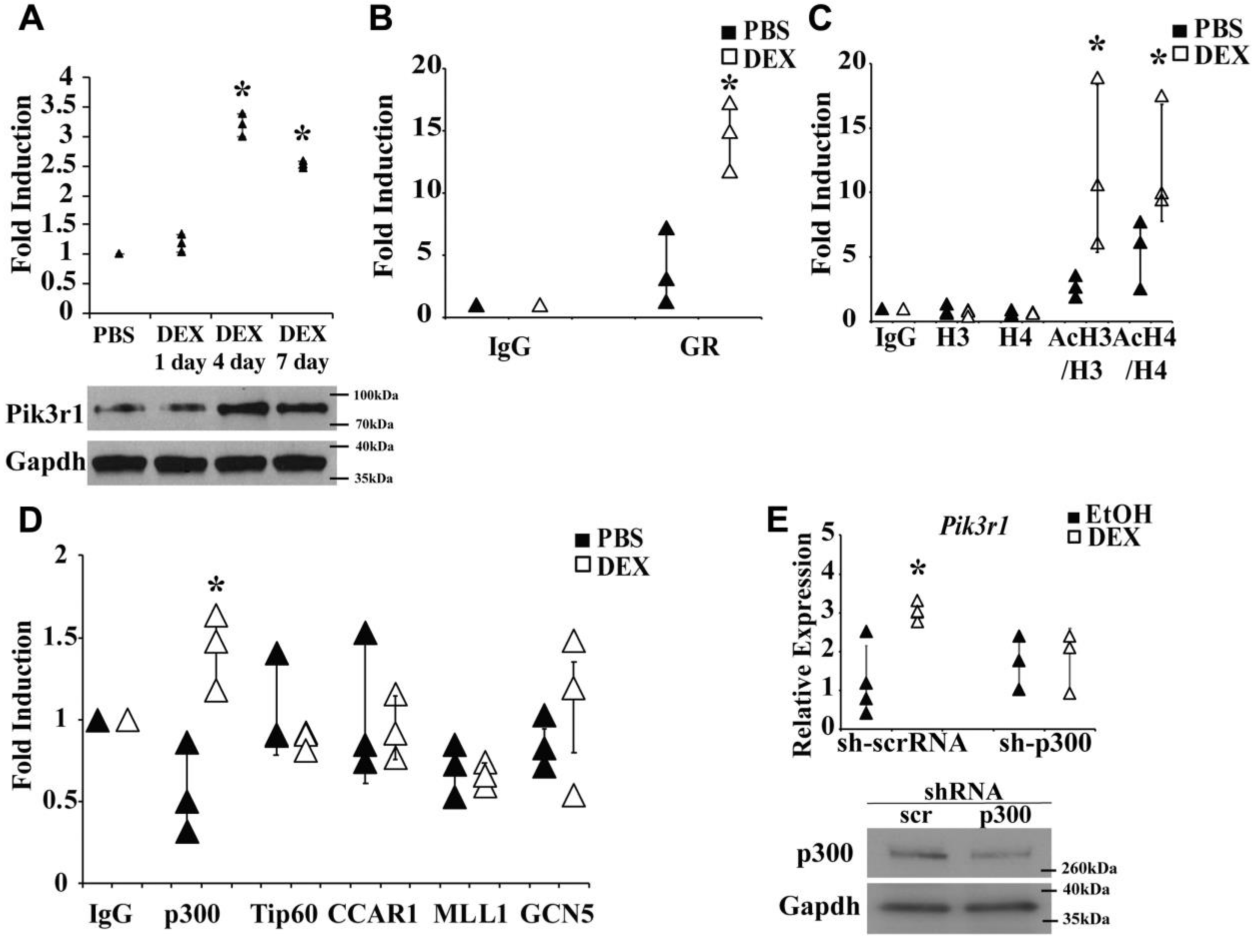

Figure 1: DEX induces Pik3r1 expression in skeletal muscle in vivo and P300 mediates the transactivation of Pik3r1 in skeletal muscle male 8-week-old WT mice were treated with PBS or 5 mg/kg of daily dexamethasone (DEX) through IP injection for 1, 4, 7 days. The Pik3r1 expression was examined by immunoblot in (A) gastrocnemius muscle and normalized to internal control Gapdh. Representative immunoblots are shown (n = 3). Error bars represent the SD of relative Pik3r1 expression level (DEX versus PBS), and $*p < 0.05$ male 8-week-old Pik3r1 Flox (WT) mice were treated with 5 mg/kg of DEX for 4 days. Then, their GA muscles were collected.

ChIP experiments were performed on these GA muscles to study the recruitment of glucocorticoid receptor (GR) (B), the histone modification (C), and the recruitment of transcription cofactor p300, Tip60, CCAR1, MLL1, and CGN5 (D) on glucocorticoid response element of Pik3r1. Primer flanking the Pik3r1 glucocorticoid response element and Rpl19 (internal control) were used in qPCR. Error bars represent the SD of relative fold enrichment compared to IgG control from three independent experiments and $*p < 0.05$. E, C2C12 myoblasts were infected with lentivirus particles expressing scramble sh-RNA (sh-scrRNA, control) or sh-p300. After puromycin selection, cells were differentiated into myotubes and were then treated with 1 μM DEX or EtOH for 6 h. QPCR was performed to monitor the expression of Pik3r1 and Western blot was shown to confirm the knockdown of p300. Error bars represent the SD of fold induction of Pik3r1. $*p < 0.05$.

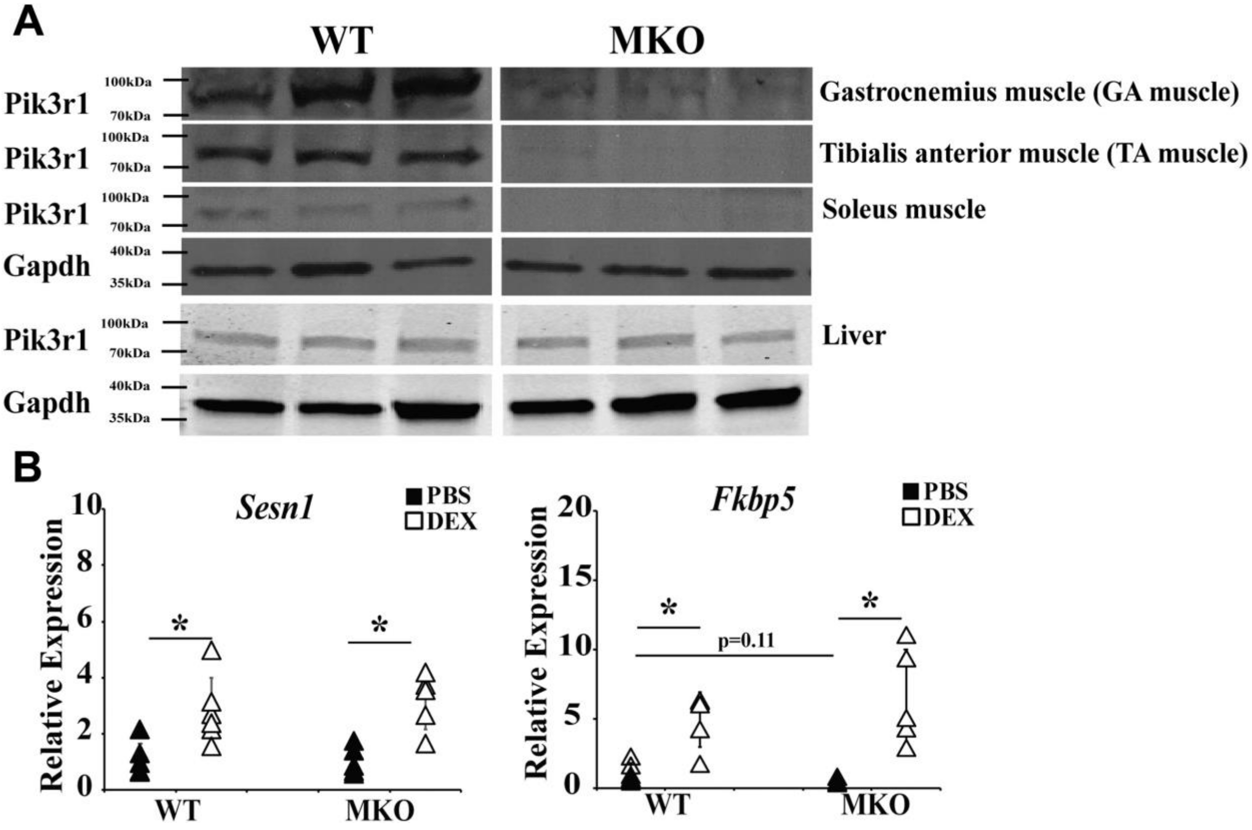

Figure 2: GC-induced gene expression in MKO mice. Muscle specific Pik3r1 knockout (MKO) mice were generated. A, the expression of Pik3r1 in gastrocnemius (GA) muscle, tibialis anterior (TA) muscle, and soleus muscle of WT and MKO was examined by immunoblots and normalized to internal control Gapdh. Representative immunoblots are shown (n = 3). B, the expression of Sesn1 and Fkbp5 was evaluated in WT and MKO mouse gastrocnemius muscle treated with PBS or DEX (10 mg/kg bodyweight) in drinking water for 1 week. Error bars represent SD, n = 5 to 6 and $*p \leq 0.05$. DEX, dexamethasone.

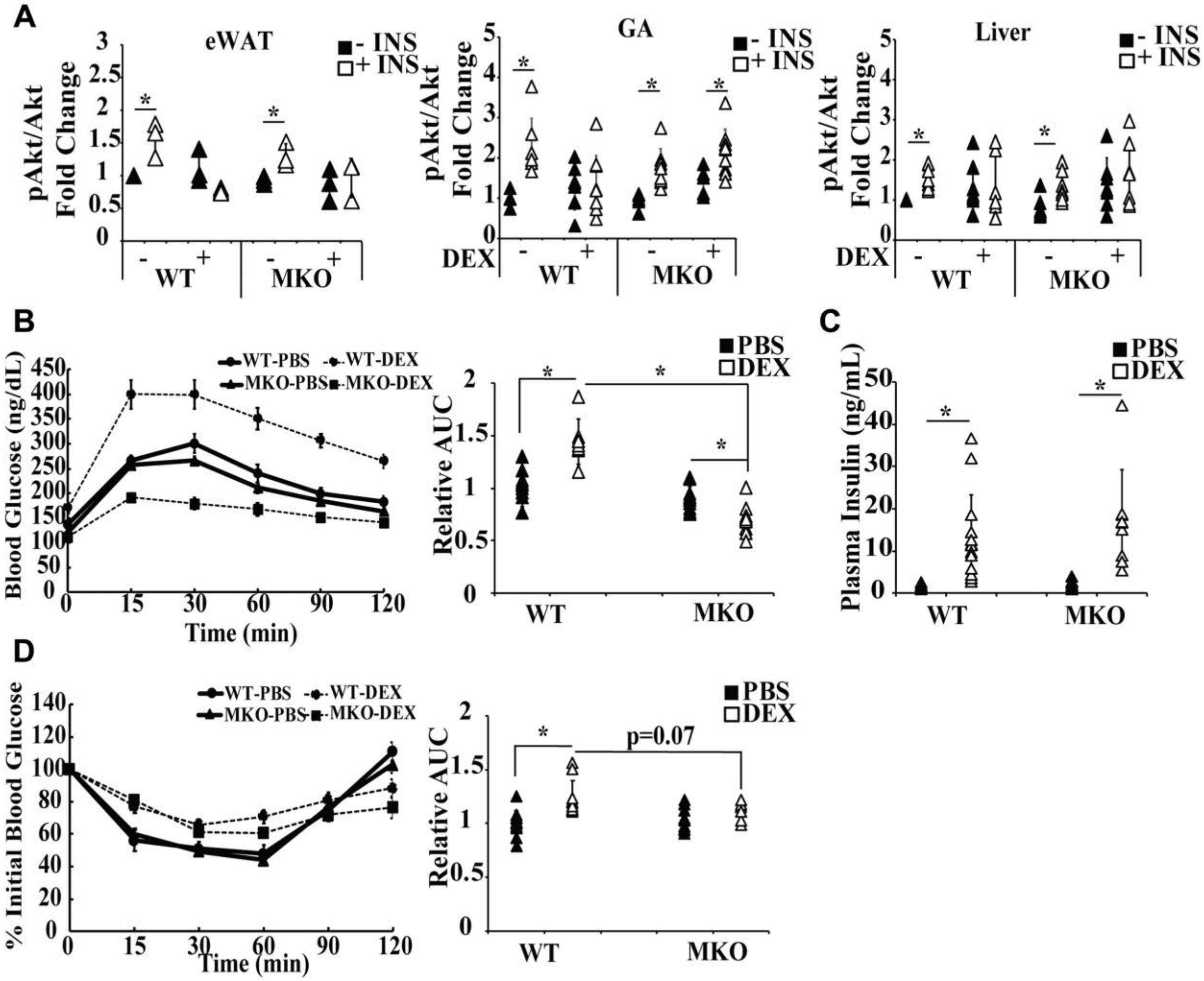

Figure 3: GC-induced glucose intolerance is compromised in MKO mice. A, male 8-week-old WT and MKO mice were treated with 10 mg/kg of PBS or DEX in drinking water for 1 week. On the last day, mice were injected intraperitoneally with insulin (1 unit/body weight) for 10 min, and then various tissues were collected. ELISA kits were used to monitor the level of Akt and phosphor-Akt in eWAT, liver, and GA muscle. The results are presented as relative pAkt/AKt level. Error bars represent the SD, n = 3 to 9 and $*p \leq 0.05$ comparing no insulin treatment to insulin treatment. B, male 8-week-old WT mice and MKO mice were treated with 10 mg/kg of DEX for 7 days. On the last day, mice were fasted for 15 h, and the IPGTT was performed. Relative area under curve (AUC) for IPGTT results (relative to PBS-treated WT mice). Error bars represent the SD, n = 6–12 and $*p \leq 0.05$. C, plasma insulin level was measured before glucose injection (0 min time point). Error bars represent the SD, n = 6 to 12 and $*p \leq 0.05$. D, ITT was performed in mice as described in Methods. ITT results were depicted as percentage of initial plasma glucose level (the plasma glucose level before insulin injection). Error bars represent the SD, n = 3 to 7. Relative area under curve (AUC) for ITT results (relative to PBS-treated WT mice) is shown. Error bars represent the SD, n = 6 to 11 and $*p \leq 0.05$. DEX, dexamethasone; IPGTT, intraperitoneal glucose tolerance test; ITT, insulin tolerance test.

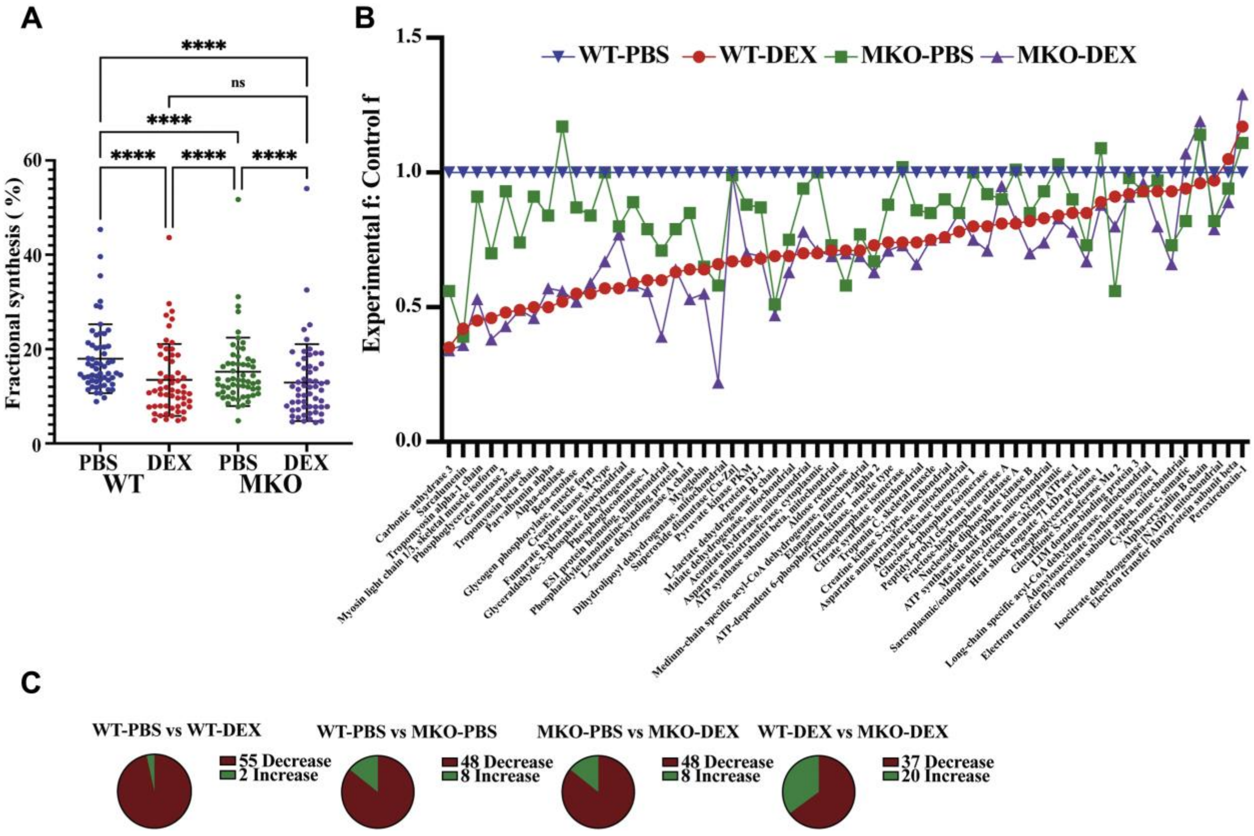

Figure 4: Proteome dynamics of WT and MKO mice gastrocnemius muscle treated with DEX. male 8-week-old WT and MKO mice were treated with 10 mg/kg of PBS or DEX in drinking water for 10 days. Heavy water labeling was conducted in final 7 days. To determine the difference in protein fractional synthesis rates (f), four groups were categorized as the following: wildtype controls treated with PBS (WT-PBS, n = 6), wildtype treated with DEX (WT-DEX, n = 6), MKO treated with PBS (MKO-PBS, n = 5), and MKO treated with DEX (MKO-DEX, n = 5). A, average gastrocnemius protein fraction synthesis in WT and MKO animals treated with DEX ($n \geq 3$). Bar graph displays the mean fractional synthesis ±SD for 57 proteins common among each group. The average fractional synthesis values were 18.0%, 13.5%, 15.2%, and 12.9% for WT-PBS, WT-DEX, MKO-PBS, and MKO-DEX treated mice, respectively. The difference in the average protein fractional synthesis were assessed by ANOVA followed by Benjamini and Hochberg test for multiple comparisons (FDR = 0.05) using Prism V8.0. The percent change of the DEX effect on lowering gastrocnemius muscle protein synthesis in WT-PBS versus WT-DEX was −28.1% but was reduced to −17.9% in the MKO-PBS versus MKO-DEX. This effect remained significant ($p < 0.04$, Student t test with Welch's correction). The values for MKO-PBS were significantly lower than for WT-PBS (15.5% reduced [15.2%/18.0%], $p \leq 0.0001$). $****p \leq 0.0001$. B, relative comparison in the degree change of individual gastrocnemius muscle protein fractional synthesis. Experimental f: control f ratio for 57 proteins common among each model. The symbols donate a given protein and each group are highlighted by color. For clarity, the proteins are sorted from greatest to least reduction of f in WT-DEX relative to WT-PBS. C, Parts of the whole comparison of the percent change in gastrocnemius protein fractional synthesis compared across each group for the 57 common proteins identified. An increase or decrease in f for each protein was determined. A binomial distribution statistic was used to calculate the

significance of the number of gastrocnemius muscle proteins with either higher or lower mean fractional synthesis values. 55/57 ($p \leq 0.0001$), 48/56 ($p \leq 0.0001$), 48/56 ($p \leq 0.0001$) and 37/57 ($p = 0.016$) gastrocnemius muscle proteins were lower in WT-PBS versus WT-DEX, WT-PBS versus MKO-PBS, MKO-PBS versus MKO-DEX, and WT-DEX versus MKO-DEX, respectively. DEX, dexamethasone.

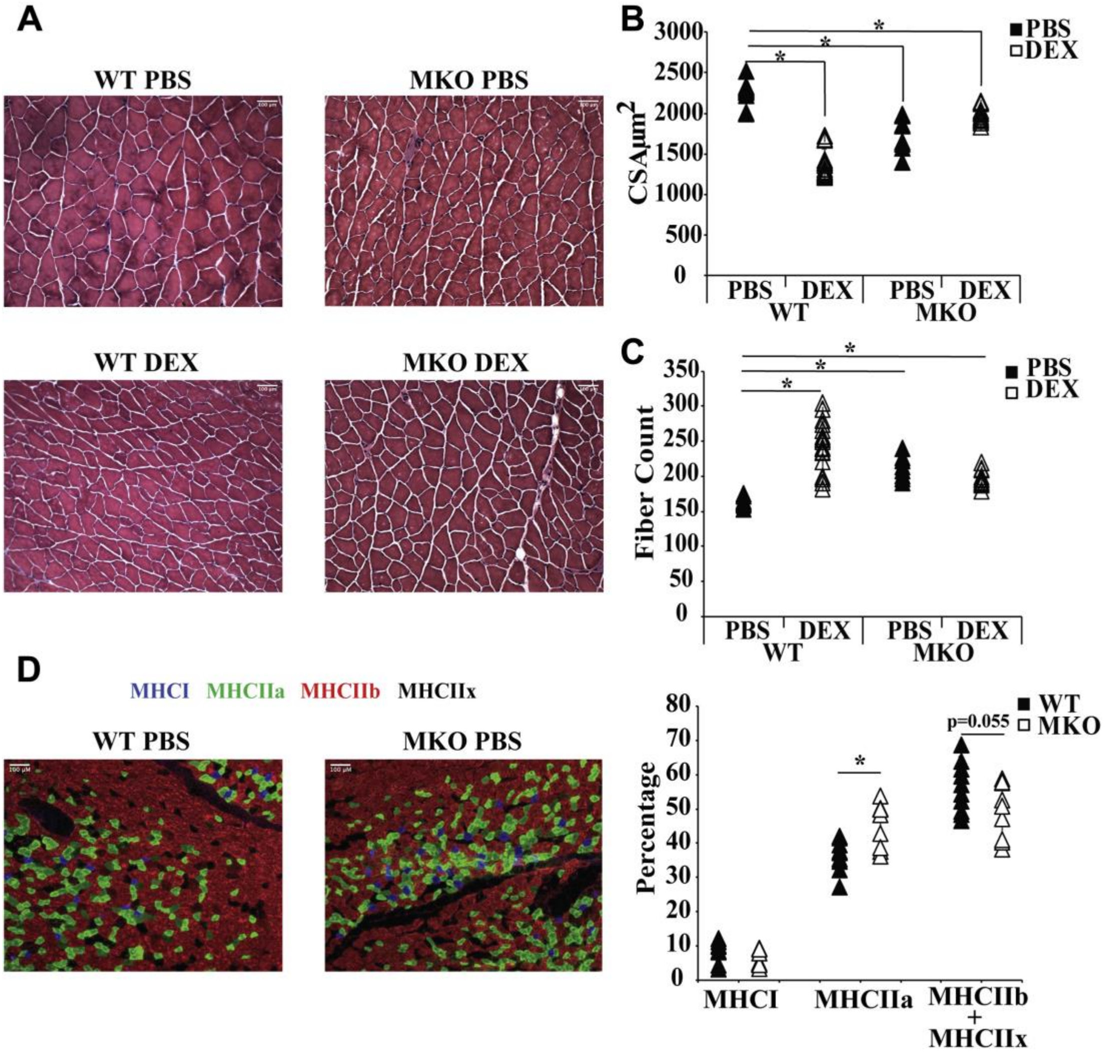

Figure 5: Analysis of cross-sectional area and fiber number and immunochemistry of gastrocnemius muscle of WT and MKO mice. A, hematoxylin and eosin staining of gastrocnemius muscle of following mice treated with PBS or DEX for 10 days: WT PBS (n = 5), WT DEX (n = 5), MKO PBS (n = 3), and MKO DEX (n = 4). Bar is 100 µm. B, cross sectional area and C, fiber count were quantified with image J. Statistical differences calculated with an unpaired Student t test as compared with only the WT-PBS animals (n = 5). Error Bars represent SD, significance was denoted as $*p \leq 0.05$. D, immunohistochemical staining was performed on gastrocnemius muscle of WT PBS and MKO PBS mice using antibodies of MHCI, MHCIIa, MHCIIb, and MHCIIx. All fibers in each picture were counted and then calculated the percentage of each fiber type in the total number of fibers. For WT PBS, 12 pictures were counted whereas for MKO PBS 10 pictures were counted. Bar is 100 µm. Error bars represent SD, significance denoted as $*p \leq 0.05$. DEX, dexamethasone.

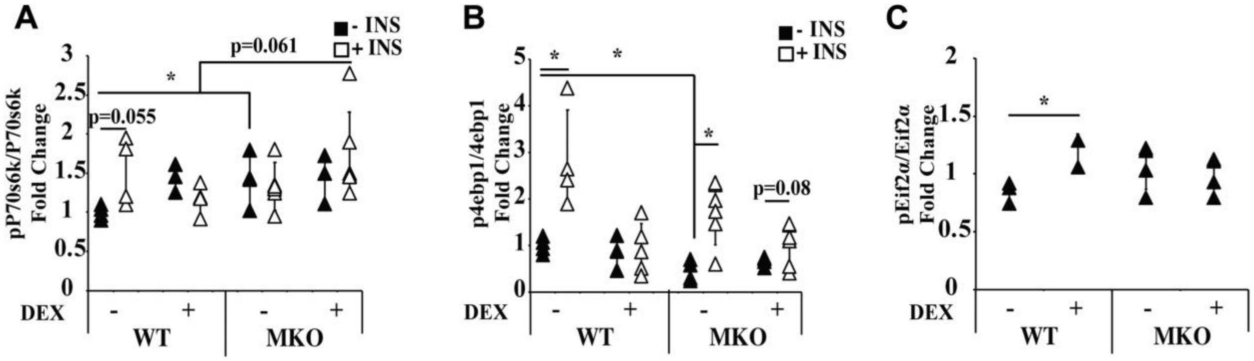

Figure 6: Comparing signaling pathways that regulate protein synthesis in gastrocnemius muscle of WT and MKO mice. WT and MKO mice were treated with or without DEX (10 mg/kg body weight) for 1 week. At the end of treatment, mice were IP injected with insulin (1 unit per kg body weight) or PBS for 10 min, and gastrocnemius muscle was isolated and processed for ELISA to monitor the phosphorylation status of (A) p70S6K at Thr389, (B) 4E-BP1 at Thr37/Ser46 and (C) eIF2α at Ser52. n = 3 to 6, significance was denoted as $*p \leq 0.05$. Error bars represent the SD. DEX, dexamethasone.

7.4. Discussion

Glucocorticoids modulate protein and glucose metabolism through suppressing insulin signaling in skeletal muscle[228,229]. The mechanisms governing this process, however, are not completely understood. GR is a transcription factor and its primary target genes initiate the physiological responses of glucocorticoids. We previously identified Pik3r1 as a GR primary target gene that mediates glucocorticoid responses in murine C2C12 myotubes. In this study, we further demonstrated that the Pik3r1 gene is activated by GR in mouse gastrocnemius muscle, because GR was recruited to the Pik3r1 GRE and the levels of histone acetylation were elevated upon DEX treatment. GR was also recruited to the Pik3r1 GRE and there were significant levels of acetylated H3, and H4 at the Pik3r1 GRE in PBS treated mice. These results suggest that physiological corticosterone levels at the time we performed ChIP contribute the basal expression of Pik3r1 in mouse gastrocnemius muscle. As plasma corticosterone levels are modulated by circadian rhythm, we predict that the degree of GR recruitment to the Pik3r1 GRE could vary depending on the time we conduct ChIP experiments. Notably, even during the refeeding stage when plasma corticosterone levels are low, GR is recruited to certain GREs[258]. However, such recruitment is usually much weaker than times of high plasma corticosterone levels, such as fasting[258].

While Pik3r1 serves as a regulatory subunit for PI3K, a key signaling molecule in insulin signaling, previous studies have shown that overexpression of Pik3r1 reduces whereas depletion of Pik3r1 enhances insulin action in metabolic tissues, such as skeletal muscle, white adipose tissue, and liver[237,238,239,240,259]. Human genomic studies have associated Pik3r1 to insulin resistance[260,261,262]. In this study we further demonstrated the role of Pik3r1 in glucocorticoid-induced glucose and insulin intolerance in vivo. We found that depletion of Pik3r1 in gastrocnemius muscle compromised the ability of glucocorticoids to suppress insulin signaling in gastrocnemius muscle but not in two other insulin responsive metabolic tissues, epididymal white adipose tissue and liver. This likely results in improved glucose and insulin intolerance in Dex treated MKO mice.

Using the combination of stable isotope labeling and LC/MS-MS technology, we were able to further investigate DEX effects on gastrocnemius muscle in vivo protein turnover[41] and the role of Pik3r1 in this process. Not surprisingly, DEX treatment significantly reduced the overall protein synthesis rate[263]. Intriguingly, among 57 proteins with kinetics quantified by LC/MS-MS in all 4 groups, 55 had lower protein synthesis rate with DEX treatment. Ontology analysis showed that these 55 proteins contained enzymes in the glycolysis and TCA cycle, as well as mitochondrial and myofibrillar proteins. The protein synthesis rate suppression by DEX treatment was significantly attenuated upon the depletion of Pik3r1. Not surprisingly, the DEX suppressed protein synthesis rate was not entirely abolished by the depletion of Pik3r1, as other GR primary target genes, such as MuRF1 (a.k.a. Trim63) and Ddit4, are known to play a role in this process[263,264]. The results from gastrocnemius skeletal muscle cross-section area and fiber counts are consistent with and complement the protein synthesis data, revealing decreased myotube diameters in DEX treated WT and in MKO mice, but no further reduction by DEX treatment in MKO mice.

Our study was not designed to investigate the effects of glucocorticoids on protein degradation. Measurement of protein breakdown by in vivo metabolic labeling is best determined by analyzing replacement (turnover) rates at steady-state, where synthesis is balanced by breakdown so high turnover rates and a lower protein pool size can be taken to reflect stimulated breakdown, even in the presence of reduced absolute synthesis rates[41,265]. Our studies here were carried out during the early phase of decreasing skeletal muscle mass after DEX treatment, not during steady state, so it is problematic to infer breakdown rates. Accordingly, our findings document globally lower protein synthesis rates during the 10 days after initiation of DEX treatment but do not rule out a contribution from higher protein breakdown rates as well[228,263,266,267,268,269].

One surprising result is that the basal protein synthesis rate in MKO mice gastrocnemius muscle was significantly lower than that of WT mice. Thus, Pik3r1 appears to play a role in basal protein synthesis that is in addition to its role in glucocorticoid action. Our signaling studies found that the basal phosphorylation of 4E-BP1 was lower in gastrocnemius muscle of MKO mice than in WT mice. This observation might explain, at least in part, a lower protein synthesis rate in gastrocnemius muscle of MKO mice. Gastrocnemius muscle of MKO mice also contained high percentages of fast oxidative fibers, which could be the reason for smaller fiber sizes of gastrocnemius muscle in MKO mice. Notably, in gastrocnemius muscle of MKO mice, insulin failed to enhance p70S6K. However, we do not think that this contributes to a lower protein synthesis rate in MKO mice, as pp70S6K/p70S6K ratio was similar between WT and MKO mice that were treated with insulin. It is not surprising that DEX treatment inhibited insulin induced p70S6K phosphorylation in WT mice. However, it is unclear why p70S6K was not induced by insulin in MKO mice, whereas its upstream kinase Akt was stimulated by insulin in MKO mice. More detailed studies are needed to explain this observation.

The regulation of 4E-BP1 by insulin and DEX was somewhat similar to their regulation of its upstream kinase, Akt, in MKO mice (Fig. 2c). Thus, in Pik3r1 depleted gastrocnemius muscle, the ability of DEX to suppress insulin increased 4E-BP1 phosphorylation was decreased. We also found that DEX treatment increased eIF2α phosphorylation in WT mice gastrocnemius muscle, which agreed with a reduced protein synthesis rate. This DEX effect was not observed in MKO mice. These results could explain a partially restored protein synthesis rate in gastrocnemius muscle of MKO mice. Interestingly, the induction of eIF2α phosphorylation by DEX was not found in previous studies[270,271]. In one report, eIF2α phosphorylation was analyzed in gastrocnemius muscle of male Sprague-Dawley rats were IP injected with DEX for 4 hours[270]. In another report eIF2α phosphorylation was examined in biopsies that were conducted in young health male volunteers taking oral DEX every 6 hours for 3 days[271]. In addition to species difference, our treatment conditions were distinct to theirs, as we treated mice with DEX for 1 week. It is possible that a longer DEX exposure results in the activation of eIF2α kinase(s), such as PKR, PERK, GCN2, and/or HRI[272,273]. This notion will need to be tested in future.

The role of Pik3r1 in DEX effects on eIF2α phosphorylation, basal 4E-BP1 phosphorylation and maintaining proper proportions of fast oxidative fibers in gastrocnemius muscle are likely independent of its function in insulin actions. Pik3r1 has been shown to participate in cellular functions that are independent of its role in insulin action. For example, Pik3r1 is involved in glucocorticoid-induced lipolysis in adipose tissue by increasing PKA signaling in the lipid droplet[274]. Moreover, Pik3r1 has been shown to participate in trafficking of receptor tyrosine kinases and the erythropoietin receptor[275,276], and is required for the nuclear localization of XBP1[260,277]. How Pik3r1 acts in basal, and DEX reduced protein synthesis rates in skeletal muscle requires further studies.

In conclusion, we demonstrate for the first time that Pik3r1 is involved in glucocorticoid inhibition of insulin signaling and protein synthesis rate in gastrocnemius muscle in vivo. Moreover, Pik3r1 plays a role in maintaining basal protein synthesis rates and the proper proportion of fast oxidative fibers in murine gastrocnemius muscle.

7.5. Experimental Procedures

Animal Subjects

Mice with a conditional allele of Pik3r1 gene flanked with LoxP sites at exon7 (Pik3r1$^{flox/flox}$, will be referred as WT, WT, mice) were provided by the laboratory of Lewis Cantley (Weill Cornell Medical College, New York)[278]. Muscle specific Pik3r1 knockout mice (MKO) were generated by crossing Pik3r1$^{flox/flox}$ with transgenic mice expressing Cre recombinase under control of muscle creatine kinase (B6.FVB(129S4)-Tg(Ckmm-cre)5Khn/J)[247]. The following primers were used for genotyping: Pik3r1_loxP_F (CACCGAGCACTGGAGCACTG), Pik3r1_loxP_R (CCAGTTACTTTCAAATCAGCACAG), AdipoQ_Cre_F (GCGGTCTGGCAGTAAAAACTATC), AdipoQ_Cre_R (GTGAAACAGCATTGCTGTCACTT), Ckmm_Cre_F (TAAGTCTGAACCCGGTCTGC), Ckmm_Cre_R (GTGAAACAGCATTGCTGTCACTT). In AKO mice, ~310 bps amplified by Pik3r1_loxP_F and Pik3r1_loxP_R primers and ~100 bps amplified by AdipoQ_Cre_F and AdipoQ_Cre_R primers were observed. In MKO mice, ~310 bps amplified by Pik3r1_loxP_F and Pik3r1_loxP_R primers and ~500 bps amplified by Ckmm_Cre_F and Ckmm_Cre_R primers were observed. In Pik3r1$^{flox/flox}$ (WT) mice only ~310 bps amplified by Pik3r1_loxP_F and Pik3r1_loxP_R primers were observed. Eight-week old male MKO and WT mice were injected intraperitoneally with 5 or 10 mg/kg body weight of DEXamethasone (DEX, water soluble DEXamethasone, Sigma D2915) or PBS (control) for 1, 4 or 7 days. At the end of the treatment period, blood, inguinal and epididymal adipose tissues, liver and gastrocnemius muscle were isolated from mice for protein expression analysis. Mice were housed in ventilated cages with Sanichip bedding along with a cotton Nestlet and a 4gm puck of crinkled paper. They were co-housed and were fed a diet of 18% protein, 6% fat (Envigo 2918) with a 12 hour light and dark cycle in a temperature controlled room of approximately 22°C. The Office of Laboratory Animal Care at the University of California, Berkeley (AUP-2014-08-6617) approved all animal experiments conducted in this work.

Western Blot

The protein concentration for samples were measured with Bradford protein dye (BioRad). Proteins (~ 30 ug) were mixed with 1X NuPAGE LDS Sample Buffer (ThermoFisher, Waltham, MA NP0007) and 1X NuPAGE Sample Reducing Agent (ThermoFisher, Waltham, MA, NP0009), boiled for 5 min before being applied to SDS-PAGE. The following antibodies we used in this study: anti-Gapdh (Santa Cruz, sc-25778), anti-Pik3r1 (Cell Signaling, 4292s). The intensity of the bands was quantified using Image J software (Rapsand NIH, 1997-2018) and normalized to Gapdh.

Chromatin Immunoprecipitation

WT mice were intraperitoneally injected with 10 mg/kg body weight of DEX (water soluble DEX, Sigma D2915) for 4 days. On the last day, gastrocnemius muscles were harvested and snap frozen with liquid nitrogen. Frozen muscles were ground to fine powder with pestle. Then, tissue powder was cross-linked with 1% formaldehyde in 20 ml PBS at 37°C for 10 min with gentle shaking. After quenching the cross-linking reaction with 125 mM glycine, samples were centrifuged at 1,000 g, 4°C for 5 min. Pellets were washed with ice-cold PBS, then resuspended in 3 ml buffer S (50 mM Tris pH 8.0, 1% SDS, 10 mM EDTA, 1mM DTT, 100 mM MG 132 and protease inhibitor cocktail). Samples were incubated on ice for 10 min, then sonicated with the Branson Sonifier 250 sonicator for 50 seconds (60% output, 10s pulse with 40s rest). After centrifugation for 10 min at 32,000 g, 4°C, supernatant containing sheared DNA fragments, was collected and mixed with one sample volume of buffer D (0.01% SDS, 1.1% Triton x-100, 1.2 mM EDTA, 16.7mM Tris [pH 8.0], 167 mM NaCl, 100 mM MG132 and a protease inhibitor cocktail). Diluted sample was then incubated with 100 ul of 50% protein A/G agarose beads (sc-2003, Santa Cruz) for 1hr at 4°C with gentle shaking to pre-clean the sample. After centrifugation at 4,000 g for 3 min at 4°C to pellet the agarose beads, supernatant was used to set up the IP reactions. The following antibodies were used in this study: anti-IgG (sc-2027, Santa Cruz), anti-GR (sc-393232, Santa Cruz), anti-H3 histone (ab1791, abcam), anti-H4 (05-858, Millipore), anti-AcH3 (ab47915, abcam), anti-AcH4 (06-866, Millipore), anti-H3K4me3 (ab8580, abcam), anti-H3K4me1 (ab8895, abcam), and anti-p300 (sc-584x, Santa Cruz). Samples were allowed to react with antibody for 18 hrs (overnight incubation) at 4°C with gentle shaking. Then, 50 ul of 50% protein A/G agarose beads were added into each IP reaction and were rotated for 2 hr at 4°C. Then, agarose beads were washed with the following conditions: 1x low-salt wash buffer (0.1% SDS, 1% Triton X-100, 2 mM EDTA, 20 mM Tris [pH 8.0] and 150 mM NaCl), 1x high-salt wash buffer (0.1% SDS, 1% Triton X-100, 2mM EDTA, 20 mM Tris [pH 8.0], and 500 m NaCl), 1x LiCl wash buffer (0.25M LiCl, 1% NP-40, 1% sodium deoxycholate, 1mM EDTA and 10 mM Tris [pH 8.0]) and 2x Tris-EDTA buffer. After the last wash, all supernatant was removed, then 400 ul of elution buffer (10 mM DTT, 1% SDS and 0.1M NaHCO3) was added. Samples were rotated at room temperature for 1hr, then centrifuged at 8,000 g for 1 min. Supernatant was transferred to a new tube and were mixed with 16 ul of 5M NaCl and were incubated at 65°C overnight. On the last day, 16 ul of Tris [pH 6.5], 8 ul of 0.5 M EDTA, and 1.5 ul of proteinase K (EO0491, Thermo Scientific) were added to the sample and were incubated at 55°C for 3hrs. The immune-precipitated DNA fragments were extracted with a PCR clean up kit (28106, Qiagen), then were applied to qPCR to quantify the IP result.

Intraperitoneal Glucose Tolerance Test (GTT)

Eight-week old male MKO and WT mice were injected intraperitoneally with 10 mg/kg body weight of DEX. After a 15 hr fast, mice were injected with 1g/kg body weight glucose for an intraperitoneal glucose tolerance test (GTT). Tail vein blood was used to monitor blood glucose levels at different time points: 0 (before glucose injection), 15, 30, 60 90, and 120 mins after glucose injection using a Blood Glucose meter (Contour, Bayer).

Insulin Tolerance Test (ITT)

Fed mice were injected with 1 unit/kg body weight insulin (Sigma, I0516-5ML) intraperitoneally. Tail vein blood was used to monitor blood glucose levels at different time points: 0 (before glucose injection), 15, 30, 60 90, and 120 mins after glucose injection using a Blood Glucose meter (Contour, Bayer).

Plasma insulin analysis

Plasma insulin levels were examined using an ultra-sensitive mouse insulin ELISA kit (Crystal Chem Inc., Cat. No: 90080).

ELISA using tissue homogenates

Mice (as described above) were treated with 10 mg/kg bodyweight of DEX (water-soluble) or PBS (control) for 7 days. After intraperitoneal injection of 1 unit/kg bodyweight insulin for 10 minutes, mice were euthanized and gastrocnemius muscle were collected. The tissue was homogenized in Cell Lysis Buffer (Cell Signaling Technology, #9803 or Multispecies InstantOne ELISA Kit Lysis Buffer (Invitrogen Catalog #85-86046-11) using the BeadBug 6 Homogenizer (Benchmark Scientific.) Homogenized lysate were centrifuged at 13,300 rpm for 15 minutes at 4°C. Supernatant was transferred into fresh tubes and used for the following ELISAs

Akt and pAkt ELISA

Relative Akt and pAkt levels were measured using the Akt (Total/Phospho) Multispecies InstantOne ELISA kit (Invitrogen, Catalog #85-86046-11.) Tissue lysate were loaded with a protein concentration of 0.5 μg/μl. All steps afterward were followed according to manufacturer’s instructions.

S6 Kinase and p70S6 Kinase ELISA

Relative S6 kinase and p70S6 levels were measured using the p70 S6 Kinase (Total/Phospho) Multispecies InstantOne ELISA Kit (Invitrogen, Catalog #85-86053-11.) Tissue lysates were loaded with a protein concentration of 1 µg/µl. All steps afterward were followed according to manufacturer's instructions.

4E-BP1 (total and phosphorylated) ELISA

Relative total 4E-BP1 and phosphorylated 4E-BP1 levels were measured using the Phospho-4E-BP1 (Thr36) and Total 4E-BP1 ELISA kit (RayBiotech, Catalog #PEL-4EBP1-T36-T.) Tissue lysates were loaded with a protein concentration of 1.25 µg/µl and 1 µg/µl. All steps afterward were followed according to manufacturer's instructions.

eIF2α and phospho-eIF2α ELISA

Relative total eIF2α and phosphorylated eIF2α levels were measured using the PathScan Phospho-eIF2α (Ser51) and total eIF2α Sandwich ELISA kits (Cell Signaling Technology, Catalog #7286 and Catalog #7952.) Tissue lysates were loaded with a protein concentration of 0.25 µg/µl.

Chemicals and reagents

All reagents were purchased or made with the highest quality experimental conditions. 1x PBS (Gibco), hyclone molecular grade water (GE healthcare), 0.5M EDTA (Gibco), 0.1M PMSF (Sigma), Halt protease inhibitor (78429, Thermo scientific), 2,2,2-triflouroethanol (TFE) (Sigma), ammonium bicarbonate (Sigma), DTT (Sigma), IAA (Sigma), trypsin (Sigma), acetonitrile (Fisher), formic acid (Fisher), deuterium oxide (Cambridge isotope labs).

^2H_2O labeling protocol

Mice were administered 99.0 % sterile deuterium oxide (^2H_2O) (Cambridge isotope laboratories) at the third day of DEX treatment via intraperitoneal injection. The animals remained on DEX and ^2H_2O for seven more days until time of sacrifice. Animals were maintained on a maintenance dose of 8.0% ^2H_2O in drinking water to maintain approximately 5.0% excess ^2H enrichment in total body water[279].

Tissue harvesting

Mice were euthanized with 2L/min flow rate of CO_2 followed by cervical dislocation. Blood was collected via cardiac puncture and was centrifuged at 12,000 g for 10 minutes to obtain plasma and stored at -20°C. GA muscle samples were flash frozen with liquid nitrogen and stored at -80°C until processing.

Histology and cross sectional fiber determination

Whole gastrocnemius muscle was carefully dissected, placed in a cryomold with an optimal cutting temperature (OCT) solution and was flash frozen in a liquid nitrogen cooled metal block. 10µm transverse muscle sections were performed using a cryotome at -20°C, followed by transfer to positively charged microscope slides for hematoxylin and eosin staining. Muscle fiber diameter was recorded using a light microscope and cross-sectional area was analyzed via Image J (Rapsand NIH, 1997-2018).

For immunohistochemistry[280,281,282], 10 µm transverse sections from the midportion of the gastrocnemius muscles were obtained. Slides were air dried for 10 mins followed by washing with phosphate buffered saline (PBS) + 0.05% Triton X for 10 min and then for 5 min. Next, sections were blocked in PBS + 0.05% Triton X (PBST) containing 10% goat serum for 1 h at room temperature and then incubated overnight at 4°C with a mixture of three primary mouse monoclonal antibodies (MYH7 (BA-F8, IgG2b), MYH2 (SC-71, IgG1), and MYH4 (BF-F3, IgM), obtained from DSHB at the University of Iowa) in PBS + 0.05% Triton X (PBST) containing 10% goat serum. Next day, slides were washed with PBS + 0.05% Triton X for 10 min and then with new PBST for 5 min. After washes in PBST, sections were incubated for one hour with a mixture of three goat anti-mouse secondary antibodies against IgG2b (Alexa 350), IgG1 (Alexa 488), and IgM (Alexa 555) in 10% GS/PBST, followed by washes with PBS + 0.05% Triton X for 10 min and then with new PBST for 5 min. Sections were then mounted with Fluromount-G, SouthernBiotech and sealed with nail polish. Muscle fibers positive for each MHC isoform were counted manually using Image J and presented as a percentage of fiber types.

Measurement of heavy water body enrichment using acetone exchange and GC/MS

Heavy body water enrichment was analyzed by distillation of water from plasma followed by acetone exchange and was measured by gas chromatography/mass spectrometry (GC/MS)[41]. Deuterium enrichment was used in the calculation of fractional synthesis values based on mass isotopomer distribution analysis (MIDA)[44]. This enrichment tells us the maximal theoretical enrichment of each particular isotopomer at a given exposure to ^2H_2O. This maximal enrichment, representing 100% newly synthesized protein molecules, is then compared to the experimentally measured value to determine the fractional synthesis of the protein based on the rise to plateau precursor-product relationship[41,44]. 100 ul of mouse plasma was distilled overnight at 80°C. Deuterium labeled water was exchanged with acetone in an alkaline environment by incubating 1.0ul of 10.0M NaOH and 5.0ul of acetone overnight at room temperature. 300ul of hexane was added followed by removal of the organic layer to another tube with sodium sulfate. The hexane sample with deuterium enriched acetone was then injected into the GC/MS. Unlabeled M0 and labeled M1 was quantified by integrating the area under the curve. A standard curve of percent enrichment as a function of the M1 ratio was simultaneously generated during sample processing. A quadratic equation was used to measure the percent enrichment of the unknown sample based on the given M1 ratio. Body water enrichments were used as the precursor pool enrichment for determining protein product enrichments based on MIDA calculations[41,279].

In solution digest for dynamic proteomics

Dynamic proteomic technologies developed in our laboratory was used to determine how DEX treatment and/or MKO affected the turnover of gastrocnemius (GA) muscle protein synthesis rates[41,279]. This approach is able to measure the synthesis rates of large numbers of proteins across the proteome in a single experiment that combines tandem mass spectrometry with stable isotopic metabolic labeling with ^2H_2O. Approximately 100 mg of GA muscle underwent an in-solution digest protocol[41]. Briefly 500ul of 1x PBS, 1mM PMSF, 5mM EDTA, 1X halt protease inhibitor was added to each sample, homogenized with Qiagen tissue lyzer at 30Hz for 2.0 min, then centrifuged at 10,000 RPM for 10 min at 4°C. 250 ug of supernatants were quantified with a bicinchoninic acid (BCA) assay (Pierce™ BCA Protein Assay Kit) and speed vacuumed until completely dried. 25ul of 2,2,2-trifloroethanol, 25ul of 100mM ammonium bicarbonate and 2.3 ul of 100mM DTT were added to each sample and incubated at 60°C for 1 hr, followed by 10ul of 100mM of IAA and incubated at room temperature (RT) for 1hr in the dark. 2.0ul of of 100mM DTT was added to remove residual IAA, incubated for 20 min at RT and diluted with 100ul of 100mM ammonium bicarbonate and 300ul of pure water. 1:50 of trypsin to protein ratio was used for overnight digest at 37°C and 5.0ul of formic acid was used to stop digest. Samples were concentrated with a speed vac until ~300ul, centrifuged at 10,000 RPM for 30 min. Supernatants were cleaned up with a C18 SPEC tip, speed vacuumed dried and submitted in 30 ul of 3.0% acetonitrile/0.1% formic acid LC-MS submission buffer.

Experimental design and statistical rationale for LC-MS/MS analysis of proteome dynamics

To determine how DEX treatment in WT and MKO mice leads to muscle atrophy, we measured GA muscle protein fractional synthesis rates using shot-gun LC-MS/MS analysis after in vivo ^2H_2O labeling[41,43,279]. Mice were treated with PBS or DEX for 10 days. During the final 7 days, mice were also labeled with ^2H_2O. The sample size for wild type controls treated with PBS (WT-PBS, n=6), wild type treated with DEX (WT-DEX, n=6), MKO treated with PBS (MKO-PBS, n=5) and MKO treated with DEX (MKO-DEX, n=5). The rational for biological replicates of n=5-6 were based on prior data for biologic and analytic variability of proteome-wide protein fluxes[41,43,279]. Biological replicates were chosen to assess biological variability rather than sole reliance on technical replicates. Controls included WT-PBS treated mice (n=6). Two separate dynamic proteomic experiments were completed and combined for final data analysis. This consisted of experiment 1 that included WT-PBS (n=4) and WT-DEX (n=4). Experiment 2 included the final biological replicates of WT-PBS (n=2), WT-DEX (n=2), MKO-PBS (n=5) and MKO-DEX (n=5). The data sets were combined and annotated as described by the following. We used several filtering criteria for inclusion of protein kinetic data that were included in the comparisons[41,43,279]: more than one peptide had to be present for all proteins included each peptide had to meet analytic accuracy criteria for fractional mass isotopomer abundances and for reproducibility among mass isotopomers; a protein had to be present in at least 3 animals per group; and these criteria had to be met for the protein in all 4 groups. The number of proteins meeting these criteria was 81 in WT-PBS, 88 in WT-DEX, 124 in MKO-PBS and 134 in MKO-DEX and 57 proteins met these criteria in gastrocnemius muscle in all 4 groups. To determine the difference in protein fractional synthesis rates (f), four groups were categorized as the following: WT-PBS, WT-DEX, MKO-PBS and MKO-DEX. The mean, medium, and standard deviation for each protein ($n \geq 3$ for each group) were calculated, and a 2X2 ANOVA analysis (InfernoRDN v1.1.6970; January 31, 2019) was performed to compare the treatment, genotype, and interaction effects. Protein fractional synthesis were averaged within groups and the percent changes were compared across each group. An increase or decrease in fractional synthesis was assessed as ± 0.0 %. A binomial distribution statistical analysis was used to calculate the significance of the relative percent increase or decrease in GA protein fractional synthesis. Average protein fractional synthesis was also assessed by ANOVA followed by the Benjamini and Hochberg test for multiple comparisons (FDR=0.05, $p \leq 0.05$) using GraphPad Prism version 8.0 for Mac, GraphPad Software, La Jolla California USA.

Search parameters and acceptance criteria (MS/MS and/or peptide fingerprint data)

MassHunter release version B.07.00 was the software used for peak list generation. The search engine for proteomic analysis based on MS/MS identifications was Spectrum Mill released version B.04.01. Uniprot (2018) was the sequence database searched for mouse protein identifications[283]. The overall number of entries searched in the data base were 17,019. Specificity of all proteases included conical tryptic cleavage site of the C-terminal side of lysine and arginine amino acid residues. The number of missed cleavages permitted were 2. Fixed modifications included cystines carbamidomethylation (C). Variable modifications included acetylated lysine (K), oxidized methionine (M), N-terminal pyroglutamic acid (N-termQ), deamidated asparagine (N), and hydroxylated prolines (P). Mass tolerance for precursor ions and fragment ions were 20 ppm and 30 ppm, respectively. For accepting individual spectra, the threshold score/expected value was 30% based on the minimum match peak intensity. Estimation of global false discovery rate (FDR) was 1.0% that was determined by algorithms of the Spectrum Mill software and validated at the peptide and protein levels.

LC-MS proteomics and mass isotopomer kinetic analysis

Comprehensive reviews of proteome dynamics have previously been described in detail[41,43,279]. Briefly, the distribution of deuterium labeled peptides for determining GA muscle protein replacement rates were separated, analyzed and quantified using Agilent 6550 liquid chromatography tandem mass spectrometer (LC/MS-MS) equipped with chip cube nano ESI source and quadrupole time of flight (Q-TOF) mass analyzer (Agilent technologies, Santa Clara, CA). High performance liquid chromatography (HPLC) separated the complex mixture using capillary and nano binary flow. Mobile phase consisted of 3.0% acetonitrile (v/v) and 0.1% formic acid in LC/MS grade water (buffer A) to 95% acetonitrile, 0.1% formic acid in LC/MS grade water. Samples were enriched on the chip cube enrichment column with buffer A for 18 minutes and were eluted with an increasing gradient with final percentages of 95.0% acetonitrile to 5.0% water for 12 minutes and columns were finally equilibrated with buffer A for 10 minutes. Samples were injected once and mass spectra were collected in MS/MS mode. Peptide isotope ratios and abundances were collected in MS mode. MS/MS data was analyzed with Agilent Spectrum Mill software B.04.01 and Swissprot/Uniport (2018) database for protein identification against the mouse protein database[283]. The mass isotopomer patterns that contain the kinetic information in the MS spectrum for each peptide was extracted using Agilent Mass hunter B.07.00 analysis software[279]. Filtering criteria included a false discovery rate of 1.0% and ± 5.0% of the predicted isotopomers distribution, and baseline abundance of 30,000 counts. Peptide elemental composition was calculated from peptide sequence. Formula, mass and retention time for a particular peptide was used to obtain mass isotope abundances from the MS files. Mass isotopomer distribution patterns for kinetic measurements were determined from precursor body water enrichments (p), number deuterium label (n) amino acid from active metabolic labeling with ^{2}H from heavy water. Mass isotopomer distribution analysis (MIDA) was employed using programs developed by Hellerstein and colleagues to determine the fractional synthesis of the parent protein[41,43] for each peptide based on the isotopomer distribution pattern and enrichments of the labeled tryptic peptides. The labeled tryptic peptides were analyzed by LC/MS-MS to obtain the fractional synthesis rates (change in enrichment of M_0 isotopomers at time (t)/ asymptomatic enrichment of M_0 isotopomer as predicted by MIDA) of the parent protein, and calculated from the rounded up values of its labeled peptides[41,44,45]. The data analysis was handled with Microsoft excel (Version 16.28), Prism V8.0, and InfernoRDN (v1.1.6970; January 31, 2019). Gene ontology analysis was completed with the Database for Annotation, Visualization, and Integrated Discover (DAVID) for pathway analysis[284,285]. Proteins were then grouped in functional categories such as glycolytic, mitochondrial, cytosolic, and myofibrillar proteins.

Data Availability

Data can be accessed publicly online via Figshare here: https://figshare.com/projects/The_Role_of_Striated_Muscle_Pik3r1_in_Chronic_Glucocorticoid_Exposure_Induced_Insulin_Resistance_and_Reduced_Muscle_Protein_Synthesis/82868.
Project ID was 82868. One can access raw mass spectrometry data for identifications and mass isotopomer distribution analysis protein kinetic data as well. Supporting information tables can be found in supporting information files 1-7. They contain protein identification, uniport accession number, number of distinct peptides assigned for each protein, percent coverage, and quantification measurements for each protein for identification and kinetic analysis.

Statistics and gene ontology

Dynamic proteomics statistics analysis was explained in the section above. Data are expressed as standard error of the mean (S.E.M) for each group and comparisons were analyzed by Student's t test.

Acknowledgments

We are grateful for our animal care workers at OLAC. We acknowledge the Pacific Northwest National Laboratory InfernoRDN website and program for quantitative proteomic analysis of protein synthesis rates https://omics.pnl.gov/software/infernordn. Dynamic proteomic design, execution and analysis using ^2H_2O labeling and LC-MS/MS were completed by Mohamad Dandan, Mahalakshmi Shankaran, Hussein Mohammed, Marc K. Hellerstein.

Funding and Additional Information

This work was supported by the NIH R01DK083591. The content is solely the responsibility of the authors and does not necessarily represent the office views of the National Institutes of Health.

Conflict of Interest

The authors declare that they have no conflicts of interest with the contents of this article.

7.6. Supplemental Material

Additional information pertaining to supplemental materials can be found online here: https://www.jbc.org/article/S0021-9258(21)00167-8/fulltext#secsectitle0200

8. Chapter 8

Conclusion and Future Directions

For this dissertation, the common themes and connections between each chapter were: metabolism, metabolic diseases, protein turnover and metabolic fluxes[286]. I emphasize the development and methodology of measuring rare, unique, low-abundant, and key molecules that are hallmarks for various metabolic diseases[69,70,71,154]. We employed new stable isotopic metabolic labeling techniques with tandem mass spectrometric analysis to measure in both preclinical models and human subjects, the synthesis and breakdown rates of low abundance proteins (i.e., targeted, and untargeted) that play key roles in common metabolic disorders such as heart disease, diabetes, non-alcoholic fatty liver disease and muscle atrophy[1,72,164,228].

For chapter 2, I developed a mass spectrometry method to measure the turnover rates of the low-density lipoprotein receptor (LDLR) and proprotein convertase subtilisin/kexin type 9 (PCSK9) using stable isotope labeling. In liver of mice fed high-cholesterol diets, LDLR mRNA levels and synthesis rates were markedly lower with complete suppression of cholesterol synthesis and higher cholesterol content, consistent with the Brown-Goldstein model of tissue cholesterol homeostasis[15]. We observed markedly lower PCSK9 mRNA levels and synthesis rates in liver and lower concentrations and synthesis rates in plasma. Hepatic LDLR half-life (t ½) was prolonged, consistent with an effect of reduced PCSK9, and resulted in no reduction in hepatic LDLR content despite reduced mRNA levels and LDLR synthesis rates. These changes in PCSK9 synthesis complement and expand the well-established model of tissue cholesterol homeostasis in mouse liver, in that reduced synthesis and levels of PCSK9 counterbalance lower LDLR synthesis by promoting less LDLR catabolism, thereby maintaining uptake of LDL cholesterol into liver despite high intracellular cholesterol concentrations. Lower hepatic synthesis and secretion of PCSK9, an SREBP-2 target gene, results in longer hepatic LDLR t ½ in response to cholesterol feeding in mice in the face of high intracellular cholesterol content. PCSK9 modulation opposes the canonical lowering of LDLR mRNA and synthesis by cholesterol surplus and preserves LDLR levels. The physiologic and therapeutic implications of these opposing control mechanisms over liver LDLR are of interest and may reflect subservience of hepatic cholesterol homeostasis to whole body cholesterol needs. We then turned our attention from receptor and signaling molecule kinetics in heart diseases to hormonal kinetics in human beings with diabetes.

For chapter 4, I developed a non-invasive technique using ^2H_2O labeling and mass spectrometry for measuring the synthesis of pancreatic beta cell insulin in circulation as a tool to monitor the progression of diabetes in human beings. Type 2 diabetes is characterized by progressive loss of insulin secretory reserve in pancreatic beta cells[72,73]. My objective was to measure the replacement rate of serum insulin in humans using our tracer techniques. In this pilot study, we measured the replacement rate of serum insulin in humans as a marker of insulin half-life in the pancreatic beta cell, using metabolic labeling with heavy water and mass spectrometric analysis. We show here for the first time the rate of newly synthesized insulin appearance in human plasma and of C-peptide in urine and blood. This measurement reveals the lifespan or transit time of insulin stored in secretory granules in the beta cell. Insulin replacement rates were in the range of 24.1%/day in fasted state in normal subjects and was 2.4%/day in an obese subject. C-peptide turnover rates were also measured in urine and blood. From the measurement of hormonal kinetics in human beings, we sought to determine the kinetics of key signaling molecules in the development of non-alcoholic fatty liver disease[164,165].

For chapter 5, I developed a method to determine the kinetics of PNPLA3, Patatin-like phospholipase domain-containing protein 3. This gene single nucleotide polymorphisms confers susceptibility for non-alcoholic fatty liver disease (NAFLD) by accumulating PNPLA3 proteins on lipid droplets. To understand the kinetic basis of this genetic polymorphisms associated with NAFLD, we determined how PNPLA3 turnover rates are altered in the liver in NAFLD patients with different PNPLA3 genetic backgrounds. Subjects with NAFLD and different PNPLA3 genetic polymorphisms were studied. PNPLA3 fractional synthesis rates were slower ($t_{1/2}$ of 7-49 days) than predicted from ex-vivo studies in isolated hepatocytes (2-5 hours) and displayed a trend of slower turnover from wildtype to heterozygote to homozygote genotypes, and slower PNPLA3 turnover correlated significantly with intrahepatic triglyceride content (IHTG). Hepatic absolute synthesis rates of palmitate in triglycerides were higher in heterozygotes vs wild-type patients, and faster PNPLA3 turnover correlated with fractional synthesis rates of palmitate in liver triglycerides. These results suggest that impaired PNPLA3 clearance in I148M mutations leads to higher IHTG. This research provides a flux-based approach to measure the synthesis of low abundance intracellular molecules such as PNPLA3 to examine its molecular kinetics in NAFLD, and response to diet and therapies targeted at PNPLA3 kinetics. Not only did we assess the kinetics of pathophysiological proteins in the liver in NAFLD, but we also determined the effects of pharmacological treatment of Apolipoprotein kinetics in non-alcoholic steatohepatitis (NASH).

For chapter 6, we investigated how the treatment with acetyl-CoA carboxylase inhibitors (ACCi) increases plasma triglyceride (TG) concentrations in patients with non-alcoholic steatohepatitis (NASH), with variable results reported for concentrations of plasma apolipoprotein B (ApoB). Our objectives were to determine the effects of treatment with the ACCi, firsocostat, on production and clearance rates of plasma low-density lipoprotein (LDL) ApoB-containing particles, and to evaluate the effects of combination therapy with fenofibrate in patients with NASH. Metabolic labeling with heavy water and tandem mass spectrometric analysis of LDL-ApoB was carried out in NASH patients treated with firsocostat for 12 weeks; in 29 NASH subjects treated with firsocostat and fenofibrate combination therapy for 12 weeks; and in 9 normolipidemic healthy volunteers treated with firsocostat for 4 weeks. In NASH patients on firsocostat, plasma TG increased from baseline to week 12. Significant increases were also observed in LDL-ApoB fractional synthesis rate (FSR) and absolute synthesis rate (ASR), but not plasma ApoB concentration. The effect of firsocostat on LDL-ApoB ASR was restricted to patients with cirrhosis and the ASR in non-cirrhotic patients did not change. No effects of ACCi treatment on FSR, ASR, or concentrations of ApoB or TG were observed in healthy controls. Combination treatment with fenofibrate and firsocostat prevented the increases in plasma TG and LDL-ApoB FSR and ASR in NASH patients. In summary, in NASH patients with cirrhosis, ACCi treatment increases LDL-ApoB100 production rate, but this effect can be prevented by concurrent fenofibrate therapy. To tie in the relationship with protein turnover in metabolic diseases, we turned our attention to assessing protein turnover on the proteome wide level, rather than the kinetics of low abundant proteins.

For the last part of this dissertation, I used stable isotopic labeling with ^2H_2O combined with mass spectrometry to measure the turnover rates of proteins across the proteome in response to glucocorticoid treatment and/or in a Pik3r1 (a glucocorticoid response gene) knockout mouse model. Chronic glucocorticoid exposure causes insulin resistance and muscle atrophy in skeletal muscle. We previously identified phosphoinositide-3-Kinase regulatory subunit 1 (Pik3r1) as a glucocorticoid receptor primary target gene in skeletal muscle involved in glucocorticoid suppressed insulin action. We generated striated muscle specific Pik3r1 knockout mice (MKO) to investigate its role in glucocorticoid actions in vivo. Treating wild type (WT) mice with dexamethasone (DEX), a synthetic glucocorticoid, attenuated insulin activated Akt activity in liver, epididymal white adipose tissue, and gastrocnemius muscle. This DEX effect was attenuated in gastrocnemius muscle of MKO mice, resulting in better glucose and insulin tolerance in DEX treated MKO mice. Stable isotope labeling techniques revealed that in WT mice, DEX treatment decreased protein fractional synthesis rates in gastrocnemius muscle. Histology showed that in WT mice, DEX treatment reduced gastrocnemius muscle myotube diameters. In MKO mice, myotube diameters were smaller than WT mice and there were more fast oxidative fibers. Importantly, DEX failed to further reduce myotube diameters. In MKO mice, the basal protein synthesis rate was decreased (likely caused by lower 4E-BP1 phosphorylation at Thr37/Thr46) and the ability of DEX to attenuate protein synthesis rate was attenuated. DEX-reduced protein synthesis was likely caused by its ability to increase eIF2α phosphorylation at Ser51 and inhibit insulin-induced p70S6 kinase phosphorylation at Thr389, and 4E-BP1 at Thr37/Thr46. In MKO mice, the ability of DEX to inhibit eIF2α phosphorylation and insulin-induced 4E-BP1 phosphorylation was reduced. Overall, our results demonstrate Pik3r1's role in glucocorticoid actions on glucose and protein metabolism in skeletal muscle.

In conclusion, the degradation, synthesis, transport, and assembly of macromolecules are intrinsically intertwined by their turnover. Biochemical phenotypes are a collection of genes and environmental factors that boils down to the flux of metabolic and molecular pathways. Genomic, metabolic, proteomics and -omic etc. have shed light onto the static molecules affected in human health and disease, but kinetic measurement of low abundant intracellular molecules from hormones to receptors to intracellular molecules have been lacking, however[286]. This methodology involves the use a universal tracer known as heavy water than can essentially be used as a metabolical label to track the turnover of molecules from proteins, fats, nucleic acids, and vitamins to name a few. Our lab and others have been successful in applying this technology on the proteome wide level to capture the global rate of protein turnover in a physiological setting[41,43]. What remains to be further investigated are to develop a working assay for measuring the molecular kinetics of any molecule of interest (i.e., other receptors, signaling molecules and hormones)? Whether you are interested in studying a specific pathway or molecules of interest like LDLR turnover, or hormonal secretory dynamics like insulin, or interesting intracellular molecules that confer genetic predisposition to heart diseases such as PCSK9, or fatty liver disease targets such as PNPLA3. For this dissertation, I emphasize the development and methodology of measuring rare, unique, low-abundant, and interesting molecules that are hallmarks of various metabolic diseases. Once there is an established procedure to measure these molecules and their respective process, a working assay will be further developed to test how these molecules are altered in human health, disease, therapy, diet, and genetics. Collectively, these studies are anticipated to shed insight into the metabolic physiology of common metabolic diseases such as atherosclerotic cardiovascular disease, type 2 diabetes mellitus, non-alcoholic fatty liver disease, and muscle protein atrophy.

9. References

1. Virani SS, Alonso A, Aparicio HJ, Benjamin EJ, Bittencourt MS, Callaway CW, et al. Heart disease and stroke statistics—2021 update: a report from the American Heart Associationexternal icon. Circulation. 2021;143:e254–e743.
2. World Health Organization. (2021). Cardiovascular diseases (CVDs). https://www.who.int/en/news-room/fact-sheets/detail/cardiovascular-diseases-(cvds).
3. Gertler, M.M., and White, P.D. (1954). Coronary heart disease in young adults:A multidisciplinary study (Cambridge: Harvard University Press), p. 218
4. Heron, M. (2013). Deaths: leading causes for 2010. Natl. Vital Stat. Rep.62,1–96.
5. University of California - Irvine. (2009, November 17). Heart disease found in Egyptian mummies. ScienceDaily. Retrieved May 31, 2020 from www.sciencedaily.com/releases/2009/11/091117161017.htm.
6. Leibowitz, J.O. (1970). The history of coronary heart disease (Berkeley, Los Angeles: University of California Press), p. 227.
7. Shampo, M. A., & Kyle, R. A. (2001). Adolf Windaus--Nobel Prize for research on sterols. Mayo Clinic proceedings, 76(2), 119. https://doi.org/10.1016/s0025-6196(11)63115-7.
8. Konstantinov, I. E., Mejevoi, N., & Anichkov, N. M. (2006). Nikolai N. Anichkov and his theory of atherosclerosis. Texas Heart Institute journal, 33(4), 417–423.
9. Schoenheimer, R., and Breusch, F. (1933). Synthesis and destruction of cholesterol in the organism. J. Biol. Chem.103, 439–448.
10. Bloch, K. (1965). The biological synthesis of cholesterol. Science, 150, 19–28.
11. Lands W. E. (2003). Diets could prevent many diseases. Lipids, 38(4), 317–321. https://doi.org/10.1007/s11745-003-1066-0.
12. KEYS, A., KIMURA, N., KUSUKAWA, A., BRONTE-STEWART, B., LARSEN, N., & KEYS, M. H. (1958). Lessons from serum cholesterol studies in Japan, Hawaii and Los Angeles. Annals of internal medicine, 48(1), 83–94.
13. Gofman, J. W., Delalla, O., Glazier, F., Freeman, N. K., Lindgren, F. T., Nichols, A. V., Strisower, B., & Tamplin, A. R. (2007). The serum lipoprotein transport system in health, metabolic disorders, atherosclerosis and coronary heart disease. Journal of clinical lipidology, 1(2), 104–141.
14. Gordon, T., Castelli, W. P., Hjortland, M. C., Kannel, W. B., & Dawber, T. R. (1977). High density lipoprotein as a protective factor against coronary heart disease. The Framingham Study. The American journal of medicine, 62(5), 707–714.
15. Goldstein, J. L., & Brown, M. S. (2015). A century of cholesterol and coronaries: from plaques to genes to statins. Cell, 161(1), 161–172.
16. Müller, C. (1938). Xanthomata, hypercholesterolemia, angina pectoris. ActaMed. Scand.89, 75–84.
17. Vance, D.E & Vance, J.E. (2008). Biochemistry of lipids, lipoproteins, and membranes (4rd edition). Elsevier Science. 36:1-648.
18. Nair P. (2013). Brown and Goldstein: the cholesterol chronicles. Proceedings of the National Academy of Sciences of the United States of America, 110(37), 14829–14832.
19. Brown MS, Goldstein JL (1974) Familial hypercholesterolemia: Defective binding of lipoproteins to cultured fibroblasts associated with impaired regulation of 3-hydroxy-3-methylglutaryl coenzyme A reductase activity. Proc Natl Acad Sci USA 71(3):788–792.

20. Mello, R. J., Brown, M. S., Goldstein, J. L., & Anderson, R. G. (1980). LDL receptors in coated vesicles isolated from bovine adrenal cortex: binding sites unmasked by detergent treatment. Cell, 20(3), 829–837.
21. Goldstein, J. L., & Brown, M. S. (2009). History of Discovery: The LDL Receptor. Arteriosclerosis,Thrombosis, and Vascular Biology, 29(4), 431–438.
22. Brown, M. S., & Goldstein, J. L. (1986). A receptor-mediated pathway for cholesterol homeostasis. Science (New York, N.Y.), 232(4746), 34–47.
23. Cohen JC, Boerwinkle E, Mosley TH, Jr., Hobbs HH (2006) Sequence variations in PCSK9, low LDL, and protection against coronary heart disease. N Engl J Med 354(12): 1264–1272.
24. Lagace T. A. (2014). PCSK9 and LDLR degradation: regulatory mechanisms in circulation and in cells. Current opinion in lipidology, 25(5), 387–393.
25. Horton, J. D., Cohen, J. C., & Hobbs, H. H. Molecular biology of PCSK9: its role in LDL metabolism. Trends in biochemical sciences. 2007;32:71–77.
26. Weider, E., Susan-Resiga, D., Essalmani, R., Hamelin, J., Asselin, M. C., Nimesh, S., Ashraf, Y., Wycoff, K. L., Zhang, J., Prat, A., & Seidah, N. G. (2016). Proprotein Convertase Subtilisin/Kexin Type 9 (PCSK9) Single Domain Antibodies Are Potent Inhibitors of Low Density Lipoprotein Receptor Degradation. The Journal of biological chemistry, 291(32), 16659–16671.
27. Schneider, W. J., Beisiegel, U., Goldstein, J. L., & Brown, M. S. (1982). Purification of the low density lipoprotein receptor, an acidic glycoprotein of 164,000 molecular weight. The Journal of biological chemistry, 257(5), 2664–2673.
28. Schneider, W. J., Goldstein, J. L., & Brown, M. S. (1980). Partial purification and characterization of the low density lipoprotein receptor from bovine adrenal cortex. The Journal of biological chemistry, 255(23), 11442–11447.
29. Tolleshaug, H., Goldstein, J. L., Schneider, W. J., & Brown, M. S. (1982). Posttranslational processing of the LDL receptor and its genetic disruption in familial hypercholesterolemia. Cell, 30(3), 715–724.
30. Knight, B. L., Patel, D. D., & Soutar, A. K. (1987). Regulation of synthesis and cell content of the low-density-lipoprotein receptor protein in cultured fibroblasts from normal and familial hypercholesterolaemic subjects. European journal of biochemistry, 163(1), 189–196.
31. Hare J.F. 1990. Compartmentation and turnover of low-density lipoprotein receptor in skin fibroblst. JBC. Vol. 265, No. 35 pp. 21756-21763.
32. Hare J. F. (1990). Mechanisms of membrane protein turnover. Biochimica et biophysica acta, 1031(1), 71–90.
33. Ross, R. (1986) N. Engl. J. Med. 314, 488-500.
34. Tsuchiya, S., Kobayashi, Y., Goto, Y., Okamura, H., Nakae, S., Kohno, T. and Tada, K. (1982) Cancer Reg. 42, 1530-1536.
35. Hamanaka, R., Seguchi, T., Sato, Y., Ono, M., Kohno, K., & Kuwano, M. (1991). Rapid turnover of low-density lipoprotein receptor in human monocytic THP-1 cells. FEBS letters, 294(3), 261–263.
36. Casciola, L. A. F., D. R van der Westhuyzen, W. Gevers, and G. A. Coetxee. Low density lipoprotein receptor degradation is influenced by a mediator protein(s) with a rapid turnover rate, but is unaffected by receptor up- or down-regulation. J. Lipid. Res. 1988. 29: 1481-1489.

37. Hua, X., Yokoyama, C., Wu, J., Briggs, M.R., Brown, M.S., Goldstein, J.L. & Wang, X. (1993) SREBP-2, a second basic-helixloop-helix-leucine zipper protein that stimulates transcription by binding to a sterol regulatory element. Proc. Natl Acad. Sci. USA 90, 11603–11607.
38. Grefhorst, A., McNutt, M. C., Lagace, T. A., & Horton, J. D. (2008). Plasma PCSK9 preferentially reduces liver LDL receptors in mice. Journal of lipid research, 49(6), 1303–1311.
39. Lassman, M. E., McAvoy, T., Lee, A. Y., Chappell, D., Wong, O., Zhou, H., Reyes-Soffer, G., Ginsberg, H. N., Millar, J. S., Rader, D. J., Gutstein, D. E., & Laterza, O. (2014). Practical immunoaffinity-enrichment LC-MS for measuring protein kinetics of low-abundance proteins. Clinical chemistry, 60(9), 1217–1224.
40. Welder, G., Zineh, I., Pacanowski, M. A., Troutt, J. S., Cao, G., & Konrad, R. J. High-dose atorvastatin causes a rapid sustained increase in human serum PCSK9 and disrupts its correlation with LDL cholesterol. Journal of lipid research. 2010;51:2714–2721.
41. W.E. Holmes, T.E. Angel, K.W. Li, M.K. Hellerstein. (2015). Dynamic Proteomics: In Vivo Proteome Wide Measurement of Protein Kinetics Using Metabolic Labeling. Methods in Enzymology, Volume 561:219-276.
42. Beysen C., Angel T.E., Hellerstein M.K., Turner S.M. (2019) Isotopic Tracers for the Measurement of Metabolic Flux Rates. In: Krentz A., Weyer C., Hompesch M. (eds) Translational Research Methods in Diabetes, Obesity, and Nonalcoholic Fatty Liver Disease. Springer, Cham.
43. Busch, R., Kim, Y. K., Neese, R. A., Schade-Serin, V., Collins, M., Awada, M., Gardner, J. L., Beysen, C., Marino, M. E., Misell, L. M., & Hellerstein, M. K. (2006). Measurement of protein turnover rates by heavy water labeling of nonessential amino acids. Biochimica et biophysica acta, 1760(5), 730–744.
44. Papageorgopoulos, C., Caldwell, K., Shackleton, C., Schweingrubber, H., & Hellerstein, M. K. Measuring protein synthesis by mass isotopomer distribution analysis (MIDA). Analytical biochemistry.1999;267:1–16.
45. Price, J. C., Holmes, W. E., Li, K. W., Floreani, N. A., Neese, R. A., Turner, S. M., & Hellerstein, M. K. (2012). Measurement of human plasma proteome dynamics with (2)H(2)O and liquid chromatography tandem mass spectrometry. Analytical biochemistry, 420(1), 73–83.
46. Angel, T. E., Naylor, B. C., Price, J. C., Evans, C., & Szapacs, M. (2019). Improved Sensitivity for Protein Turnover Quantification by Monitoring Immonium Ion Isotopologue Abundance. Analytical chemistry, 91(15), 9732–9740. https://doi.org/10.1021/acs.analchem.9b01329.
47. Lebeau, P. F., Byun, J. H., Platko, K., MacDonald, M. E., Poon, S. V., Faiyaz, M., Seidah, N. G., & Austin, R. C. (2019). Diet-induced hepatic steatosis abrogates cell-surface LDLR by inducing de novo PCSK9 expression in mice. The Journal of biological chemistry, 294(23), 9037–9047.
48. Rashid S, Curtis DE, Garuti R, et al. Decreased plasma cholesterol and hypersensitivity to statins in mice lacking Pcsk9. Proc Natl Acad Sci U S A. 2005;102(15):5374-5379.
49. Maxwell, K. N., Soccio, R. E., Duncan, E. M., Sehayek, E. & Breslow, J. L. (2003) J. Lipid Res. 44, 2109–2119.
50. Maxwell, K. N., Fisher, E. A., & Breslow, J. L. (2005). Overexpression of PCSK9 accelerates the degradation of the LDLR in a post-endoplasmic reticulum

compartment. Proceedings of the National Academy of Sciences of the United States of America, 102(6), 2069–2074.

51. Peterson, A. S., Fong, L. G., & Young, S. G. (2008). PCSK9 function and physiology. Journal of lipid research, 49(7), 1595–1599.
52. Abifadel, M., Varret, M., Rabès, J. P., Allard, D., Ouguerram, K., Devillers, M., Cruaud, C., Benjannet, S., Wickham, L., Erlich, D., Derré, A., Villéger, L., Farnier, M., Beucler, I., Bruckert, E., et al. (2003) Mutations in PCSK9 cause autosomal dominant hypercholesterolemia. Nat. Genet. 34, 154–156.
53. Park, S. W., Moon, Y. A., & Horton, J. D. Post-transcriptional regulation of low density lipoprotein receptor protein by proprotein convertase subtilisin/kexin type 9a in mouse liver. The Journal of biological chemistry. 2004;279:50630–50638.
54. Kwon, H. J., Lagace, T. A., McNutt, M. C., Horton, J. D., & Deisenhofer, J. Molecular basis for LDL receptor recognition by PCSK9. Proceedings of the National Academy of Sciences of the United States of America. 2008;105:1820–1825.
55. Jeong, H. J., Lee, H. S., Kim, K. S., Kim, Y. K., Yoon, D., & Park, S. W. Sterol-dependent regulation of proprotein convertase subtilisin/kexin type 9 expression by sterol-regulatory element binding protein-2. Journal of lipid research. 2008;49:399–409.
56. Arias, I.M., Doyle, D., Schimke, R.T. Studies on the synthesis and degradation of proteins of the endoplasmic reticulum of rat liver. Journal of Biological Chemistry. 1969;244:3303-3315.
57. Hubbard, A., L., Cohn Z., A. Externally disposed plasma membrane proteins. I. Enzymatic iodination of mouse L cells. Journal of Cell Biology. 1975;64:438–460.
58. Hellerstein, M. K., & Neese, R. A. Mass isotopomer distribution analysis: a technique for measuring biosynthesis and turnover of polymers. The American journal of physiology. 1992;263:988–1001.
59. Smith, P. K., Krohn, R. I., Hermanson, G. T., Mallia, A. K., Gartner, F. H., Provenzano, M. D., Fujimoto, E. K., Goeke, N. M., Olson, B. J., & Klenk, D. C. Measurement of protein using bicinchoninic acid. Analytical biochemistry. 1985;150:76–85.
60. The UniProt Consortium, UniProt: a worldwide hub of protein knowledge, Nucleic Acids Research. 2019;47:506–515.
61. Tsutsumi, K., Hagi, A., & Inoue, Y. The relationship between plasma high density lipoprotein cholesterol levels and cholesteryl ester transfer protein activity in six species of healthy experimental animals. Biological & pharmaceutical bulletin. 2001;24:579–581.
62. Von Scheidt, M., Zhao, Y., Kurt, Z., Pan, C., Zeng, L., Yang, X., Schunkert, H., & Lusis, A. J. Applications and Limitations of Mouse Models for Understanding Human Atherosclerosis. Cell metabolism. 2017;25:248–261.
63. Getz, G. S., & Reardon, C. A. Diet and murine atherosclerosis. Arteriosclerosis, thrombosis, and vascular biology. 2006;26:242–249.
64. Hellerstein, M., & Evans, W. Recent advances for measurement of protein synthesis rates, use of the 'Virtual Biopsy' approach, and measurement of muscle mass. Current opinion in clinical nutrition and metabolic care. 2017;20:191–200.
65. Rorsman, P., Eliasson, L., Renström, E., Gromada, J., Barg, S., & Göpel, S. The Cell Physiology of Biphasic Insulin Secretion. News in physiological sciences: an international journal of physiology produced jointly by the International Union of Physiological Sciences and the American Physiological Society. 2000;15:72–77.

66. Rorsman, P., & Renström, E. Insulin granule dynamics in pancreatic beta cells. Diabetologia. 2003;46:1029–1045.
67. Rizzo M. A. Emptying the Pool: Modular Insulin Secretion From the Pancreas. Diabetes. 2016;65:542–544.
68. Decaris, M. L., Emson, C. L., Li, K., Gatmaitan, M., Luo, F., Cattin, J., Nakamura, C., Holmes, W. E., Angel, T. E., Peters, M. G., Turner, S. M., & Hellerstein, M. K. Turnover rates of hepatic collagen and circulating collagen-associated proteins in humans with chronic liver disease. PLOS one. 2015;10:1-13.
69. Decaris, M. L., Li, K. W., Emson, C. L., et al. Identifying nonalcoholic fatty liver disease patients with active fibrosis by measuring extracellular matrix remodeling rates in tissue and blood. Hepatology. 2017;65:78–88.
70. Shankaran, M., King, C. L., Angel, T. E., Holmes, W. E., Li, K. W., Colangelo, M., Price, J. C., Turner, S. M., Bell, C., Hamilton, K. L., Miller, B. F., & Hellerstein, M. K. Circulating protein synthesis rates reveal skeletal muscle proteome dynamics. The Journal of clinical investigation. 2016;126:288–302.
71. Loomba, R., Decaris, M., Li, K., et al. Discovery of Half-life of Circulating Hepatitis B Surface Antigen in Patients With Chronic Hepatitis B Infection Using Heavy Water Labeling. Clinical infectious diseases: an official publication of the Infectious Diseases Society of America. 2019;69:542–545.
72. Centers for Disease Control and Prevention. National Diabetes Statistics Report, 2020. Atlanta, GA: Centers for Disease Control and Prevention, U.S. Dept of Health, and Human Services.
73. Kahn, S. E., Hull, R. L., & Utzschneider, K. M. (2006). Mechanisms linking obesity to insulin resistance and type 2 diabetes. Nature, 444(7121), 840–846. https://doi.org/10.1038/nature05482.
74. Solis-Herrera C, Triplitt C, Reasner C, et al. Classification of Diabetes Mellitus. [Updated 2018 Feb 24]. In: Feingold KR, Anawalt B, Boyce A, et al., editors. Endotext [Internet]. South Dartmouth (MA): MDText.com, Inc.; 2000-. Available from: https://www.ncbi.nlm.nih.gov/books/NBK279119.
75. Nussey, S., & Whitehead, S. (2001). Endocrinology: An Integrated Approach. BIOS Scientific Publishers.
76. Diabetes Control and Complications Trial Research Group, Nathan, D. M., Genuth, S., Lachin, J., Cleary, P., Crofford, O., Davis, M., Rand, L., & Siebert, C. (1993). The effect of intensive treatment of diabetes on the development and progression of long-term complications in insulin-dependent diabetes mellitus. The New England journal of medicine, 329(14), 977–986. https://doi.org/10.1056/NEJM199309303291401.
77. Guillausseau, P. J., Meas, T., Virally, M., Laloi-Michelin, M., Médeau, V., & Kevorkian, J. P. (2008). Abnormalities in insulin secretion in type 2 diabetes mellitus. Diabetes & metabolism, 34 Suppl 2, S43–S48. https://doi.org/10.1016/S1262-3636(08)73394-9.
78. Prentki, M., & Nolan, C. J. (2006). Islet beta cell failure in type 2 diabetes. The Journal of clinical investigation, 116(7), 1802–1812. https://doi.org/10.1172/JCI29103.
79. Alper J. Biomedicine. New insights into type 2 diabetes. Science 2000;289:37-39.
80. Butler, A. E. et al. Beta-cell deficit and increased beta-cell apoptosis in humans with type 2 diabetes. Diabetes 52, 102–110 (2003).
81. Linnemann AK, Baan M, Davis DB. Pancreatic beta-cell proliferation in obesity. Adv Nutr.2014;5(3):278–88.

82. Wajchenberg B. L. (2007). beta-cell failure in diabetes and preservation by clinical treatment. Endocrine reviews, 28(2), 187–218. https://doi.org/10.1210/10.1210/er.2006-0038.
83. Wajchenberg B. L. (2010). Clinical approaches to preserve beta-cell function in diabetes. Advances in experimental medicine and biology, 654, 515–535. https://doi.org/10.1007/978-90-481-3271-3_23.
84. RISE Consortium (2014). Restoring Insulin Secretion (RISE): design of studies of β-cell preservation in prediabetes and early type 2 diabetes across the life span. Diabetes care, 37(3), 780–788. https://doi.org/10.2337/dc13-1879.
85. Itoh, N., & Okamoto, H. (1980). Translational control of proinsulin synthesis by glucose. Nature, 283(5742), 100–102. https://doi.org/10.1038/283100a0.
86. Vasiljević, J., Torkko, J. M., Knoch, K. P., & Solimena, M. (2020). The making of insulin in health and disease. Diabetologia, 63(10), 1981–1989. https://doi.org/10.1007/s00125-020-05192-7.
87. Greenman, I. C., Gomez, E., Moore, C. E., & Herbert, T. P. (2005). The selective recruitment of mRNA to the ER and an increase in initiation are important for glucose-stimulated proinsulin synthesis in pancreatic beta-cells. The Biochemical journal, 391(Pt 2), 291–300. https://doi.org/10.1042/BJ20050468.
88. Galgani, J. E., de Jonge, L., Rood, J. C., Smith, S. R., Young, A. A., & Ravussin, E. (2010). Urinary C-peptide excretion: a novel alternate measure of insulin sensitivity in physiological conditions. Obesity (Silver Spring, Md.), 18(9), 1852–1857. https://doi.org/10.1038/oby.2010.70.
89. Ward, W. K., LaCava, E. C., Paquette, T. L., Beard, J. C., Wallum, B. J., & Porte, D., Jr (1987). Disproportionate elevation of immunoreactive proinsulin in type 2 (non-insulin-dependent) diabetes mellitus and in experimental insulin resistance. Diabetologia, 30(9), 698–702. https://doi.org/10.1007/BF00296991.
90. Yudkin JS: Circulating proinsulin-like molecules. J Diabetes Complications 7:113-123, 1993.
91. Caumo, Andrea, and Livio Luzi. First-phase insulin secretion: does it exist in real life? Considerations on shape and function. Am J Physiol Endocrinol Metab 287: E371–E385, 2004; 10.1152/ajpendo.00139.2003.
92. Pørksen N. The in vivo regulation of pulsatile insulin secretion. Diabetologia 45: 3–20, 2002.
93. Pørksen N, Hollingdal M, Juhl C, Butler P, Veldhuis JD, and Schmitz O. Pulsatile insulin secretion: detection, regulation, and role in diabetes. Diabetes 51: S245–S254, 2002.
94. Pørksen N, Munn S, Steers J, Veldhuis JD, and Butler PC. Effects of glucose ingestion versus infusion on pulsatile insulin secretion. The incretin effect is achieved by amplification of insulin secretory burst mass. Diabetes 45: 1317–1323, 1996.
95. Eaton RP, Allen RC, Schade DS, Erickson KM, and Standefer J. Prehepatic insulin production in man: kinetic analysis using peripheral connecting peptide behavior. J Clin Endocrinol Metab 51: 520–528, 1980.
96. Polonsky KS, Given BD, Pugh W, Licinio-Paixao J, Thompson JE, Karrison T, and Rubenstein AH. Calculation of the systemic delivery rate of insulin in normal man. J Clin Endocrinol Metab 63: 113–118, 1986.

97. Polonsky, K., Frank, B., Pugh, W., Addis, A., Karrison, T., Meier, P., Tager, H., & Rubenstein, A. (1986). The limitations to and valid use of C-peptide as a marker of the secretion of insulin. Diabetes, 35(4), 379–386. https://doi.org/10.2337/diab.35.4.379.
98. Van Cauter, E., Mestrez, F., Sturis, J., & Polonsky, K. S. (1992). Estimation of insulin secretion rates from C-peptide levels. Comparison of individual and standard kinetic parameters for C-peptide clearance. Diabetes, 41(3), 368–377. https://doi.org/10.2337/diab.41.3.368
99. Volund A, Polonsky KS, and Bergman RN. Calculated pattern of intraportal insulin appearance without independent assessment of Cpeptide kinetics. Diabetes 36: 1195–1202, 1987.
100. Toffolo, G., De Grandi, F., & Cobelli, C. (1995). Estimation of beta-cell sensitivity from intravenous glucose tolerance test C-peptide data. Knowledge of the kinetics avoids errors in modeling the secretion. Diabetes, 44(7), 845–854. https://doi.org/10.2337/diab.44.7.845.
101. HUMBEL, R. E., & RENOLD, A. E. (1963). Studies on isolated islets of Langerhans (Brockmann bodies) of teleost fishes. I. Metabolic activity in vitro. Biochimica et biophysica acta, 74, 84–95. https://doi.org/10.1016/0006-3002(63)91332-5.
102. HUMBEL R. E. (1965). BIOSYNTHESIS OF THE TWO CHAINS OF INSULIN. Proceedings of the National Academy of Sciences of the United States of America, 53(4), 853–859. https://doi.org/10.1073/pnas.53.4.853.
103. TAYLOR, K. W., PARRY, D. G., & SMITH, G. H. (1964). BIOSYNTHETIC LABELLING OF MAMMALIAN INSULINS IN VITRO. Nature, 203, 1144–1145. https://doi.org/10.1038/2031144a0.
104. TAYLOR, K. W., GARDNER, G., PARRY, D. G., & JONES, V. E. (1965). THE PURIFICATION OF TRITIUM-LABELLED INSULIN BY PRECIPITATION WITH INSULIN ANTIBODIES. Biochimica et biophysica acta, 100, 521–529. https://doi.org/10.1016/0304-4165(65)90022-x.
105. Mallory, A., Smith, G. H., & Taylor, K. W. (1964). The incorporation of tritium-labelled amino acids into insulins in rat pancreas in vitro. The Biochemical journal, 91(3), 484–491. https://doi.org/10.1042/bj0910484.
106. Howell, S. L., & Taylor, K. W. (1967). The secretion of newly synthesized insulin in vitro. The Biochemical journal, 102(3), 922–927. https://doi.org/10.1042/bj1020922
107. Morenkova S. A. (1966). Incorporation of S35-methionine into insulin. Nature, 209(5026), 917. https://doi.org/10.1038/209917a0.
108. JONES, V. E., & CUNLIFFE, A. C. (1961). A precipitating antibody to insulin. Nature, 192, 136–138. https://doi.org/10.1038/192136a0.
109. Guo, H., Xiong, Y., Witkowski, P., Cui, J., Wang, L. J., Sun, J., Lara-Lemus, R., Haataja, L., Hutchison, K., Shan, S. O., Arvan, P., & Liu, M. (2014). Inefficient translocation of preproinsulin contributes to pancreatic β cell failure and late-onset diabetes. The Journal of biological chemistry, 289(23), 16290–16302. https://doi.org/10.1074/jbc.M114.562355.
110. Guo, H., Sun, J., Li, X., Xiong, Y., Wang, H., Shu, H., Zhu, R., Liu, Q., Huang, Y., Madley, R., Wang, Y., Cui, J., Arvan, P., & Liu, M. (2018). Positive charge in the n-region of the signal peptide contributes to efficient post-translational translocation of small secretory preproteins. The Journal of biological chemistry, 293(6), 1899–1907. https://doi.org/10.1074/jbc.RA117.000922.

111. Steiner, D. F., Clark, J. L., Nolan, C., Rubenstein, A. H., Margoliash, E., Aten, B., & Oyer, P. E. (1969). Proinsulin and the biosynthesis of insulin. Recent progress in hormone research, 25, 207–282. https://doi.org/10.1016/b978-0-12-571125-8.50008-9.
112. Taylor K. W. (1972). The biosynthesis and secretion of insulin. Clinics in endocrinology and metabolism, 1(3), 601–622. https://doi.org/10.1016/s0300-595x(72)80036-7.
113. Berson, S. A., & Yalow, R. S. (1967). Radioimmunoassays of peptide hormones in plasma. The New England journal of medicine, 277(12), 640–647. https://doi.org/10.1056/NEJM196709212771208.
114. Katz, A. I., & Rubenstein, A. H. (1973). Metabolism of proinsulin, insulin, and C-peptide in the rat. The Journal of clinical investigation, 52(5), 1113–1121. https://doi.org/10.1172/JCI107277.
115. Sherwin, R. S., Kramer, K. J., Tobin, J. D., Insel, P. A., Liljenquist, J. E., Berman, M., & Andres, R. (1974). A model of the kinetics of insulin in man. The Journal of clinical investigation, 53(5), 1481–1492. https://doi.org/10.1172/JCI107697.
116. Navalesi, R., Pilo, A., & Ferrannini, E. (1978). Kinetic analysis of plasma insulin disappearance in nonketotic diabetic patients and in normal subjects. A tracer study with 125I-insulin. The Journal of clinical investigation, 61(1), 197–208. https://doi.org/10.1172/JCI108918.
117. Rhodes, C. J., & Halban, P. A. (1987). Newly synthesized proinsulin/insulin and stored insulin are released from pancreatic B cells predominantly via a regulated, rather than a constitutive, pathway. The Journal of cell biology, 105(1), 145–153. https://doi.org/10.1083/jcb.105.1.145.
118. Ferrannini E and Cobelli C. The kinetics of insulin in man. I. General aspects. Diabetes Metab Rev 3: 335–363, 1987.
119. Schuit, F. C., Kiekens, R., & Pipeleers, D. G. (1991). Measuring the balance between insulin synthesis and insulin release. Biochemical and biophysical research communications, 178(3), 1182–1187. https://doi.org/10.1016/0006-291x(91)91017-7.
120. Povazhenko, A. A., Ryzhova, T. I., & Kozyreva, E. V. (1997). Measurement of proinsulin, insulin, and C-peptide in human blood by high performance liquid chromatography. Klinicheskaia laboratornaia diagnostika, (9), 34–36.
121. Thomas, A., Schänzer, W., & Thevis, M. (2017). Immunoaffinity techniques coupled to mass spectrometry for the analysis of human peptide hormones: advances and applications. Expert review of proteomics, 14(9), 799–807. https://doi.org/10.1080/14789450.2017.1362338.
122. Andreas Thomas, Mario Thevis. (2019). Recent advances in the determination of insulins from biological fluids. Advances in Clinical Chemistry, Elsevier, Volume 93, Pages 115-167, (https://www.sciencedirect.com/science/article/pii/S0065242319300605)
123. Bowers GNJ, Fassett JD, White E: Isotope dilution mass spectrometry and the National Reference System. Anal Chem 65:475R-479R, (1993).
124. Stöcklin, R., Vu, L., Vadas, L., Cerini, F., Kippen, A. D., Offord, R. E., & Rose, K. (1997). A stable isotope dilution assay for the in vivo determination of insulin levels in humans by mass spectrometry. Diabetes, 46(1), 44–50. https://doi.org/10.2337/diab.46.1.44.
125. Kippen, A. D., Cerini, F., Vadas, L., Stöcklin, R., Vu, L., Offord, R. E., & Rose, K. (1997). Development of an isotope dilution assay for precise determination of insulin, C-peptide, and proinsulin levels in non-diabetic and type II diabetic individuals with comparison to

immunoassay. The Journal of biological chemistry, 272(19), 12513–12522. https://doi.org/10.1074/jbc.272.19.12513.

126. Sakaguchi, Y., Kinumi, T., & Takatsu, A. (2017). Isotope-dilution liquid chromatography-tandem mass spectrometry for sensitive quantification of human insulin in serum using derivatization-technique. Analytical biochemistry, 537, 26–32. https://doi.org/10.1016/j.ab.2017.08.019.
127. Darby, S. M., Miller, M. L., Allen, R. O., & LeBeau, M. (2001). A mass spectrometric method for quantitation of intact insulin in blood samples. Journal of analytical toxicology, 25(1), 8–14. https://doi.org/10.1093/jat/25.1.8.
128. Taylor, S. W., Clarke, N. J., Chen, Z., & McPhaul, M. J. (2016). A high-throughput mass spectrometry assay to simultaneously measure intact insulin and C-peptide. Clinica chimica acta; international journal of clinical chemistry, 455, 202–208. https://doi.org/10.1016/j.cca.2016.01.019.
129. Judák, P., Van Eenoo, P., & Deventer, K. (2018). Utilizing ELISA-plate based immunoprecitation and liquid chromatography-tandem mass spectrometry for the urinary detection of short- and long-acting human insulin analogues. Journal of pharmaceutical and biomedical analysis, 153, 76–81. https://doi.org/10.1016/j.jpba.2018.02.024.
130. Thomas, A., Schänzer, W., & Thevis, M. (2014). Determination of human insulin and its analogues in human blood using liquid chromatography coupled to ion mobility mass spectrometry (LC-IM-MS). Drug testing and analysis, 6(11-12), 1125–1132. https://doi.org/10.1002/dta.1710.
131. Thevis, M., Thomas, A., Delahaut, P., Bosseloir, A., & Schänzer, W. (2005). Qualitative determination of synthetic analogues of insulin in human plasma by immunoaffinity purification and liquid chromatography-tandem mass spectrometry for doping control purposes. Analytical chemistry, 77(11), 3579–3585. https://doi.org/10.1021/ac050066i.
132. Thomas, A., Schänzer, W., Delahaut, P., & Thevis, M. (2009). Sensitive and fast identification of urinary human, synthetic and animal insulin by means of nano-UPLC coupled with high-resolution/high-accuracy mass spectrometry. Drug testing and analysis, 1(5), 219–227. https://doi.org/10.1002/dta.35.
133. Thomas, A., & Thevis, M. (2018). Analysis of insulin and insulin analogs from dried blood spots by means of liquid chromatography-high resolution mass spectrometry. Drug testing and analysis, 10(11-12), 1761–1768. https://doi.org/10.1002/dta.2518.
134. Thomas, W. Schänzer, P. Delahaut, M. Thevis. Immunoaffinity purification of peptide hormones prior to liquid chromatography-mass spectrometry in doping controls. Methods 2012, 56, 230.
135. Thomas, A., Yang, R., Petring, S., Bally, L., & Thevis, M. (2020). Simplified quantification of insulin, its synthetic analogs and C-peptide in human plasma by means of LC-HRMS. Drug testing and analysis, 12(3), 382–390. https://doi.org/10.1002/dta.2765.
136. Chen, Z., Caulfield, M. P., McPhaul, M. J., Reitz, R. E., Taylor, S. W., & Clarke, N. J. (2013). Quantitative insulin analysis using liquid chromatography-tandem mass spectrometry in a high-throughput clinical laboratory. Clinical chemistry, 59(9), 1349–1356. https://doi.org/10.1373/clinchem.2012.199794.
137. Lee, A. Y., Chappell, D. L., Bak, M. J., Judo, M., Liang, L., Churakova, T., Ayanoglu, G., Castro-Perez, J., Zhou, H., Previs, S., Souza, S. C., Lassman, M. E., & Laterza, O. F. (2016). Multiplexed Quantification of Proglucagon-Derived Peptides by Immunoaffinity

Enrichment and Tandem Mass Spectrometry after a Meal Tolerance Test. Clinical chemistry, 62(1), 227–235. https://doi.org/10.1373/clinchem.2015.244251.

138. Ketha, H., & Singh, R. J. (2016). Quantitation of Insulin-Like Growth Factor 1 in Serum by Liquid Chromatography High Resolution Accurate-Mass Mass Spectrometry. Methods in molecular biology (Clifton, N.J.), 1378, 131–137. https://doi.org/10.1007/978-1-4939-3182-8_15.
139. Görgens, C., Guddat, S., Thomas, A., & Thevis, M. (2018). Recent improvements in sports drug testing concerning the initial testing for peptidic drugs (< 2 kDa) - sample preparation, mass spectrometric detection, and data review. Drug testing and analysis, 10(11-12), 1755–1760. https://doi.org/10.1002/dta.2503.
140. Putz, M., Piper, T., Dubois, M., Delahaut, P., & Thevis, M. (2019). Analysis of endogenous steroids in urine by means of multi-immunoaffinity chromatography and isotope ratio mass spectrometry for sports drug testing. Analytical and bioanalytical chemistry, 411(28), 7563–7571. https://doi.org/10.1007/s00216-019-02169-3.
141. Marc H. Hellerstein. 2014. Molecular flux rates through critical pathways measured by stable isotope labeling in vivo, as biomarkers of drug action and disease activity. US 2014/0193828A1. 1-90. https://patents.google.com/patent/US20140193828A1/en.
142. Jainandunsing, S., van Miert, J., Rietveld, T., Darcos Wattimena, J. L., Sijbrands, E., & de Rooij, F. (2016). A stable isotope method for in vivo assessment of human insulin synthesis and secretion. Acta diabetologica, 53(6), 935–944. https://doi.org/10.1007/s00592-016-0896-3.
143. Gold, G., Gishizky, M. L., & Grodsky, G. M. (1982). Evidence that glucose "marks" beta cells resulting in preferential release of newly synthesized insulin. Science (New York, N.Y.), 218(4567), 56–58. https://doi.org/10.1126/science.6181562.
144. Klein, S., Gastaldelli, A., Yki-Järvinen, H., & Scherer, P. E. (2022). Why does obesity cause diabetes? Cell metabolism, 34(1), 11–20. https://doi.org/10.1016/j.cmet.2021.12.012.
145. Najjar SM, Perdomo G. Hepatic insulin clearance: mechanism and physiology. Physiology (Bethesda). 2019;34(3):198–215.
146. Smith, G. I., Polidori, D. C., Yoshino, M., Kearney, M. L., Patterson, B. W., Mittendorfer, B., & Klein, S. (2020). Influence of adiposity, insulin resistance, and intrahepatic triglyceride content on insulin kinetics. The Journal of clinical investigation, 130(6), 3305–3314. https://doi.org/10.1172/JCI136756.
147. Polidori, D. C., Bergman, R. N., Chung, S. T., & Sumner, A. E. (2016). Hepatic and Extrahepatic Insulin Clearance Are Differentially Regulated: Results from a Novel Model-Based Analysis of Intravenous Glucose Tolerance Data. Diabetes, 65(6), 1556–1564. https://doi.org/10.2337/db15-1373.
148. Gastaldelli, A., Abdul Ghani, M., & DeFronzo, R. A. (2021). Adaptation of Insulin Clearance to Metabolic Demand Is a Key Determinant of Glucose Tolerance. Diabetes, 70(2), 377–385. https://doi.org/10.2337/db19-1152.
149. Utzschneider, K. M., Kahn, S. E., & Polidori, D. C. (2019). Hepatic Insulin Extraction in NAFLD Is Related to Insulin Resistance Rather Than Liver Fat Content. The Journal of clinical endocrinology and metabolism, 104(5), 1855–1865. https://doi.org/10.1210/jc.2018-01808.
150. van Vliet, S., Koh, H. E., Patterson, B. W., Yoshino, M., LaForest, R., Gropler, R. J., Klein, S., & Mittendorfer, B. (2020). Obesity Is Associated with Increased Basal and Postprandial

β-Cell Insulin Secretion Even in the Absence of Insulin Resistance. Diabetes, 69(10), 2112–2119. https://doi.org/10.2337/db20-0377.

151. Germanos, M., Gao, A., Taper, M., Yau, B., & Kebede, M. A. (2021). Inside the Insulin Secretory Granule. Metabolites, 11(8), 515. https://doi.org/10.3390/metabo11080515.
152. Hou, J. C., Min, L., & Pessin, J. E. (2009). Insulin granule biogenesis, trafficking, and exocytosis. Vitamins and hormones, 80, 473–506. https://doi.org/10.1016/S0083-6729(08)00616-X.
153. Hellerstein, M. K.; Neese, R. A. Mass isotopomer distribution analysis at eight years: theoretical, analytic, and experimental considerations. Am. J. Physiol. 1999, 276, E1146– 1170, DOI: 10.1152/ajpendo.1999.276.6. E1146.
154. Dandan, M., Han, J., Mann, S., Kim, R., Mohammed, H., Nyangau, E., & Hellerstein, M. (2021). Turnover Rates of the Low-Density Lipoprotein Receptor and PCSK9: Added Dimension to the Cholesterol Homeostasis Model. Arteriosclerosis, thrombosis, and vascular biology, 41(12), 2866–2876. https://doi.org/10.1161/ATVBAHA.121.316764.
155. Clark, A., Jones, L. C., de Koning, E., Hansen, B. C., & Matthews, D. R. (2001). Decreased insulin secretion in type 2 diabetes: a problem of cellular mass or function? Diabetes, 50 Suppl 1, S169–S171. https://doi.org/10.2337/diabetes.50.2007.s169.
156. Bonser, A. M., & Garcia-Webb, P. (1984). C-peptide measurement: methods and clinical utility. Critical reviews in clinical laboratory sciences, 19(4), 297–352. https://doi.org/10.3109/10408368409165766.
157. Duckworth, W. C., Bennett, R. G., & Hamel, F. G. (1998). Insulin degradation: progress and potential. Endocrine reviews, 19(5), 608–624. https://doi.org/10.1210/edrv.19.5.0349
158. Mittendorfer B, Patterson BW, Smith GI, Yoshino M, Klein S. β Cell function and plasma insulin clearance in people with obesity and different glycemic status. J Clin Invest. 2022;132(3): e154068. doi:10.1172/JCI154068.
159. Christensen, A.A., Gannon, M. The Beta Cell in Type 2 Diabetes. Curr Diab Rep 19, 81 (2019). https://doi.org/10.1007/s11892-019-1196-4.
160. Muoio, D. M., & Newgard, C. B. (2008). Mechanisms of disease: Molecular and metabolic mechanisms of insulin resistance and beta-cell failure in type 2 diabetes. Nature reviews. Molecular cell biology, 9(3), 193–205. https://doi.org/10.1038/nrm2327.
161. Uchizono, Y., Alarcón, C., Wicksteed, B. L., Marsh, B. J., & Rhodes, C. J. (2007). The balance between proinsulin biosynthesis and insulin secretion: where can imbalance lead? Diabetes, obesity & metabolism, 9 Suppl 2, 56–66. https://doi.org/10.1111/j.1463-1326.2007.00774.x.
162. Yang, Y., Wang, M., Tong, J., Dong, Z., Deng, M., Ren, X., Li, H., Yang, J., Meng, Z., Sun, J., He, Q., & Liu, M. (2019). Impaired Glucose-Stimulated Proinsulin Secretion Is an Early Marker of β-Cell Impairment Before Prediabetes Stage. The Journal of clinical endocrinology and metabolism, 104(10), 4341–4346. https://doi.org/10.1210/jc.2019-00549.
163. Belongie, K. J., Ferrannini, E., Johnson, K., Andrade-Gordon, P., Hansen, M. K., & Petrie, J. R. (2017). Identification of novel biomarkers to monitor β-cell function and enable early detection of type 2 diabetes risk. PloS one, 12(8), e0182932. https://doi.org/10.1371/journal.pone.0182932.
164. Harrison SA, Neuschwander-Tetri BA. Nonalcoholic fatty liver disease and nonalcoholic steatohepatitis. Clin Liver Dis. 2004; 8:861–879.

165. Jou J, Choi SS, Diehl AM. Mechanisms of disease progression in nonalcoholic fatty liver disease. Semin Liver Dis. 2008; 28:370–379.
166. Younossi, Z. et al. Global burden of NAFLD and NASH: trends, predictions, risk factors and prevention. Nat. Rev. Gastroenterol. Hepatol. 15, 11–20 (2018).
167. Younossi, Z. M., Loomba, R., Anstee, Q. M., Rinella, M. E., Bugianesi, E., Marchesini, G., Neuschwander-Tetri, B. A., Serfaty, L., Negro, F., Caldwell, S. H., Ratziu, V., Corey, K. E., Friedman, S. L., Abdelmalek, M. F., Harrison, S. A., Sanyal, A. J., Lavine, J. E., Mathurin, P., Charlton, M. R., Goodman, Z. D., … Lindor, K. (2018). Diagnostic modalities for nonalcoholic fatty liver disease, nonalcoholic steatohepatitis, and associated fibrosis. Hepatology (Baltimore, Md.), 68(1), 349–360. https://doi.org/10.1002/hep.29721
168. Romeo S, Kozlitina J, Xing C, Pertsemlidis A, Cox D, Pennacchio LA, et al. Genetic variation in PNPLA3 confers susceptibility to nonalcoholic fatty liver disease. Nat Genet. 2008; 40:1461–1465.
169. Dongiovanni P, Donati B, Fares R, et al. PNPLA3 I148M polymorphism and progressive liver disease. World J Gastroenterol 2013; 19:6969.
170. Dongiovanni P, Romeo S, Valenti L. Genetic factors in the pathogenesis of nonalcoholic fatty liver and steatohepatitis. Biomed Res Int 2015; 2015:460190.
171. Kotronen A, Johansson LE, Johansson LM, Roos C, Westerbacka J, Hamsten A, et al. A common variant in PNPLA3, which encodes adiponutrin, is associated with liver fat content in humans. Diabetologia. 2009; 52:1056–1060.
172. Schwimmer, J. B. et al. Heritability of nonalcoholic fatty liver disease. Gastroenterology 136, 1585–1592 (2009).
173. Jenkins CM, Mancuso DJ, Yan W, Sims HF, Gibson B, Gross RW. Identification, cloning, expression, and purification of three novel human calcium-independent phospholipase A2 family members possessing triacylglycerol lipase and acylglycerol transacylase activities. J Biol Chem. (2004) 279:48968–75. doi: 10.1074/jbc.M407841200.
174. Dong X. C. (2019). PNPLA3-A Potential Therapeutic Target for Personalized Treatment of Chronic Liver Disease. Frontiers in medicine, 6, 304. https://doi.org/10.3389/fmed.2019.00304.
175. Sookoian, S., Castaño, G. O., Burgueño, A. L., Gianotti, T. F., Rosselli, M. S., & Pirola, C. J. (2009). A nonsynonymous gene variant in the adiponutrin gene is associated with nonalcoholic fatty liver disease severity. Journal of lipid research, 50(10), 2111–2116. https://doi.org/10.1194/jlr.P900013-JLR200
176. Li JZ, Huang Y, Karaman R, Ivanova PT, Brown HA, Roddy T, et al. Chronic overexpression of PNPLA3I148M in mouse liver causes hepatic steatosis. J Clin Invest. (2012) 122:4130–44. doi: 10.1172/JCI65179
177. Smagris E, BasuRay S, Li J, Huang Y, Lai KM, Gromada J, et al. Pnpla3I148M knockin mice accumulate PNPLA3 on lipid droplets and develop hepatic steatosis. Hepatology. (2015) 61:108–18. doi: 10.1002/hep.27242
178. BasuRay, S., Smagris, E., Cohen, J. C., & Hobbs, H. H. (2017). The PNPLA3 variant associated with fatty liver disease (I148M) accumulates on lipid droplets by evading ubiquitylation. Hepatology (Baltimore, Md.), 66(4), 1111–1124. https://doi.org/10.1002/hep.29273
179. Huang Y, Cohen JC, Hobbs HH. Expression and characterization of a PNPLA3 protein isoform. (I148M) associated with nonalcoholic fatty liver disease. J Biol Chem. (2011) 286:37085–93. doi: 10.1074/jbc.M111.290114

180. He S, McPhaul C, Li JZ, Garuti R, Kinch LN, Grishin NV, et al. A sequence variation (I148M) in PNPlA3 associated with nonalcoholic fatty liver disease disrupts triglyceride hydrolysis. J Biol Chem. 2010; 285:6706–6715.
181. Wang Y, Kory N, BasuRay S, Cohen JC, Hobbs HH. PNPLA3, CGI-58, and inhibition of hepatic triglyceride hydrolysis in mice. Hepatology. (2019) 69:2427–41. doi: 10.1002/hep.30583
182. Chamoun Z, Vacca F, Parton RG, Gruenberg J. PNPLA3/adiponutrin functions in lipid droplet formation. Biol Cell. (2013) 105:219–33. doi: 10.1111/boc.201200036
183. Yang A, Mottillo EP, Mladenovic-Lucas L, Zhou L, Granneman JG. Dynamic interactions of ABHD5 with PNPLA3 regulate triacylglycerol metabolism in brown adipocytes. Nat Metab. (2019) 1:560–9. doi: 10.1038/s42255-019-0066-3
184. BasuRay S, Wang Y, Smagris E, Cohen JC, Hobbs HH. Accumulation of PNPLA3 on lipid droplets is the basis of associated hepatic steatosis. Proc Natl Acad Sci USA. (2019) 116:9521–6. doi: 10.1073/pnas.1901974116
185. Smith, G. I., Shankaran, M., Yoshino, M., Schweitzer, G. G., Chondronikola, M., Beals, J. W., Okunade, A. L., Patterson, B. W., Nyangau, E., Field, T., Sirlin, C. B., Talukdar, S., Hellerstein, M. K., & Klein, S. (2020). Insulin resistance drives hepatic de novo lipogenesis in nonalcoholic fatty liver disease. The Journal of clinical investigation, 130(3), 1453–1460. https://doi.org/10.1172/JCI134165.
186. The UniProt Consortium
UniProt: the universal protein knowledgebase in 2021
Nucleic Acids Res. 49: D1 (2021).
187. Romeo S, Sentinelli F, Dash S, Yeo GS, Savage DB, Leonetti F, et al. Morbid obesity exposes the association between PNPLA3 I148M (rs738409) and indices of hepatic injury in individuals of European descent. Int J Obes (Lond) 2010; 34:190-194.
188. Sookoian S, Pirola CJ. Meta-analysis of the influence of I148M variant of patatin-like phospholipase domain containing 3 gene (PNPLA3) on the susceptibility and histological severity of nonalcoholic fatty liver disease. Hepatology. 2011;53(6):1883–1894.
189. Huang, Y., He, S., Li, J. Z., Seo, Y. K., Osborne, T. F., Cohen, J. C., & Hobbs, H. H. (2010). A feed-forward loop amplifies nutritional regulation of PNPLA3. Proceedings of the National Academy of Sciences of the United States of America, 107(17), 7892–7897. https://doi.org/10.1073/pnas.1003585107.
190. Min HK, Sookoian S, Pirola CJ, Cheng J, Mirshahi F, Sanyal AJ. Metabolic profiling reveals that PNPLA3 induces widespread effects on metabolism beyond triacylglycerol remodeling in Huh-7 hepatoma cells. Am J Physiol Gastrointest Liver Physiol. 2014;307(1): G66–G76.
191. Green CJ, et al. Characterization of lipid metabolism in a novel immortalized human hepatocyte cell line. Am J Physiol Endocrinol Metab. 2015;309(6): E511–E522.
192. Pirazzi, C., Adiels, M., Burza, M. A., Mancina, R. M., Levin, M., Ståhlman, M., Taskinen, M. R., Orho-Melander, M., Perman, J., Pujia, A., Andersson, L., Maglio, C., Montalcini, T., Wiklund, O., Borén, J., & Romeo, S. (2012). Patatin-like phospholipase domain-containing 3 (PNPLA3) I148M (rs738409) affects hepatic VLDL secretion in humans and in vitro. Journal of hepatology, 57(6), 1276–1282. https://doi.org/10.1016/j.jhep.2012.07.030.
193. Kumari M, Schoiswohl G, Chitraju C, Paar M, Cornaciu I, Rangrez AY, et al. Adiponutrin functions as a nutritionally regulated lysophosphatidic acid acyltransferase. Cell Metab 2012; 15:691-702.

194. Donnelly, K. L., Smith, C. I., Schwarzenberg, S. J., Jessurun, J., Boldt, M. D., & Parks, E. J. (2005). Sources of fatty acids stored in liver and secreted via lipoproteins in patients with nonalcoholic fatty liver disease. The Journal of clinical investigation, 115(5), 1343–1351. https://doi.org/10.1172/JCI23621.
195. Yuan, L., & Terrrault, N. A. (2020). PNPLA3 and nonalcoholic fatty liver disease: towards personalized medicine for fatty liver. Hepatobiliary surgery and nutrition, 9(3), 353–356. https://doi.org/10.21037/hbsn.2019.10.35.
196. McCullough A. J. (2002). Update on nonalcoholic fatty liver disease. Journal of clinical gastroenterology, 34(3), 255–262. https://doi.org/10.1097/00004836-200203000-00013.
197. Lindenmeyer, C. C., & McCullough, A. J. (2018). The Natural History of Nonalcoholic Fatty Liver Disease-An Evolving View. Clinics in liver disease, 22(1), 11–21. https://doi.org/10.1016/j.cld.2017.08.003.
198. Marengo, A., Jouness, R. I., & Bugianesi, E. (2016). Progression and Natural History of Nonalcoholic Fatty Liver Disease in Adults. Clinics in liver disease, 20(2), 313–324. https://doi.org/10.1016/j.cld.2015.10.010.
199. Farrell, G. C., & Larter, C. Z. (2006). Nonalcoholic fatty liver disease: from steatosis to cirrhosis. Hepatology (Baltimore, Md.), 43(2 Suppl 1), S99–S112. https://doi.org/10.1002/hep.20973.
200. Chatrath, H., Vuppalanchi, R., & Chalasani, N. (2012). Dyslipidemia in patients with nonalcoholic fatty liver disease. Seminars in liver disease, 32(1), 22–29. https://doi.org/10.1055/s-0032-1306423.
201. Corey, K. E., Misdraji, J., Gelrud, L., Zheng, H., Chung, R. T., & Krauss, R. M. (2014). Nonalcoholic steatohepatitis is associated with an atherogenic lipoprotein subfraction profile. Lipids in health and disease, 13, 100. https://doi.org/10.1186/1476-511X-13-100.
202. Jiang, Z. G., Robson, S. C., & Yao, Z. (2013). Lipoprotein metabolism in nonalcoholic fatty liver disease. Journal of biomedical research, 27(1), 1–13. https://doi.org/10.7555/JBR.27.20120077.
203. Sniderman, A. D., Thanassoulis, G., Glavinovic, T., Navar, A. M., Pencina, M., Catapano, A., & Ference, B. A. (2019). Apolipoprotein B Particles and Cardiovascular Disease: A Narrative Review. JAMA cardiology, 4(12), 1287–1295. https://doi.org/10.1001/jamacardio.2019.3780.
204. Kim, C. W., Addy, C., Kusunoki, J., Anderson, N. N., Deja, S., Fu, X., Burgess, S. C., Li, C., Ruddy, M., Chakravarthy, M., Previs, S., Milstein, S., Fitzgerald, K., Kelley, D. E., & Horton, J. D. (2017). Acetyl CoA Carboxylase Inhibition Reduces Hepatic Steatosis but Elevates Plasma Triglycerides in Mice and Humans: A Bedside to Bench Investigation. Cell metabolism, 26(2), 394–406.e6. https://doi.org/10.1016/j.cmet.2017.07.009.
205. Tong, L., & Harwood, H. J., Jr. (2006). Acetyl-coenzyme A carboxylases: versatile targets for drug discovery. Journal of cellular biochemistry, 99(6), 1476–1488. https://doi.org/10.1002/jcb.21077. Vance, D.E & Vance, J.E. (2008). Biochemistry of lipids, lipoproteins, and membranes, 4th Ed., Elsevier Science. 36:1-648.
206. Alkhouri, N., Lawitz, E., Noureddin, M., DeFronzo, R., & Shulman, G. I. (2020). GS-0976 (Firsocostat): an investigational liver-directed acetyl-CoA carboxylase (ACC) inhibitor for the treatment of non-alcoholic steatohepatitis (NASH). Expert opinion on investigational drugs, 29(2), 135–141. https://doi.org/10.1080/13543784.2020.1668374.
207. Goedeke, L., Bates, J., Vatner, D. F., Perry, R. J., Wang, T., Ramirez, R., Li, L., Ellis, M. W., Zhang, D., Wong, K. E., Beysen, C., Cline, G. W., Ray, A. S., & Shulman, G. I. (2018).

Acetyl-CoA Carboxylase Inhibition Reverses NAFLD and Hepatic Insulin Resistance but Promotes Hypertriglyceridemia in Rodents. Hepatology (Baltimore, Md.), 68(6), 2197–2211. https://doi.org/10.1002/hep.30097.

208. Loomba, R., Kayali, Z., Noureddin, M., Ruane, P., Lawitz, E. J., Bennett, M., Wang, L., Harting, E., Tarrant, J. M., McColgan, B. J., Chung, C., Ray, A. S., Subramanian, G. M., Myers, R. P., Middleton, M. S., Lai, M., Charlton, M., & Harrison, S. A. (2018). GS-0976 Reduces Hepatic Steatosis and Fibrosis Markers in Patients With Nonalcoholic Fatty Liver Disease. Gastroenterology, 155(5), 1463–1473.e6. https://doi.org/10.1053/j.gastro.2018.07.027.
209. Loomba, R., Noureddin, M., Kowdley, K. V., Kohli, A., Sheikh, A., Neff, G., Bhandari, B. R., Gunn, N., Caldwell, S. H., Goodman, Z., Wapinski, I., Resnick, M., Beck, A. H., Ding, D., Jia, C., Chuang, J. C., Huss, R. S., Chung, C., Subramanian, G. M., Myers, R. P., … ATLAS Investigators (2021). Combination Therapies Including Cilofexor and Firsocostat for Bridging Fibrosis and Cirrhosis Attributable to NASH. Hepatology (Baltimore, Md.), 73(2), 625–643. https://doi.org/10.1002/hep.31622.
210. Lawitz, E. J., Coste, A., Poordad, F., Alkhouri, N., Loo, N., McColgan, B. J., Tarrant, J. M., Nguyen, T., Han, L., Chung, C., Ray, A. S., McHutchison, J. G., Subramanian, G. M., Myers, R. P., Middleton, M. S., Sirlin, C., Loomba, R., Nyangau, E., Fitch, M., Li, K., Hellerstein, M. (2018). Acetyl-CoA Carboxylase Inhibitor GS-0976 for 12 Weeks Reduces Hepatic De Novo Lipogenesis and Steatosis in Patients With Nonalcoholic Steatohepatitis. Clinical gastroenterology and hepatology: the official clinical practice journal of the American Gastroenterological Association, 16(12), 1983–1991.e3. https://doi.org/10.1016/j.cgh.2018.04.042.
211. Lawitz, E. J., Bhandari, B. R., Ruane, P. J., Kohli, A., Harting, E., Ding, D., Chuang, J. C., Huss, R. S., Chung, C., Myers, R. P., & Loomba, R. (2022). Fenofibrate Mitigates Hypertriglyceridemia in Nonalcoholic Steatohepatitis Patients Treated With Cilofexor/Firsocostat. Clinical gastroenterology and hepatology : the official clinical practice journal of the American Gastroenterological Association, S1542-3565(22)00002-7. Advance online publication. https://doi.org/10.1016/j.cgh.2021.12.044
212. Calle, R. A., Amin, N. B., Carvajal-Gonzalez, S., Ross, T. T., Bergman, A., Aggarwal, S., Crowley, C., Rinaldi, A., Mancuso, J., Aggarwal, N., Somayaji, V., Inglot, M., Tuthill, T. A., Kou, K., Boucher, M., Tesz, G., Dullea, R., Bence, K. K., Kim, A. M., Pfefferkorn, J. A., … Esler, W. P. (2021). ACC inhibitor alone or co-administered with a DGAT2 inhibitor in patients with non-alcoholic fatty liver disease: two parallel, placebo-controlled, randomized phase 2a trials. Nature medicine, 27(10), 1836–1848. https://doi.org/10.1038/s41591-021-01489-1.
213. McGarry, J. D., Mannaerts, G. P., & Foster, D. W. (1977). A possible role for malonyl-CoA in the regulation of hepatic fatty acid oxidation and ketogenesis. The Journal of clinical investigation, 60(1), 265–270. https://doi.org/10.1172/JCI108764.
214. Elovson, J., Chatterton, J. E., Bell, G. T., Schumaker, V. N., Reuben, M. A., Puppione, D. L., Reeve, J. R., Jr, & Young, N. L. (1988). Plasma very low-density lipoproteins contain a single molecule of apolipoprotein B. Journal of lipid research, 29(11), 1461–1473.
215. Kesäniemi, Y. A., Beltz, W. F., & Grundy, S. M. (1985). Comparisons of metabolism of apolipoprotein B in normal subjects, obese patients, and patients with coronary heart disease. The Journal of clinical investigation, 76(2), 586–595. https://doi.org/10.1172/JCI112010.

216. Cohn, J. S., Wagner, D. A., Cohn, S. D., Millar, J. S., & Schaefer, E. J. (1990). Measurement of very low density and low density lipoprotein apolipoprotein (Apo) B-100 and high density lipoprotein Apo A-I production in human subjects using deuterated leucine. Effect of fasting and feeding. The Journal of clinical investigation, 85(3), 804–811. https://doi.org/10.1172/JCI114507.
217. Bilz, S., Wagner, S., Schmitz, M., Bedynek, A., Keller, U., & Demant, T. (2004). Effects of atorvastatin versus fenofibrate on apoB-100 and apoA-I kinetics in mixed hyperlipidemia. Journal of lipid research, 45(1), 174–185. https://doi.org/10.1194/jlr.M300309-JLR200
218. Matthan, N. R., Jalbert, S. M., Lamon-Fava, S., Dolnikowski, G. G., Welty, F. K., Barrett, H. R., Schaefer, E. J., & Lichtenstein, A. H. (2005). TRL, IDL, and LDL apolipoprotein B-100 and HDL apolipoprotein A-I kinetics as a function of age and menopausal status. Arteriosclerosis, thrombosis, and vascular biology, 25(8), 1691–1696. https://doi.org/10.1161/01.ATV.0000172629.12846.b8.
219. LINDGREN, F. T., NICHOLS, A. V., FREEMAN, N. K., WILLS, R. D., WING, L., & GULLBERG, J. E. (1964). ANALYSIS OF LOW-DENSITY LIPOPROTEINS BY PREPARATIVE ULTRACENTRIFUGATION AND REFRACTOMETRY. Journal of lipid research, 5, 68–74.
220. Welty, F. K., Lichtenstein, A. H., Barrett, P. H., Dolnikowski, G. G., & Schaefer, E. J. (1999). Human apolipoprotein (Apo) B-48 and ApoB-100 kinetics with stable isotopes. Arteriosclerosis, thrombosis, and vascular biology, 19(12), 2966–2974. https://doi.org/10.1161/01.atv.19.12.2966.
221. Ross, T. T., Crowley, C., Kelly, K. L., Rinaldi, A., Beebe, D. A., Lech, M. P., Martinez, R. V., Carvajal-Gonzalez, S., Boucher, M., Hirenallur-Shanthappa, D., Morin, J., Opsahl, A. C., Vargas, S. R., Bence, K. K., Pfefferkorn, J. A., & Esler, W. P. (2020). Acetyl-CoA Carboxylase Inhibition Improves Multiple Dimensions of NASH Pathogenesis in Model Systems. Cellular and molecular gastroenterology and hepatology, 10(4), 829–851. https://doi.org/10.1016/j.jcmgh.2020.06.001.
222. Staels, B., Dallongeville, J., Auwerx, J., Schoonjans, K., Leitersdorf, E., & Fruchart, J. C. (1998). Mechanism of action of fibrates on lipid and lipoprotein metabolism. Circulation, 98(19), 2088–2093. https://doi.org/10.1161/01.cir.98.19.2088.
223. Watts, G. F., Barrett, P. H., Ji, J., Serone, A. P., Chan, D. C., Croft, K. D., Loehrer, F., & Johnson, A. G. (2003). Differential regulation of lipoprotein kinetics by atorvastatin and fenofibrate in subjects with the metabolic syndrome. Diabetes, 52(3), 803–811. https://doi.org/10.2337/diabetes.52.3.803.
224. Caslake, M. J., Packard, C. J., Gaw, A., Murray, E., Griffin, B. A., Vallance, B. D., & Shepherd, J. (1993). Fenofibrate and LDL metabolic heterogeneity in hypercholesterolemia. Arteriosclerosis and thrombosis : a journal of vascular biology, 13(5), 702–711. https://doi.org/10.1161/01.atv.13.5.702.
225. Hogue, J. C., Lamarche, B., Deshaies, Y., Tremblay, A. J., Bergeron, J., Gagné, C., & Couture, P. (2008). Differential effect of fenofibrate and atorvastatin on in vivo kinetics of apolipoproteins B-100 and B-48 in subjects with type 2 diabetes mellitus with marked hypertriglyceridemia. Metabolism: clinical and experimental, 57(2), 246–254. https://doi.org/10.1016/j.metabol.2007.09.008.
226. Fabbrini, E., Mohammed, B. S., Korenblat, K. M., Magkos, F., McCrea, J., Patterson, B. W., & Klein, S. (2010). Effect of fenofibrate and niacin on intrahepatic triglyceride content,

very low-density lipoprotein kinetics, and insulin action in obese subjects with nonalcoholic fatty liver disease. The Journal of clinical endocrinology and metabolism, 95(6), 2727–2735. https://doi.org/10.1210/jc.2009-2622.

227. Charlton, M., Sreekumar, R., Rasmussen, D., Lindor, K., & Nair, K. S. (2002). Apolipoprotein synthesis in nonalcoholic steatohepatitis. Hepatology (Baltimore, Md.), 35(4), 898–904. https://doi.org/10.1053/jhep.2002.32527.
228. Kuo, T., Harris, C. A., and Wang, J. C. (2013) Metabolic functions of glucocorticoid receptor in skeletal muscle. Mol Cell Endocrinol 380, 79-88.
229. Bodine, S. C., and Furlow, J. D. (2015) Glucocorticoids and Skeletal Muscle. Advances in experimental medicine and biology 872, 145-176.
230. Rose, A. J., and Herzig, S. (2013) Metabolic control through glucocorticoid hormones: an update. Mol Cell Endocrinol 380, 65-78.
231. Kuo, T., McQueen, A., Chen, T. C., and Wang, J. C. (2015) Regulation of Glucose Homeostasis by Glucocorticoids. Advances in experimental medicine and biology 872, 99-126.
232. Magomedova, L., and Cummins, C. L. (2015) Glucocorticoids and Metabolic Control. Handb Exp Pharmacol.
233. Kuo, T., Lew, M. J., Mayba, O., Harris, C. A., Speed, T. P., and Wang, J. C. (2012) Genome-wide analysis of glucocorticoid receptor-binding sites in myotubes identifies gene networks modulating insulin signaling. Proc Natl Acad Sci U S A 109, 11160-11165.
234. Cantley, L. C. (2002) The phosphoinositide 3-kinase pathway. Science 296, 1655-1657
235. Jean, S., and Kiger, A. A. (2014) Classes of phosphoinositide 3-kinases at a glance. J Cell Sci 127, 923-928.
236. Hemmings, B. A., and Restuccia, D. F. (2012) PI3K-PKB/Akt pathway. Cold Spring Harb Perspect Biol 4, a011189.
237. Barbour, L. A., Mizanoor Rahman, S., Gurevich, I., Leitner, J. W., Fischer, S. J., Roper, M. D., Knotts, T. A., Vo, Y., McCurdy, C. E., Yakar, S., Leroith, D., Kahn, C. R., Cantley, L. C., Friedman, J. E., and Draznin, B. (2005) Increased P85alpha is a potent negative regulator of skeletal muscle insulin signaling and induces in vivo insulin resistance associated with growth hormone excess. J Biol Chem 280, 37489-37494.
238. Taniguchi, C. M., Aleman, J. O., Ueki, K., Luo, J., Asano, T., Kaneto, H., Stephanopoulos, G., Cantley, L. C., and Kahn, C. R. (2007) The p85alpha regulatory subunit of phosphoinositide 3-kinase potentiates c-Jun N-terminal kinase-mediated insulin resistance. Mol Cell Biol 27, 2830-2840.
239. Mauvais-Jarvis, F., Ueki, K., Fruman, D. A., Hirshman, M. F., Sakamoto, K., Goodyear, L. J., Iannacone, M., Accili, D., Cantley, L. C., and Kahn, C. R. (2002) Reduced expression of the murine p85alpha subunit of phosphoinositide 3-kinase improves insulin signaling and ameliorates diabetes. J Clin Invest 109, 141-149.
240. Terauchi, Y., Tsuji, Y., Satoh, S., Minoura, H., Murakami, K., Okuno, A., Inukai, K., Asano, T., Kaburagi, Y., Ueki, K., Nakajima, H., Hanafusa, T., Matsuzawa, Y., Sekihara, H., Yin, Y., Barrett, J. C., Oda, H., Ishikawa, T., Akanuma, Y., Komuro, I., Suzuki, M., Yamamura, K., Kodama, T., Suzuki, H., Yamamura, K., Kodama, T., Suzuki, H., Koyasu, S., Aizawa, S., Tobe, K., Fukui, Y., Yazaki, Y., and Kadowaki, T. (1999) Increased insulin sensitivity and hypoglycaemia in mice lacking the p85 alpha subunit of phosphoinositide 3-kinase. Nat Genet 21, 230-235.

241. Luo, J., Field, S. J., Lee, J. Y., Engelman, J. A., and Cantley, L. C. (2005) The p85 regulatory subunit of phosphoinositide 3-kinase down-regulates IRS-1 signaling via the formation of a sequestration complex. J Cell Biol 170, 455-464.
242. Chagpar, R. B., Links, P. H., Pastor, M. C., Furber, L. A., Hawrysh, A. D., Chamberlain, M. D., and Anderson, D. H. (2010) Direct positive regulation of PTEN by the p85 subunit of phosphatidylinositol 3-kinase. Proc Natl Acad Sci U S A 107, 5471-5476.
243. Cheung, L. W., Walkiewicz, K. W., Besong, T. M., Guo, H., Hawke, D. H., Arold, S. T., and Mills, G. B. (2015) Regulation of the PI3K pathway through a p85alpha monomer-homodimer equilibrium. eLife 4, e06866.
244. Luo, J., Sobkiw, C. L., Hirshman, M. F., Logsdon, M. N., Li, T. Q., Goodyear, L. J., and Cantley, L. C. (2006) Loss of class IA PI3K signaling in muscle leads to impaired muscle growth, insulin response, and hyperlipidemia. Cell Metab 3, 355-366.
245. Shahbazian, M. D., and Grunstein, M. (2007) Functions of site-specific histone acetylation and deacetylation. Annu Rev Biochem 76, 75-100.
246. Calo, E., and Wysocka, J. (2013) Modification of enhancer chromatin: what, how, and why? Mol Cell 49, 825-837.
247. Bruning, J. C., Michael, M. D., Winnay, J. N., Hayashi, T., Horsch, D., Accili, D., Goodyear, L. J., and Kahn, C. R. (1998) A muscle-specific insulin receptor knockout exhibits features of the metabolic syndrome of NIDDM without altering glucose tolerance. Mol Cell 2, 559-569.
248. Paakinaho, V., Makkonen, H., Jaaskelainen, T., and Palvimo, J. J. (2010) Glucocorticoid receptor activates poised FKBP51 locus through long-distance interactions. Mol Endocrinol 24, 511-525.
249. Franke, T. F., Yang, S. I., Chan, T. O., Datta, K., Kazlauskas, A., Morrison, D. K., Kaplan, D. R., and Tsichlis, P. N. (1995) The protein kinase encoded by the Akt proto-oncogene is a target of the PDGF-activated phosphatidylinositol 3-kinase. Cell 81, 727-736.
250. Schiaffino, S. (2018) Muscle fiber type diversity revealed by anti-myosin heavy chain antibodies. FEBS J 285, 3688-3694.
251. Kammoun, M., Cassar-Malek, I., Meunier, B., and Picard, B. (2014) A simplified immunohistochemical classification of skeletal muscle fibres in mouse. Eur J Histochem 58, 2254.
252. Pullen, N., and Thomas, G. (1997) The modular phosphorylation and activation of p70s6k. FEBS Lett 410, 78-82.
253. Gingras, A. C., Gygi, S. P., Raught, B., Polakiewicz, R. D., Abraham, R. T., Hoekstra, M. F., Aebersold, R., and Sonenberg, N. (1999) Regulation of 4E-BP1 phosphorylation: a novel two-step mechanism. Genes Dev 13, 1422-1437.
254. Pause, A., Belsham, G. J., Gingras, A. C., Donze, O., Lin, T. A., Lawrence, J. C., Jr., and Sonenberg, N. (1994) Insulin-dependent stimulation of protein synthesis by phosphorylation of a regulator of 5'-cap function. Nature 371, 762-767.
255. Musa, J., Orth, M. F., Dallmayer, M., Baldauf, M., Pardo, C., Rotblat, B., Kirchner, T., Leprivier, G., and Grunewald, T. G. (2016) Eukaryotic initiation factor 4E-binding protein 1 (4E-BP1): a master regulator of mRNA translation involved in tumorigenesis. Oncogene 35, 4675-4688.
256. Bolster, D. R., Kimball, S. R., and Jefferson, L. S. (2003) Translational control mechanisms modulate skeletal muscle gene expression during hypertrophy. Exerc Sport Sci Rev 31, 111-116.

257. Roux, P. P., and Topisirovic, I. (2018) Signaling Pathways Involved in the Regulation of mRNA Translation. Mol Cell Biol 38.
258. Kalvisa, A., Siersbaek, M. S., Praestholm, S. M., Christensen, L. J. L., Nielsen, R., Stohr, O., Vettorazzi, S., Tuckermann, J., White, M., Mandrup, S., and Grontved, L. (2018) Insulin signaling and reduced glucocorticoid receptor activity attenuate postprandial gene expression in liver. PLoS Biol 16, e2006249.
259. McCurdy, C. E., Schenk, S., Holliday, M. J., Philp, A., Houck, J. A., Patsouris, D., MacLean, P. S., Majka, S. M., Klemm, D. J., and Friedman, J. E. (2012) Attenuated Pik3r1 expression prevents insulin resistance and adipose tissue macrophage accumulation in diet-induced obese mice. Diabetes 61, 2495-2505.
260. Winnay, J. N., Solheim, M. H., Dirice, E., Sakaguchi, M., Noh, H. L., Kang, H. J., Takahashi, H., Chudasama, K. K., Kim, J. K., Molven, A., Kahn, C. R., and Njolstad, P. R. (2016) PI3-kinase mutation linked to insulin and growth factor resistance in vivo. J Clin Invest 126, 1401-1412.
261. Thauvin-Robinet, C., Auclair, M., Duplomb, L., Caron-Debarle, M., Avila, M., St-Onge, J., Le Merrer, M., Le Luyer, B., Heron, D., Mathieu-Dramard, M., Bitoun, P., Petit, J. M., Odent, S., Amiel, J., Picot, D., Carmignac, V., Thevenon, J., Callier, P., Laville, M., Reznik, Y., Fagour, C., Nunes, M. L., Capeau, J., Lascols, O., Huet, F., Faivre, L., Vigouroux, C., and Riviere, J. B. (2013) PIK3R1 mutations cause syndromic insulin resistance with lipoatrophy. American journal of human genetics 93, 141-149.
262. Huang-Doran, I., Tomlinson, P., Payne, F., Gast, A., Sleigh, A., Bottomley, W., Harris, J., Daly, A., Rocha, N., Rudge, S., Clark, J., Kwok, A., Romeo, S., McCann, E., Muksch, B., Dattani, M., Zucchini, S., Wakelam, M., Foukas, L. C., Savage, D. B., Murphy, R., O'Rahilly, S., Barroso, I., and Semple, R. K. (2016) Insulin resistance uncoupled from dyslipidemia due to C-terminal PIK3R1 mutations. JCI Insight 1, e88766.
263. Baehr, L. M., Furlow, J. D., and Bodine, S. C. (2011) Muscle sparing in muscle RING finger 1 null mice: response to synthetic glucocorticoids. J Physiol 589, 4759-4776.
264. Britto, F. A., Begue, G., Rossano, B., Docquier, A., Vernus, B., Sar, C., Ferry, A., Bonnieu, A., Ollendorff, V., and Favier, F. B. (2014) REDD1 deletion prevents dexamethasone-induced skeletal muscle atrophy. Am J Physiol Endocrinol Metab 307, E983-993.
265. Waterlow, J. C., Garlick, P. J., and Millward, D. J. (1978) Protein turnover in mammalian tissues and in the whole body, North-Holland Pub. Co. ;sole distributors for the U.S.A. and Canada, Elsevier North-Holland, Amsterdam ; New York, New York.
266. Schakman, O., Gilson, H., Kalista, S., and Thissen, J. P. (2009) Mechanisms of muscle atrophy induced by glucocorticoids. Horm Res 72 Suppl 1, 36-41.
267. Zheng, B., Ohkawa, S., Li, H., Roberts-Wilson, T. K., and Price, S. R. (2010) FOXO3a mediates signaling crosstalk that coordinates ubiquitin and atrogin-1/MAFbx expression during glucocorticoid-induced skeletal muscle atrophy. Faseb J 24, 2660-2669.
268. Waddell, D. S., Baehr, L. M., van den Brandt, J., Johnsen, S. A., Reichardt, H. M., Furlow, J. D., and Bodine, S. C. (2008) The glucocorticoid receptor and FOXO1 synergistically activate the skeletal muscle atrophy-associated MuRF1 gene. Am J Physiol Endocrinol Metab 295, E785-797.
269. Shimizu, N., Yoshikawa, N., Ito, N., Maruyama, T., Suzuki, Y., Takeda, S., Nakae, J., Tagata, Y., Nishitani, S., Takehana, K., Sano, M., Fukuda, K., Suematsu, M., Morimoto, C., and Tanaka, H. (2011) Crosstalk between glucocorticoid receptor and nutritional sensor mTOR in skeletal muscle. Cell Metab 13, 170-182.

270. Shah, O. J., Kimball, S. R., and Jefferson, L. S. (2000) Acute attenuation of translation initiation and protein synthesis by glucocorticoids in skeletal muscle. Am J Physiol Endocrinol Metab 278, E76-82.
271. Liu, Z., Li, G., Kimball, S. R., Jahn, L. A., and Barrett, E. J. (2004) Glucocorticoids modulate amino acid-induced translation initiation in human skeletal muscle. Am J Physiol Endocrinol Metab 287, E275-281.
272. Donnelly, N., Gorman, A. M., Gupta, S., and Samali, A. (2013) The eIF2alpha kinases: their structures and functions. Cellular and molecular life sciences : CMLS 70, 3493-3511.
273. Costa-Mattioli, M., and Walter, P. (2020) The integrated stress response: From mechanism to disease. Science 368.
274. Kuo, T., Chen, T. C., Lee, R. A., Nguyen, N. H. T., Broughton, A. E., Zhang, D., and Wang, J. C. (2017) Pik3r1 Is Required for Glucocorticoid-Induced Perilipin 1 Phosphorylation in Lipid Droplet for Adipocyte Lipolysis. Diabetes 66, 1601-1610.
275. Bulut, G. B., Sulahian, R., Yao, H., and Huang, L. J. (2013) Cbl ubiquitination of p85 is essential for Epo-induced EpoR endocytosis. Blood 122, 3964-3972.
276. Chamberlain, M. D., Berry, T. R., Pastor, M. C., and Anderson, D. H. (2004) The p85alpha subunit of phosphatidylinositol 3'-kinase binds to and stimulates the GTPase activity of Rab proteins. J Biol Chem 279, 48607-48614.
277. Park, S. W., Zhou, Y., Lee, J., Lu, A., Sun, C., Chung, J., Ueki, K., and Ozcan, U. (2010) The regulatory subunits of PI3K, p85alpha and p85beta, interact with XBP-1 and increase its nuclear translocation. Nat Med 16, 429-437.
278. Luo, J., McMullen, J. R., Sobkiw, C. L., Zhang, L., Dorfman, A. L., Sherwood, M. C., Logsdon, M. N., Horner, J. W., DePinho, R. A., Izumo, S., and Cantley, L. C. (2005) Class IA phosphoinositide 3-kinase regulates heart size and physiological cardiac hypertrophy. Mol Cell Biol 25, 9491-9502.
279. Price, J. C., Khambatta, C. F., Li, K. W., Bruss, M. D., Shankaran, M., Dalidd, M., Floreani, N. A., Roberts, L. S., Turner, S. M., Holmes, W. E., and Hellerstein, M. K. (2012) The effect of long term calorie restriction on in vivo hepatic proteostatis: a novel combination of dynamic and quantitative proteomics. Molecular & cellular proteomics : MCP 11, 1801-1814.
280. Bergmeister, K. D., Groger, M., Aman, M., Willensdorfer, A., Manzano-Szalai, K., Salminger, S., and Aszmann, O. C. (2017) A Rapid Automated Protocol for Muscle Fiber Population Analysis in Rat Muscle Cross Sections Using Myosin Heavy Chain Immunohistochemistry. Journal of visualized experiments : JoVE.
281. Ringseis, R., Gessner, D. K., Beer, A. M., Albrecht, Y., Wen, G., Most, E., Kruger, K., and Eder, K. (2020) Nicotinic Acid Improves Endurance Performance of Mice Subjected to Treadmill Exercise. Metabolites 10.
282. Fan, W., Waizenegger, W., Lin, C. S., Sorrentino, V., He, M. X., Wall, C. E., Li, H., Liddle, C., Yu, R. T., Atkins, A. R., Auwerx, J., Downes, M., and Evans, R. M. (2017) PPARdelta Promotes Running Endurance by Preserving Glucose. Cell Metab 25, 1186-1193 e1184.
283. UniProt Consortium, T. (2018) UniProt: the universal protein knowledgebase. Nucleic Acids Res 46, 2699.
284. Huang da, W., Sherman, B. T., and Lempicki, R. A. (2009) Systematic and integrative analysis of large gene lists using DAVID bioinformatics resources. Nat Protoc 4, 44-57.

285. Dennis, G., Jr., Sherman, B. T., Hosack, D. A., Yang, J., Gao, W., Lane, H. C., and Lempicki, R. A. (2003) DAVID: Database for Annotation, Visualization, and Integrated Discovery. Genome biology 4, P3.
286. Ross, A. B., Langer, J. D., & Jovanovic, M. (2021). Proteome Turnover in the Spotlight: Approaches, Applications, and Perspectives. Molecular & cellular proteomics : MCP, 20, 100016. https://doi.org/10.1074/mcp.R120.002190